

PL-CP-- 91-3003

SL# 31285 cy2

AFFTC TECH LIB EAFB, CA



5 0619 01188049 5

PL-CP--

91-3003

**PROCEEDINGS OF THE HIGH ENERGY
DENSITY MATTER (HEDM) CONFERENCE
Held 24-27 February 1991 in Albuquerque, NM**

M.E. Cordonnier

October 1991

Special Report

APPROVED FOR PUBLIC RELEASE; DISTRIBUTION UNLIMITED.



**PHILLIPS LABORATORY
Propulsion Directorate
AIR FORCE SYSTEMS COMMAND
EDWARDS AIR FORCE BASE CA 93523-5000**

NOTICE

When U.S. Government drawings, specifications, or other data are used for any purpose other than a definitely related Government procurement operation, the fact that the Government may have formulated, furnished, or in any way supplied the said drawings, specifications, or other data, is not to be regarded by implication or otherwise, or in any way licensing the holder or any other person or corporation, or conveying any rights or permission to manufacture, use or sell any patented invention that may be related thereto.

FOREWORD

This special report was submitted upon completion of the compilation of the High Energy Density Matter (HEDM) conference proceedings, February 1991, under JON: 573000N2 by the OLAC PL/RFE Branch at the Phillips Laboratory (AFSC), Edwards AFB CA 93523-5000. OLAC Project Manager was Michelle Cordonnier.

This report has been reviewed and is approved for release and distribution in accordance with the distribution statement on the cover and on the SF Form 298.

Michelle E. Cordonnier

MICHELLE E. CORDONNIER
Editor

Stephen L. Rodgers

STEPHEN L. RODGERS
Chief, Emerging Technologies Branch

FOR THE COMMANDER

David W. Lewis

DAVID W. LEWIS, MAJOR, USAF
Acting Director
Fundamental Technologies Division

Ranney G. Adams

RANNEY G. ADAMS
Public Affairs Director

REPORT DOCUMENTATION PAGE

Form Approved
OMB No. 0704-0183

Public reporting burden for this collection of information is estimated to average 1 hour per response, including the time for reviewing instructions, searching existing data sources, gathering and maintaining the data needed, and completing and reviewing the collection of information. Send comments regarding this burden estimate or any other aspect of this collection of information, including suggestions for reducing this burden, to Washington Headquarters Services, Directorate for Information Operations and Reports, 1215 Jefferson Davis Highway, Suite 1204, Arlington, VA 22202-4302, and to the Office of Management and Budget, Paperwork Reduction Project (0704-0188), Washington, DC 20503.

1. AGENCY USE ONLY (Leave blank)			2. REPORT DATE Sep 1991	3. REPORT TYPE AND DATES COVERED Special; 90/03 to 91/02	
4. TITLE AND SUBTITLE Proceedings of the High Energy Density Matter (HEDM) Conference Held 24-27 February 1991 in Albuquerque, NM			5. FUNDING NUMBERS PE: 62302F PR: 5730 TA: 00N2		
6. AUTHOR(S) Michelle E. Cordonnier, editor					
7. PERFORMING ORGANIZATION NAME(S) AND ADDRESS(ES) Phillips Laboratory (AFSC) Propulsion Directorate Edwards Air Force Base CA 93523-5000			8. PERFORMING ORGANIZATION REPORT NUMBER PL-CP-91-3003		
9. SPONSORING/MONITORING AGENCY NAME(S) AND ADDRESS(ES)			10. SPONSORING/MONITORING AGENCY REPORT NUMBER		
11. SUPPLEMENTARY NOTES Extended abstracts from the Fifth High Energy Density Matter Contractors Conference					
12a. DISTRIBUTION/AVAILABILITY STATEMENT Approved for public release. Distribution is unlimited.			12b. DISTRIBUTION CODE		
13. ABSTRACT (Maximum 200 words) This report documents the information presented at the fifth annual High Energy Density Matter (HEDM) Contractors Conference held 24-27 February 1991 in Albuquerque, NM. This report contains the extended abstracts of the presentations, oral and poster, given by Air Force funded contractors and by in-house researchers from the Phillips Laboratory.					
14. SUBJECT TERMS HEDM, High Energy Density Matter, propellant, CBES, chemically bound excited states, metastability, spectroscopy, solid			15. NUMBER OF PAGES 298		
			16. PRICE CODE		
17. SECURITY CLASSIFICATION OF REPORT Unclassified	18. SECURITY CLASSIFICATION OF THIS PAGE Unclassified	19. SECURITY CLASSIFICATION OF ABSTRACT Unclassified	20. LIMITATION OF ABSTRACT SAR		

14. (continued)

hydrogen, matrices, dication, metallic hydrogen, ab initio calculations, oxidizers, potential energy surfaces, surface crossing, laser spectroscopy, Fourier transform spectroscopy, cluster-impact fusion, hypervalent anions, HNIW, HN_3 , hydrogen azide, FN_3 , fluorine azide, photodynamics, photodissociation, cryogenic matrices, infrared spectroscopy, slater-type orbitals, momentum space, Fock hypersphere, N_6 , matrix, nitrocyclopropenes, electronic spectroscopy, supersonic beam, metastable metals, metastable materials, metastable ions, lithium-aluminum, stability, amorphous materials, ultra high resolution spectroscopy, isotopic substitution, modeling studies, radiationless decay, state-resolved dynamics, photoelectron spectroscopy, matrix materials, metastable molecules, van der Waals interaction, solid rare gases, spin-forbidden, state-resolved dynamics, alkali metal atoms, xenon(II) cations, tritiated solid hydrogen.

Table of Contents

Introduction.....	ix
Technical Program Agenda.....	xi
Expected Attendance List.....	xv
Extended Abstracts of Oral Presentations	
"Survey of Potential Novel High Energy Content Metastable Materials," W. C. Stwalley, A. M. Lyyra, and W. T. Zemke University of Iowa.....	1
"Stability of High Energy Amorphous Materials," C. A. Wight University of Utah.....	7
"Short Wavelength Chemical Lasers: A Here and Now Application of Chemically Bound Excited State Molecules," D. J. Benard, B. K. Winker, and T. A. Seder Rockwell International Science Center.....	11
"Is the Hydrogen-A Phase Metallic," I. F. Silvera Harvard University.....	17
"Ultrahigh Resolution Spectroscopy of Solid Hydrogen," T. Oka University of Chicago.....	23
"Modeling Studies of Atom Production, Recombination and Storage in Solid Hydrogen," J. R. Gaines and Y. Cao University of Hawaii.....	31
"Kinetics of Hydrogen Atom Storage in Condensed Molecular Hydrogen: Theory," C. A. Vause, III University of Hawaii at Manoa.....	37
"Enhancing Atom Densities in Solid Hydrogen by Isotopic Substitution," G. W. Collins, P. C. Souers, E. R. Mapoles, and F. Magnotta Lawrence Livermore National Laboratory.....	43
"O(³ P) Atom Lifetimes and Mobilities in Xenon Matrices," H. Krueger and E. Weitz Northwestern University.....	49

"Theoretical/Experimental Studies of Dications," W. C. Lineberger, S. V. O'Neil, and S. R. Leone University of Colorado.....	55
"Metal Atoms in Solid Rare Gases," M. E. Fajardo Phillips Laboratory.....	61
"Ab Initio Calculations on Low-Lying States of AlLi," M. E. Rosenkrantz University of Dayton Research Institute.....	67
"Electronic Structure and Thermochemical Properties of Advanced Oxidizers," H. H. Michels and J. A. Montgomery, Jr. United Technologies Research Center.....	75
"Potential Energy Surfaces and Dynamics of Potential HEDM Molecules," M. S. Gordon, T. L. Windus, K. A. Nguyen, and N. Matsunaga North Dakota State University.....	83
"Theoretical Studies of Spin-Forbidden and Electronically Nonadiabatic Processes: Actual/Avoided Surface Crossings Spin-Forbidden Radiationless Decay in Dications," D. R. Yarkony The Johns Hopkins University.....	89
"Laser and Fourier Transform Spectroscopy of Novel Propellant Molecules," P. Bernath University of Waterloo.....	95
"Experimental Confirmation of Cluster-Impact Fusion," Y. K. Bae, D. C. Lorents, S. Young, and K. Stalder SRI International.....	101
"Inorganic Halogen Oxidizers," W. W. Wilson and K. O. Christe Rocketdyne.....	111
"Lewis Acid Behavior of Xenon(II) cations and the Synthesis and Characterization of the Hypervalent Anions XeF_5^- , XeF_7^- , XeOF_5^- , IOF_6^- , TeF_7^- , TeF_8^{2-} and IF_8^{2-} " N. T. Arner, H. P. Mercier, M. Rokoss, J. C. P. Sanders, G. J. Schrobilgen, and J. S. Thrasher McMaster University.....	115

"Characterization of HNIW at the Naval Weapons Center," M. P. Nadler, A. T. Nielsen, R. A. Nissan, D. J. Vanderah, and R. Y. Yee Naval Weapons Center.....	119
"Metastability in Molecules," R. J. Bartlett, W. J. Lauderdale, J. F. Stanton, J. Gauss, and K. Ferris University of Florida.....	125
"Potential Surface Control of the Dynamics of the Decomposition of HN ₃ ," M. H. Alexander University of Maryland P. J. Dagdigian The Johns Hopkins University.....	131
"The Reaction of Metal Atoms with HN ₃ and HNCO," P. J. Dagdigian The Johns Hopkins University.....	137
"State-Resolved Dynamics of Intramolecular Relaxations in Superexcited Molecules: Isoelectronic Analogies of BH ₂ and AlH ₂ with NO ₂ ," K. S. Haber, Y. Jiang, G. P. Bryant, Y. -F. Zhu, R. Shehadeh, and E. R. Grant Purdue University.....	143
Extended Abstracts of Poster Presentations	
"Photodynamics in Solids Under High Pressure," E. Sekreta and V. A. Apkarian University of California, Irvine.....	151
"Photodissociation of HN ₃ and (NO) ₂ ," M. P. Casassa, B. R. Foy, J. R. Hetzler, D. S. King, and J. C. Stephenson National Institute of Standards and Technology.....	161
"Trapped Atoms in Cryogenic Matrices--Correlations Between Trapping Sites and MCD Spectra," J. W. Kenney, III Eastern New Mexico University.....	167
"Theoretical Study of HEDM Materials: a-N ₂ O ₂ and LiNe," B. H. Lengsfield III Lawrence Livermore National Laboratory.....	169

"Functionalized Pentacyclo[5.4.0.0 ² ,6.0 ³ ,10.0.5,9]undecanes (Non-Photochemically)," S. C. Suri and N. Q. Vu University of Dayton Research Institute.....	173
"Theoretical Studies of the Spectroscopy of Alkali Metal Atoms in Condensed Phases: Inert Gases and Hydrogen," N. R. Kestner, J. Yang, N. Brener, and S. Gupta Louisiana State University.....	177
"Infrared Spectroscopy of SF ₆ In and On Argon Clusters: New Results for and Extended Range of Cluster Sizes," S. Goyal, G. N. Robinson, D. L. Schutt and G. Scoles Princeton University.....	183
"Multicenter Molecular Integrals Over Slater-Type Orbitals: Momentum Space and the Fock Hypershphere," C. A. Weatherford Florida A&M University.....	187
"Interacting Correlated Fragments Treatment of Li _n -H ₂ van der Waals Interaction," D. D. Konowalow University of Dayton Research Institute.....	197
"Novel Bonding in Molecules: Metastable Molecular Fuels," R. P. Saxon SRI International.....	203
"Optical and Thermal Energy Discharge from Tritiated Solid Hydrogen," F. Magnotta, E. R. Mapoles, G. W. Collins, and P. C. Souers Lawrence Livermore National Laboratory.....	209
"Variable Energy Photoelectron Spectroscopy of Volatile Fluorides," R. G. Cavell University of Alberta.....	217
"Photochemical Synthesis of N ₆ ," T. Seder Rockwell International Science Center.....	221
"Matrix Reactions of Boron Atoms with Molecular Oxygen: Infrared Spectra of BO, BO ₂ , B ₂ O ₂ , B ₂ O ₃ and BO ₂ ⁻ in Solid Argon," T. R. Burkholder, G. D. Brabson, and L. Andrews University of Virginia.....	225

"Synthesis and Properties of Novel Nitrocyclopropenes and Ab Initio Calculations on Potential High Energy Density Materials," W. P. Daily University of Pennsylvania.....	231
"Weak Interactions at Metal Atoms and Clusters Studied with Electronic Spectroscopy in Supersonic Beams," M. A. Duncan University of Georgia.....	237
"Metastable Metals in Matrix Materials," N. Presser and D. Randall The Aerospace Corporation.....	243
"High Symmetry Metastable Molecules," H. Helm, C. Bordas, M. J. Dyer, D. L. Huestis, D. C. Lorents, Y. K. Bae, and H. Bissantz SRI International.....	249
"Theoretical Studies of Metastable Ions: NH ₄ ⁻ and PH ₄ ⁻ ," N. Matsunaga and M. S. Gordon North Dakota State University.....	259
"The Search for Lithium-Aluminum," P. G. Carrick Phillips Laboratory C. R. Brazier University of Dayton Research Institute.....	269

Introduction

The main purpose of the High Energy Density Matter (HEDM) program is to research and develop advanced high energy compounds containing increased energy densities (energy to mass ratios) and greater specific impulses (thrust per weight flow rate of propellant) which will enable spacecraft to carry larger payloads. With these advanced propellants, future space-bound payloads could be possibly four times greater than they are today. Theoretical and experimental research is carried out by in-house researchers at the Phillips Laboratory at Edwards Air Force Base (PL) and through Air Force funded contracts with numerous researchers in the academic and industrial communities.

The HEDM program is administered by a steering group made up of representatives from the Propulsion Directorate of the Phillips Laboratory and the Air Force Office of Scientific Research (AFOSR). A technical panel administered by the National Research Council (NRC) and chaired by Dr William Stwalley assists the steering group in ensuring the high technical content of the program.

Annual conferences, alternately hosted by the AFOSR and the PL, are arranged in order to allow in-house and contract researchers to report on their progress and new developments. The Fifth High Energy Density Matter Contractors Conference was held 24-28 February 1991 in Albuquerque, New Mexico. The conference consisted of a poster session Sunday afternoon, followed by an oral presentation session on Monday, Tuesday, and Wednesday. This report documents the information presented at this conference and contains extended abstracts of all presentations, poster and oral, given at the conference.

The next High Energy Density Matter Conference is scheduled for April 1992.

1991 HIGH ENERGY DENSITY MATERIALS CONFERENCE

Technical Program

Sunday, 24 February 1991

1:00 - 6:00 PM: Registration, Reception and Poster Session

Monday, 25 February 1991

7:00 AM - Continental Breakfast

8:00 - Welcome by Dr Joseph Janni, Chief Scientist, Phillips Laboratory

8:15 - "HEDM Program Overview," Stephen L. Rodgers and Lt Col Larry Burggraf

8:30 - "Survey of Potential Novel High Energy Content Metastable Materials," William C. Stwalley, University of Iowa

9:00 - "Stability of High Energy Amorphous Materials," Charles A. Wight, University of Utah

9:30 - BREAK

10:00 - "Visible Wavelength Chemical Lasers: A Here and Now Application of Chemically Bound Excited State Molecules," D.J. Benard, Rockwell International Science Center

10:30 - "Is the Hydrogen - A Phase Metallic?," Isaac F. Silvera, Harvard University

11:00 - LUNCH

1:00 - "Ultrahigh Resolution Spectroscopy of Solid Hydrogen," Takeshi Oka, University of Chicago

1:30 - "Modeling Studies of Atom Production, Recombination and Storage in Solid Hydrogen," James R. Gaines and Yue Cao, University of Hawaii

2:00 - "Kinetics of Hydrogen Atom Storage in Condensed Molecular Hydrogen: Theory," Chester A. Vause III, University of Hawaii

2:30 - BREAK

3:00 - "Enhancing Atom Densities in Solid Hydrogen by Isotopic Substitution," Gilbert Collins, Evan Mapoles, Frank Magnotta, and Clark Souers, Lawrence Livermore National Laboratory

3:30 - "Diffusion of O Atoms in Condensed Phase Rare Gases," Eric Weitz, Northwestern University

4:00 - "Experimental/Theoretical Studies of Dications," W. Carl Lineberger, Stephen R. Leone, and Stephen V. O'Neil, Joint Institute for Laboratory Astrophysics, University of Colorado

4:30 - ADJOURN

6:00 - RECEPTION

7:00 - BANQUET

Tuesday, 26 February 1991

7:00 AM - Continental Breakfast

8:00 - "Metal Atoms in Solid Rare Gases," Mario E. Fajardo, Propulsion Directorate, Phillips Laboratory

8:30 - "Ab initio Calculations on Low Lying Electronic States of AlLi," Marcy E. Rosenkrantz, University of Dayton Research Institute

9:00 - "Electronic Structure and Thermochemical Properties of Advanced Oxidizers: OF₆ and Dinitramide Salts," H.H. Michels and J.A. Montgomery, Jr., United Technologies Research Center

9:30 - BREAK

10:00 - "Potential Energy Surfaces and Dynamics of Potential HEDM Compounds," Mark Gordon, Theresa Windus, Kiet Nguyen, and Nikita Matsunaga, North Dakota State University

10:30 - "Theoretical Studies of Spin-Forbidden and Electronically Nonadiabatic Processes: Actual/Avoided Surface Crossings Spin-Forbidden Radiationless Decay in Dications," David R. Yarkony, The Johns Hopkins University

11:00 - LUNCH

1:00 - "Laser and Fourier Transform Spectroscopy of Novel Propellant Molecules," Peter Bernath, University of Arizona and University of Waterloo

1:30 - "Experimental Confirmation of Cluster-Impact Fusion," Y.K. Bae, D.C. Lorents, K. Stalder, and S. Young, SRI International

2:00 - BREAK

2:30 - "Inorganic Halogen Oxidizers," Karl Christe and William Wilson, Rocketdyne

3:00 - "Lewis Acid Behavior of Xenon(II) Cations and the Synthesis and Characterization of the Hypervalent Anions XeF₅⁻, XeF₇⁻, XeOF₅⁻, IOF₆⁻, TeF₇⁻, TeF₈²⁻, and IF₈⁻," Neil T. Arner, Helene P. Mercier, Michael Rokoss, Jeremy C.P. Sanders, G.J. Schrobilgen, and Joseph S. Thrasher, McMaster University

3:30 - "Characterization of HNIW at the Naval Weapons Center," M.P. Nadler, A.T. Nielson, R.A. Nissan, D.J. Vanderah, and R.Y. Yee, Naval Weapons Center

4:00 - ADJOURN

Wednesday, 27 February 1990

7:00 AM - Continental Breakfast

8:00 - "Metastability in Molecules," Rodney J. Bartlett, University of Florida

8:30 - "Sulfur clusters: Structure, Infrared, and Raman Spectra of Cyclo-S₆ and Comparison with the Hypothetical Cyclo-O₆ Molecule," Henry F. Schaefer III, University of Georgia

9:00 - "Potential Surface Control of the Dynamics of Decomposition of Azides," Millard Alexander,
University of Maryland

9:30 - BREAK

10:00 - "The Reaction of Metal Atoms with HN₃ and HNCO," Paul Dagdigian, The Johns Hopkins University

10:30 - "State-Resolved Dynamics of Intramolecular Relaxation in Superexcited Molecules," K.S. Haber,
Y. Jiang, G.P. Bryant, and E.R. Grant, Purdue University

11:00 - ADJOURN

POSTERS

"Photodynamics in Solids Under High Pressure," V.A. Apkarian, University of California, Irvine

"The Energy Increase and Lattice Distortions Due to Atomic Hydrogen Impurities in Solid Hydrogen Hosts," Yue
Cao and James R. Gaines, University of Hawaii

"Photodissociation of HN₃ and (NO)₂," Michael Casassa, NIST

"Diamond Fuel Tanks for Metallic Hydrogen Fuel," Robert L. Forward, Forward Unlimited

"Trapped Atoms in Cryogenic Matrices--Correlations Between Trapping Sites and MCD Spectra,"
John W. Kenney, III, Eastern New Mexico University

"Theoretical Study of HEDM Materials: a-N₂O₂, LiNe and N₄," Byron Lengsfield, Lawrence Livermore National
Laboratory

"Samarium (II) Induced Synthesis of Functionalized Pentacyclo[5.4.0.0^{2,6}.0^{3,10}.0^{5,9}]undecane,"
Suresh Chander Suri, University of Dayton Research Institute

"Theoretical Studies of Energetic Nitrogen Molecules (N₄, N₆, N₈) and the Adsorption of FN₃ and HN₃ on
Surfaces," N.E. Brener, N.R. Kestner, J. Callaway, and P. Vashishta, Louisiana State University

"Theoretical Studies of the Spectroscopy of Alkali Metal Atoms in Condensed Phases: Inert Gases and
Hydrogen," N.R. Kestner, J. Yang, S. Gupta, and N.E. Brener, Louisiana State University

"Infrared Photodissociation Spectroscopy of Large Classical and Quantum Clusters: Finite Size Particles Attaining
Bulk-Like Properties," S. Goyal, D.L. Schutt, and G. Scoles, Princeton University

"Molecular Dynamics Simulation of Energetics and Fragmentation of Microclusters," P. Vashishta,
R.K. Kalia, and N.E. Brener, Louisiana State University

"Multicenter Molecular Integrals Over Slater-Type Orbitals: Momentum Space and the Fock Hypersphere," C.A.
Weatherford, Florida A&M University

"LiH₂ and Li₂H₂ Interactions," D.D. Konowalow, University of Dayton Research Institute

"Novel Bonding in Molecules: Metastable Molecular Fuels," Roberta P. Saxon, SRI International

"Molecular States in Ionic Solids and H₂ Matrices," Cleanthes A. Nicolaides, Hellenic Research Foundation

"Optical and Thermal Energy Discharge from Tritiated Solid Hydrogen," Gilbert Collins, Evan Mapoles, Frank Magnotta, and Clark Souers, Lawrence Livermore National Laboratory

"Variable Energy Photoelectron Spectroscopy of Volatile Fluorides," Ronald G. Cavell, University of Alberta

"Photochemical Synthesis of N₆," Thomas Seder, Rockwell International Science Center

"Analysis of the Crystal and Molecular Structure of Explosives," James P. Ritchie, Edward M. Kober, and Ann S. Copenhaver, Los Alamos National Laboratory

"Matrix Reactions of Boron Atoms with Oxygen Molecules. Infrared Spectra of Several Boron-Oxygen Species," T. Burkholder, G.D. Brabson, and L. Andrews, University of Virginia

"Synthesis and Properties of Novel Nitrocyclopropenes and ab initio Calculations on Potential High Energy Density Materials," William Dailey, University of Pennsylvania

"Weak Interactions at Metal Atoms and Clusters Studied with Electronic Spectroscopy in Supersonic Beams," Michael Duncan, University of Georgia

"Metastable Metals in Matrix Materials," N. Presser and D. Randall, The Aerospace Corporation

"High Symmetry Metastable Molecules," H. Helm, M.C. Bordas, M.J. Dyer, D.L. Huestis, D.C. Lorents, Y.K. Bae, and H. Bissantz, SRI International

"Theoretical Studies of Metastable Anions: NH₄⁻ and PH₄⁻," Nikita Matsunaga and Mark S. Gordon, North Dakota State University

Survey of Potential Novel High Energy Content Metastable Materials*

William C. Stwalley¹, A. Marjatta Lyyra² and Warren T. Zemke³

Center for Laser Science and Engineering, University of Iowa, Iowa City, IA
52242

The increase in specific impulse of propellants is of major interest to both the Air Force (e.g. through the activities of the Phillips Laboratory of the Air Force and the related High Energy Density Materials (HEDM) Program involving principally the Phillips Laboratory and the Air Force Office of Scientific Research) and the National Aeronautics and Space Administration (e.g. through the activities of the Lewis Research Center). In 1986, the Air Force convened a workshop at Georgetown University which outlined a focused research program in the area of "High Energy Density Materials", i.e. advanced chemical propellants. The purpose of this program was to pursue concepts both theoretically and experimentally which held (high risk) promise for significant improvements in existing propellants. The standard to exceed in such considerations was "Lox-hydrogen", i.e. $H_2(l) + \frac{1}{2}O_2(l) \rightarrow H_2O(g)$. As shown in Figure 1, this reaction has specific enthalpy of 12.56 MJ/kg, corresponding to an "ideal" specific impulse of 511 seconds and a realistic specific impulse of ~460 seconds (~80% of ideal enthalpy release). It is clear that a precise calculation of realistic specific impulse for a particular propellant is propulsion system dependent. For this reason, a follow-up HEDM workshop in September 1989, organized by the National Research Council, recommended that primary emphasis in the HEDM program focus on propellants with a specific enthalpy of ≥ 15 MJ/kg (corresponding to ~500 seconds realistic specific impulse). Note that even the seemingly modest increase from 460 to 500 seconds is capable of doubling payloads in some systems!

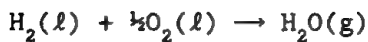
* Supported by NASA Lewis Research Center

¹ Also Department of Chemistry and Department of Physics and Astronomy

² Present address: Department of Physics, Temple University, Philadelphia, PA 19122

³ Permanent address: Department of Chemistry, Wartburg College, Waverly, IA 50677

$$I_{sp} = 1/g\sqrt{2\eta\Delta H}$$



$$\Delta H = \frac{-0.216}{2.015} - \frac{1.628}{16.00} + \frac{57.826}{18.015} = 3.0001 \frac{\text{kcal}}{\text{gram}} = 12.56 \frac{\text{MJ}}{\text{kilogram}}$$

$$I_{sp}(\eta = 1) = \frac{1}{9.80665} \sqrt{2(12.56 \times 10^6)} \text{ seconds} = 511 \text{ seconds}$$

$$I_{sp}(\text{actual}) = 444, 454.5 \text{ seconds} \rightarrow \eta = 0.755, 0.788$$

Figure 1. Specific impulse (I_{sp}) and reaction exothermicity per unit mass (ΔH).

NASA, through its Lewis Research Center, has also been seeking to define promising topics for research in the HEDM area. However, they have commissioned us to survey a much higher risk (but also higher payoff) area: chemical propellants which might produce ≥ 600 seconds specific impulse, or more precisely, chemical reactants which produce ≥ 22 MJ/kg (Table I). It is systems which satisfy this last criterion which we have surveyed during the past year. The results of this survey (of over 700 articles and reports) are being prepared for submission in two parts to the AIAA Journal. The first part of this survey includes neutral species only and will be discussed here in more detail. The second part of this survey focuses on the issue of separated charged ions and is not yet complete.

As an introduction to this survey, consider the thermodynamic measured (or estimated ~) values for chemical reactions involving hydrogen and oxygen

Table I. Reaction specific enthalpy (MJ/kg) and specific impulse (seconds) criteria.

reaction	$\Delta H \left[\frac{\text{MJ}}{\text{kg}} \right]$	I_{sp} (seconds)	
		ideal	realistic (80% of ΔH)
Lox-Hydrogen	12.56	511	~460
Air Force HEDM Program	15	558	~500
NASA Survey	22	671	~600

in Table II. Consider first the reactions of molecular hydrogen, the current fuel of choice, with a variety of pure oxygen species. It is clear that O atoms are dramatically better than any other oxygen compound, not only O₂ and O₃, but also the extensively calculated D_{3h} O₃ species (at least 17 studies since 1967), but also the fascinating set of O_n rings (n = 4, 6, 8, 12) studied by H. F. Schaefer et al. Cyclic O₃, O₄, O₆, O₈ and O₁₂ are all very interesting potential HEDM species, especially if they can be synthesized and stabilized, but they do not meet the NASA criterion for this survey.

Table II. Examples of potential high energy density materials involving hydrogen and oxygen.

reaction	$\Delta H \left(\frac{\text{MJ}}{\text{kg}} \right)$	$I_{sp} (\eta=0.8)$ seconds
H ₂ (l) + O(g) → H ₂ O(g)	28.53	689
H ₂ (l) + $\frac{1}{2}$ O ₂ (l) → H ₂ O(g)	12.56	457
H ₂ (g) + $\frac{1}{2}$ O ₂ (g) → H ₂ O(g)	13.44	473
H ₂ (l) + $\frac{1}{3}$ O ₃ (s) → H ₂ O(g)	14.65	494
H ₂ (l) + $\frac{1}{3}$ O ₃ (g) → H ₂ O(g)	15.94	515
H ₂ (l) + $\frac{1}{3}$ metastable D _{3h} O ₃ (g) → H ₂ O(g)	-17.15	-535
H ₂ (l) + $\frac{1}{4}$ cyclic O ₄ (s) → H ₂ O(g)	-19.1	-564
H ₂ (l) + $\frac{1}{6}$ O ₆ (g) → H ₂ O(g)	-16.6	-525
H ₂ (l) + $\frac{1}{8}$ O ₈ (g) → H ₂ O(g)	-16.6	-525
H ₂ (l) + $\frac{1}{12}$ O ₁₂ (g) → H ₂ O(g)	-16.8	-529
2H(g) + $\frac{1}{2}$ O ₂ (l) → H ₂ O(g)	36.5	780
H ₂ ⁺ (g) + O ⁻ (g) → H ₂ O(g)	102.8	1308
2 metallic H(s) + $\frac{1}{2}$ O ₂ (l) → H ₂ O(g)	?(>22)	?(>600)
2H(g) → H ₂ (g)	209.5	1866
H ⁺ (g) + H ⁻ (g) → H ₂ (g)	834.9	3726

One way of viewing this series is to examine (Figure 1) the large ΔH difference between $O(g)$ and $O_2(g)$ of 15.09 MJ/kg, i.e. between the least stable ("contained atom limit") and most stable (standard state) form of oxygen. As shown in Figure 1, $O_3(g)$ gains only 17% of this difference, while the most energetic compound, cyclic $O_4(g)$ gains only -38% of this difference. Other compounds ($D_{3h} O_3$, O_6 , O_8 , O_{12}) are in the 20-25% range. Clearly stabilization of atoms will provide significantly greater benefits than stabilization of even unstable compounds in this case.

Consider the other atoms which exceed the NASA 22 MJ/kg criterion in reactions with H_2 (Table III). Similar results are found, for example, for nitrogen compounds, carbon compounds, boron compounds and mixed element compounds. For example, on a per atom mass basis, N_4 and N_8 gain roughly half of the $N \rightarrow N_2(g) \Delta H$. In summary atomic fuels, e.g. stabilized in cryogenic molecular solids such as H_2 and O_2 , hold significantly greater promise for high specific impulse than do high energy content molecular fuels.

Table III. Molecular Hydrogen/Contained Atom Limits (all gaseous).

reaction	$\Delta H_{298}(kJ/mole)^*$	$\Delta H \left(\frac{MJ}{kg} \right)$
$\frac{1}{2}H_2 + H \rightarrow H_2$	211	104.0*
$\frac{1}{2}H_2 + Li \rightarrow LiH$	20	2.5
$H_2 + Be \rightarrow BeH_2$	202	18.4
$\frac{1}{2}H_2 + B \rightarrow \frac{1}{2}B_2H_6$	515	37.3*
$2H_2 + C \rightarrow CH_4$	790	49.4*
$\frac{3}{2}H_2 + N \rightarrow NH_3$	519	30.5*
$H_2 + O \rightarrow H_2O$	491	27.3*
$\frac{1}{2}H_2 + F \rightarrow HF$	315	17.6

* Exceeds NASA criterion.

Note also the other reactions at the bottom of Table II. Clearly these species all exceed our 22 MJ/kg criteria, but require either stabilized atomic hydrogen or dilute, separated ions. As noted above, we postpone consideration of ions. Considerable research is already underway on both stored atomic hydrogen and metallic hydrogen. About 20% atomic H in H_2 (i.e. 10% of H_2 dissociated) meets the NASA criterion and nearly 0.5% atomic H has been achieved by

Gaines et al. in samples heavily damaged by tritium β decay.

Finally, it is important to emphasize that we are seeking research concepts not merely for isolated atoms and molecules, but for materials. It is convenient to distinguish between pure high energy density molecular solids or liquids (e.g. $D_{3h}O_3$) versus doped ordinary cryogenic solids (e.g. H_2 , O_2) versus novel solids (e.g. metallic hydrogen). All three categories hold considerable promise, but the doping of ordinary cryogenic solids can be studied immediately, albeit with some difficulty, especially for H_2 . Surprisingly, only 27 of ~3700 references on matrix isolation spectroscopy in D. W. Ball et al. Bibliography of Matrix Isolation Spectroscopy: 1954-1985 (Rice University Press, Houston, 1988) involve H_2 ! The significant results of Fajardo on Li stability in H_2 at 3K for days (reported at this meeting) are quite encouraging for atomic storage. Clearly work on B, C, N and O as well as H is of high interest as well. For example, the reaction of $O + H_2 \rightarrow H_2O$ is spin-forbidden and $\{\ddot{N}\} + H_2 \rightarrow \{\ddot{NH}\} + H$ are endoergic. Of particular significance in such studies of doped solid H_2 are the limits of atomic density which can be achieved. The atomic diffusion and recombination rates will be critically important; they will probably be significantly influenced by the quality of the solid lattice and thus its method of preparation. The study of atoms in H_2 clusters may also be very useful in establishing greater theoretical understanding in bridging to the doped bulk solid.

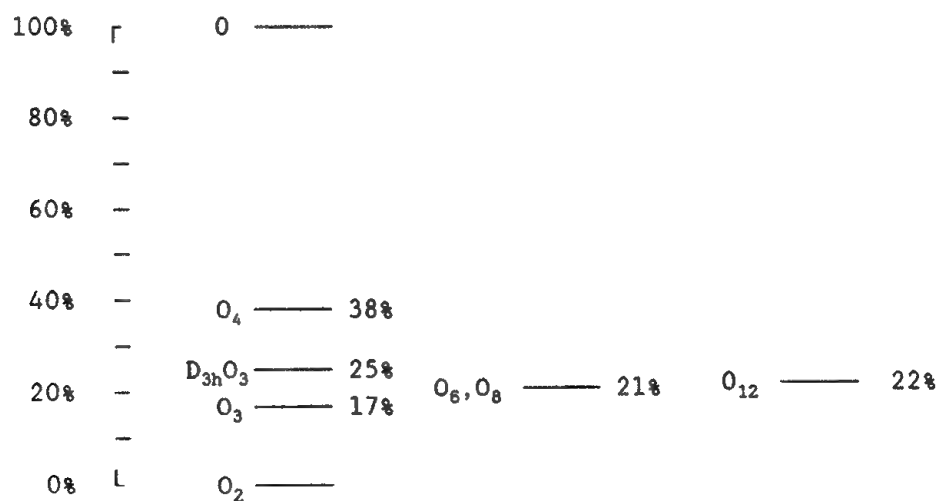


Figure 2. Percentage of the contained atom limit specific enthalpy [$\Delta H_f(O(g)) = \Delta H(H_2(l)+O(g)) - \Delta H(H_2(l)+\frac{1}{2}O_2(g))$] for various pure oxygen compounds.

STABILITY OF HIGH ENERGY AMORPHOUS MATERIALS*

Charles A. Wight

Department of Chemistry
University of Utah
Salt Lake City, UT 84112

Abstract

Thin films of chlorine azide have been formed by vapor deposition onto the surface of an optical substrate at cryogenic temperatures. Amorphous, semi-crystalline, or crystalline films of this energetic material can be made, depending on the deposition rate and substrate temperature. Crystalline films are easily detonated by exposure to the unfocused output of a XeCl excimer laser. Amorphous samples, on the other hand, are significantly desensitized. A few tempered samples formed by rapid vapor deposition could be exploded using a focused laser pulse, but most amorphous samples did not explode at all. The detonation velocity in crystalline samples is about 1330 m/s, but can be decreased to about 640 m/s in the amorphous form. Semi-crystalline samples exhibit intermediate values of the detonation velocity. These results are interpreted in terms of physical fracture of polycrystalline materials at grain boundaries. Heat released by decomposition of energetic molecules at the grain boundaries initiates and sustains the detonation wave as it propagates through the thin film.

Introduction

In their 1987 paper on the synthesis of fluorine azide, Willner *et al.* reported that this material explodes spontaneously when cooled to liquid nitrogen temperature (77 K).¹ This seemed strange to us, since most materials become less reactive at lower temperatures, not more reactive. Benard and Cohn² reported that thin films of FN₃ could be formed at 77 K by vapor deposition onto low temperature optical windows, but these films were highly sensitive to pulsed nitrogen laser-induced detonation. Our informal analysis led us to believe that both of these groups had formed polycrystalline FN₃. We hypothesized that the explosions could be initiated by contraction of the crystal grains during cooling. Internal stresses caused by differential contraction would be concentrated at the grain boundaries, eventually leading to physical fracture of the material. The heat released by decomposition of molecules at the fracture sites could then lead to an explosion.

We further hypothesized that if fluorine azide were formed as an amorphous (disordered) solid, the material might be desensitized with respect to detonation due to the absence of grain boundaries. For technical reasons, it was more convenient to demonstrate this concept with chlorine azide rather than fluorine azide. The two compounds have similar physical and chemical properties. We were able to synthesize small quantities of ClN₃ from NaN₃ and Cl₂ and deposit the purified material as a thin film on the surface of a CsI optical

* Work supported by AL Contract F-04611-90-K-0036

window. Infrared spectra of the films showed that polycrystalline, semi-crystalline or amorphous films could be formed, depending on the deposition rate and substrate temperature. The amorphous films are resistant to pulsed laser detonation, whereas the crystalline films were found to be quite sensitive. The velocity of the detonation wave was found to be sensitive to the degree of crystallinity of the sample, varying from 1330 m/s in crystalline samples to about 640 m/s in amorphous samples.

Batch Synthesis of Chlorine Azide

Chlorine azide was synthesized in a diffusion-pumped glass vacuum manifold, pictured schematically in Figure 1. About 20 mg of sodium azide was placed in finger #1 and evacuated. Approximately 2.5 torr-liter of chlorine gas and 1.5 torr-liter of water vapor were condensed in to the finger, and the mixture was allowed to react at room temperature for 40-80 minutes. Coombe et al. previously reported that moist NaN_3 reacts with chlorine to form the desired chlorine azide product in a continuous flow apparatus.³

Following the reaction period, the gaseous products were condensed into a glass finger (#3 in Figure 1) which had been pre-cooled to 77 K. The product was distilled under vacuum to separate the chlorine azide from small amounts of unreacted Cl_2 as well as H_2O and HN_3 impurities. The sample was then deposited directly onto a sample window (either CsI or quartz) cooled by liquid nitrogen in a stainless steel vacuum dewar vessel equipped with a rotatable shroud and optical windows for obtaining IR or UV absorption spectra of the films.

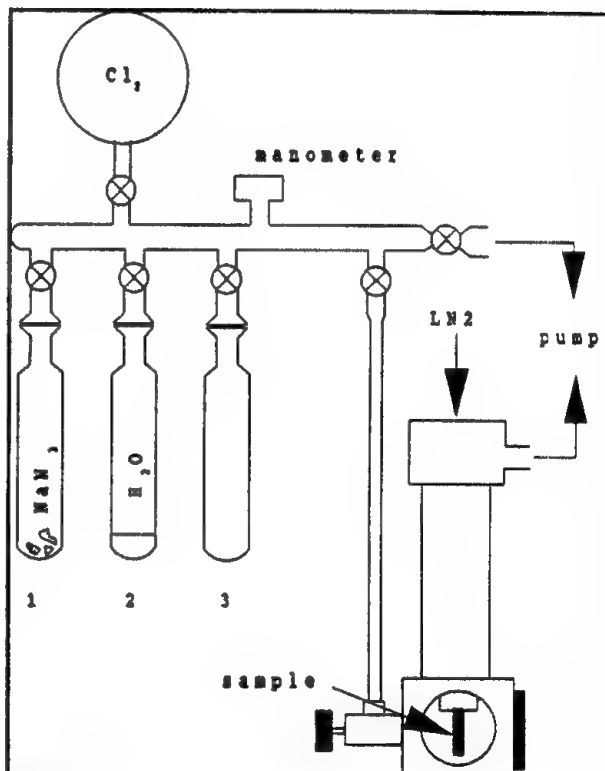


Figure 1

Results

Amorphous samples of ClN_3 were formed by vapor deposition onto a CsI window at 77 K. A portion of the infrared spectrum is shown in Figure 2. Spectra of the amorphous samples were characterized by broad unstructured absorption bands ($\text{FWHM} = 27.5 \text{ cm}^{-1}$ at 2070 cm^{-1}). The breadth of the bands is presumably due to inhomogeneous broadening associated with a distribution of micro-environments of different ClN_3 molecules in the disordered solid.

Crystalline samples were formed by rapid vapor deposition onto a substrate at elevated temperature, usually 120 K. The infrared spectrum in Figure 2 shows that the absorption bands are considerably narrower than their amorphous counterparts because all of the

molecules in the crystal have essentially the same microenvironment. We found that IR spectroscopy was a useful diagnostic for assessing the degree of crystallinity for this compound.

Crystalline samples exposed to the unfocused output of a XeCl excimer laser (308 nm, 15 nm pulse width, 10 mJ/cm² fluence) detonated with unit probability. The explosion was accompanied by a flash of visible light and an audible report, even though the sample was under vacuum at the time of detonation.

Amorphous samples, on the other hand, were quite difficult to detonate with the laser. We found that some samples which had been deposited rapidly onto a 77 K substrate could be detonated with a focused UV laser pulse (approximately 2 J/cm² fluence), but samples which were deposited slowly often did not detonate, even when the laser fluence was high enough to vaporize a small spot from the sample window.

A simple apparatus (shown schematically in Figure 3) was constructed to measure the detonation velocity of amorphous and polycrystalline samples. The UV laser was focused to a small spot on one side of the film. A low-power cw HeNe laser was then focused to a spot on the same sample about 6 mm from the UV laser. The intensity of the HeNe laser was then monitored with a transient recorder (Transiac Model 2101) following the UV laser pulse. A representative trace is shown at the bottom of Figure 3. Scattered UV light from the XeCl laser provides a time marker for the transient recorder at t=0. About 4 microseconds later, the detonation wave traverses the spot where the HeNe laser passes through the sample. The detonation velocity is then calculated by dividing the laser beam separation distance by the delay time observed in the transient recording.

The detonation velocity for crystalline samples was found to be about 1330 m/s. This value is typical of thin film detonations of several inorganic azides. Amorphous samples exhibited a detonation velocity of

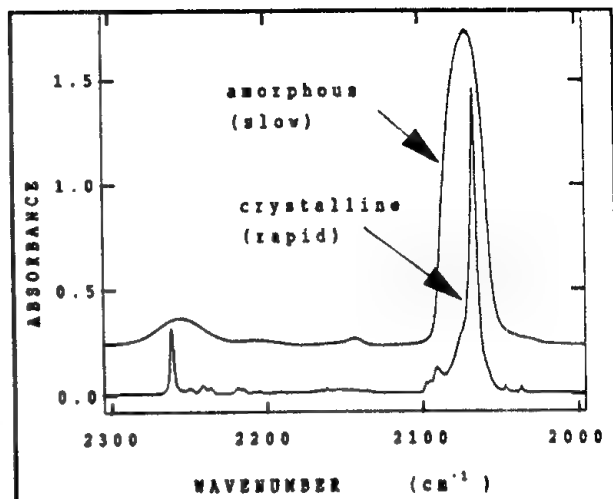


Figure 2

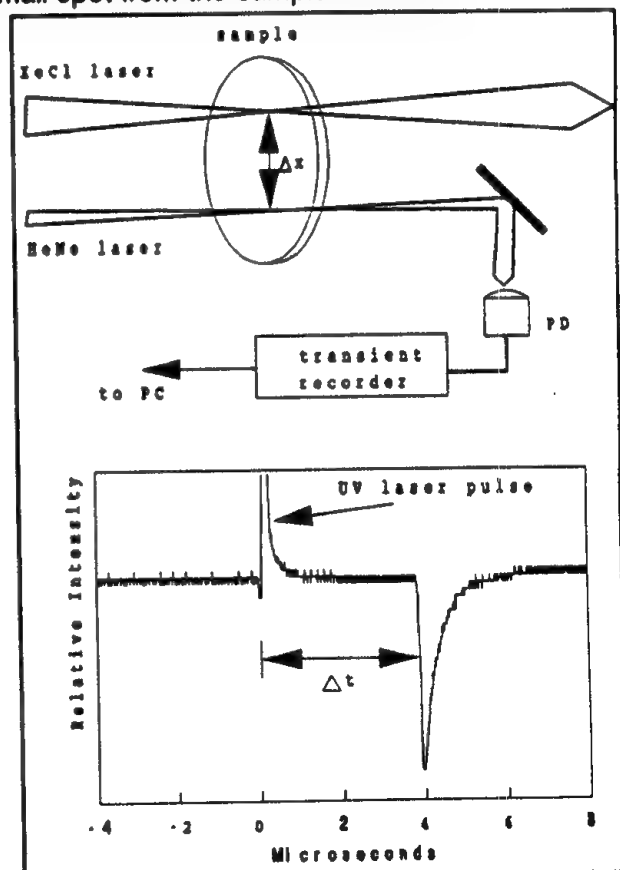


Figure 3

640 m/s. Additional measurements for semi-crystalline samples formed at deposition temperatures of 90 and 100 K are shown in Table I.

Table I. Detonation velocities for thin-film chlorine azide.

Deposition Temperature	Sample Character	Detonation Velocity (m/s)
120 K	crystalline	1330
100 K	semi-crystalline	1040
90 K	semi-crystalline	820
77 K	amorphous	640

Discussion

Our experimental results provide support for the hypothesis that grain boundaries in polycrystalline samples play a central role in the initiation of solid state explosions at low temperatures. Amorphous samples, which have no such boundaries, are desensitized with respect to pulsed laser detonation.

In addition, grain boundaries appear to play a role in the propagation of detonation waves. The detonation velocity in amorphous samples is reduced by about half that of polycrystalline samples. Our results suggest that the mechanism by which a detonation wave is propagated in this type of sample involves sample fracture at grain boundaries as the shock wave traverses the sample. Heat released by reaction of energetic molecules near these boundaries causes the surrounding area to expand. This, in turn, provides mechanical energy to sustain the shock wave as it propagates through the sample.

Although chlorine azide is not a realistic candidate for a HEDM propellant (due to its relatively large mass), it is nevertheless an appropriate model compound for these studies due to its high energy density. If and when suitable candidates for HEDM propellants are identified, they may exhibit the kind of kinetic instability towards mechanically-induced detonation which is common of many azides. It may be useful to consider storage of large quantities of such materials as amorphous, rather than polycrystalline, solids in order to take advantage of the desensitization which accompanies removal of grain boundaries from the material.

References

1. K. Gholivand, G. Schatte, and H. Willner, Inorg. Chem. 26, 2137 (1987).
2. D. J. Benard and R. H. Cohn, Quarterly R&D Status Report #4, Air Force Contract F04611-86-C-0072, December 1987.
3. R. D. Coombe, D. Patel, A. T. Pritt, Jr., and F. Wodarczyk, J. Chem. Phys. 75, 2177 (1981).

HEDM CONTRACTORS' MEETING
February 24-27, 1991
Albuquerque, NM

SHORT WAVELENGTH CHEMICAL LASERS: A HERE
AND NOW APPLICATION OF CHEMICALLY BOUND EXCITED STATE MOLECULES

D.J. Benard, B.K. Winkler and T.A. Seder
Rockwell International Science Center
Thousand Oaks, CA 91360

ABSTRACT

The development of new highly energetic molecules promises a revolution in propulsion, chemical explosives, electric power generation and high energy laser systems. In most cases, these applications are well into the future since the energetic molecules of interest are for the most part presently either theoretical or are only produced in microscopic quantities. Efforts to develop visible wavelength lasers that are directly powered by chemical reactions have been underway for the better part of two decades. Lasers with these characteristics are of interest to the DoD and are capable of fulfilling a number of critical missions that are not achievable by other technologies. Since high energy molecules can potentially dissociate into electronically excited products, they may find practical use as fuels to drive these new laser systems.

A prototype chemical laser system that we have studied involves the rapid thermal dissociation of FN_3 and $\text{Bi}(\text{CH}_3)_3$. In an actual high energy device, these species would be dissociated by a shock wave, however, in our laboratory we have used a pulsed CO_2 laser and SF_6 as a sensitizer to achieve 1200-1800°K temperatures in 1-2 μs . Under these conditions, the energetic FN_3 molecule dissociates into N_2 and metastable $\text{NF}(\text{a}^1\Delta)$, which carries 1.4 eV of electronic excitation, while the $\text{Bi}(\text{CH}_3)_3$ yields Bi-atoms and eventually BiF after subsequent reactions.^{1,2} The BiF molecule is then

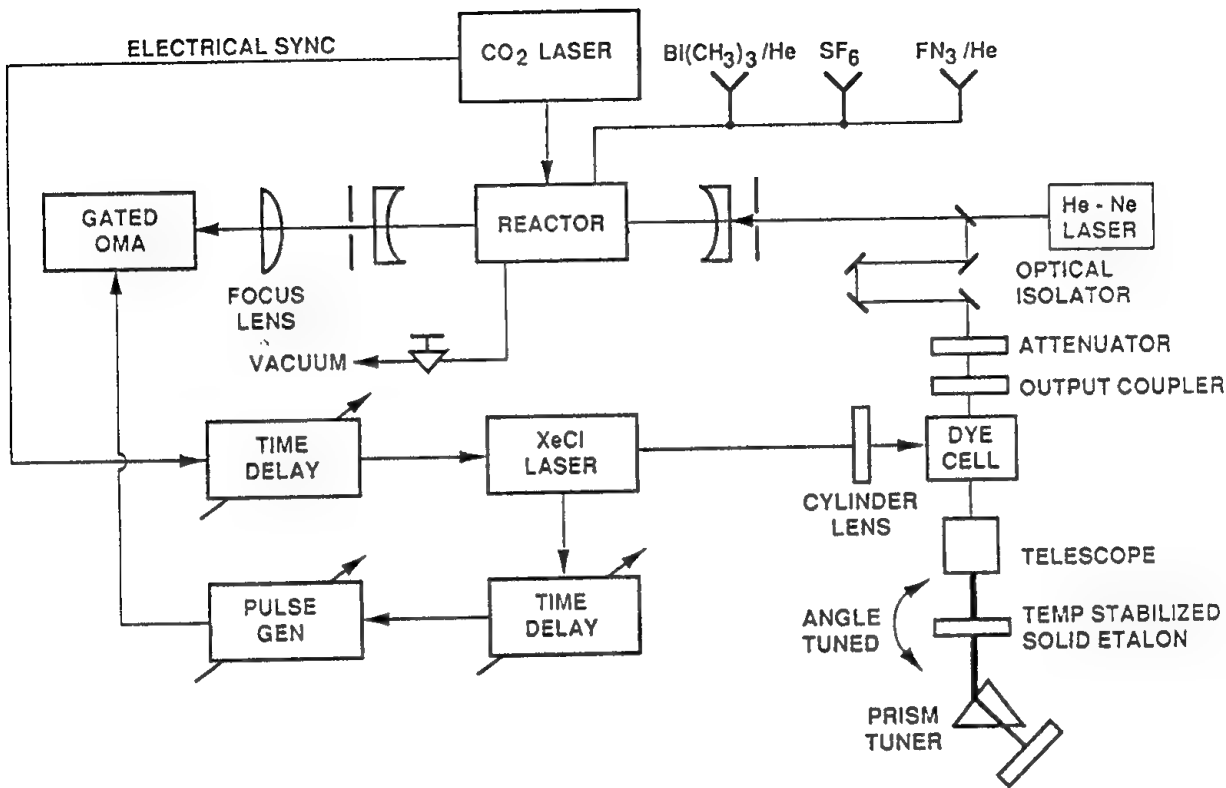
pumped by two successive energy transfer collisions³ with $\text{NF}(\text{a}^1\Delta)$ to a state that emits with a 1.4 μs lifetime in the 420-480 nm region of the visible spectrum.⁴ Therefore, with sufficiently large concentrations of $\text{NF}(\text{a}^1\Delta)$, a population inversion can be generated on selected vibrational transitions of the BiF(A-X) band system.

The molecule FN_3 was initially discovered by Haller in 1942 as the product of the slow reaction between HN_3 and F_2 . Haller found that FN_3 was highly volatile (ten times the vapor pressure of HF) and relatively stable in the gas phase but subject to easy detonation when condensed.⁵ We have routinely produced FN_3 at 2-4% concentration in 350 torr of He at 3.5 scc/s flow rates for up to 4 hours duration (without accidents) following Haller's method by using a few refinements which have been extensively documented.⁶ In parallel with our work, Michels performed calculations⁷ that reproduced the known vibrational frequencies⁸ of the molecule and demonstrated an approximate 0.5 eV barrier for exothermic dissociation of FN_3 into $\text{N}_2 + \text{NF}(\text{a}^1\Delta)$. The calculated barrier height (activation energy) was verified in our laboratory along with efficient dissociation into the expected products at high temperature which confirms the chemically bound excited state nature of this species. Yields of $\text{NF}(\text{a}^1\Delta)$ as high as $3 \times 10^{16}/\text{cm}^3$ have been consistently obtained.¹ Given a gas kinetic rate of energy transfer from $\text{NF}(\text{a}^1\Delta)$ to BiF , these concentrations are large enough to sustain a steady state inversion of the A-X transition.

We have also studied the excitation of BiF by $\text{NF}(\text{a}^1\Delta)$ and have obtained results² that closely parallel those of Herbelin,⁹ et al who used the $\text{H} + \text{NF}_2$ reaction to generate smaller concentrations of $\text{NF}(\text{a}^1\Delta)$. We found that pumping of the BiF(A) state requires $\text{Bi}({}^2\text{D})$ as a critical intermediate, thus excitation involves reactions that promote chemical change as well as energy transfer. The measured pump rate was $4 \times 10^{-11} \text{ cm}^3/\text{s}$ and under selected conditions we were able to observe several BiF(A - X)

photons per $\text{Bi}(\text{CH}_3)_3$ molecule indicating that effective recycling of the $\text{BiF}(\text{X})$ state was indeed occurring. We also found that the amount of active Bi/BiF in the system was limited by the slow ($10 \mu\text{s}$) dissociation of the $\text{Bi}(\text{CH}_3)_3$ and quenching of electronically excited states by the organometallic and its by-products. Upon optimization, which involved separating the FN_3 and $\text{Bi}(\text{CH}_3)_3$ until about 10 ms prior to thermal dissociation, peak $\text{BiF}(\text{A})$ concentrations of $3 \times 10^{13}/\text{cm}^3$ were achieved. These yields of the $\text{BiF}(\text{A})$ state are large enough to generate optical gains on the order of 10^{-4} to $10^{-3}/\text{cm}$ if the concentration of the $\text{BiF}(\text{X})$ state is negligible.

As shown in the figure, gain was demonstrated in the FN_3/BiF system by use of a sensitive cavity ringdown technique.¹⁰ The gain medium, consisting of SF_6 , FN_3 , $\text{Bi}(\text{CH}_3)_3$ and He buffer gas (active length = 2.5 cm) was located inside a high finesse optical resonator tuned to the wavelength region of the $\text{BiF}(\text{A-X})$ transitions. A pulsed CO_2 laser initiated reaction and simultaneously an electronic time delay which triggered a probing pulsed excimer-dye laser probe at the point of peak inversion density. The dye laser was tuned by an etalon and a weak prism so that a number of uniformly spaced lines were generated (each of Doppler width) that could be spectroscopically resolved by a gated optical multichannel analyzer (OMA). The dye laser output was directed through the cavity which contained the gain medium and into the OMA. The OMA gate, however, was not opened until 200 ns after the dye laser was fired and signal was collected for 100 ns thereafter. Since the rotational spacing of the BiF lines was not in resonance with the free spectral range of the etalon, it was possible to line up only one etalon mode with one line of the BiF band system, while the adjacent etalon modes fell between the nearby BiF transitions and served as a zero-gain/zero-loss reference. Data was collected with the CO_2 laser blocked to establish the baseline mode to mode pattern of the dye laser and gain or loss was inferred from changes in the pattern that occurred when the CO_2



laser was allowed to initiate chemical reaction. The experiment was sensitive to gains or losses of $5 \times 10^{-5}/\text{cm}$ when 128 shot averages were employed. Spectroscopic alignment was obtained by initially setting a long time delay between the CO₂ and excimer/dye lasers and using an excess of Bi(CH₃)₃ to produce a large absorption signal that could be acquired without the aid of signal averaging. The etalon was then tuned to maximize the absorption and left fixed while the time delay was shortened and the Bi(CH₃)₃ was optimized for a measurement that was signal averaged. Experiments were conducted on a selected rotational line of the v' = 0 to v'' = 0 band at [NF*] ~ $6 \times 10^{15}/\text{cm}^3$ and on a similar line in the v' = 1 to v'' = 4 band at [NF*] ~ $3 \times 10^{16}/\text{cm}^3$. In the first case, the system was not expected to show inversion and our measurements revealed only absorptions, which were used to calibrate the concentration of the BiF(X) ground state. Using this result, we predicted inversion in the second case and a gain of $3.5 \times 10^{-4}/\text{cm}$.

was indeed observed. The magnitude of the gain was in good agreement with the calculated cross section for stimulated emission and the concentration of the BiF(A) state as measured by absolute photometry, assuming a negligible concentration of the BiF(X) state. This result clearly establishes the feasibility of a lasing demonstration upon scaling the active length of our reacting medium.

We are currently planning to demonstrate lasing in the FN₃/BiF system using a shock tube to suddenly heat the reactive gas mixture in place of the CO₂ laser. This work has been partially sponsored by AFAL, AFWL, SDI and AFOSR.

REFERENCES

1. D.J. Benard, B.K. Winker, T.A. Seder and R.H. Cohn, J. Phys. Chem. 93 (1989) 4790.
2. B.K. Winker, D.J. Benard and T.A. Seder, Proc. SPIE 1225 (1990) 543.
3. R.F. Heidner, H. Helvajian, J.S. Holloway and J.B. Koffend, J. Chem. Phys. 84 (1986) 2137.
4. J.M. Herbelin and R.A. Klingberg, Int. J. Chem. Kinetics 16 (1984) 849.
5. J.F. Haller, Ph.D. Thesis, Cornell University, Ithaca, NY, 1942.
6. D.J. Benard and B.K. Winker, AFAL-TR-90-026 (October, 1990).
7. H.H. Michels, United Technologies Research Center, E. Hartford, CT, private communication.
8. K. Gholivand, G. Schatte and H. Willner, Inorg. Chem. 26 (1987) 2137.
9. J.M. Herbelin and M.A. Kwok, Proc. SPIE 1225 (1990) 560.
10. D.J. Benard and B.K. Winker, scheduled to appear in March 1991 issue of J. Appl. Phys.

Is the Hydrogen-A Phase Metallic

Isaac F. Silvera

Lyman Laboratory of Physics

Harvard University, Cambridge MA 02138

In this article we discuss recent progress in the study of hydrogen at ultra high pressure. There has been a large amount of indirect evidence collected in the past year indicating that the H-A phase of hydrogen is metallic. However, recent optical studies fail to provide the expected evidence of the insulator-metal transition.

Over a year ago we established that a new phase, called the hydrogen-A (H-A) phase, was a unique phase of hydrogen which existed for pressures greater than 149 GPa, independent of the ortho-para concentration¹ This phase line is shown in figure 1. It is believed that the H-A phase is the metallic molecular phase of hydrogen. In this article we discuss the evidence that has accrued up until now.

For a number of reasons it was suspected that transition to the H-A phase was the insulator-metal (IM) transition in hydrogen. The sharp discontinuous decrease in the frequency of the vibron upon entering the H-A phase was consistent with electron transfer from the hydrogen bond to a conduction band. To prove this hypothesis of the IM transition, dielectric measurements were made of the dispersion of the index of refraction as a function of pressure.² These measurements, which were carried out below 100 GPa, could be related to the average valence-conduction band gap, and by extrapolation implied that the indirect gap in hydrogen closed at a pressure between 150 and 200 GPa. Subsequently, we calculated the electronic band structure of hydrogen using a new model which took into account the effect of orientational order on the gap.³ This model predicted metallization by indirect band gap closure at 180 (20) GPa, in rather good agreement with the experimentally observed

transition pressure of the H-A phase; subsequent calculations by Chacham and Louie⁴ have predicted a critical pressure of 150 GPa. We then showed that the H-A phase line ends in a critical point, shown in figure 1.⁵ It should be noted that the Mott model of the IM transition predicts that such a point exists. An analyses of the transition was made in terms of a combined orientational order-IM transition, and based on this we were able to determine the order parameter. We then showed that this transition could be modeled by a 3-states Potts model,⁶ which is known to have a first order transition and critical point, as observed. Still, there was no direct evidence of metallization.

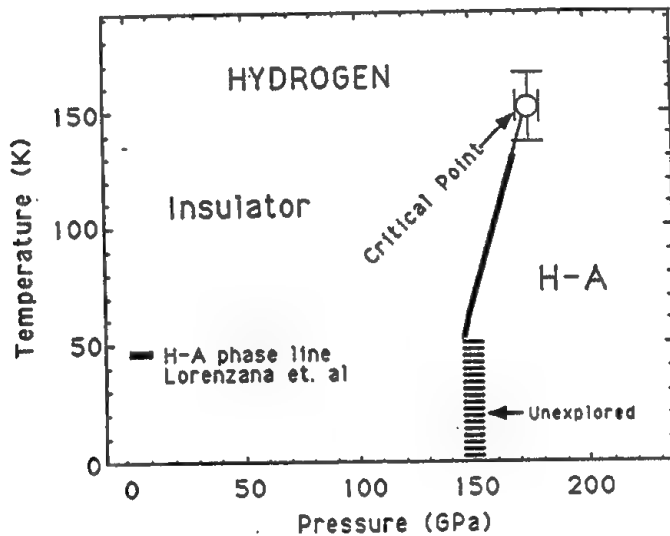


Figure 1. The phase diagram of molecular hydrogen in the high pressure region showing the recently observed critical point. The crosshatched region has not yet been carefully explored.

In the summer of 1990, two groups studied the optical properties of hydrogen at high pressure, the Carnegie Geophysical group, of Mao, Hemley and Hanfland (MHH), and our group. The idea was to establish the IM transition by showing a Drude reflectivity or absorption edge in the IR, characteristic of a free electron metal. MHH⁷ reported rising reflection in the IR for pressures above 149 GPa and carried their study up to 176 GPa at room temperature. They

claimed direct evidence of metallization. At Harvard experiments were being carried out on hydrogen at low temperature, measuring both reflection and absorption. These experiments were conducted to the highest pressures yet reported, 230 GPa, and the results are shown in figure 2. It is seen that there is no evidence of a rising edge in the IR (neither in absorption or reflection). Temperatures were raised to 295 K to reproduce conditions used by MHH, with no change in the spectrum. Thus, our measurements did not confirm those of MHH and cast doubt on their claim

Since it may be possible that the two samples were different, for some unaccounted reason, it was useful to make a careful comparison. The MHH experiment had a dense amount of ruby powder mixed in with their hydrogen. The strategy was to suppress Fabry-Perot fringes (powder particles destroy the coherence of the light) which were believed to be annoying for the analyses of the Drude edge. The Harvard sample only had a small amount of ruby, with a region of hydrogen completely clear of ruby. The MHH paper reported one sample, sparse in ruby, that showed fringes, yet still had a rising edge in the IR. By reanalyzing this data we were able to show that the MHH data was inconsistent with their Drude model and their claim to metallization must be laid to rest. The argument is as follows. The Drude model predicts a rising absorption when there is a rising reflection. As a consequence in the spectral region of rising reflectivity, interference fringes must be attenuated. Fringes are the result of multiple reflection of light back and forth through the sample. However, if the sample is absorbing, the multiple beams are attenuated and thus no fringes occur. The presence of fringes in the MHH spectra, reproduced in figure 2, provides strong evidence against Drude reflectivity in the spectral region which was studied.

Recently Ruoff and Vanderborgh⁸ have offered a possible explanation of the MHH observations. They calculate that at about 130 GPa the ruby (Al_2O_3) should react with the hydrogen and partially convert to metallic aluminum. It would then be this Al which was responsible for their observed rising reflectivity.

In summary, there is a large amount of evidence that the H-A phase is the molecular metallic phase of hydrogen, but no direct

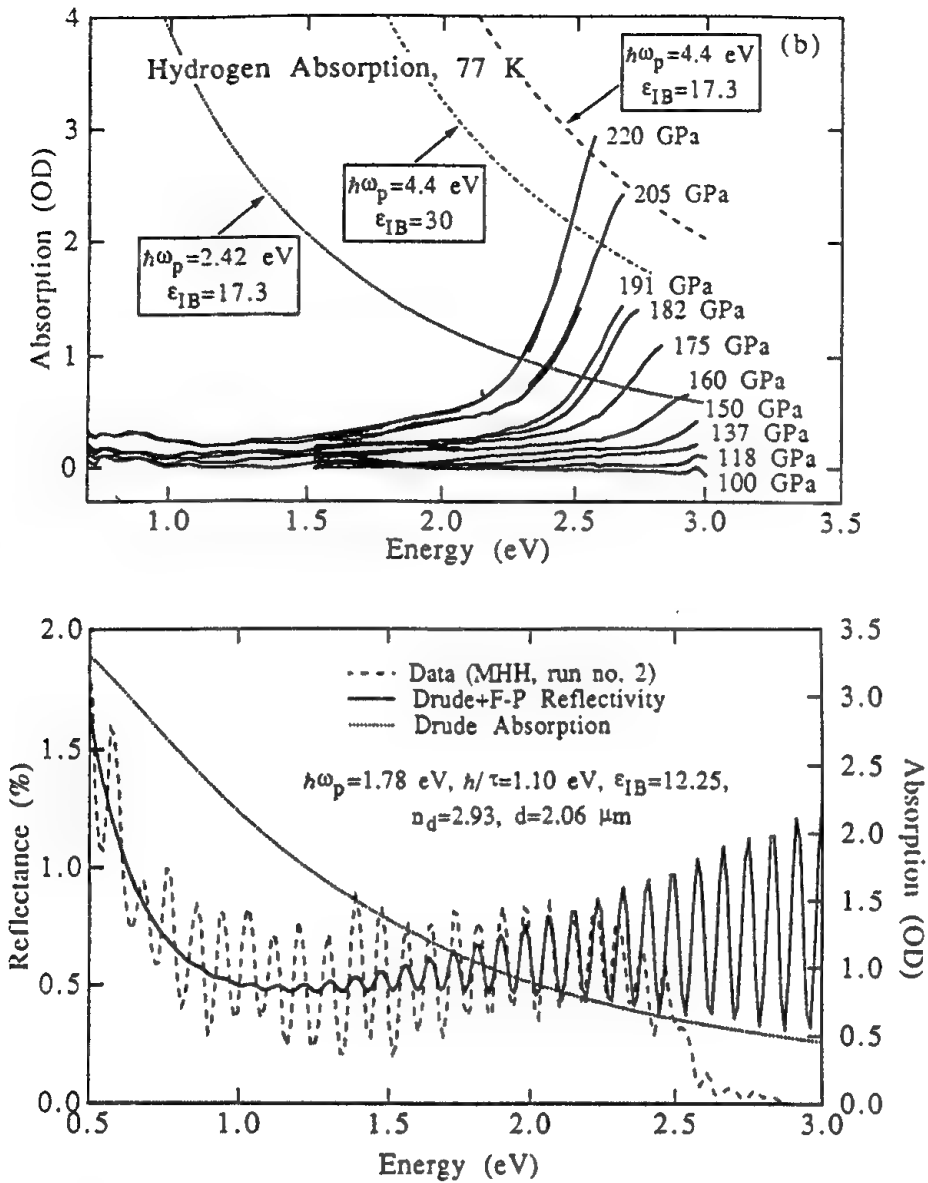


Figure 2. The upper figure shows the measured optical absorption in hydrogen to pressures of 220 GPa at 77 K. A Drude edge would cause rising absorption at low energies. The dotted curve is a calculation of the expected absorption based on the MHH report of Drude reflectivity at 177 GPa, which is not observed in our results. The other two curves are the expected absorption at 220 GPa based on extrapolation of the MHH results, using two different values of the interband dielectric contribution. The strong absorption at high energy is due to the diamond. The lower figure reproduces the MHH data and shows how the fringes would be attenuated if Drude absorption existed.

evidence. The failure to observe a Drude edge is not evidence that the H-A phase is not metallic; this would require an investigation down to zero frequency whereas the recent studies were only carried out down to 0.5 eV. In order to determine metallization the spectral range must be extended to lower energies, or a new technique, such as a measurement of the dc conductivity at low temperature should be employed.

Support of this research by the U.S. Air Force Astronautics Laboratory contract No. F04611-89K-003 is gratefully acknowledged.

References

1. H.E. Lorenzana, I.F. Silvera, and K.A. Goettel, Phys. Rev. Lett. **63**, 2080 (1989).
2. J.H. Eggert, K.A. Goettel, and I.F. Silvera, Europhys. Lett. **11**, 775 (1990); addendum, **12**, 381 (1990).
3. A. Garcia, T.W. Barbee, M.L. Cohen, and I.F. Silvera, Europhys. Lett. (1990)
4. H. Chacham and S.G. Louie, Phys. Rev. Lett. **66**, 64 (1991).
5. H.E. Lorenzana, I.F. Silvera, and K.A. Goettel, Phys. Rev. Lett. **65**, 1901 (1990).
6. I.F. Silvera, Proceeding of LT19, August 1991, Sussex, England, accepted for publication.
7. H.K. Mao, R.J. Hemley, and M. Hanfland, Phys. Rev. Lett. **65**, 484 (1990).
8. A.L. Ruoff and C.A. Vanderborgh, Phys. Rev. Lett. **66**, 754 (1991).

Ultrahigh Resolution Spectroscopy
of Solid Hydrogen

Takeshi Oka

Department of Chemistry and
Department of Astronomy and Astrophysics
The University of Chicago
Chicago, IL 60637

With our first Airforce grant (FO 4611-86-K0068) which started in 1986, two subjects were studied: (1) the infrared spectra of H_3^+ and its hydrogen clusters $H_3^+ (H_2)_n$ in solid hydrogen, and (2) the infrared spectrum of vibrationally excited H_3^+ in liquid N_2 -cooled hydrogen plasmas. Our experiments worked more or less as envisaged in our proposal but the most exciting developments were those not anticipated in the proposal: (1) the observation of ultrahigh resolution spectrum in solid para-hydrogen and (2) identification of vibrationally excited H_3^+ in Jupiter (Ref. 1-8). We will pursue their new progress in this new project.

1. The Tetrahexacontapole-induced $\Delta J=6$ Transition, Observation
of Crystal Induced Fine Structure and its Theoretical Interpretation.

Optical spectra of matter in condensed phases are usually quite broad due to homogeneous and inhomogeneous broadening caused by

strong intermolecular interactions. The high resolution of laser spectroscopy is seldom applicable for studying such systems. We have observed, contrary to expectation, extremely sharp lines in solid hydrogen indicating the well defined quantum states in solid and their slow relaxation time. This allows us to study the condensed phase spectroscopy based on the first principle. We have come up with some theoretical understanding of the spectrum. Much of the theory had been developed by Van Kranendonk⁹ and others and our understanding is based on applications of their theory and some modest extensions of the theory.

We have taken the $J=6 \leftarrow 0$ rotational spectrum of para-H₂ using purer para-H₂ samples (~0.06% ortho) and with variable polarization of the laser radiation.⁸ The result is shown in Fig. 1. The three distinct lines which are clearly seen in the bottom trace are the result of the lifting of the sevenfold degeneracy of the $J=6$ level ($M = \pm 6, \pm 5, \pm 4, \pm 3, \pm 2, \pm 1, 0$) due to the molecule-crystal interaction. The interaction occurs through two effects: (a) Dynamic hopping of the excitons in the crystal and (b) Static molecule-crystal interactions through the quadrupole moment Q of the $J=6$ molecule and the polarizability α of the surrounding $J=0$ molecules. It turns out that the former effect which is much larger than the latter for the $J=2$ levels is negligible compared with the latter effect.

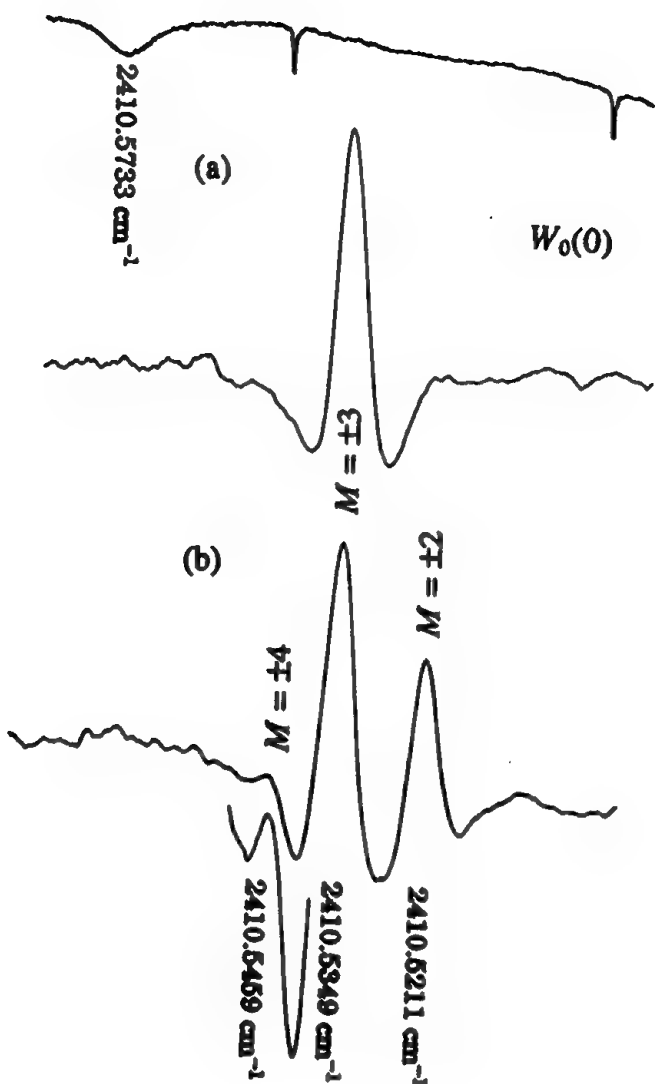


FIG. 1. Effect of the laser polarizations on the relative intensities of the components in the $W_0(0)$ transition. (a) The transition of a sample containing 0.06% of $\alpha\text{-H}_2$ was recorded using a difference frequency laser spectrometer with 40 MHz RF tone-burst modulated at 6 kHz. The peak is at $2410.5349 \text{ cm}^{-1}$ with HWHM 0.0023 cm^{-1} . The optical path is 11.5 cm. Spectrum (b) shows the same transition taken with laser polarization perpendicular to that used in (a). Two additional lines at $2410.5459 \text{ cm}^{-1}$ and $2410.5211 \text{ cm}^{-1}$ are observed. The latter corresponds to the shoulder line in FIG. 3. The weak line at $2410.5459 \text{ cm}^{-1}$ was magnified in the bottom trace. The drastic dependence of the relative intensity of these components on the laser polarization indicates some orientation of the crystal.

The total polarization energy summed over the crystal is given by:

$$E_{pol} = \frac{105}{2} \frac{\alpha Q^2}{R_s^3} \sum_{l=0,2,4} \left\{ \begin{matrix} 3 & 3 & l \\ 2 & 2 & 1 \end{matrix} \right\} C(22l; 000) C(33l; 000) \times \\ \sum_{\sigma} (-1)^{\sigma} C_{\sigma}(\Omega) \sum_{\sigma'} \left[\frac{R_s}{R_s'} \right]^{\sigma'} C_{\sigma'}(\Omega_{\sigma'}) .$$

and explains pretty well the observed splitting. The selection rules and the relative intensities have been understood by using the extended group of S_2^* for H_2 and D_{3h} for the hcp crystal. This gives an extended group which is isomorphic to D_{6h} and gives clear perspective for the whole situation. A paper is accepted in J. Chem. Phys.⁸

2. The $J=1$ Impurity Spectrum in Solid Para Hydrogen.

An ultrahigh resolution spectrum of the $Q_1(0)$ and $Q_1(1)$ transitions have been observed and their interpretation has been sought. We used purer para hydrogen and various laser polarizations. Part of the spectrum is shown in Fig. 2. The sharpness of the observed lines (10 ~ 50 MHz HWHM) is amazing. They are one to two orders of magnitude narrower than the corresponding gaseous lines! While we have global ideas about the theoretical interpretation of the spectrum, we are far from completely understanding the spectrum. We plan to decipher the mystery of these 200 lines using new techniques such as infrared-microwave double

FIG. 2

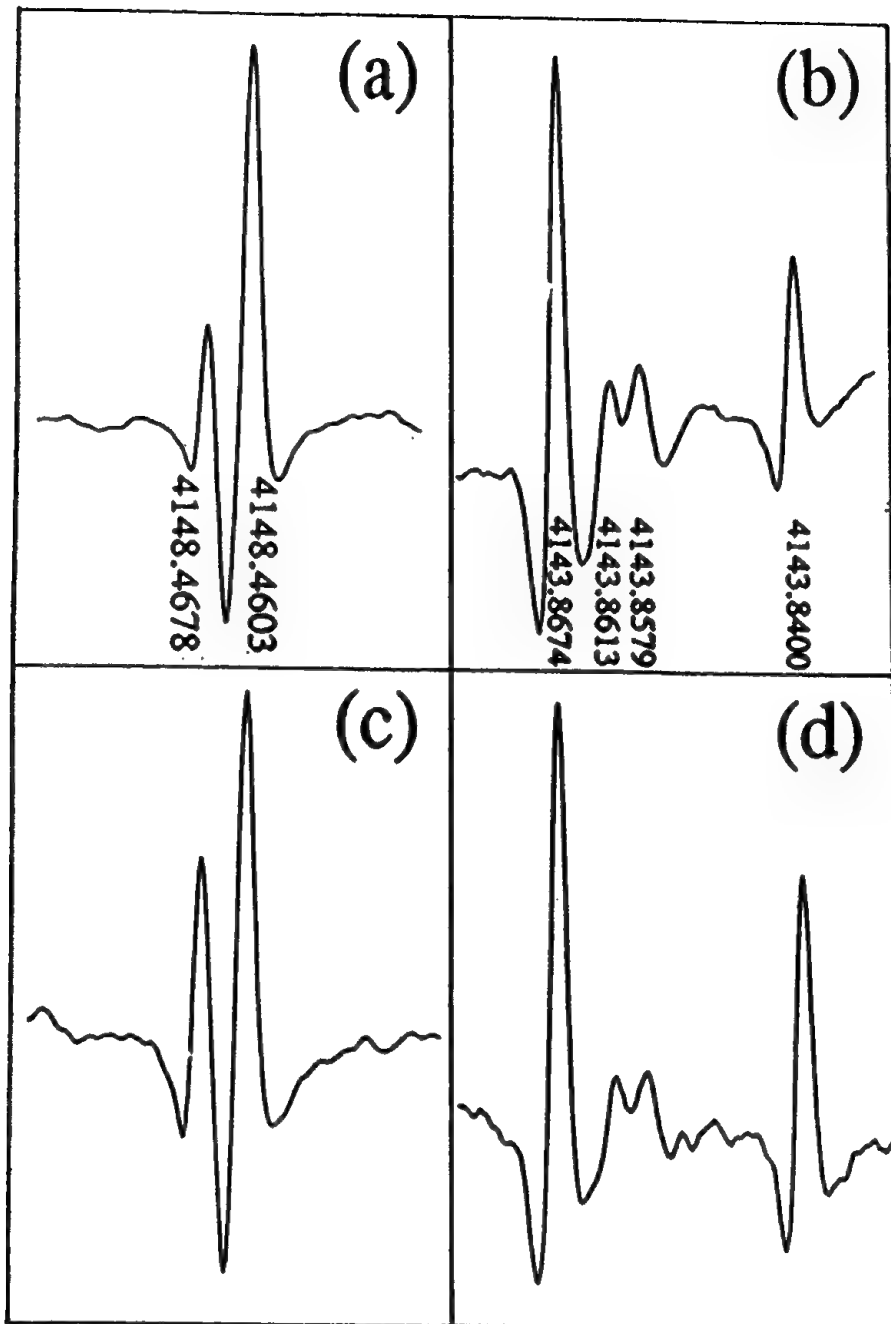


FIG. 2. Two pairs of strong doublets due to (a) $(1,1)'_{\pm} \leftarrow (2,1)'_{\mp}$ and (b) $(2,1)'_{\pm} \leftarrow (1,1)'_{\mp}$ transitions. The lower traces (c) and (d) show the same spectral lines taken with laser polarization perpendicular to that used for (a) and (b). The $\sigma\text{-H}_2$ concentration was 0.06 %. Tone-burst modulation of 40 MHz was used. The time constant of detection was 0.3 second.

resonance and laser heterodyne spectroscopy. A considerable amount of theoretical calculation will also be needed. The preliminary results have been submitted to Physical Review Letters and been accepted.⁶

References.

1. High Resolution Infrared Spectroscopy of Solid Hydrogen. The Tetra-hexacontapole-Induced $\Delta J=6$ Transitions, M. Okumura, M.C. Chan and T. Oka, Phys. Rev. Lett. 62, 32-35 (1989).
2. Observation of the 4 Micron Fundamental Band of H_3^+ in Jupiter, T. Oka and T.R. Geballe, Astrophys. J. Lett. 35, L53-L56 (1990).
3. Observation of the $U_{1 \leftarrow 0}(1)$ Transition of Solid Deuterium, M.C. Chan and T. Oka, J. Chem. Phys. 93, 979-982 (1990).
4. Laboratory Observation of Hot Bands of H_3^+ , M.G. Bawendi, B.D. Rehfuss and T. Oka, J. Chem. Phys. 93, 6200-6209 (1990).
5. Observation of the $2v_2(l=2) \leftarrow 0$ Overtone Band of H_3^+ , L.W. Xu, C. Gabrys and T. Oka, J. Chem. Phys. 93, 6210-6215 (1990).
6. High-Resolution Infrared Spectroscopy of Solid Hydrogen, M.C. Chan, M. Okumura, C.M. Gabrys, L.W. Xu, B.D. Rehfuss and T. Oka, Phys. Rev. Lett., in press.

7. A Table of Astronomically Important Ro-Vibrational Transitions for the H_3^+ Molecular Ion, L. Kao, T. Oka, S. Miller and J. Tennyson, *Astrophys. J.* Supplement, in press.
8. Laser Spectroscopic Studies of the Pure Rotational $U_o(o)$ and $W_o(o)$ Transitions of Solid Parahydrogen, M.C. Chan, S.S. Lee, M. Okumura and T. Oka, *J. Chem. Phys.*, in press.
9. J. Van Kranendonk, Solid Hydrogen, Plenum Press, New York (1983).

Modeling Studies of Atom Production, Recombination and Storage in Solid Hydrogen

James R. Gaines and Yue Cao
Department of Physics and Astronomy
University of Hawaii at Manoa
2505 Correa Road
Honolulu, Hawaii 96822

1. Current State of Knowledge

When atoms are produced in solid hydrogen isotopes by the beta decay of tritium inclusions, a steady-state atom population develops. The steady-state population is determined by a balance between the constant production from the radioactive decay and a temperature dependent recombination that depends on the atom's mobility. Since the mobility is reduced at low temperatures, the steady-state atom population increases with decreasing temperature.

If a sample of solid hydrogen containing tritium is cooled quickly from a much higher temperature, the initial atom concentration can be orders of magnitude smaller than the steady-state concentration at that temperature. ESR techniques have been used at LLNL to observe the transient behavior of the atom buildup and measure the absolute magnitude of the atom concentration⁽¹⁾. The atom concentration has also been inferred from measurements of the ortho to para conversion rate in T₂ (2-4) and DT. The values measured by ESR techniques are smaller than those inferred from NMR data by about an order of magnitude.

The existence of triggered and spontaneous heat spikes⁽⁵⁾ and emission of light pulses⁽⁶⁾ has been demonstrated and attributed to rapid atomic recombination. The heat spikes can be understood by combining the concept that steady-state atom concentration decreases with increasing temperature with the sample's limited ability to transfer heat to an external heat bath. Thus a sudden increase in sample temperature can result in a run-away thermal response until all the unpaired atoms have recombined.

The demonstration that light pulses are emitted by the sample focuses attention on the details of the atom recombination process. At high temperatures, where the steady-state atom concentration is negligible, the beta decay energy appears in the sample as heat energy. At lower temperatures, if the light pulses result from recombination as postulated, a significant fraction of the beta energy may be available as light.

2. Problems with the current understanding

One routine measurement is made for nearly all cryostats or sample assemblies, namely the equilibrium temperature for a given external power input, the "critical power curve". From this curve, one can predict the final temperature of a sample that generates heat. The critical power curve measurements indicate that below 4 K not all the beta energy is converted into heat. This argues for a more sophisticated model of atom production and recombination.

The measured time constants from ESR do not scale properly with the sample radioactivity (or temperature) but appear to have a more diffusive nature. The two determinations of the steady-

state atom concentration differ by an order of magnitude. In the determination made by modeling the ortho-para rate in solid T₂, it is known how much sample exists in the sample cell from NMR signal measurements referred to the liquid state but the actual amount of sample present in the ESR cell is not known.

To reconcile these problem areas, we have made a more fundamental study of the atom production and recombination processes in order to optimize the storage of atoms in solid hydrogen and efficiently recover the stored energy.

3. The New Model

Our present understanding is based on a homogeneous atom production process. There the atoms are constantly produced uniformly throughout the sample and there is no concentration gradient. There is but one type of atom. We replace this with a local rather than a global picture.

We have developed a quantitative model that will be used to describe the generation of atoms due to the tritium beta decay when tritium is present in solid hydrogen isotopes. One major problem to be attacked (in the future) is the limitation on the number of atoms that can be stored.

To generate atoms and store them in solid hydrogen isotopes, the easiest way is to use the energy of the natural beta decay of T₂. In solid T₂ there are 1.15×10^{14} disintegrations per cm³ per sec. Sater et al⁽⁴⁾ estimated that $(2.2 \pm 0.5) \times 10^{17}$ atoms per cm³ per sec were formed by the beta decay in solid T₂. Thus each beta particle generates 1860 atoms. The average energy of a beta decay is 5.7 keV but a continuous spectrum of electrons with energies as large as 18 keV is produced. The dissociation energy of H₂ is 4.5 eV. Thus 4.2 keV out of the 5.7 keV average energy is used to generate atoms from molecules. The local effect of a single beta decay is the starting point in our treatment.

Two basic questions are: (i) how does a beta particle lose its energy?; and (ii) how far does it travel in a solid hydrogen host? The beta particle loses its energy through collisions with the molecules in the solid hydrogen hosts. Two processes dominate the energy loss: (i) ionization and (ii) molecular excitation. At the higher beta-particle energies, ionization is the favored process but below 1 keV, molecular excitation becomes more important and most of the excited states produce atoms.

From studies of electron energy loss in H₂ and D₂, an empirical relationship can be established between the initial electron energy and its range (x). Although the experiments are troublesome to analyze because of the numerous large corrections, it is possible to estimate that for T₂ the range-energy relationship is:

$$(1) \quad x(T_2) = (1.11 \times 10^{-10} \text{ cm}) [E(\text{in eV})]^{1.72}$$

For an electron energy of 5.7 keV, x is 3.2 μm in T₂, while if E is 400 eV, then x is 330 Å. This latter energy is significant because it is representative of the low energy end of the beta-particle spectrum, where molecular excitation is the dominant loss mechanism. Such a beta-particle would be able to produce of the order of 100 atoms over a track length of 330 Å leading to an average separation between atoms of about a lattice spacing (3.6 Å).

For two atoms in an applied magnetic field, the ESR spectrum is a sequence of broadened, doublet lines. If the two atoms are a lattice spacing apart, the scale of the broadening is 340 gauss. Typically in T_2 , the width of the lines observed in ESR experiments at approximately the gas phase hyperfine splittings is a few gauss (in H_2 , it is less than 1 gauss) with a significant contribution possible from the nuclear spins on nearby molecules. Thus atoms near another atom have a shifted position in the ESR spectrum that is outside the observation window when observing the hyperfine split spectrum. The problem of counting how many atomic configurations fall outside this window is complex but a single estimate by Drabold and Fedders⁽⁷⁾ indicates that about one fifth of the atoms in a sample with 0.1 % atoms could be detected by ESR. Another estimate, namely from measurement of the ortho-para conversion rate in T_2 , indicates that there are ten times more atoms in the sample than counted by ESR techniques. We conclude that ESR techniques are not capable of detecting all the atoms in a hydrogen host but only those that are "gas-like".

Atoms can be generated by the original electron, scattered ones, and ions produced by the beta particle-molecular collisions. Also, the beta particle -molecule collisions generate molecular excitations and vibrational excitations. This part of the energy will be released by photon emission instead of heat. From the above discussion, there is about 1.5 keV residual energy (one beta particle carries 5.7 keV on average and 4.2 keV is used to produce 1860 atoms) for one beta particle to have to release either by photon emission or be heat. It is assumed that a fraction (f') of the total residual energy 1.5 keV is converted into heat energy. The heat energy will raise the local temperature surrounding each beta particle track in a solid hydrogen isotope. The regions that have been strongly affected by the beta particles will be called hot spots since they have a higher temperature and are embedded in the solid. The hot spot will have the following characteristics: (1) higher temperature than surrounding solid; (2) higher atom density than the average atom density; (3) random lattice structure due to radiation damage; (4) higher mobility of atoms due to the higher temperature; (5) higher atom recombination rate due to the higher mobility; and (6) atoms in hot spots may not be observable with ESR techniques. All these characteristics must be addressed but we have only treated a few of them.

4. Model Results

First, the temperature and size of the hot spot have to be estimated. We can calculate the effective volume of a hot spot from data on the ortho to para conversion rate in solid tritium. In solid T_2 at the lowest temperatures, the conversion time was 150 min for T_2 and twice that for "DT". Assuming that no motion of atoms or molecules is possible, then the conversion is "local" and all ortho molecules in a region V_c surrounding the site of the beta decay are converted.

From the known time for conversion and the known beta decay rate (1.15×10^{14} disintegrations per cm^3 per sec.), $V_c = 6 \times 10^{-19} cm^3$, a volume that contains 1.8×10^4 molecules. If 1000 atoms are produced by a single beta decay, the atom concentration in a hot spot is 5%. The size of the hot spot is determined by the thermal response of the solid. The solid could warm to the triple point, melt, or vaporize. Each response gives a different size. After a beta decay has occurred and deposited an amount of heat energy (a fraction f' of the residual energy) into a small region of the solid, we ignore heat conduction out of the region (ball volume V_c) and find the temperature increase of the ball volume using the solid heat capacity. Since melting of the solid takes a lot of energy (through the large latent heat) we could begin by making the final

temperature equal to the melting temperature (T_m). This is about 20.6 K for solid T_2 . For an initial temperature T_i we could calculate the ball volume from the equation

$$(2) \quad f'q' = \frac{C_0 V_c (T_m^4 - T_i^4)}{4}$$

where f' is a fraction of q' , the residual energy that is converted to heat and deposited into the solid and $C_0 T^3$ is the Debye heat capacity of the solid. If we assume the ball is a cylinder with height of $3.2 \mu\text{m}$, the radius of the cylinder and the hot spot volume have been calculated (and listed in Table I) for an initial temperature of 4 K, under various assumptions such as: heating to the melting point; heating plus melting; and heating, melting, and vaporization.

TABLE I

Thermal Response	Radius ($f' = 1$)	N_m	Radius ($f' = 0.01$)	N_m
Heat from 4K to T.P.	24.5 Å	1.8×10^6	2.45 Å	1.8×10^4
Heat to T.P. & melt	11.8 Å	4.6×10^5	1.2 Å	4.6×10^3
Vaporize Region	5.2 Å	8.2×10^4	0.5 Å	8.2×10^2

The concentration of atoms in the hot spot depends on the thermal response. If the sample heats to the triple point, the atom concentration is 10% when $f' = 0.01$ but only 100 PPM when $f' = 1$. When the sample also melts, for $f' = 0.01$, the atom concentration is 40% while if the region is vaporized, all the molecules would be converted into atoms. For a given amount of heat energy and a given value for f' , the maximum entropy is obtained when the sample heats just to the triple point but doesn't melt.

We have used this model to calculate parameters such as the lifetime of the hot spot, the number of atoms that recombine in a hot spot and the number that escape. The latter are able to diffuse through the solid and act as a "source term" for production of atoms that can be detected by ESR techniques.

If the sample thermal response is heating from the initial temperature to the triple point (TP), we find that the number of atoms that recombine in a ball = the number generated by one beta decay - the number of atoms that escape = $1860 - 860 = 1000$; and the energy generated by recombination in $\text{k}' \text{ balls/cm}^3\text{s} = 500 q k'$ where $500 q = 2.25 \text{ keV}$. f is the fraction of the recombination energy that appears as heat energy.

The calculated thermal response of the host solid and atomic excitations represents a dynamic balance between the heat loss to the external reservoir and two sources of heating. Those sources are: the residual beta decay energy that is converted to heat and the recombination energy converted into heat both inside and outside the hot spots. The coupling of the sample cell to the heat bath can be obtained from a measurement of the critical power curve. In Collins thesis he found:

$$(3) \quad \frac{dQ}{dt} = - h(\Delta T)$$

where h is the heat transfer coefficient is given by:

$$(4) \quad h = \left[\frac{2.45 \text{ mW}}{\text{K}} \right] (T - T_0)^{0.78}$$

The change in heat energy (Q) per unit time is:

$$(5) \quad \frac{dQ}{dt} = - h(\Delta T) + f(k'q500 + q\alpha m^2) + k'q'f'$$

Solving this equation for the dynamic equilibrium condition yields:

$$(6) \quad m^2 = \frac{1}{q\alpha f} [h (T - T_0)^{0.22} - f k' q 500 - f' k' q]$$

Fitting this expression to Collins ESR data on T_2 in his thesis gives values for the two adjustable parameters in the fit are: the fraction of the residual energy that is converted into heat (f') and the fraction of the recombination energy of 4.5 eV per event (f) that is converted into heat.

We obtain $f = 0.0345$ and $f' = 0.02$ with $T_0 = 1.1$ K. The fit is very good where data is available making it possible to conclude that the fraction of the beta decay energy that is immediately converted into heat is very small, of the order of a few percent! The experiments that will test the modeling are: (1) a careful measurement of the critical power curve and the final operating temperature of a sample of T_2 of known radioactivity and (2) a differential measurement of the sample's magnetization using a SQUID magnetometer. These measurements will provide determinations of the ratio of heat to light energy in the recombination process and the number of free electron spins in the sample.

References

1. Gilbert Collins, Ph. D. Thesis, Ohio State University 1988.
2. J.R. Gaines, J.D. Sater, Evelyn Fearon, P.C. Souers, Fred E. McMurphy, and Evan R. Mapoles, Phys. Rev. Lett. 59, 563 (1987).
3. Yue Cao, J.R. Gaines, Peter Fedders, and P.C. Souers, Phys. Rev. B37, 1474 (1988).
4. J.D. Sater, J.R. Gaines, Evelyn Fearon, P.C. Souers, Fred E. McMurphy, and Evan R. Mapoles, Phys. Rev. B37, 1482 (1988).
5. G.W. Collins, E.M. Fearon, J.L. Maienschein, E.R. Mapoles, R.T. Tsugawa, P.C. Souers, and J.R. Gaines. Phys. Rev. Lett. 65, 444 (1990).
6. E. R. Mapoles, F. Magnotta, G.W. Collins, and P.C. Souers, Phys. Rev. B41, 11653 (1990).
7. D.A. Drabold and P.A. Fedders, Phys. Rev. B37, 3440 (1988).

KINETICS OF HYDROGEN ATOM STORAGE IN CONDENSED MOLECULAR HYDROGEN: THEORY

Chester A. Vause, III
Department of Physics and Astronomy
University of Hawaii at Manoa
2505 Correa Road
Honolulu, HI 96822

I. INTRODUCTION

We would like to discuss a formulation of the kinetic theory for the storage of hydrogen atoms (H) in a molecular hydrogen host (H_2) which includes diffusion, recombination, and fluctuation effects. Typically, kinetic equations are written for the averaged quantities from phenomenological arguments in which it has been understood that some underlying average over fluctuations has been performed. We will start from a more fundamental point of view in which we deal with the unaveraged quantities and then explicitly perform the statistical averaging.

To be specific, let us start by assuming that the most important degree of freedom in the system (consisting of the atoms and molecular host) is the atomic particle density, $n(r,t)$, giving the number of atoms per unit volume at position r at time t . In the temperature range of interest (below the melting point on the order of 10 K) thermodynamic equilibrium is established for $\langle n(r,t) \rangle = 0$ in the absence of sources, where $\langle \dots \rangle$ denotes the equilibrium average. If a nonzero $n(r,t)$ is generated by some means, either externally or by some fluctuation, then the system has the tendency to return to its equilibrium state, that which minimizes the grand thermodynamic potential, Ω . Since Ω is a functional of $n(r,t)$, we may expand the *nonequilibrium* Ω in a power series in the atomic density

$$\Omega[n(r,t)] = - \int d^3r \mu(r,t) n(r,t) + \frac{1}{2} \int d^3r \int d^3r' \varphi^{(2)}(|r-r'|) n(r,t) n(r',t) + O(n^3).$$

In this expression, (1), $\mu(r,t)$ is the local fluctuation chemical potential for the atoms which has the thermodynamic equilibrium value $\langle \mu(r,t) \rangle = 0$ (in the absence of sources) since the number of (unbound) atoms is not conserved. The function $\varphi^{(2)}(|r-r'|)$ can be interpreted as the macroscopic contribution (at quadratic order) due to many-body interactions and is assumed to be a short-ranged function.

The kinetic equation expresses the rate of change of the density in terms of the deviation from equilibrium

$$\frac{\partial n(r,t)}{\partial t} = - \left(\frac{\Gamma_0}{V k_B T} \right) \frac{\delta \Omega[n(r,t)]}{\delta n(r,t)},$$

where Γ_0 is the Onsager kinetic coefficient, V is the volume of the system, T is the absolute tem-

perature, and k_B is Boltzmann's constant.

In the presence of external sources, $\langle \mu(r, t) \rangle \neq 0$, the system responds with the production of a nonzero average particle density

$$\bar{n}(t) = \frac{1}{V} \int d^3r \langle n(r, t) \rangle ,$$

which, to linear order, is given by the expression

$$\bar{n}(t) = \int d^3r \int d^3r' \int_{-\infty}^t dt' \left(\frac{\Gamma_0}{V k_B T} \right) G(|r - r'|, t - t') \langle \mu(r', t') \rangle .$$

The linear response function $G(|r - r'|, t - t')$, or *retarded* Green's function is central to the calculation. There is an important constraint that must be imposed on the system which relates spontaneous fluctuations to dissipative properties. If we decompose $\mu(r, t)$ into its *fluctuation* (noise) $v(r, t)$ and *external source* $\sigma(r, t)$ parts

$$\left(\frac{\Gamma_0}{k_B T} \right) \mu(r, t) = v(r, t) + \sigma(r, t) ,$$

and denote by a “~” the Fourier transform, for example the fluctuation part

$$\tilde{v}(k, \omega) = \int d^3r \int_{-\infty}^{\infty} dt v(r, t) e^{-i(k \cdot r - \omega t)} ,$$

the *fluctuation-dissipation theorem* (FDT) constraint relates the correlation of the spontaneous fluctuations to the dissipative part of the retarded Green's function

$$\langle \tilde{v}(0, \omega) \tilde{v}(0, \omega') \rangle = \left(\frac{4\pi\Gamma_0}{\omega} \right) \frac{\text{Im}\tilde{G}(0, \omega)}{|\tilde{G}(0, \omega)|^2} \delta(\omega + \omega') .$$

With these general comments in mind, the kinetic equation may be obtained. The details of the derivation will be published elsewhere. Since the underlying interactions are “bimolecular”, one has to include terms up to third order in the density in the thermodynamic potential. Also, a hydrodynamic (long-wavelength) approximation is made to leading order. The resulting kinetic equation is

$$\frac{\partial n(r, t)}{\partial t} = D_0 \nabla^2 n(r, t) - \alpha_0 n(r, t)^2 + v(r, t) + \sigma(r, t) ,$$

with the accompanying FDT constraint

$$\langle v(r, t) \rangle = 0 ,$$

$$\langle v(r, t)v(r', t') \rangle = 2\Gamma_0 \delta(r - r') \delta(t - t') .$$

The constant D_0 is the diffusion coefficient, and α_0 is the bimolecular recombination coefficient. The task at hand is to find the kinetic equation for $\bar{n}(t)$ and its solution.

II. KINETIC EQUATION FOR $\bar{n}(t)$

Space will not allow for the presentation of the complete derivation of the kinetic equation for $\bar{n}(t)$ in this report, rather a summary will be given. It is convenient to work with the Fourier amplitudes, $\tilde{n}(k, \omega)$. The kinetic equation then takes the form

$$\tilde{n}(k, \omega) = \tilde{G}_0(k, \omega) [\tilde{v}(k, \omega) + \tilde{\sigma}(k, \omega)] - \tilde{G}_0(k, \omega) \alpha_0 \frac{1}{V} \sum_{k'}^{\infty} \int_{-\infty}^{\infty} \frac{d\omega'}{2\pi} \tilde{n}(k', \omega') \tilde{n}(k - k', \omega - \omega') ,$$

where

$$\tilde{G}_0(k, \omega) = \frac{1}{-i\omega + D_0 k^2}$$

is the Green's function for $\alpha_0 = 0$, and the corresponding FDT constraints are

$$\langle \tilde{v}(k, \omega) \rangle = 0 ,$$

$$\langle \tilde{v}(k, \omega) \tilde{v}(k', \omega') \rangle = 4\pi \Gamma_0 V \delta_{k, -k'} \delta(\omega + \omega') .$$

The equation is now iterated treating α_0 as a perturbation. The statistical average is then performed. It turns out that each term in the perturbation expansion diverges and many-body resummation techniques must be employed to obtain a finite result. When this is performed, one can assemble the result as a kinetic equation for the average density

$$\frac{d\bar{n}(t)}{dt} = \frac{\sigma_0}{3} - A\bar{n}(t) - \frac{\alpha_0}{3}\bar{n}(t)^2 .$$

In this expression, we have assumed a constant external source term, σ_0 . The term linear in the average density is generated by the fluctuations, the coefficient is

$$A = \left(\frac{\sqrt{2} \alpha_0^2 \Gamma_0}{4\pi D_0^{3/2}} \right)^{2/3} .$$

Note that A scales like $1/D_0$ so that as $D_0 \rightarrow \infty$, "gas-like" regime, $A \rightarrow 0$ and one obtains the "usual" bimolecular kinetic equation for a dilute gas of atoms.

The solution of the kinetic equation is

$$\bar{n}(t) = \frac{3R(\cos\phi)^2}{\alpha_0} \frac{\tanh(Rt)}{1 + (\sin\phi)\tanh(Rt)},$$

where

$$R = \sqrt{\frac{\alpha_0 \sigma_0}{9} + \frac{A^2}{4}},$$

and

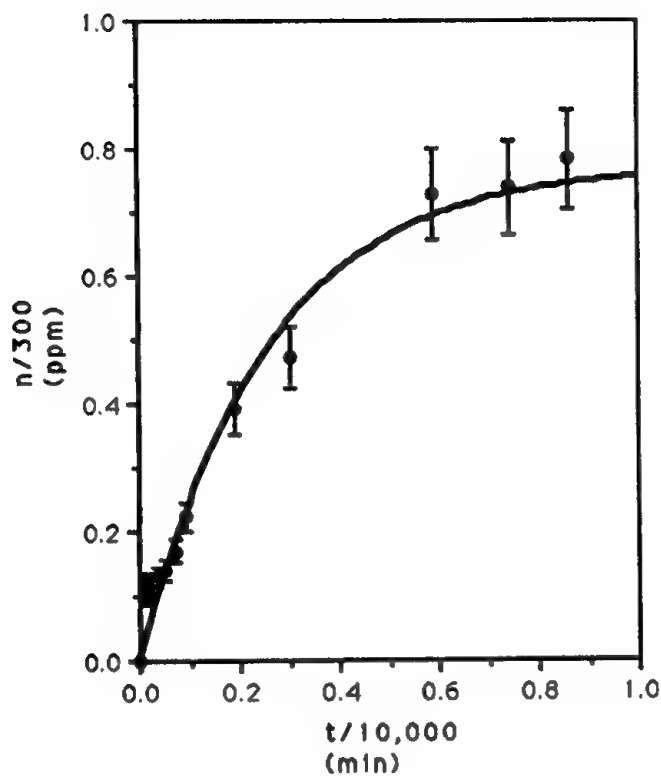
$$\phi = \arctan\left(\frac{3A}{2\sqrt{\alpha_0 \sigma_0}}\right).$$

The "gas limit" is $\phi = 0$.

We have fit the solution to an experiment by Collins [1] using the system $H_2 + 2\% T_2$ at $T=1.4$ K. The fit (shown in the figure below) gives $\phi = 67.8^\circ$, revealing a significant departure from gas-phase dynamic. The other parameters are $A = 6.1 \times 10^{-6}$ 1/sec, $\alpha_0 = 1.2 \times 10^{-25}$ cc/sec, and $\sigma_0 = 1.2 \times 10^{14}$ 1/cc-sec. This gives a saturation value of $\bar{n}(t \rightarrow \infty) = 6.1 \times 10^{18}$ 1/cc, a stored energy density of 2.2 MJ/m³, and an average atom production rate by the tritium source of 3,073 atoms/ β -decay. These results are the "best fit" to the data with a reduced chi-squared of 1.95. If A is set to zero (corresponding to "gas-phase" behavior) the reduced chi-squared increases to 4.12. This suggests that nontrivial fluctuation effects may be important in the problem of production and storage of atomic hydrogen.

REFERENCES

- [1] G. W. Collins, Ph. D. Dissertation, Ohio State University, "Magnetic Resonance Study of Atomic Excitations in Solid Molecular Hydrogens", 1989.



ENHANCING ATOM DENSITIES IN SOLID HYDROGEN BY ISOTOPIC SUBSTITUTION

Gilbert W. Collins, P. Clark Souers, Evan R. Mapoles, and Frank Magnotta

Atomic hydrogen inside solid H₂ increases the energy density by 200 Megajoules/m³, for each percent mole fraction stored. How many atoms can be stored in solid hydrogen? To answer this, we need to know: (1) how to produce and trap hydrogen atoms in solid hydrogen, (2) how to keep the atoms from recombining into the ground molecular state, and (3) how to measure the atom density in solid hydrogen. We will address each of these topics in this paper.

Hydrogen atoms can be trapped in solid hydrogen by co-condensing atoms and molecules, external irradiation of solid H₂, or introducing a radioactive impurity inside the hydrogen lattice. Tritium, a heavy isotope of hydrogen, is easily condensed as a radioactive isotopic impurity in solid H₂. Although tritium will probably not be used in future rockets, it provides a way of applying a large, homogenous dose to solid hydrogen. In all of the data presented here, the atoms are produced by the decay of tritium and thus knowing how many atoms are produced from the tritium decay in the solid phase is important. Solid T₂ generates about 100,000 W/m³. In the gas phase each triton decay produces about 155 ion pairs resulting in 780 atoms. We have recently measured the number of atoms that are produced in the solid phase by measuring the exchange time for the reaction



at 6 K¹. We found that tritium produces the same number of atoms in the solid phase as in the gas phase ($K = f_t \cdot 10^{23}$ atoms/m³·sec in solid hydrogen, where K is the atom production rate constant and f_t is the mole fraction of tritium).

We will now focus our attention on reducing the recombination rate of the atoms. The quantum nature of atomic hydrogen allows the atoms to move through the lattice and recombine rapidly, even at low temperatures (~1 K). This rapid quantum diffusion and recombination has limited the atom concentration in solid H₂ in previous experiments. Yu Kagan and L. Maximov have developed a theory of quantum diffusion of H and D atoms in H₂ and D₂ respectively^{2,3,4,5}. Simply stated the theory treats the diffusion of atoms in solid hydrogen as a band type of diffusion⁶. The tunneling bandwidth, Δ , is directly related to the tunneling probability. Δ decreases with increasing mass of the diffusing particle and host. Interaction with other defects cause the energy levels for atoms at neighboring sites to shift. If the level shift, δ , is larger than the tunneling bandwidth, band diffusion is impossible without the aid of phonons. The phonons move the energy levels at neighboring sites allowing the energy bands to overlap and the trapped atoms to tunnel. This creates a temperature dependence on the tunneling rate of atoms. To relate the atom density to the recombination coefficient we assume that to first order

$$\frac{d[H]}{dt} = K[H_2] - \alpha[H]^2$$

¹G. W. Collins, E. M. Fearon, E. R. Mapoles, P. C. Souers and P. A. Fedders, "J=1-to-0 Conversion in Solid D-T", submitted to Phys. Rev. B.

²Kagan, Yu and M. I. Klinger, J. Phys. C:Solid State Phys., 7 (1974).

³Kagan, Yu and L. A. Maksimov, Sov. Phys. JETP, 38, 2 (1974).

⁴Kagan, Yu and L. A. Maksimov, Sov. Phys. JETP, 57, 2 (1983).

⁵Kagan, Yu and L. A. Maksimov, Sov. Phys. JETP, 52, 4 (1980).

⁶Andreev, A. F. and I. M. Lifshitz, Soviet Phys. JETP, Vol. 29, No. 6 (1969).

where K is the atomic production rate described above, α is the recombination coefficient which is proportional to the tunneling rate, $[H]$ is the atom concentration, and t is the time. The solution to the differential equation is

$$[H] = \sqrt{\frac{K}{\alpha}} \tanh(\sqrt{K\alpha} t)$$

which increases while $t \leq 1/\sqrt{K\alpha}$ and then saturates to a steady state atom concentration

$$[H]_{ss} = \sqrt{\frac{K}{\alpha}}$$

Even though, as we will show later, the atom density cannot be described by this simple rate equation, the atom density will increase as the recombination rate decreases. Thus we can increase the atom concentration by (1) decreasing the temperature (2) increasing the mass of the diffusing particle and host lattice, and (3) increasing the energy level shifts, δ , by creating a disordered lattice.

We will now focus on ways to measure the atom concentration. We begin by discussing atom densities which are measured directly with electron spin resonance (ESR) (that is atom densities obtained by integrating the ESR absorption and comparing with a calibrated standard). Figure 1 shows the atom density vs dose for $H_2 + 2\%T_2$, $D_2 + 2\%T_2$, $HD + 2\%T_2$, D-T (25% T_2 -50% T_2 -25% D_2), and T_2 , at about 4 K. This figure shows that atom densities vs dose, measured directly with ESR, is lower in H_2 than the other isotopic mixtures of hydrogen. Figure 2 shows the atom concentrations vs dose of the same mixtures at about 2 K. This figure shows that the atom density increases with decreasing temperature and again the atoms densities are lower in H_2 than the other isotopic mixtures of hydrogen. Moreover, in the mixture, D-T, the atom density is the largest. This fits well with the theory of Kagan since this mixture has the greatest degree of lattice disorder.

Figures 1 and 2 also show that the simple tanh function solution that we arrived at above cannot be used to model the atom concentration because the atom density does not saturate with time. For most of the atom buildup data, the nonsaturating part can be considered as a small perturbation of the total atom buildup. To account for the nonsaturating part we assume that a separate process is leaking atoms into the ESR spectrum at a rate proportional to the dose. The simple equation we used to fit to our data was

$$[H] = \sqrt{\frac{K_{ESR}}{\alpha}} \tanh(\sqrt{K_{ESR}\alpha} t) + mt$$

where m is a constant and K_{ESR} is the production rate for atoms seen with ESR and not necessarily the total atom production rate. One can obtain this same solution by assuming that there is a small time dependent part to the production term and solving the differential equation perturbatively. When we use this equation to fit to our data, and solve for K_{ESR} , α , and m from the adjustable parameters used in the fit, we find that the recombination coefficient, α , is close to values found from previous experiments on H_2 and D_2 but K_{ESR} is temperature dependent and orders of magnitude smaller than the true solid phase value for the atomic production term! Moreover K_{ESR} can be fit to an exponential function

$$K_{ESR} = k_0 \exp\left[\frac{E_a}{k_b T}\right]$$

where k_0 is a constant, k_b is Boltzmann's constant, E_a is the binding energy for trapped atoms seen with ESR, and T is the temperature. Figure 3 shows the plot of K_{ESR}/K vs inverse temperature for D-T and T_2 , and the exponential fit to the 4 warmest data points. From this fit we find a binding energy for trapped atoms seen with ESR, E_a , of 33 K in T_2 and 14.5 K in D-T. This is strong support for a two atom model. One type of atom can be counted directly with ESR and is trapped in the lattice with energy E_a , and a second type of atom that is unobserved directly with ESR. The obvious question then becomes, is the concentration of "hidden atoms" large enough to make atomic hydrogen a vehicle for energy density enhancement of solid hydrogen for use as a next generation rocket fuel propellant?

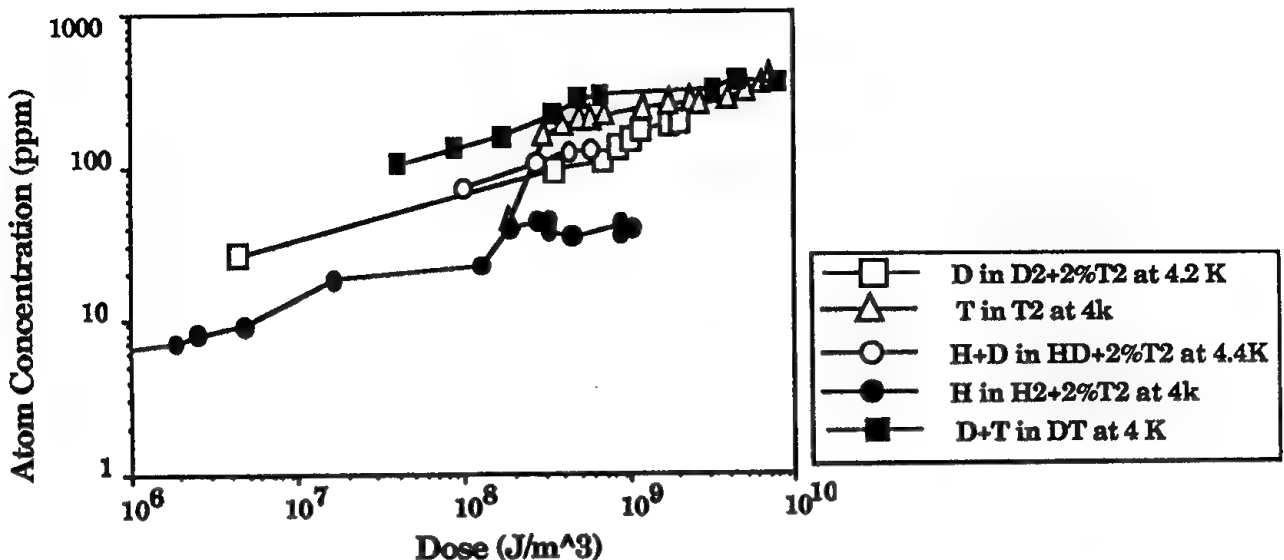


Fig 1: Atom concentrations in the solid hydrogens vs dose at about 4 K.

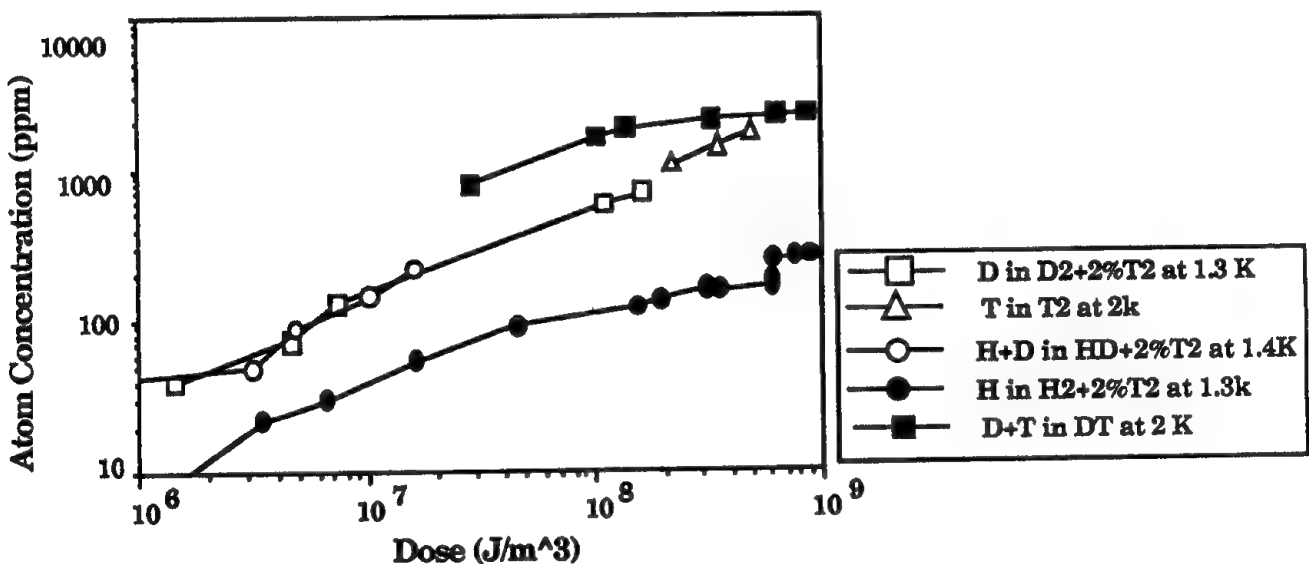


Fig. 2: Atom concentrations in the solid hydrogens vs dose at about 2 K.

To measure the number of "hidden atoms" we have began a series of experiments and analyses. We are currently setting up a magnetization experiment using a differential loop squid magnetometer. This will measure the total concentration of magnetic species in our tritiated hydrogen samples. We have also used nuclear magnetic resonance to measure the $J=1$ to 0 conversion in solid T_2 and $D-T^{7,1}$ and we are presently extending these experiments to H_2 , D_2 , and HD containing tritium. From the $J=1$ to 0 conversion one can calculate a model dependent atom concentration. Finally, the dipolar

⁷J. D. Sater, J. R. Gaines, E. M. Fearon, P. C. Souers, F. E. McMurphy, and E. R. Maples, Phys. Rev. B37, 1482 (1988).

broadening of the ESR spectrum can be analyzed to obtain an atom concentration. We will discuss some of our recent results from NMR and ESR experiments below.

The J=1 to 0 conversion experiments have proved that the atom concentration measured with ESR is a small fraction of the total number of paramagnets in the lattice. The J=1 to 0 conversion in solid H₂ + 2%T₂ is catalyzed by the unpaired atoms in the same way as in solid T₂ and D-T. The time for atom buildup, as measured by ESR, is relatively slow as compared to pure T₂. The rate equation describing J=1 to 0 conversion in solid H₂ + 2%T₂ can be written as

$$\frac{d[J=1\ H_2]}{dt} = -k[J=1\ H_2][H] + \frac{3}{4}a[H]^2$$

where [J=1 H₂] is the J=1 H₂ concentration and k is the rate characterizing the decay of J=1 molecules due to atoms. The second term on the right hand side shows that J=1 molecules are constantly created due to the recombination of atoms. The first term on the right hand side shows that if the atom concentration is a constant, then the decay of J=1 molecules will be a perfect exponential. If the atom concentration is not constant, the decay of the J=1 concentration will be a convolution of the time dependent atom concentration and an exponential. Figure 4 shows the atom concentration measured by ESR and the J=1 H₂ concentration measured by NMR in solid H₂ + 2%T₂ at about 1.5 K. The J=1 concentration decays in as perfect exponential while the atom density measured with ESR is not at all a constant! If the atoms are the magnetic centers catalyzing the J=1 to 0 conversion, Figure 4 proves that the atom concentration seen by the molecules is essentially a constant by the time our ESR or NMR experiments begin.

We have also started analyzing the linewidth of the ESR lineshape. The linewidth of the hydrogen atoms in solid hydrogen is due to the distribution of local magnetic fields seen by the atoms. Because the local magnetic fields are produced by all the magnetic centers in the lattice, the linewidth provides a way of quantifying the atom density indirectly with ESR without the concern of a limited bandwidth. Because the linewidth is due to both magnetic molecules and paramagnetic atoms we must first calculate and remove the nuclear part to the ESR linewidth. We will first discuss only the results for H₂+2%T₂. Using NMR we have measured the concentration of magnetic molecules ([J=1 H₂]). When the concentration of magnetic molecules is large ([J=1 H₂] > 1%) the linewidth due to the molecules can be calculated almost exactly. We use the expression⁸

$$\Delta H(\text{nuclear}) = \sqrt{\frac{3.87}{a^6} \gamma_n^2 \gamma_e^2 h^2 I(I+1) [J=1\ H_2]}$$

where γ_n is the nuclear gyromagnetic ratio, γ_e is the electron gyromagnetic ratio, a is the lattice distance in H₂ (~3.8E-10 m), I is the nuclear spin quantum number (I=1 for J=1 H₂), and h is Plank's constant. After subtracting out the nuclear contribution to ΔH we are left with the dipolar broadening from the atoms. When we calculate the atom concentration needed to yield the measured ΔH , we obtain about an order of magnitude larger atom density than that obtained directly with ESR. Figure 5 shows the number of atoms calculated from the linewidth in H₂ + 2%T₂ and T₂ as a function of dose. The atom density is larger than that measured directly with ESR and we find that the heavier isotope, T₂, has a much larger atom density/dose than H₂.

⁸C. P. Poole, Electron Spin Resonance, 2nded. (John Wiley, New York, 1983), chapter 13.

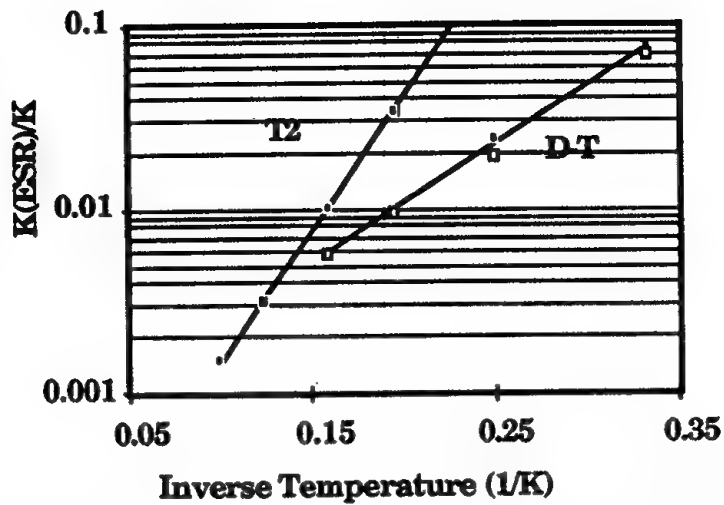


Fig. 3: Ratio of the atom production rates from ESR to gas-solid values in T_2 and D-T.

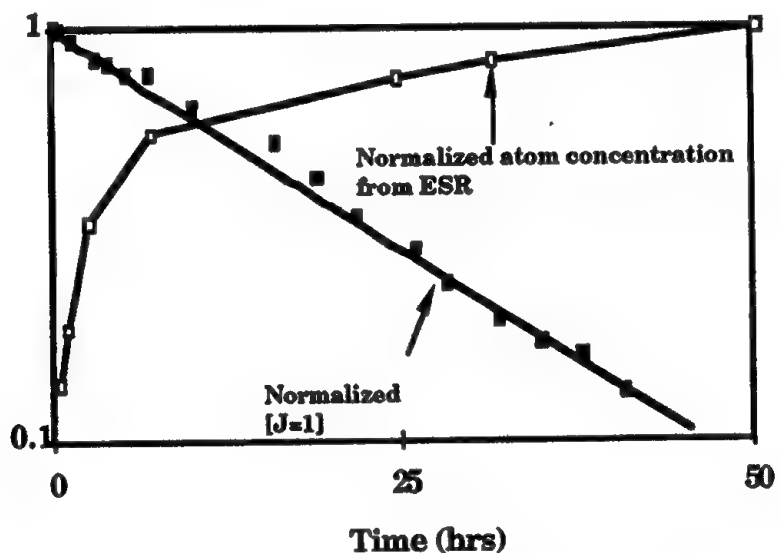


Fig. 4: Normalized decay of the $J=1$ concentration and the normalized atom concentration measured directly with ESR in Solid $H_2 + 2\%T_2$ at 1.5 K.

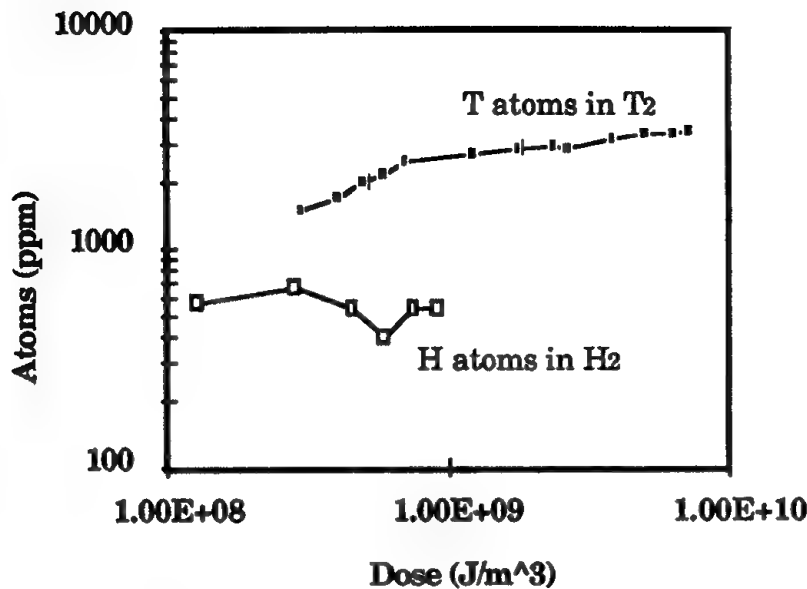


Fig. 5: Atom densities calculated from the linewidth of the ESR spectrum in $\text{H}_2 + 2\% \text{T}_2$ at 1.5 K and T_2 at about 2 K.

Finally, we have started a series of new experiments, injecting impurities into the hydrogen lattice, creating lattice stains to trap larger atom densities. Figure 6 shows the results of an ESR linewidth study of D-T and D-T containing 2% Neon. The linewidth in D-T + 2%Neon is about twice as large as in regular D-T. Although the linewidth is not completely understood, it does imply that the hydrogen lattice contains possibly twice as many atoms when doped with only 2%Neon.

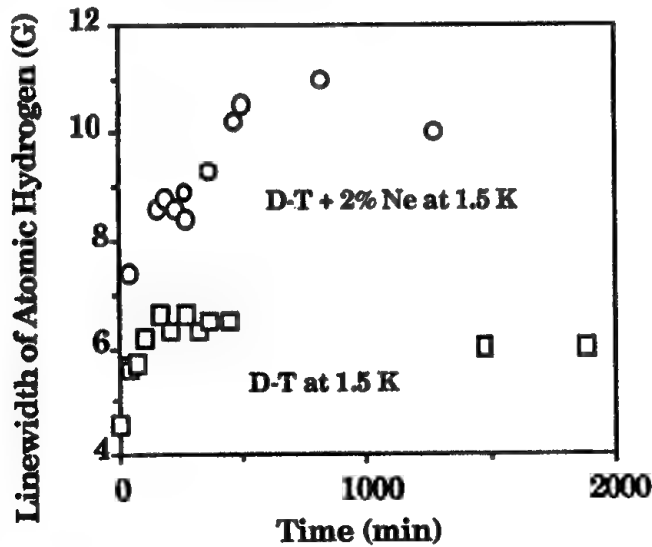


Fig 6: ESR linewidth in D-T and D-T + 2%Ne at about 1.5 K.

*This work was performed under the auspices of the U. S. Department of Energy by Lawrence Livermore National Laboratory under contract No.W-7405-Eng-48.

O(³P) Atom Lifetimes and Mobilities in Xenon Matrices

Herman Krueger and Eric Weitz
Department of Chemistry
Northwestern University
Evanston, IL 60208-3113

Abstract

The concentration of O atoms in xenon matrices at 32 and 40 K is followed by monitoring 736 nm emission from XeO(¹D) eximers. Emission is induced by excitation of O atoms Xe pairs with 193 or 248 nm radiation. O atoms are initially produced via UV photolysis of N₂O. At both temperatures the concentration of O atoms decays on two distinct timescales: one on the order of hours and the second on the order of days. The most likely mechanism for O atom decay is O + O recombination. Based on this mechanism, diffusion coefficients for the longer timescale diffusion process are 5.4×10^{-18} and 2.0×10^{-17} cm²/s at 32 and 40 K, respectively. These values should be viewed as upper limits for the diffusion coefficients of O atoms in crystalline xenon.

Introduction

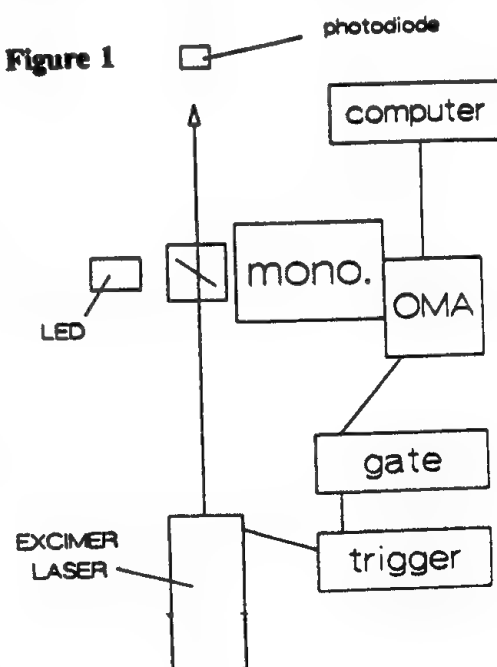
The technique of matrix isolation spectroscopy¹ has served as a powerful tool for the study of reactive chemical species. The utilization of a low-temperature inert gas matrix allows for the study, over long periods of time, of a variety of radical species. The species of interest can be prepared in various ways. One common technique involves the photolysis of a precursor molecule in the matrix to produce the radical directly as a photoproduct. Another technique involves the production of an atom or radical by photolysis which subsequently reacts with some other radical or molecule in the matrix to produce the species of interest.^{1,2}

In both of the above techniques, the processes of atomic and molecular diffusion through the matrix are of prime importance. If the radical is produced by reaction of two species in the matrix, the timescale for its production will be affected by the diffusion time of the reactants in the matrix. Once a radical is produced, its lifetime will be determined in part by the time that it takes for the radical to diffuse to some other reactant in the matrix. The ability to "store" reactive chemical species in a matrix will thus be effected by the timescale of atomic and/or molecular diffusion.

We present a study of the lifetime of oxygen atoms in Xe matrices, and an analysis of the data to infer the diffusion coefficient of the oxygen atoms in the matrix.

Experimental

A diagram of the experimental apparatus is shown in figure 1. The output of an excimer laser operating on ArF (193 nm) is used to irradiate a N₂O:Xe (1:729) matrix. Fluorescence in the 700-800 nm region, produced upon matrix irradiation, is viewed by a gated optical multichannel analyzer (OMA) attached to a monochromator equipped with a 300 grooves/mm grating blazed at 600 nm. The gate width of the OMA is set to be significantly



longer than the fluorescence decay time. The output from the OMA is thus the integrated fluorescence signal over the entire duration of fluorescence which is normalized by the excimer laser energy. Further experimental details are reported in reference 3.

Results

A set of experimental signals is displayed in figure 2 which consist of the fluorescence intensity in the 700 - 800 nm region observed upon irradiation of an N₂O/Xe matrix at 193 nm. The signals are collected after the n^{th} laser pulse in the course of photolyzing the matrix with a total of one hundred pulses. The observed emission is at nearly the same wavelength and has approximately the same halfwidth as that observed previously by Monahan and Rehn upon vuv excitation of N₂O/Xe matrices⁴ which was ascribed to XeO(¹D) excimers. The intensity of the fluorescence in the 700 - 800 nm region following a single excimer laser pulse increases with the number of pulses to which the sample has been exposed. Such behavior implies that the signal intensity is tied to the extent of N₂O photolysis in that matrix. Supporting this interpretation is the observation that similar emission is induced by irradiating an already photolyzed matrix with 248 nm radiation which cannot photolyze N₂O.

Gas phase photolysis of N₂O at 193 nm results in the production O(¹D) atoms and nitrogen with near unity quantum yield.⁵ However relaxation of O(¹D) atoms in a xenon matrix is reported to be very rapid. The increase in XeO(¹D) emission intensity with the number of laser pulses to which the sample has been exposed is almost certainly the result of a buildup of O atom concentration in the matrix due to N₂O photolysis. The 193 nm laser pulse would be expected to excite some XeO pairs into a charge transfer state.^{4,6} This state will eventually decay and has sufficient energy to produce oxygen atoms in excited electronic states. The mechanism thus proposed for the XeO(¹D) emission observed in the current experiments is:



where the pair of arrows in (1b) implies that XeO(¹D) may be produced either directly upon relaxation of Xe[•]O⁻, or indirectly, in which case O atoms would be initially produced in a higher electronic state (e.g. XeO(¹S)) that would subsequently relax into the XeO(¹D) state. This mechanism implies that the intensity of the fluorescence signal will be proportional to the total O atom concentration in the matrix and will thus increase with the extent of N₂O photolysis. This is in fact what is observed experimentally.

The preceding discussion implies a convenient procedure for monitoring the time evolution of an ensemble of oxygen atoms in a xenon matrix. The N₂O/Xe matrix is first subjected to a large

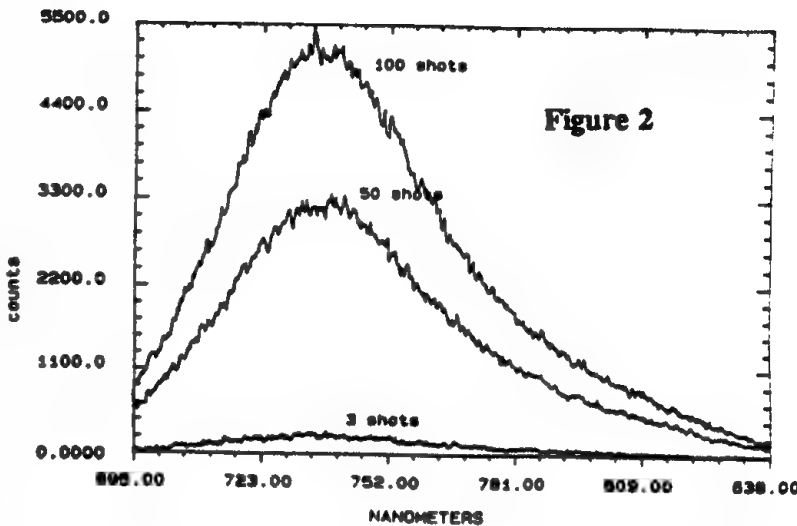
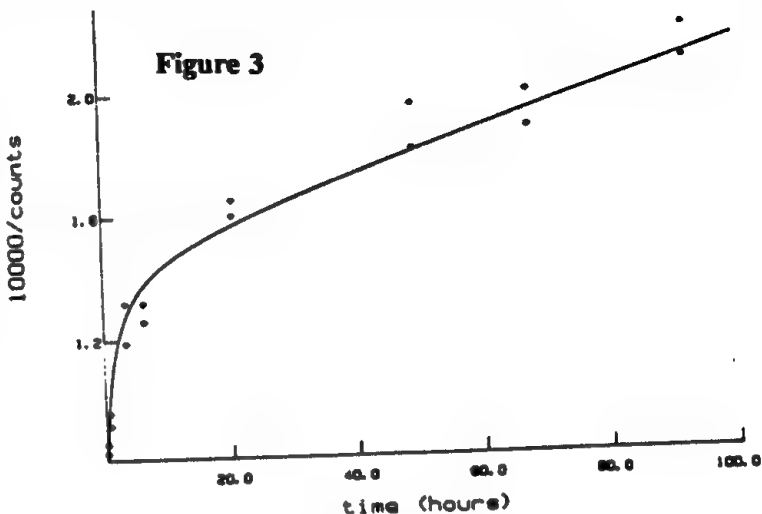


Figure 2

number of laser pulses (typically 300). This photolyzes N₂O molecules producing oxygen atoms in the matrix. Fluorescence signals in the 700 - 800 nm region will be proportional to the amount of oxygen atoms present in the matrix. If a series of such signals is collected over a sufficiently long timescale (hours to days) the decay of O atom concentration in the matrix can be followed.

Figure 3 contains a plot of the reciprocal of the intensity of XeO('D) emission following uv laser excitation of a matrix at 32 K as a function of the time that has transpired between initial N₂O photolysis and collection of the particular fluorescence signal. Similar plots, with somewhat faster decay times, were also obtained for matrices at 40 K. It is evident that the oxygen atom decay is indeed slow. The observed initial halflives are on the order of several hours, and an easily observable O atom concentration is seen to persist for days!



Discussion

One possible O atom loss mechanism involves chemical reaction of O atoms with one or more species in the matrix. All plausible reactions except for O atom recombination are either significantly activated or spin forbidden.³ Such a recombination reaction has previously been observed for O atoms in a Ne matrix, and also in Ar and Kr matrices upon slight warming.^{7,8} The bimolecular nature of recombination reaction suggests plotting the reciprocal of XeO('D) emission intensity versus time.

Figure 3 is such a plot for an experiment at 32 K. Quantitatively similar plots were obtained from other experiments at 32 K while qualitatively similar plots are obtained from data collected at 40 K. Distinct curvature can be observed in the plot. We have shown that it is unlikely this curvature is due to time dependent changes in the effective diffusion coefficient.³ One simple explanation of the experimental decay curves is that they result from the diffusion and reaction of various classes of oxygen atoms most likely differentiated by their environments. Experimental curves similar to those in figure 3 have been observed for the decay of allyl radicals produced by irradiation of polyethylene films.⁹ Two distinct decays were observed and ascribed to radicals in differing environments: those in crystalline regions and those in the lamellar surface.

The simplest explanation of the current results would thus be that various classes of oxygen atoms diffuse through the matrix on significantly different time scales. The initial "fast" decay observed would then be interpreted as due to diffusion and reaction of more mobile oxygen atoms, while the slower decay at long times would be ascribed to less mobile atoms. Anomalous local concentrations of O atoms could also contribute to these effects.

The time dependence of the concentration of a reactant A, subdivided into two classes decaying

with bimolecular (A + A $\xrightarrow{k_1}$ B) rate constants k₁ and k₂, is given by

$$\frac{1}{C_{A1} + C_{A2}} = \left[\left(\frac{1}{C_{A1}^0} + 2k_1 t \right)^{-1} + \left(\frac{1}{C_{A2}^0} + 2k_2 t \right)^{-1} \right]^{-1} \quad (2)$$

where C_{A1} and C_{A2} refer to the concentrations of the two classes of species A reacting with rate constants k_1 and k_2 respectively. C_{A1}^0 and C_{A2}^0 refer to the initial concentrations of the species. The experimentally observed quantity is the total concentration of atoms-- $C_{A1} + C_{A2}$. The data in figure 3 and analogous data collected at 40 K can be fit to this equation and is represented by the solid line in this figure. Upon converting experimental counts to concentrations³ values of k_1 and k_2 in standard units can be derived. If one equates these rate constants with the diffusion limited rate constants, diffusion coefficients can be derived, once a value of r_o is assumed. Taking $r_o \approx 1.2$ Å, the bondlength of O₂, diffusion coefficients of 1.4×10^{-15} and 5.4×10^{-18} cm²/s at 32 K and 7.3×10^{-15} and 2.0×10^{-17} cm²/s at 40 K are obtained. At each temperature, the pair of diffusion coefficients refer to those obtained from the "fast" and slow bimolecular decays respectively. There was typically a much larger range of values obtained for the larger of the two diffusion coefficients than for the smaller of the two diffusion coefficients at either temperature. At either temperature, the larger diffusion coefficient was always within a factor of three of the cited value. The smaller diffusion coefficient was typically measured to be within 25% of the values cited. This difference in range of values may be due to and is compatible with the faster diffusion process being dependent on the local microscopic structure of the matrix around the O atoms. It should be noted that while two classes of atoms, characterized by different diffusion coefficients, are sufficient to explain the results, the current experiments do not rule out the possibility of a larger number of classes, some diffusing on similar timescales.

One would anticipate that, in general, diffusion coefficients may be somewhat specific to the structure of the particular matrix environment. While the magnitudes of the diffusion coefficients do not directly provide information concerning the morphology of the environments to which they apply, one would anticipate that the class of atoms characterized by the smaller diffusion coefficients are located in a more structured environment. Whether this environment is close to that of crystalline xenon cannot be determined by the present experiments. Plans are currently being undertaken to extend the current studies to rare gas crystals. Since the foregoing discussion considered various reasons why oxygen atom migration may be faster in the matrices studied than it would be in a single crystal, the diffusion coefficients derived in the current study would be anticipated to be upper limits to the diffusion coefficient for oxygen atoms in crystalline xenon.

Conclusions

Subsequent to photolysis of N₂O doped xenon matrices, emission centered at 736 nm is observed upon excitation with uv pulses at 193 nm or 248 nm. The intensity of this emission is dependent on the extent of N₂O photolysis and is interpreted as due to emission from XeO(¹D) excimers. The XeO(¹D) is likely formed upon decay of Xe⁺O⁻ charge transfer complexes excited by the uv laser pulses. The intensity of this emission is used to monitor the concentration of atomic oxygen in the matrices over extended periods of time.

After N₂O photolysis, the concentration of atoms decays on two distinct timescales: one on the order of a few hours and the second on the order of several days. A possible explanation for these two timescales is that they reflect two (or possibly more) classes of atoms located in different environments diffusing at different rates. It is clear that a significant fraction of atoms can be stored in the matrix for many days. For example, at 32 K approximately 50% of the atoms present after initial photolysis continue to persist after eight days.

In order to derive diffusion coefficients from the experimental decay curves, it is necessary to know the mechanism of O atom decay. The most likely decay mechanism appears to be O + O recombination to produce molecular oxygen. Based on this mechanism, diffusion coefficients of 1.4×10^{-15} and 5.4×10^{-18} cm²/s at 32 K and 7.3×10^{-15} and 2.0×10^{-17} cm²/s at 40 K are obtained, where the two coefficients refer to the observed fast and slow decays. Since the structure of the matrices under study likely involve some local defects, diffusion in these solids may be faster than in a perfect crystal. The smaller of the two diffusion coefficients reported at each temperature should thus serve as an upper limits to the diffusion coefficient of O in crystalline xenon.

Acknowledgments

We acknowledge support of this work by the Aero Propulsion Laboratory at Wright Patterson Air Force Base under contract #F33615-87-C-2737 and by the U.S. Air Force, Air Force Systems Command, Astronautics Laboratory at Edwards Air Force Base under contract F29601-91-C-0016. We also thank Profs. M. Ratner and G. C. Schatz for informative discussion.

References

1. M. E. Jacox in Chemistry and Physics of Matrix-Isolated Species, L. E. Andrews and M. Moskovits eds., (Elsevier, Amsterdam, 1989).
2. For example, B. Brocklehurst and G. C. Pimentel, *J. Chem. Phys.* **36**, 2040 (1962); J. Fournier, C. Lalo, J. Deson and C. Vermeil, *J. Chem. Phys.* **66**, 2656 (1977); R. N. Perutz, *Chem. Rev.* **85**, 77 (1985).
3. H. Krueger and E. Weitz, *J. Chem. Phys.*, to be published.
4. K. M. Monahan and V. Rehn, *J. Chem. Phys.* **68**, 3814 (1978).
5. H. Okabe, Photochemistry of Small Molecules, (Wiley, New York, 1978).
6. J. Goodman, J. C. Tully, V. E. Bondybey and L. E. Brus, *J. Chem. Phys.* **66**, 4802 (1977).
7. J. Fournier, J. Deson, C. Vermeil and G. C. Pimentel, *J. Chem. Phys.* **70**, 5726 (1979).
8. J. Fournier, H. H. Mohammed, J. Deson and D. Maillard, *Chem. Phys.* **70**, 39 (1982).
9. S. Shimada, Y. Hori and H. Kashiwabara, *Polymer* **18**, 25 (1977).

Theoretical/Experimental Studies of Dications

W. Carl Lineberger, Stephen V. O'Neil, and Stephen R. Leone
Joint Institute for Laboratory Astrophysics
University of Colorado, Boulder, CO 80309

Doubly charged molecular ions are novel species with unique energetic and bonding properties.¹⁻⁵ As a class, they can exhibit high energy content, long lifetimes against predissociation, and bonding partnerships for which there are no neutral analogs. Intuition might suggest that the coexistence of two positive charges in one molecule might be feasible provided the charges can be spatially separated and mutually shielded from one another. Hence it is not surprising that an extended species such as $\text{CH}_2\text{CCCCH}_2^{2+}$ is stable.⁵ However, much more compact dication species, such as diatomics, also exist and possess a number of exceptional properties. For example, He_2^{2+} is known to be a long-lived metastable species⁶ trapped in a 1.5 eV potential well, which upon dissociation to 2He^+ releases 20.5 eV of Coulomb repulsion energy.

Ion systems in general have considerable potential to increase the specific energy content of propellant systems compared to the standard hydrogen/oxygen fuel. A brief survey of ion exoergicities shows that even the simplest ion-ion recombination process, for example $\text{H}^+ + \text{O}^-$, can release 16.5 eV of energy, compared to 2.5 eV from the reaction of $\text{H}_2 + 1/2 \text{O}_2$ to form water. The combination of high energy content and small mass makes simple dications compelling candidates for high specific energy content systems. While dication species are for the most part metastable, the prospect of trapping substantial energy in a single molecular vibrational mode and releasing it with a mechanism that initiates predissociation presents intriguing possibilities. We believe that future searches for potentially energetic species will include doubly charged molecular ions, and that species such as those listed above represent prototype "core" electronic configurations which warrant further exploration both theoretically and experimentally. Experiments to learn how to control their stability and release of their energy will be of fundamental importance.

In order to utilize ion species in propellant technology, experiments and theory will have to address a wide variety of complex topics. These include the limits of Coulomb explosion of multiply charged particles, tunneling through barriers for both heavy particles and electrons, encapsulation and trapping of ions in solids and low temperature slushes (e.g. hydrogen), the utilization of counter ions for electrical neutrality in trapping, stabilization of charges with membranes, pressure effects on particle mobility in solids, growth of low temperature crystals in which species are controlled to occupy designated sites, basic collision physics and chemistry, reaction pathways and energetics, methods to prepare large quantities of ions, and fundamental structures and stability of novel high energy species.

During the past year of this program O'Neil has carried out a broad *ab initio*

CAS-SCF survey of several classes of interesting diatomic dications and then selected several species for accurate MR-CI examination. The first row diatomic hydrides show little tendency to form quasi-bound dications. This may be because the spatially compact L-shell orbitals form a bond only at distances short enough to produce an insurmountable Coulomb repulsion of the constituent nuclei. One strong exception is BeH^{2+} ,⁷ which exhibits a strong well in the $^2\Sigma^+$ symmetry with the lowest vibrational level about three eV above the asymptote.

Perhaps because the greater spatial extent of the M-shell orbital permits bond formation at somewhat longer distances, the second row hydrides form quasi-bound dications readily, with MgH^{2+} , AlH^{2+} , SiH^{2+} , PH^{2+} , SH^{2+} , and ClH^{2+} developing wells deep enough to trap several vibrational levels. We have published⁸⁻¹⁰ detailed MR-CI studies and vibrational analyses on two of these species, PH^{2+} and SH^{2+} , the latter in parallel with the early measurements of Leone. One interesting trend is that even though hydrogen tunnels with impunity in more typical chemical systems, the lifetimes of the $v=0$ levels in the quasi-bound dications are essentially infinite. The explanation rests partly with barrier height and partly with an atypical barrier width, the outer limb falling off only as $1/R$ rather than the $1/R^6$ appropriate to the potentials of most neutrals.

Exploratory state-averaged full valence CAS-SCF calculations on CF^{2+} including all doublet states arising from the $^2P_u(\text{C}^+) + ^3P_u(\text{F}^-)$ asymptote showed the $X^2\Sigma^+$ and $A^2\Pi$ states possess deep quasi-bound potential⁸ wells, and reveal inflection points in the potential energy curves of the $^2\Delta$, $^2\Pi$, and $^1\Sigma^-$ states. The existence of another metastable doublet state correlating with the lowest asymptote cannot be ruled out from these calculations. However, as indicated by the CAS-SCF calculations such a state would lie at least 1.5 eV above the top of the barrier of the $X^2\Sigma^+$ state. The quartet states were not considered in this work since their high spin is inauspicious for bonding. The MR-CI potential energy curves of the $X^2\Sigma^+$ and $A^2\Pi$ states were calculated at 18 internuclear distances between 1.6 and 10.0 Bohr. Beyond a distance of about 8 Bohr the potentials revert to a Coulomb repulsion between C^+ and F^- . At bonding distances the situation is similar to the known NO^{2+} , with a shallow $^2\Pi$ well lying above a much deeper $^2\Sigma^+$ well. The electronic character at the well minima was consistent with $\text{C}^{2+}-\text{F}^-$. Preparation of CF^{++} by a vertical double ionization from the neutral $\text{CF}(X^2\Pi)$ molecule in $v = 0$ ($R_e = 2.4$ Bohr) will produce predominantly CF^{++} in the $X^2\Sigma^+$ ground state with vibrational quanta of $v = 2$ and 3.

In addition to the previously mentioned hydride publications, multireference-CI calculations similar to those described above for CF^{2+} have been carried out for NF^{2+} (for which measurements from Leone's laboratory are described below). In a recent study of F_2^{2+} , we have found the $X^3\Sigma^-$ ground state lying over 7 eV above the $\text{F}^+ - \text{F}^+$ asymptote and possessing a well supporting four quasi-bound vibrational levels. Analysis of the theoretical potential yields $R_e = 1.289 \text{ \AA}$, $\omega_e = 919.4 \text{ cm}^{-1}$, $\omega_{ex_e} = 16.31 \text{ cm}^{-1}$, and $B_e = 1.073 \text{ cm}^{-1}$. Because the well is shallow, even the $v=0$ lifetime is only about 16 msec.

Accurate computation of the electronic states of N_2^{2+} proved challenging because of the numerous states lying between the $N^+ - N^+$ and the $N - N^{2+}$ asymptotes. Many could be omitted safely, and other studies have examined special states in this system,^{11,12} but we characterized more electronic states than usual because the motivation for studying this system in the first place was to help with the assignment of unidentified bands in a very high resolution N_2^{2+} spectrum obtained in Lineberger's laboratory. Extensive use of the Kirtland Cray II was essential here, and the theoretical analysis provided substantial guidance in assigning the measured spectrum reported below.

The experimental apparatus of Leone consists of a jet to introduce the reagent gas into the ionizer section, an electron beam ionizer, a quadrupole mass spectrometer, and focusing lenses to collimate the beam. The dication ion beam is subsequently crossed with a jet of target gas and the primary ions may be detected directly along the beam path, or product ions are pulse-extracted at a right angle into the TOF mass spectrometer. With this apparatus, a large number of dication species have been formed by crossing the electron beam with various precursor reagents. For example, we can form NO^{2+} , CO^{2+} , N_2^{2+} , and HCl^{2+} from selected isotopes of NO , CO , N_2 , and HCl , respectively, NF^{2+} and NF_2^{2+} from NF_3 , CCl^{2+} and H_2CCl^{2+} from CH_3Cl , CF^{2+} , CF_2^{2+} , and CF_3^{2+} from CF_4 , and HS^{2+} and H_3S^{2+} from H_2S , the latter presumably due to ion reactions in the source region. Typically, the doubly charged molecular ions are a few percent of the singly charged ion yields. In our apparatus the ions are extracted with only a few volts of kinetic energy. Thus, ions with lifetimes of 10 μs or longer will survive all the way to the primary beam detector. Many of the ions under investigation are stable indefinitely without collisions. By applying retarding potentials after the initial extraction through the quadrupole, we will be able to lower the kinetic energy of the primary beam even further to make a crude test of the lifetimes and to study collision processes at near-thermal energies.

The NF^{2+} dication is formed with two distinct threshold energies, the lowest of which is attributed to the ground electronic state, and the break in the slope at 51.0 eV kinetic energy is attributed to the existence of an electronically excited state of NF^{2+} .¹³ A similar electronically excited state has been calculated for NF^{2+} , and the existence of such states will greatly facilitate Lineberger's high resolution spectroscopic investigations of the structures of these ions. Our first threshold for NF^{2+} appearance, 43.8 eV, is in good agreement with the sum of the measured $NF_3 \rightarrow NF^+ + F + F$ appearance threshold and the calculated $NF^+ \rightarrow NF^{2+} + e^-$ ionization energy, which yields 41.4 eV. The partial ionization cross section to form NF^{2+} from NF_3 is also estimated to be 10^{-20} cm^2 by comparison to other known systems studied in our apparatus.

Recent experiments of Leone and theoretical calculations of O'Neil and Senekowitsch on HS^{2+} nicely unite our efforts towards developing the predictive capability for dication stability and the ability to verify existence of the ion in the versatile ion source developed here.⁹ The observation of a single threshold for the formation of HS^{2+} in the laboratory experiments is in excellent agreement with the

theoretical prediction⁹ that there is only one bound state of this dication. An added bonus is the observation in the experiments of the formation of H₃S²⁺, which is formed by ion chemistry in the source region. This result suggests the need for further theoretical investigations to determine whether this ion involves an HS²⁺ ion core bonded to a molecular H₂ or some other structure. If the result is the former, then we might have a first example of the solvation of a dication by a hydrogen molecule.

The collision portion of Leone's apparatus has been used to study a first reaction system, the reaction of CO²⁺ with Ar which forms Ar⁺ + C⁺ + O. The doubly charged primary ion beam is mass selected and crossed with a jet of Ar target gas in the main interaction chamber. The product ions are extracted with the TOF mass spectrometer, and the ionic products are detected. These results indicate just the first of the exciting details of the collisional dynamics that will be observed for doubly excited ions. An unexpected mechanism which involves the charge transfer followed by a dissociation of the CO⁺ product appears to be occurring.

The focus of Lineberger's program has been the development of high resolution spectroscopic capability, and its application to simple dication species. Major modifications have been made to a coaxial beam apparatus to enable study of dication photodissociation and obtain high resolution photodissociation spectra of new states of N₂²⁺. Essentially, the apparatus is a high resolution coaxial negative ion-laser beam spectrometer converted for positive ion studies and with product detection capabilities modified to enable the detection of ionic photofragments.

The ions are formed into a beam, accelerated and passed through a magnetic sector mass spectrometer with a resolution M/ΔM = 50. Following this mass spectrometer, the selected ions pass through an energy analyzing quadrupole field which also serves to merge the ion beam with the coaxial single mode laser beam. The apparatus is basically designed to detect with high sensitivity those fragment ions ejected preferentially along the beam propagation axis. A second 45° electrostatic analyzer further separates the fast, forward scattered photofragments and the slower backward scattered photofragments from the primary dication beam. The forward and backward scattered photofragments strike separate multichannel plate detectors, and time-coincidence detection (1 μs window) is used to greatly reduce the background from the intense parent ion beam. The laser light source is a single mode (or, in some cases, a few modes) high power (0.5 W) tunable laser. For this work, we have supplemented our existing dye laser system (500- 720 nm) with a Ti:sapphire tunable laser which covers the spectral region from 700-1000 nm.

We chose to investigate photodissociation of N₂²⁺, a dication for which Cosby et al.¹⁴ and, more recently, Masters and Saare¹⁵ have obtained photodissociation spectra. Detecting the N⁺ photofragments in coincidence, we quickly obtained the N₂²⁺ transition previously reported. Subsequent studies were directed toward obtaining information on other N₂²⁺ electron states, and more subtle issues of dication stability. The previously reported spectra^{14,15} arose from a $^1\Pi \leftarrow ^1\Sigma$

transition, and presented a relatively simple spectrum. Our investigations near $15,000\text{ cm}^{-1}$ showed a much more complex spectrum. In higher resolution, we found over 350 individual lines in this region; this represents far too many lines to be a simple member of the previously reported band system. The detailed analysis of this spectrum was greatly aided by the electronic structure calculations of O'Neil. Their work indicated the strong possibility of a $^3\Pi \leftarrow ^3\Sigma$ transition in the energy range that we observed. Computed bond lengths for the two states gave a very good starting point for recognizing a few progressions. Armed with this information, we began a detailed fitting procedure assuming appropriate selection rules and energy levels for a $^3\Pi \leftarrow ^3\Sigma$ transition. The analysis gave an unequivocal confirmation of the assignment. All of the 27 rotational branches possible in such a transition were present in the spectrum and assigned. Of particular note is the fact that the spectroscopically analyzed triplet transition is between two excited states. The energy difference between the singlet and triplet states is determined by the accurate calculations of O'Neil and Senekowitsch, as are the overall potential energy curves.

The upper $^3\Pi$ state of N_2^{2+} appears to support only one bound vibrational level, and the shape of the barrier potential is indicative of extensive configuration mixing. Such a state provides a particularly sensitive test of the ability to compute potentials and tunneling lifetimes. Since individual rotational lines are well resolved in the high resolution spectrum, it is possible to obtain lifetimes for this electronic state for various rotational levels. There is no striking rotational dependence. The observed long lifetime of 50 ps is at variance with the initially calculated lifetime (1 psec), and indicates that unexpected additional states are producing an even larger barrier to dissociation.

1. W. Koch, F. Maquin, D. Stahl, and H. Schwarz, *Chimia* **39**, 376 (1985).
2. M. W. Wong, B. F. Yates, R. H. Nobes, and L. Radom, *J. Am. Chem. Soc.* **109**, 3181 (1987).
3. P. M. W. Gill and L. Radom, *J. Am. Chem. Soc.* **110**, 5311 (1988).
4. P. M. W. Gill and L. Radom, *J. Am. Chem. Soc.* **111**, 4613 (1989).
5. K. Lammertsma, P. von R. Schleyer, and H. Schwarz, *Angew. Chem.* **28**, 1321 (1989).
6. M. Guilhaus, A. G. Brenton, J. H. Beynon, M. Rabrenović, and P. von R. Schleyer, *J. Phys. B: At. Mol. Phys.* **17**, L605 (1984).
7. Simultaneous with our MR-CI work, BeH^{2+} was also examined theoretically by C. A. Nicolaides, M. Chryos, and P. Valtazanos, *J. Phys. B* **23**, 791 (1990).
8. In addition to our MR-CI results for PH^{2+} , see S. A. Pope, I. H. Hillier, M. F. Guest, and J. Kendrick, *Chem. Phys. Lett.* **95**, 247 (1983); S. A. Pope, I. H. Hillier, and M. F. Guest, *Faraday Symp. Chem. Soc.* **19**, 109 (1984).
9. P. J. Miller, S. A. Rogers, J. Senekowitsch, S. V. O'Neil, S. R. Leone, J.-J. Werner, and P. J. Knowles, *Int. J. Mass Spec. Ion Proc.* **100**, 505 (1990).
10. S. A. Pope, I. H. Hillier, M. F. Guest, and J. Kendrick, *Chem. Phys. Lett.* **95**, 247 (1983); S. A. Pope, I. H. Hillier, and M. F. Guest, *Faraday Symp. Chem. Soc.* **19**, 109 (1984).
11. P. R. Taylor, *Mol. Phys.* **49**, 1297 (1983); P. R. Taylor and H. Partridge, *J. Phys. Chem.* **91**, 6148 (1987).
12. P. C. Cosby, R. Möller, and H. Helm, *Phys. Rev. A* **28**, 766 (1983); B. J. Olsson, G. Kindvall, and M. Larsson, *J. Chem. Phys.* **88**, 7501 (1988); T. E. Masters and P. J. Saare, *J. Chem. Soc. Farad. Trans.* **86**, 2005 (1990).
13. S. A. Rogers, P. J. Miller, S. R. Leone, and B. Brehm, *Chem. Phys. Lett.* **166**, 137 (1990).
14. P. C. Cosby, R. Möller and H. Helm, *Phys. Rev. A* **28**, 766 (1983).
15. T. E. Masters and P. J. Saare, *J. Chem. Soc. Faraday Trans.* **86**, 2005 (1990).

HIGH ENERGY DENSITY MATTER CONTRACTORS CONFERENCE

Albuquerque, New Mexico
24 February - 27 February 1991

Metal Atoms in Solid Rare Gases

Mario E. Fajardo
Emerging Technologies Branch
Propulsion Directorate
Phillips Laboratory
Edwards AFB, CA 93523-5000

ABSTRACT

Results of experiments on lithium doped cryogenic solids (Ne, D₂, and H₂) prepared by laser ablation of solid lithium are presented.

The UV/VIS absorption spectra of Li/Ne matrices generated by cocondensing the rare gas and laser ablated Li atoms at T ≈ 3 K or T ≈ 5 K show a broad, irreproducible, "doublet" absorption feature with peaks near 625 and 650 nm. Annealing of the matrices to T ≈ 10 K consistently produces a "triplet" absorption feature with peaks at 626, 640, and 649(±1) nm.

Absorption spectra of Li/D₂ and Li/H₂ matrices deposited at T ≈ 3 K also initially show an asymmetrical doublet pattern with peaks at 650 and 671(±1) nm; however, these patterns persist upon warm-up of the matrices. Li/H₂ matrices overcoated with Ne can be warmed up to T ≈ 5 K without significant loss of Li atoms; this suggests that bulk Li/H₂ solids can be stored and handled at liquid He temperatures.

EXPERIMENTAL

The experimental techniques are essentially the same as reported previously¹⁻³ and will be described here only briefly. A significant modification is the addition of a high throughput mechanical pump to the exhaust of the liquid helium transfer cryostat system, which allows for cold tip temperatures as low as $T = 2.6(\pm 0.1)$ K. The sapphire sample substrate is attached to this cold tip by an aluminum sample mount; thin indium gaskets are used throughout the assembly. A second temperature sensor is embedded in the end of the aluminum sample mount opposite the cold tip. Quoted sample temperatures are an average of the two sensor readings and have an estimated uncertainty of ± 1 K due to problems with thermal contact inherent to a sample-in-vacuum cryostat.

Solids of Ne, D₂, and H₂ doped with lithium impurities were prepared by co-condensing a slow flow (1 to 3 mmol/hr) of the matrix host gas, along with the products of a laser ablated lithium plume, onto a thin sapphire window cooled to $T \approx 3$ K. The ablated plume was generated by focussing the output of a XeCl excimer laser (308 nm) onto a rotating disk of lithium metal; typical pulse energies were ≈ 3 mJ, with resulting incident intensities of $\approx 10^8$ W/cm².

The rate of deposition of the matrix gas was monitored by back reflection interference using a HeNe laser. Transmission spectra of the matrices were obtained using a 600 W quartz-halogen lamp and an E.G.&G. optical multichannel analyzer equipped with an unintensified silicon photodiode array.

RESULTS

Figure 1 shows transmission spectra of a Li/Ne matrix with an estimated Li molar concentration of 0.3%. Both spectra were taken at $T \approx 3$ K with the dashed curve representing the as deposited spectrum, and the solid curve the spectrum after annealing to $T \approx 10$ K. Figure 2 shows the results of a similar experiment on a Li/D₂ matrix at $T \approx 3$ K; the dashed curve is the transmission spectrum of the as deposited matrix, the solid curve is the spectrum obtained after annealing to $T \approx 6$ K.

Figure 3 shows a comparison of the transmission spectra of a pure H₂ matrix (dot-dash curve) and a Li/H₂ matrix (dashed curve), both as deposited at $T \approx 3$ K using the same H₂ gas flow rates and deposition times. The solid curve at the top of figure 3 shows the result of a direct subtraction of these two spectra. Figure 4 shows the spectrum obtained at $T \approx 3$ K after overcoating the same Li/H₂ matrix with Ne and annealing to $T \approx 6$ K.

DISCUSSION

Previous discussions of the unique properties of Li atom doped matrices prepared by the laser ablation technique have resulted in the development of a crude model of the dynamics of the matrix deposition process¹⁻³. The model invokes the existence of an "accretion layer" at the matrix surface formed due to local heating by the condensing matrix host gas. This accretion layer is characterized by the availability of excess thermal energy which causes enhanced mobility of all species, promoting both the formation of thermodynamically stable solid structures and "surface recombination" reactions⁴. The salient point of the deposition dynamics model is the penetration of the accretion layer by the fast^{5,6} Li atoms generated by laser ablation, resulting in their trapping in previously deposited solid layers. Li atoms trapped in this manner are found to reside in novel trapping sites in Ar and Kr matrices¹⁻³.

While this model was originally proposed to explain the formation of novel trapping sites in the Li/Ar and Li/Kr systems, it also predicts an improved atomic isolation efficiency for the laser ablation deposition technique over the traditional effusive oven deposition method. The problem of surface recombination of slow oven generated Li atoms stopped in the accretion layer has been posited as the cause of the failures of previous attempts at isolating Li atoms in Ne matrices^{7,8}. However, if in fact the fast laser ablated Li atoms are penetrating past the accretion layer, then they should avoid their best opportunity for recombination and isolate atomically in dilute matrices. The stabilization of Li atoms in Ne matrices in this study (figure 1) demonstrates the improved isolation efficiency of the laser ablation method and validates the prediction of the accretion layer deposition model. The successful trapping of Li atoms in D₂ and H₂ matrices further demonstrates the value of the laser ablation technique.

Having successfully demonstrated the generation and stability of dilute Li/H₂ matrices, several questions remain as to: the microscopic composition of the matrices, the ultimate attainable concentrations of trapped Li atoms, and the production of larger samples. The data gathered to date only address the first of these questions; the other two will be considered in future efforts. Defining the microscopic composition of the Li/H₂ matrices involves determining the chemical identity of the lithium species present, as well as the structure of the occupied matrix sites. Again, additional tools such as infrared absorption, Raman scattering, laser induced fluorescence, etc. should prove extremely useful in future efforts along these lines, however the UV-visible absorption spectra in this study already contain much important information.

The shape of the Li atom absorption band in well annealed Li/D₂ and Li/H₂ samples is shown in figures 2 and 4 (respectively) to be an asymmetrical doublet, in contrast to the triplet absorptions observed in most annealed alkali metal/rare gas matrices⁹. A tempting early speculation is to assign the apparent two-fold splitting of the excited Li ²P state to an axial symmetry in the H₂ matrix trapping site. Regardless, the information inherent in this lineshape should provide a valuable point of comparison for theoretical models of the Li/H₂ system. Such efforts are currently underway in other research groups involved in the HEDM program.

Direct comparison of the Li atom absorption intensities in Li/Ne and Li/H₂ matrices prepared under similar conditions indicates that the good atomic isolation efficiency of the laser ablation technique is retained even in H₂ matrices. Furthermore, loss of Li atoms to chemical reactions with the H₂ host molecules does not appear to be a fatal problem. Finally correction for the strong wavelength dependent scattering of H₂ matrices as shown in figure 3 reveals only weak absorptions in the 350 to 550 nm region which may be attributable to lithium clusters or Li_xH_y molecules. These observations all point to Li atoms as the major lithium containing species in dilute Li/H₂ matrices.

Annealing experiments on Ne overcoated Li/H₂ matrices as shown in figure 4 demonstrate the thermal stability of these samples. The Li atoms appear to be stable on a timescale of \geq days at T \approx 3 K, \geq hours at T \approx 5 K, and \geq seconds at T \approx 6 K. This result indicates that bulk Li/H₂ samples, once made, can be stored and manipulated at liquid He temperatures.

CONCLUSIONS

The laser ablation technique offers great improvements in atomic isolation yields over the conventional Knudsen effusion method, *e.g.* the direct comparison in the Li/Ne experiments. The accretion layer model of the deposition dynamics indicates that the high kinetic energy of the incident Li atoms is responsible for this improvement. In the light of this knowledge, other metal atom sources will now be investigated to provide more energy efficient alternatives to the laser ablation source.

Lithium atoms can be isolated in a H₂ matrix at T \approx 3 K ! Thermal annealing experiments indicate that bulk Li/H₂ solids should be stable at liquid He temperatures. The proof-of-concept for the metallized cryogenic propellants project has now been established.

The optical absorption spectroscopy of dilute Li doped Ne, D₂, and H₂ matrices has been characterized. A blue-shifted triplet is observed in Ne, consistent with previous findings in alkali doped rare gas matrices. An unshifted asymmetric doublet is observed in

D_2 and H_2 matrices. These spectra and the results of future experiments should prove invaluable in the determination of the structures of these materials.

The successful trapping of Li atoms in D_2 and H_2 matrices is an important milestone on the road to metal doped cryogenic propellants. Future experiments will also include efforts to increase the Li atom concentrations and sample sizes.

REFERENCES

1. M.E. Fajardo, in Proceedings of the High Energy Density Matter (HEDM) Conference, edited by T.G. Wiley and R.A. van Opijnen, AL-CP-89-002 (USAF Astronautics Laboratory, Edwards AFB, CA, 1989).
2. M.E. Fajardo, in Proceedings of the High Energy Density Materials Contractors Conference, edited by L.P. Davis and F.J. Wodarczyk (USAF Office of Scientific Research, Bolling AFB, DC, 1990).
3. M.E. Fajardo, P.G. Carrick, and J.W. Kenney III, "Matrix Isolation Spectroscopy of Metal Atoms Generated by Laser Ablation: I. The Li/Ar, Li/Kr, and Li/Xe Systems." *J. Chem. Phys.*, accepted, (1991).
4. G.C. Pimentel, *Angew. Chem. internat. edit.*, 14(4), 199-206 (1975).
5. J.F. Friichtenicht, *Rev. Sci. Instrum.*, 45(1), 51-6 (1974).
6. H. Kang and J.L. Beauchamp, *J. Phys. Chem.*, 89(15), 3364-7 (1975).
7. A.A. Belyaeva, Y.B. Predtechenskii, L.D. Shcherba, *Opt. Spektrosk.*, 34(1), 40-5 (1973).
8. J.J. Wright, L.C. Balling, *J. Chem. Phys.*, 73(7), 3103-6 (1980).
9. N Schwentner, E.E. Koch, J. Jortner, Electronic Excitations in Condensed Rare Gases, (Springer-Verlag, Berlin, 1985).

Figure 1

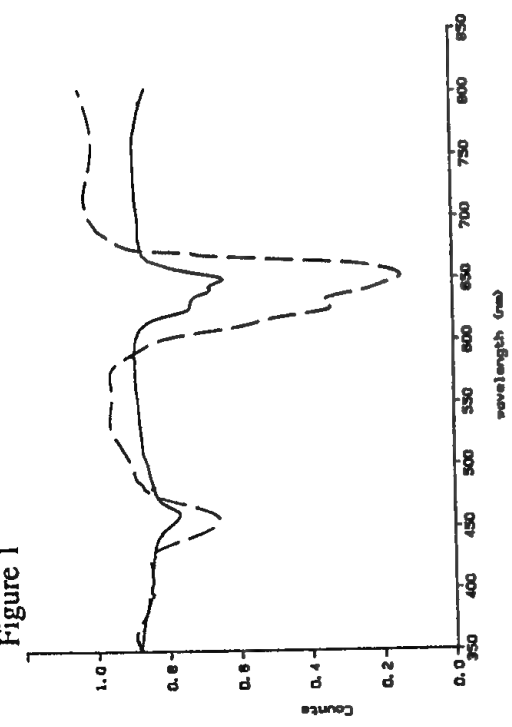


Figure 3

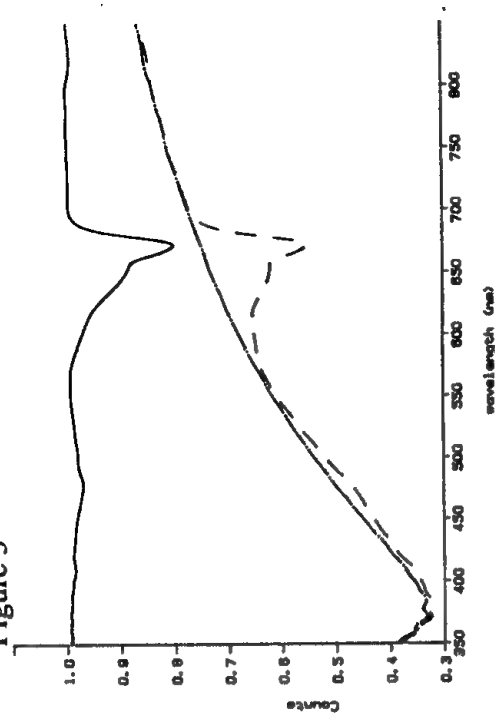


Figure 2

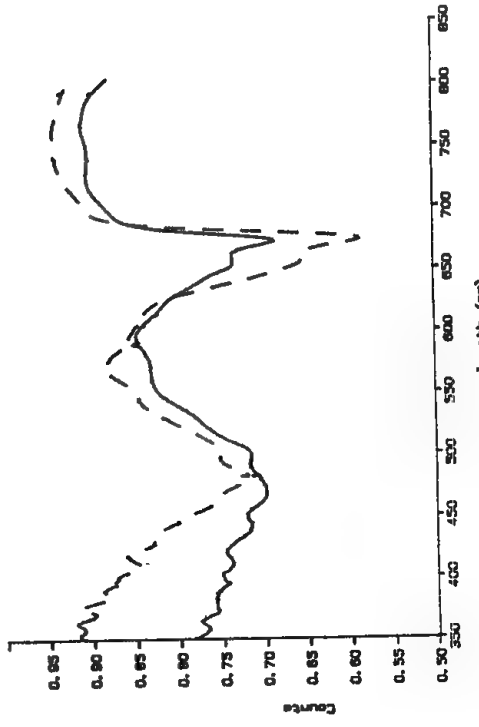
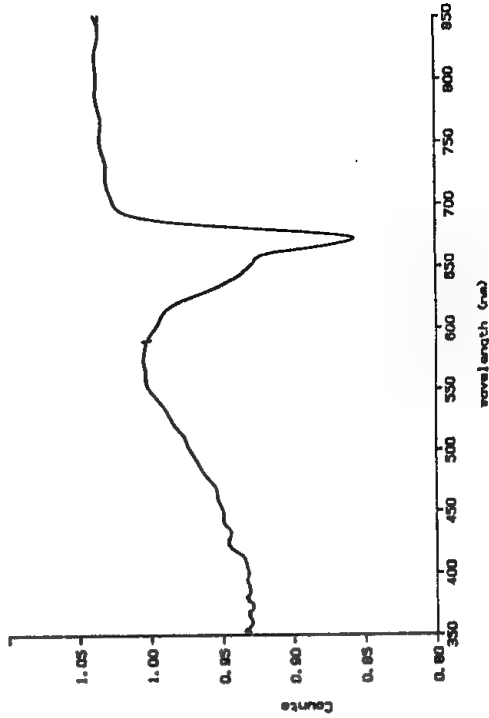


Figure 4



Ab Initio Calculations on Low-Lying States of AlLi

Marcy E. Rosenkrantz

University of Dayton Research Institute

OLAC PL/RKFE

Edwards AFB, CA 93523-5000

These calculations were designed to serve as diagnostics for experimental investigations of AlLi. We performed state averaged MCSCF (SAMC) calculations on the lowest three $^1,^3\Sigma^+$ and $^1,^3\Pi$ states of AlLi. These are the states that dissociate to Al 2P + Li 2S and Al 2P + Li 2S atoms. Using the orbitals from these SAMC results we performed 4 electron in 8 orbital multi reference CI (MRCI) calculations on these states. The SAMC calculations were done in no symmetry. From the SAMC orbitals we obtained symmetry adapted linear combinations for use in the MRCI calculations. The latter were performed in C_{2v} symmetry.

We used the McLean and Chandler [12 9p]/(6s 5p) basis for aluminum, augmented by two diffuse d functions ($\xi=2.56, 0.25$). For lithium, we used the van Duijneveldt [13s]/(7s) basis. The four most diffuse s functions were adopted for the p functions, all of which were kept uncontracted. The lithium basis gave a Li $^2S \rightarrow$ Li 2P excitation energy of 14938 cm^{-1} , which is in excellent agreement with the experimental result of 14904 cm^{-1} .

We obtain three bound $^1\Sigma^+$ states, the lowest of which is the ground state of AlLi. Only the $2^1\Pi$ state is bound among the 1-3 $^1\Pi$ states. On the otherhand all three $^3\Sigma^+$ states are repulsive but all three $^3\Pi$ states are bound. The characteristic constants of the bound states of AlLi are given in Tables 1 and 2. The potential curves are presented in Fig. 1. The $2,3^1\Sigma^+$ states exhibit an avoided curve crossing in the region of the ground state minimum, as shown in Fig. 2.

The avoided curve crossing manifests itself in the transition dipole moment and dipole moment functions (Figs. 3,4), where discontinuities in the functions exist in the region of the avoided crossing. That the $X^1\Sigma^+ - 2^1\Pi^+$ transition moment is smooth indicates that the discontinuities in the $X^1\Sigma^+ - 2,3^1\Sigma^+$ functions results from the avoided crossing. One of these transition moments is essentially zero everywhere. This accounts for the fact that evidence of the $X^1\Sigma^- - 2,3^1\Sigma^+$ transitions have not yet been observed in our laboratories. With David Yarkony, we plan to investigate the diabatic $2,3^1\Sigma^+$ states to understand the nature of the avoided curve crossing in more detail.

The $2^1\Pi$ state minimum lies very near that of the $X^1\Sigma^+$ state. However, its transition moment is significantly smaller than that of the $X^1\Sigma^+ - 3^1\Sigma^+$ transition. Evidence of transitions to the $2^1\Pi$ state has also not yet been observed. With David Yarkony, we plan to investigate the diabatic $2,3^1\Sigma^+$ states to understand the nature of the avoided curve crossing in more detail.

Table 1.

Characteristic Constants
Bound States of AlLi

Singlet States

State	$R_e (a_0)$	$D_e (cm^{-1})$	$\omega_e (cm^{-1})$	$\omega_e \times (cm^{-1})$
${}^1 \Sigma^+$	MRCI 5.44	7098.1	304.78	3.29
${}^1 \Sigma^+$	MRCI 4.65	9526.0	268.11	1.98
${}^1 \Sigma^+$	MRCI 4.88	7082.0	459.16	0.46
${}^1 \Pi$	MRCI 5.52	6404.4	266.09	2.79

Table 2.

Characteristic Constants

Bound States of AlLi

Triplet States

State	$R_e (a_0)$	$D_e (\text{cm}^{-1})$	$\omega_e (\text{cm}^{-1})$	$\omega_{e\bar{e}} (\text{cm}^{-1})$
$1^3\pi$	MRCl	5.03	5170.3	336.12
$2^3\pi$	MRCl	5.87	6848.1	218.50
$3^3\pi$	MRCl	6.03	2008.4	171.61

Figure 1. The Potential Energy curves of Low-Lying States of AlLi

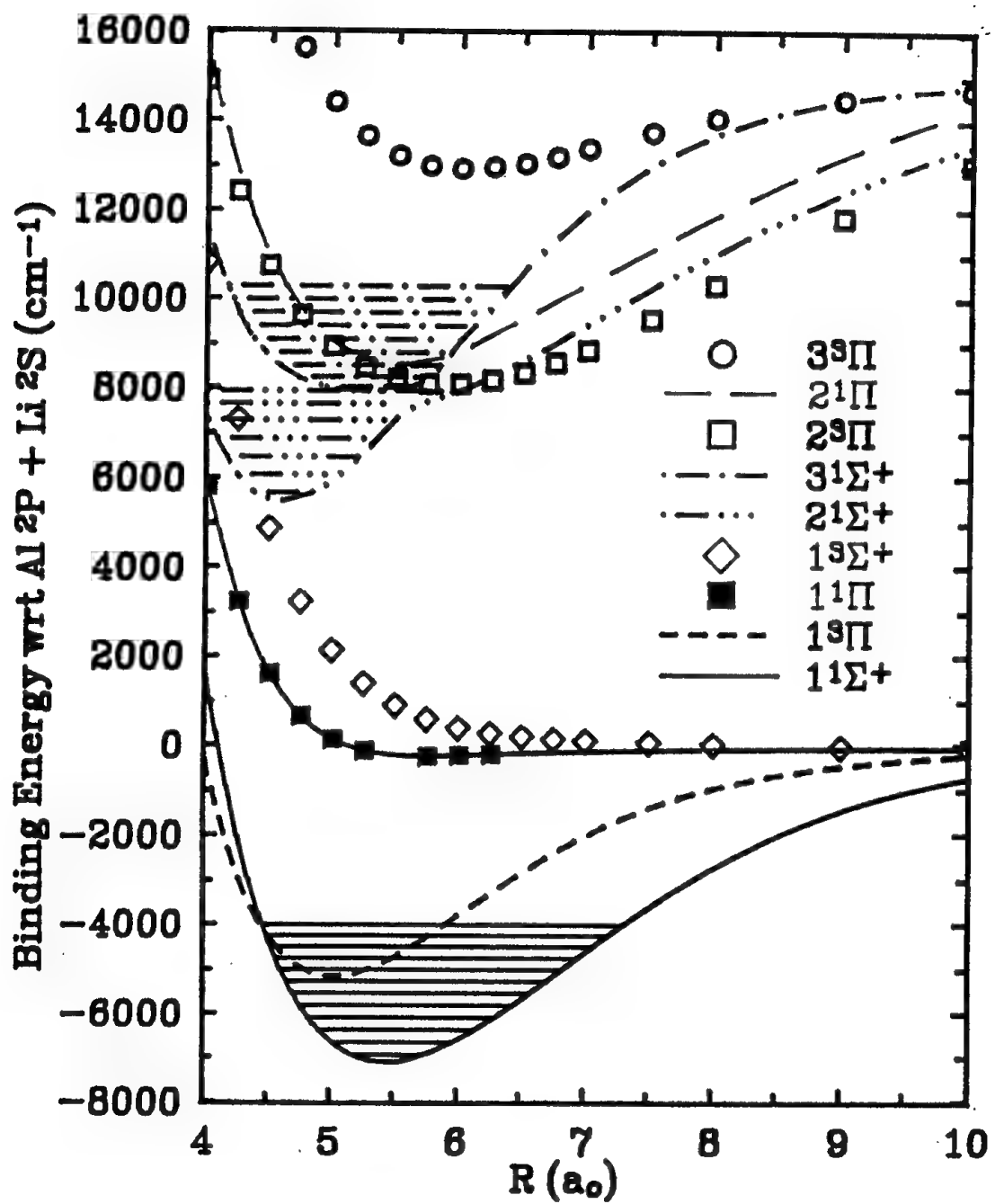


Figure 2. Potential energy curves in the region of the avoided curve crossing.

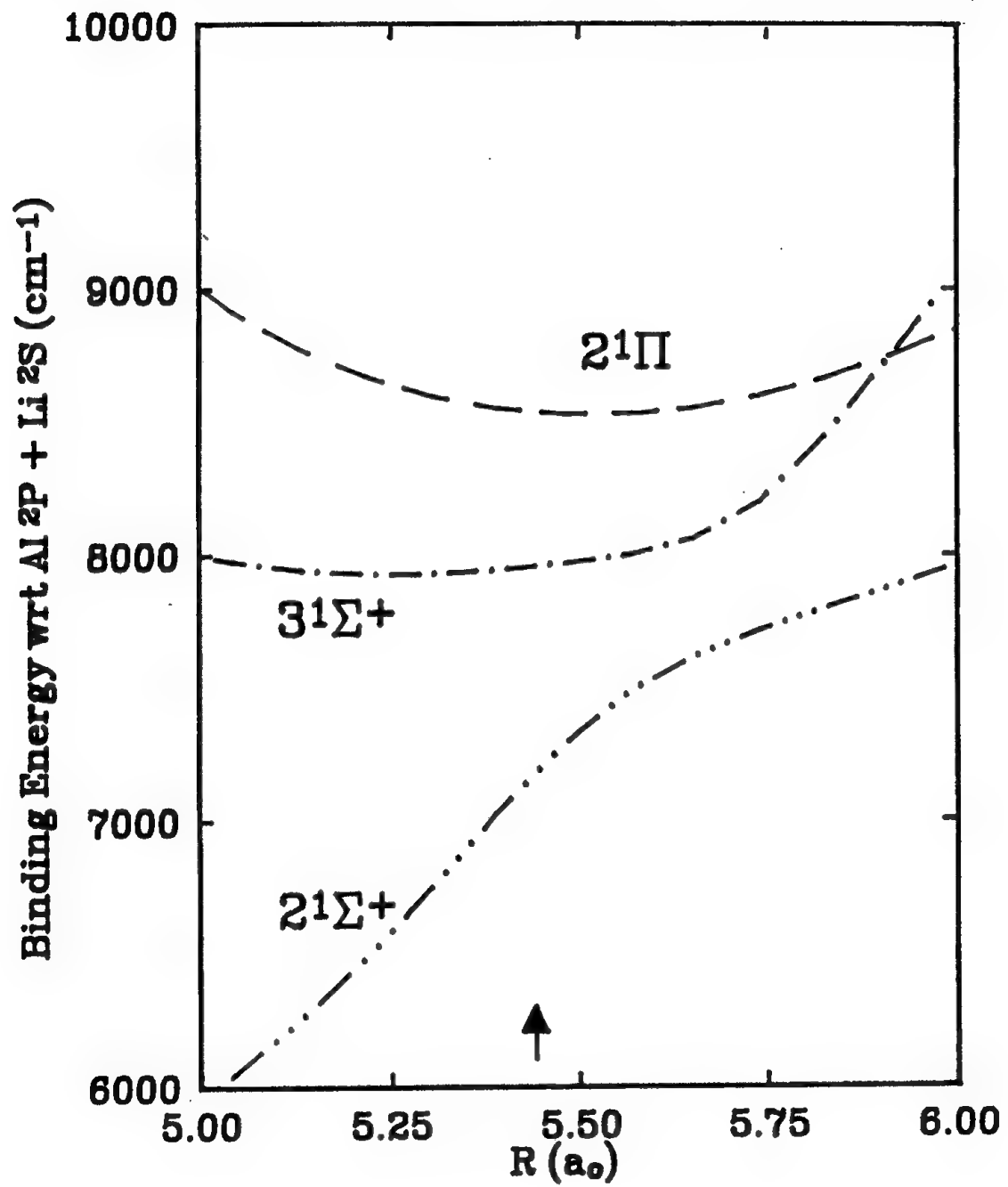


Figure 3. Transition dipole moments.

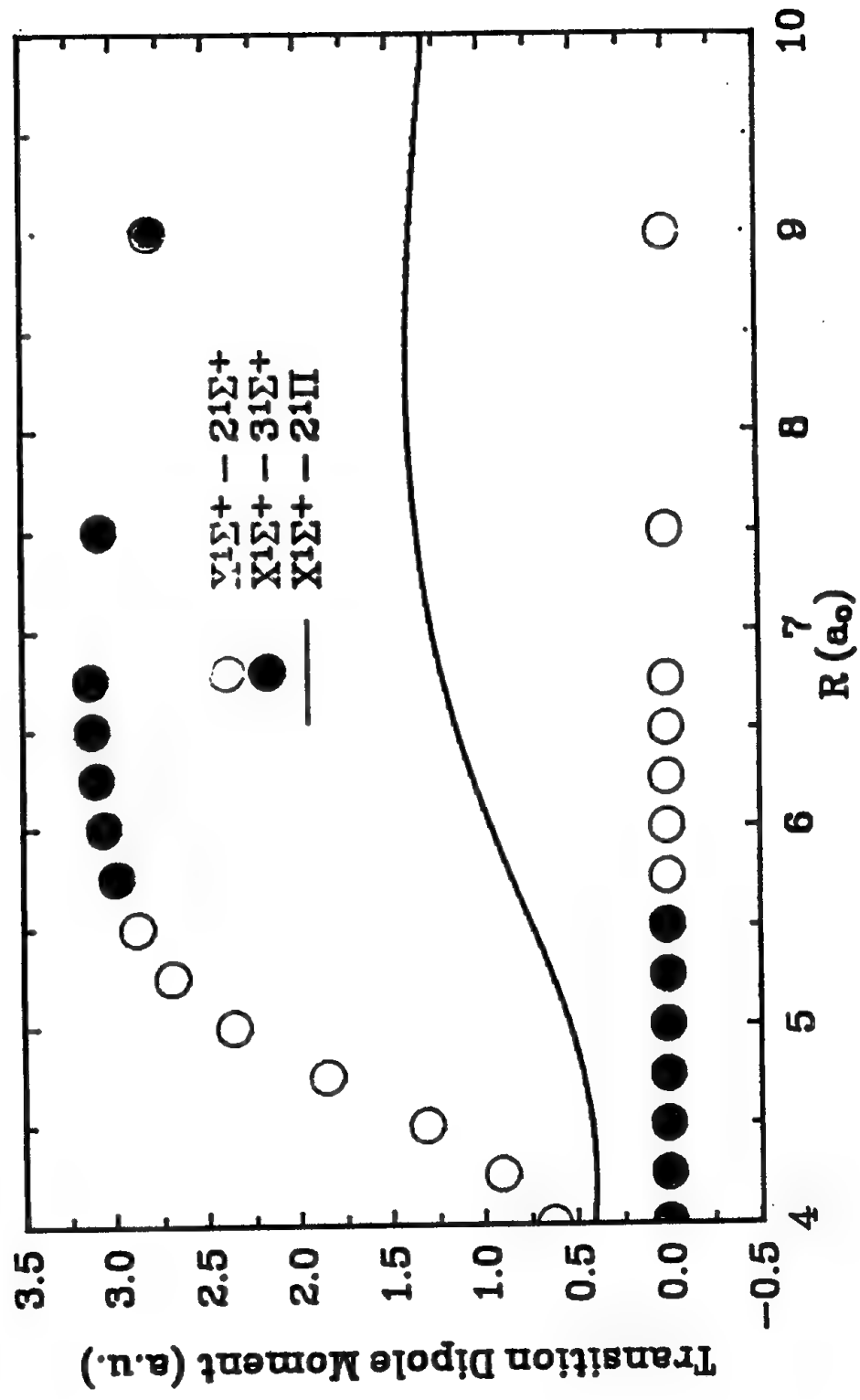
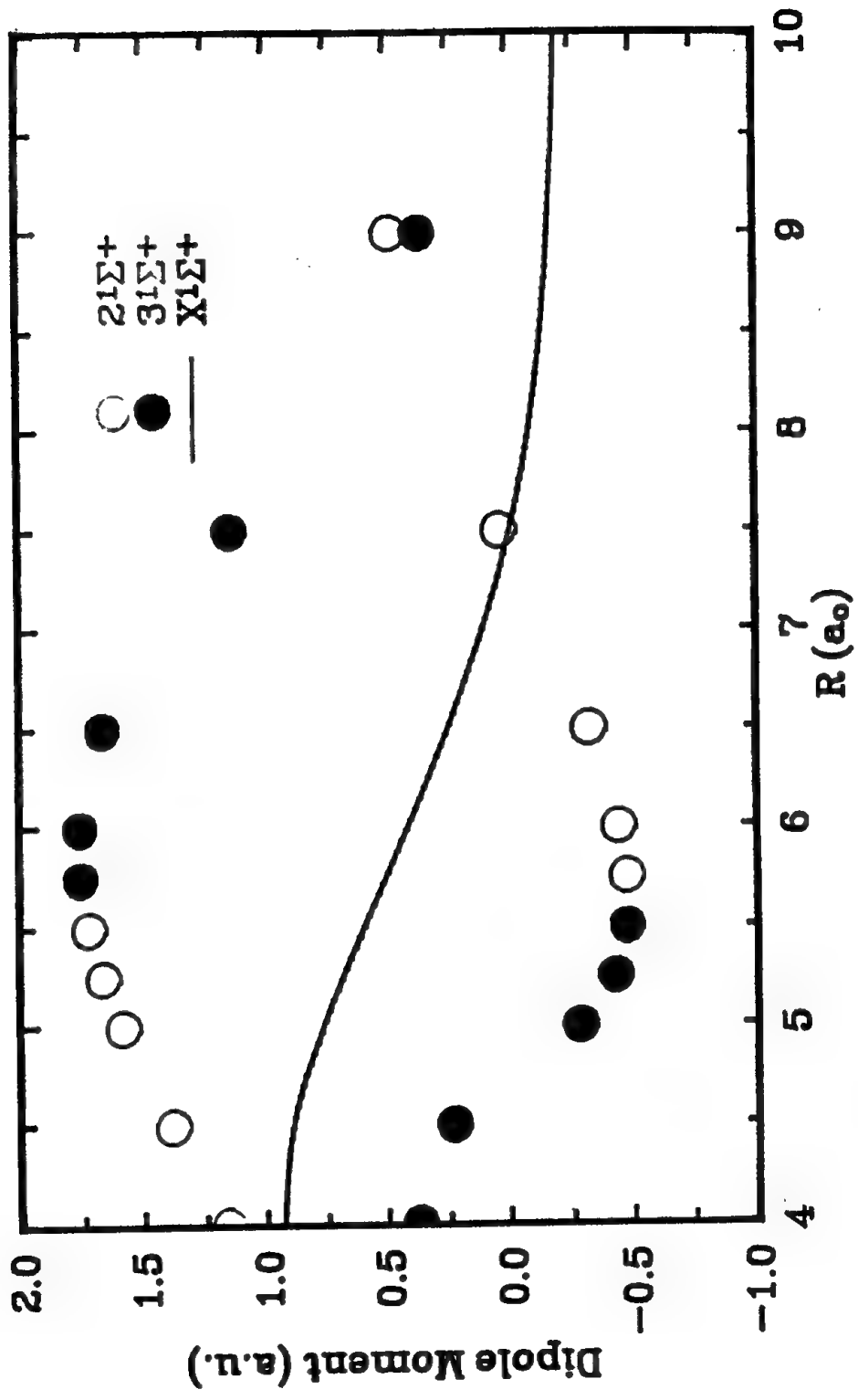


Figure 4. Dipole moments.



Electronic Structure and Thermochemical Properties of Advanced Oxidizers

H. H. Michels and J. A. Montgomery, Jr.
United Technologies Research Center
East Hartford, CT 06108

ABSTRACT

Theoretical electronic structure calculations are being carried out for several high energy species that are attractive candidates for advanced chemical propulsion systems. Using deliverable specific impulse and storability as the major criteria for the evaluation of new oxidizers or fuels, primary consideration is being given to ground state molecular structures, of low molecular weight, which exhibit a high positive heat of formation. Calculations are in progress on: 1) light element high symmetry compounds (Li_3H); 2) hypervalent systems (OF_6); 3) strained ring systems (N_6 , C_6H_6 isomers, such as 1,2,3-cyclohexatriene); and 4) nitramines and dinitramide salts (HMX, PCN, ADN). Our initial studies are on several new oxidizers that may have potential in solid propellant formulations.

An *ab initio* study of the electronic structure of OF_6 has been undertaken. Optimized geometries were calculated at the SCF and MP2 levels of theory using several basis sets, ranging from 6-31G to 6-311+G(d). Vibrational analyses indicate that OF_6 has stability in $[\text{O}_h]$ symmetry at both the SCF and MP2 level, provided diffuse functions are not included in the basis sets. The calculations to date suggest a stability competition between the covalent $[\text{O}_h]$ structure and the $[\text{C}_{4v}] \text{OF}_5^+\text{F}^-$ ion-pair structure.

Nitramines exhibit one or more covalently bonded $\text{N}-\text{NO}_2$ groups which typically result in a molecule with a high energy content. Recently, several new compounds have been synthesized which exhibit a dinitramide anion $[\text{N}-(\text{NO}_2)_2^-]$ structure. In an effort to characterize the geometry and stability of this anion, *ab initio* calculations have been carried out at the SCF/6-31G(d, p) and MP2/6-31G(d, p) levels of theory. The ground ${}^1\text{A}$ state $[\text{C}_2]$ of the dinitramide anion is found to be thermodynamically stable and exhibits a unique IR structure in the $700 - 900 \text{ cm}^{-1}$ region. Our calculations indicate vibrational stability for the Li and Na alkali salts in C_2 symmetry. In contrast, we find that ammonium dinitramide is distorted to C_1 symmetry by strong H-bonding to one of the nitro groups. Hydrogen dinitramide also exhibits asymmetric hydrogen bonding to one nitro group, but for this system the anion becomes planar resulting in overall C_s symmetry.

Performance calculations have been carried out for several new propellant formulations based on dinitramide oxidizers. These new chlorine-free systems show improved performance over present solid formulations based on ammonium perchlorate.

Supported in part by AFAL under Contract F04611-90-C-0009.

DISCUSSION

Hypervalent Compounds

In order to assess the stability of OF_6 , *ab initio* calculations have been carried out at both the SCF and MP2 levels of theory using several different basis sets. Calculations were performed using both the GAUSSIAN 90 and CADPAC series of programs, the latter mainly for second derivative analysis, at the MP2 level, for this closed shell structure. Optimized OF_6 geometries were calculated at the SCF and MP2 levels of theory. Harmonic vibrational frequencies were subsequently computed at the SCF and MP2 stationary points.

The results of our geometry optimization calculations are given in Table 1. The optimum bond length for OF_6 appears to be only weakly dependent on the chosen basis set at the HF level of theory. However, at the MP2 level of theory, we find a significant lengthening of the bond if diffuse functions are included in the basis set. If the optimum bond length becomes greater than $\sim 1.7 \text{ \AA}$, depending on the basis, we find one imaginary frequency. Displacement along this mode corresponds to an asymmetric axial stretch leading to dissociation into F^- and OF_5^+ in C_{4v} symmetry. This conformation for OF_5^+ is a saddle corresponding to the Berry pseudorotation state in the $\text{D}_{3h} \rightarrow \text{C}_{4v} \rightarrow \text{D}_{3h}$ ligand interchange process. Our calculated energy barrier for the pseudorotation process in OF_5^+ is 6.5 kJ/mol at the HF/6-31G* level of theory. This is similar to our calculated barrier of 8.8 kJ/mol for the corresponding process in NF_5 . Calculations of the thermochemistry of decomposition of OF_6 into the $\text{OF}_5^+ + \text{F}^-$ ion-pair are in progress. At the HF level of theory, the covalent OF_6 structure is energetically favored. The predicted long bond length at the MP2 level of theory, using diffuse basis functions, results in a reference state which is UHF unstable. Thus, MP2 may not provide an adequate description of the electronic structure of this system where there appears to be a stability competition between the covalent $[\text{D}_{3h}]$ structure and the OF_5^+F^- ion-pair. Calculations at the MP4 and QCISD levels of theory are currently in progress.

Nitramine Compounds

We have initiated a study of polycyclic caged nitramines, using RDX and HMX as prototype systems for evaluation and calibration of our computational approaches. Many of the molecules that we plan to investigate are too large for application of *ab initio* techniques. We are therefore comparing semi-empirical methods, such as AM1, with *ab initio* Hartree-Fock predictions for the smaller systems in order to gain some confidence in the reliability of the semi-empirical predictions. The first system that we examined was RDX in both the boat and chair structures. Our calculated bond lengths and angles are in good agreement with the data compiled by Rogers [J. T. Rogers, Physical and Chemical Properties of RDX and HMX, Holston Defense Corp., Report Control No. 20-P-26 (1962)]. We find that the AM1 predictions are very close to the optimized HF/6-31G** *ab initio* structure.

The second system studied was HMX, where only the crown [C_{4v}] structure was examined. Again the AM1 predicted structure is very close to that obtained from a very lengthy HF/STO-3G calculation. Finally, we have undertaken a study of polycyclic caged structures beginning with the six-carbon PCN isowurtzitane structure. A comparison of the *ab initio* and AM1 structures for the zeta form of this molecule are shown in Fig. 1, which clearly illustrates the near correspondence of both bond lengths and bond angles. The predicted IR spectra for the zeta [C_{2v}] and epsilon [C_s] forms of this molecule are shown in Fig. 2. These data were calculated at the AM1 level of theory and clearly illustrate the increased complexity of the spectra of the less symmetric epsilon [C_s] form. They may be of use in identifying the several polymorphs of this system.

In a separate study, we have initiated *ab initio* calculations for the dinitramide anion (DN) [$N(NO_2)_2^-$] and on several dinitramide salts. We illustrate the predicted structure of the anion at the HF/6-31+G* level of theory in Fig. 3. *Ab initio* calculations have been initiated on the Li and Na salts of DN and also on a predicted molecule, hydroxyammonium dinitramide (HADN), which has not yet been synthesized. This latter system should have both improved density and energy content over ADN.

A comparison of the predicted vacuum specific impulse of ADN and HADN with baseline AN and AP formulations is shown in Fig. 4. Both ADN and HADN indicate significant improvement over current solid propellant formulations and represent obvious goal molecules for synthesis activities.

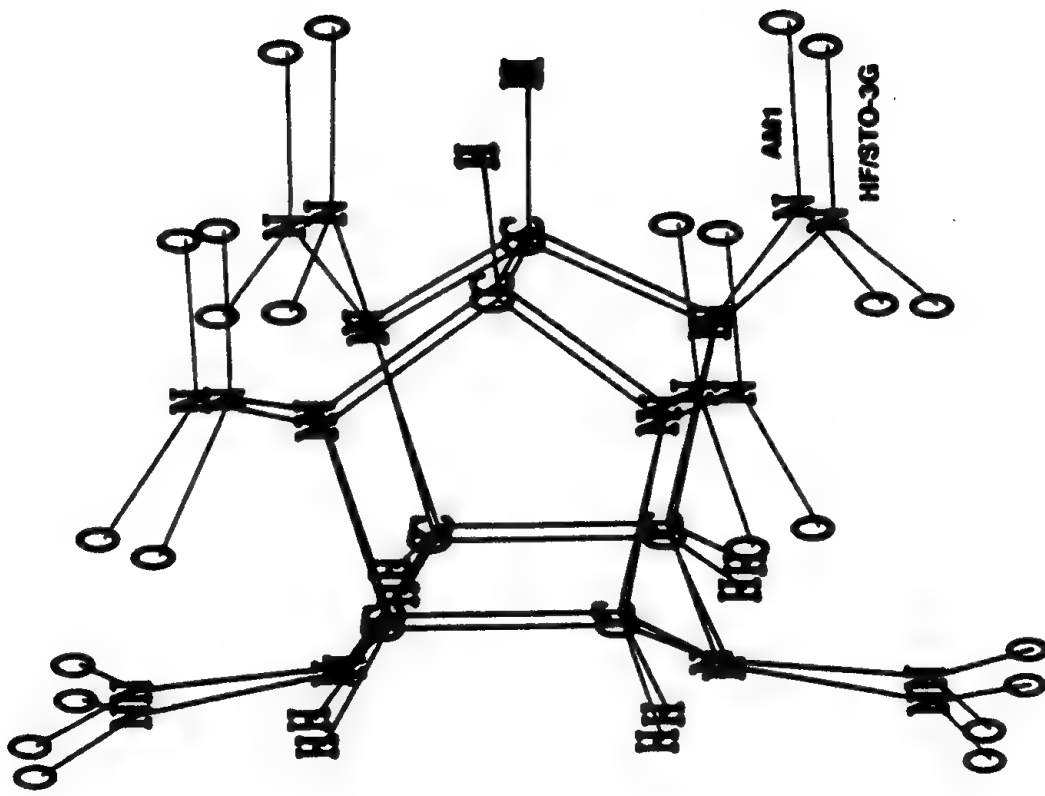
Table 1. Gradient Optimized Structures and Energies for OF₆.

Theory	R (Å)	E (h)	ZPE (h)
HF/6-31G	1.6126	- 670.2323 325	0.0168 625
HF/6-31G(d)	1.5407	- 670.3343 435	0.0183 033
HF/6-31G(2df)	1.5293	- 670.3586 884	-
HF/6-31+G(d)	1.5457	- 670.3605 824	0.0177 040
HF/6-311G(d)	1.5470	- 670.5047 141	0.0166 128
MP2/6-31G(d)	1.6673	- 671.8802 131	0.0128 721
MP2/6-31+G(d)	1.6956	- 671.9594 044	-
MP2/6-311G(d)	1.7210	- 672.4354 062	*
MP2/6-311+G(d)	1.7452	- 672.4817 277	-

* 1 imaginary frequency - asymmetric axial stretch

FIG. 1

Comparison of the Predicted Structure (Zeta Form) of PCN



Predicted IR Spectra for PCN (AM1 Level of Theory)

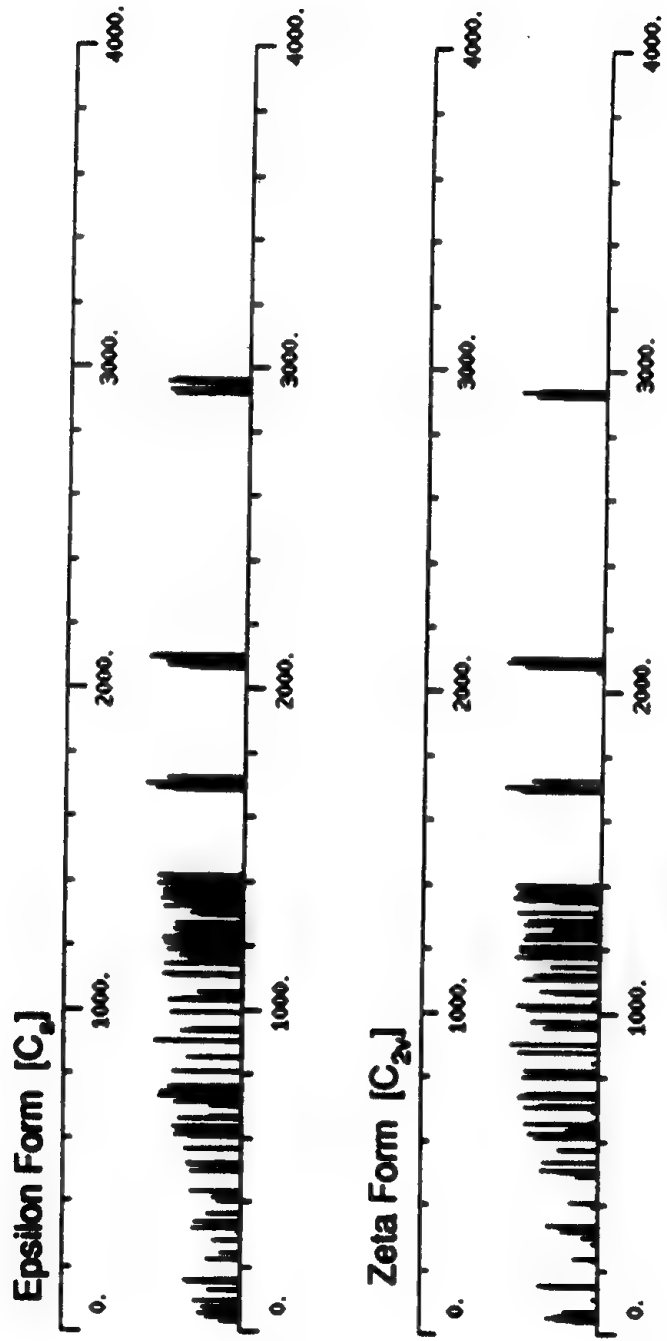


FIG. 2

**Calculated Bond Lengths and Angles
of Dinitramide Anion [N-(NO₂)₂]
(HF/6-31+G* Level of Theory)**

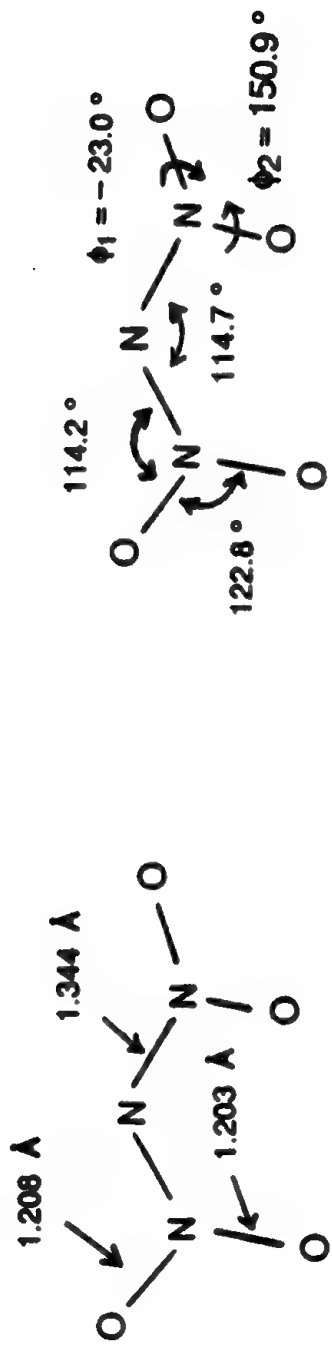
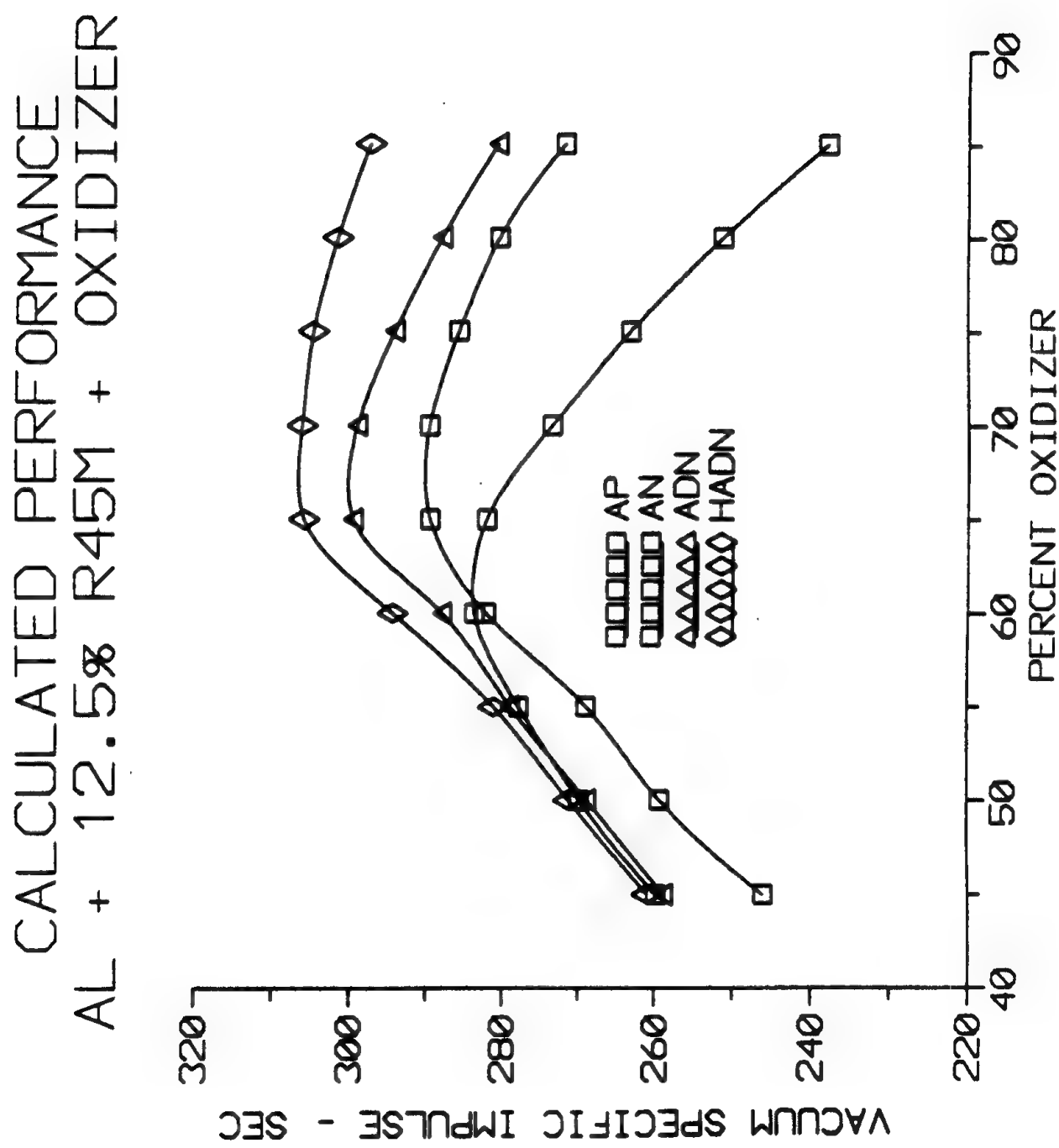


FIG. 3

HEDM10.291

FIG. 4



**POTENTIAL ENERGY SURFACES AND DYNAMICS OF POTENTIAL HEDM
MOLECULES**

Mark S. Gordon, Theresa L. Windus, Kiet A. Nguyen, and Nikita Matsunaga

North Dakota State University

EXTENDED ABSTRACT

I. PENTACOORDINATED ANIONIC SILICON COMPOUNDS

In carbon chemistry, attack of a nucleophilic anion X^- on a saturated carbon center leads to a pentacoordinated (usually trigonal bipyramidal) transition state. In contrast, the attack of the same nucleophile on a saturated silicon center generally leads downhill to a trigonal pyramidal structure which is the global minimum on the potential energy surface (PES). For monosubstituted species SiH_4X^- , the potential energy wells relative to separated $\text{SiH}_4 + \text{X}^-$ range from 1-5 kcal/mol for X taken from the third period (e.g., Cl, SH, PH₂, SiH₃) to 30 kcal/mol for second period ligands (F, OH, NH₂, CH₃)¹. $\text{X} = \text{H}$ produces a 17 kcal/mol well depth. The existence of such deep potential energy wells means these metastable species can under a variety of molecular motions and interactions, including reactions with counter-cations to form much more stable neutral pairs,



and internal isomerizations. The purpose of this part of our program is to develop global PES's for pentacoordinated silicon anions, in order to examine the dynamics of their formation and the coupling/vibrational energy transfer of this motion with internal isomerizations. Subsequent investigations will examine the PES's for reactions of the pentacoordinates with cations.

The first part of the PES to be investigated is the pseudorotational isomerization, depicted schematically in Figure 1. According to this scheme, one of the equatorial atoms is held fixed, while the other two equatorial atoms and the two axial atoms bend into a tetragonal arrangement, predicted to be the transition state on this Berry pseudorotational pathway. If X is different than H, one expects four stationary points on the PES: X axial (1), X equatorial (2), X apical in a tetragonal arrangement (3), and X basal in a tetragonal arrangement (4). If $\text{X} = \text{H}$, 1 = 2 and 3 = 4.

The PES's for pseudorotation in SiH_5^- and SiH_4F^- have been investigated at several levels of theory. The basis sets used include both 6-31G(d) and 6-31++G(d,p). Full geometry optimizations were performed with both of these basis sets with both self-consistent field (SCF) and second order perturbation theory (MP2) wavefunctions. Two approaches are being employed to examine the pseudorotational dynamics. The first of these is variational transition state theory (VTST), based on the reaction path Hamiltonian. The second approach, implemented in collaboration with Don Thompson (Oklahoma State University), is to fit the PES to an analytical function and then perform classical trajectory studies to investigate the dynamics and intramolecular vibrational energy transfer.

For SiH_5^- , the pseudorotation barrier height, $E(3) - E(1)$, is 3.0 kcal/mol at the SCF level of theory and 2.5 kcal/mol when correlation is included. When zero point vibrational energy (ZPE) corrections are included, the latter value drops to 2.15 kcal/mol. Since the level of correlation (MP4 vs. MP2) seems to have little effect on the calculated barrier height, the minimum energy path (MEP) for the reaction has been calculated at the MP2/6-31G(d) level of theory². The next step in the dynamics analysis is to develop the RPH for the reaction. This requires the calculation of the hessian (matrix of energy second derivatives) at regular intervals along the MEP. Diagonalization of the hessian (following projection onto the 3n-7-dimensional space orthogonal to the gradient direction) provides the generalized normal mode frequencies required for the evaluation of the RPH. Once these frequencies have been determined, one can calculate the free energy surface at any temperature. The MEP, ZPE-corrected MEP, and 298K free energy curve are shown in Figure 2. Superimposed on these curves are selected structures along the MEP to illustrate the progress of the geometry along the path. The information illustrated in Figure 2 may be used to calculate the reaction rate at any temperature, using VTST. The calculated rate constant ranges from 1.18×10^{10} at 150K to 1.48×10^{13} at 1000K. The broad low barrier, combined with little reaction

path curvature, results in a small transmission coefficient (1.65), even at 150K.

For SiH₄F⁻ one expects a pseudorotational pathway that leads from 1 → 3 → 2 → 4. Indeed, this is just what is found at modest levels of theory, and reports of axial → equatorial isomerizations abound in the literature. However, at higher levels of theory (i.e., a basis set at least the size of 6-31++G(d,p) and the introduction of perturbation theory in the geometry optimization) causes a dramatic change in the predicted PES: structures 2 and 3 merge into the same transition state, leaving just one minimum (1) on the potential energy surface³. This means that the pseudorotational path is much more complex than that proposed by Berry. One can calculate a minimum energy path leading from 4 → 2 (path A). Since 2 is also a transition state, there is a second MEP leading from 2 → 1 (path B). However, since both 4 and 2 are transition states, there must be a bifurcation on path A, where a second imaginary frequency appears. At this point, the system encounters a potential energy ridge, and simple MEP-driven approaches are insufficient to analyze the dynamics of the motion. A proper accounting of the motion requires the construction of a global PES.

II. NO DIMER

The second part of this project is an examination of the structures, bonding, stabilities, decomposition pathways, and dynamics of isomers of N₂O₂. Because N₂O₂ is isoelectronic with bicyclobutane, it occurred to us that there may be bicyclobutane-like structures on the N₂O₂ PES. To explore the possible existence of such structures, as well as other potential energy minima, three levels of theory have been used to date, all with the 6-31G(d) basis set. These are restricted Hartree-Fock (RHF) second order perturbation theory (MP2), and generalized valence bond (GVB). The GVB calculations include five separated pairs, corresponding to the five bonds in the molecule. At the RHF, GVB, and MP2 levels of theory, two N₂O₂ structures are found with bicyclic structures (**1a** and **1g** in Figure 3). These are minima on the RHF and GVB surfaces, while the MP2 Hessians have not been calculated at this writing. These structures correspond to the two bond stretch isomers in tetrasilabicyclobutane⁴. Like the isovalent all-silicon compound, the bond stretched isomer (**1g**) is the lower energy structure of the two, by about 13.5 kcal/mol at the GVB/6-31G(d) level of theory. Isomer **1a** is particularly exciting, because it is 77.8 and 104.0 kcal/mol above 2NO and N₂ + O₂, respectively, at the MP4/6-311G(d)/MP2/6-31G(d) level of theory. Examination of its structure reveals that this isomer could indeed dissociate to either of these two stable products, whereas it appears that **1g** is most likely to dissociate to 2NO. The next step in the investigation of these metastable high energy species is to determine the transition states leading to each set of products. This will clearly require multi-configurational wavefunctions, since each of the minima exhibit considerable configurational mixing. Note that the transition state connecting the two bicyclo minima has been determined (**2a** in Figure 3). At the GVB level of theory, this structure is 31 kcal/mol above **1a**.

Once the transition states connecting **1a** and **1g** with products have been identified, the minimum energy paths for these reactions will be determined and the decomposition dynamics determined using methods described above. Note that, in addition to the two minima displayed in Figure 3, six additional minima have been identified on the N₂O₂ PES. At least two of these have energies which are comparable to those of the bicyclo isomers and are therefore equally deserving of detailed investigation.

REFERENCES

1. M.S. Gordon, L.P. Davis, L.W. Burggraf, and R. Damrauer, J. Am. Chem. Soc., 108, 7889 (1986).
2. T.L. Windus, M.S. Gordon, L.P. Davis, and L.W. Burggraf, J. Am. Chem. Soc., 112, 7167 (1990).
3. T.L. Windus, M.S. Gordon, L.P. Davis, and L.W. Burggraf, J. Am. Chem. Soc., submitted.
4. J.A. Boatz and M.S. Gordon, J. Phys. Chem., 93, 2888 (1989).

Berry Pseudorotation (BPR)

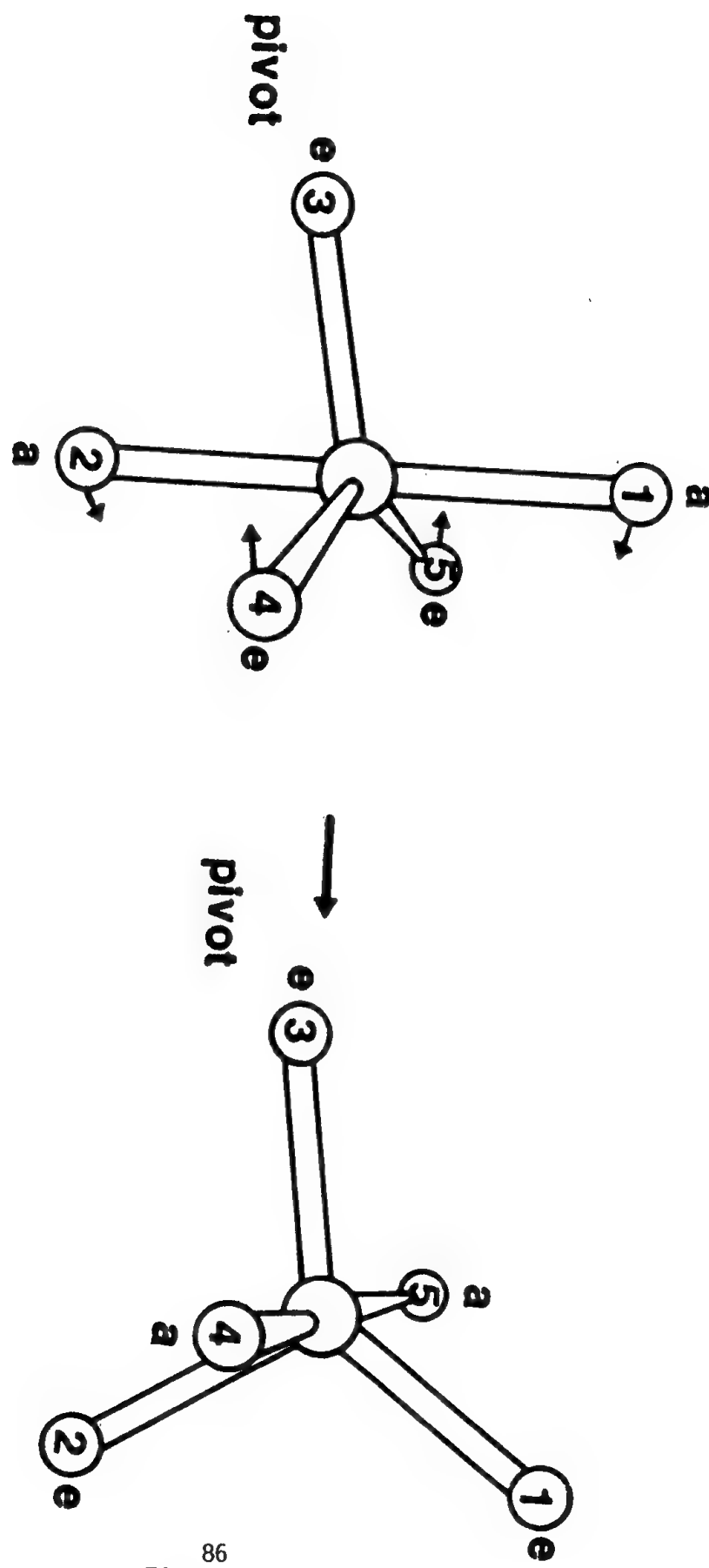


Figure 1

SiH₅ – IRC
Energy vs. Reaction Coordinates
Energy Unit is kcal/mol

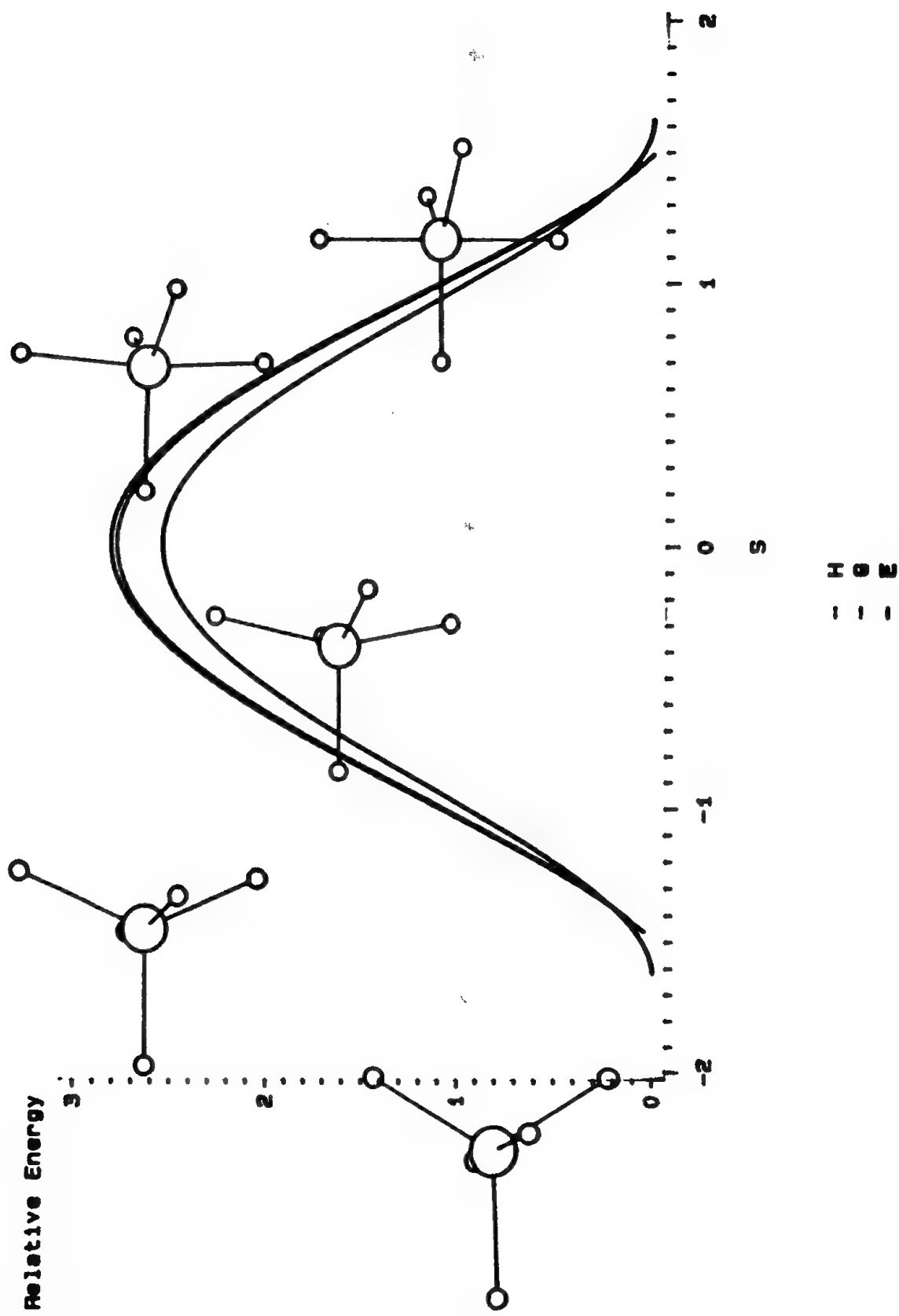
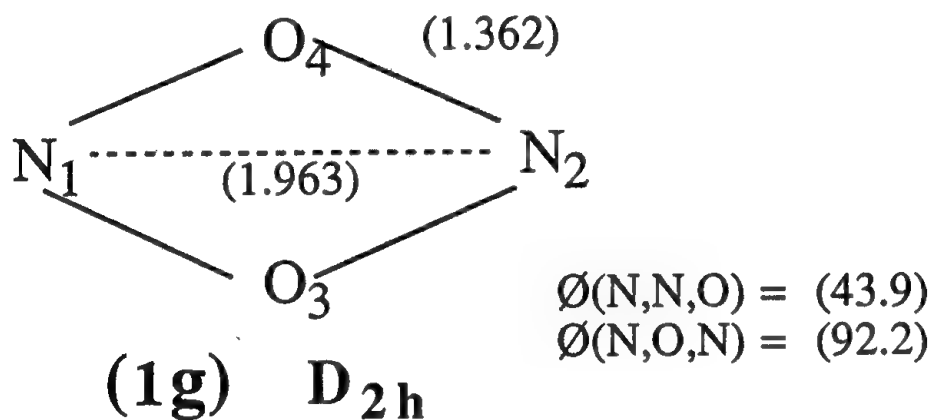
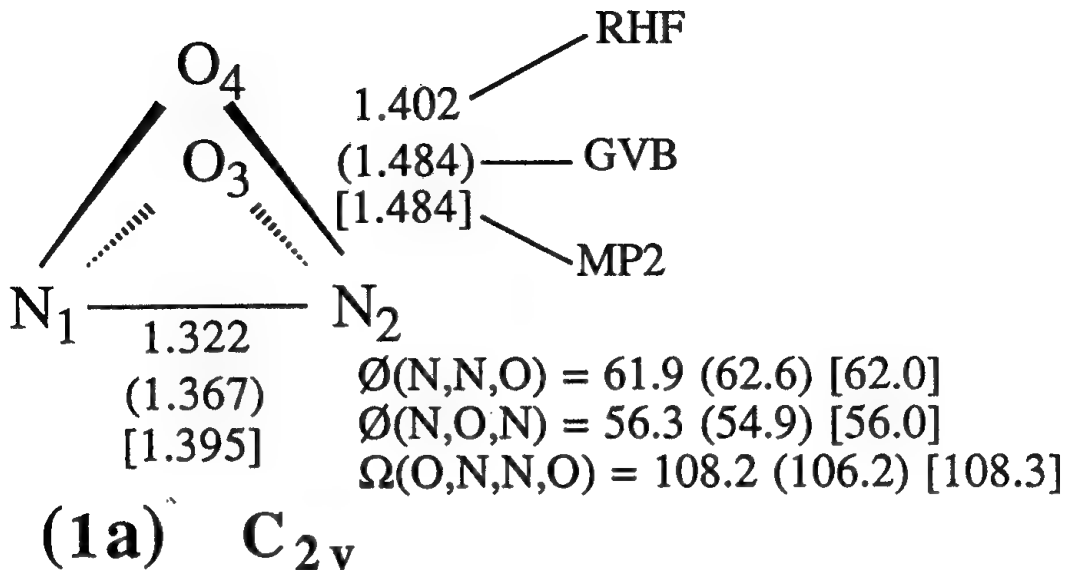
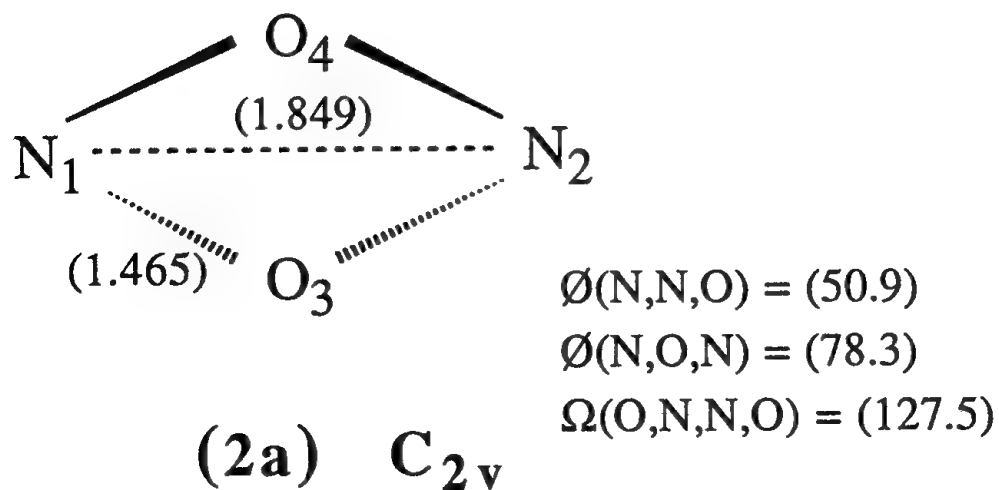


Figure 2⁸⁷



Transition State 1a \longrightarrow 1g



Theoretical Studies of Spin-Forbidden and Electronically Nonadiabatic
Processes:
Actual/Avoided Surface Crossings
Spin-Forbidden Radiationless Decay in Dications

David R. Yarkony
Department of Chemistry
The Johns Hopkins University
Baltimore, MD 21218

When considering the stability of a potential energetic material, that is a system which possesses an energetic local extremum on the ground potential energy surface, one must consider the possibility of interactions with nominally excited electronic states as these interactions may lead to dissociation channels for the metastable energetic species. These excited electronic states may be of the same or different spin symmetry as the ground electronic state. The regions to be considered comprise two distinct topological classes: *allowed or actual surface crossings and avoided surface crossings*, which are defined as follows:

(a) *Allowed surface crossings*: are intersections of two potential energy surfaces which are permitted by symmetry, that is they represent intersections of two potential energy surfaces of distinct spin-space symmetries. A point of special interest on the surface of allowed surface crossings is the minimum energy crossing point.

(b) *Actual surface crossings*: are intersections of two potential energy surfaces of the *same* spin-space symmetry which are permitted by the multidimensional breakdown of the Wigner-von Neumann noncrossing rule originally noted by Herzberg and Longuet-Higgins.¹ The locus of points corresponding to an actual surface crossing is a surface of dimension M-2 where M is the number of internal nuclear degrees of freedom.

(c) *Avoided surface crossings* result because the multidimensional breakdown of the Wigner-von Neumann noncrossing rule *permits but does not guarantee* the existence of a surface of actual crossings, that is the solutions of the equations defining the actual surface crossing may require the nuclear coordinates to take on complex values. In this case the actual crossing hypersurface merges into an avoided crossing hypersurface (of the same dimension).

In the absence of simplifications attributable to spacial symmetry these features can be difficult to isolate thus underscoring the need for algorithms for the location of these regions of close approach of potential energy surfaces. We have developed analytic gradient driven algorithms which provide a systematic procedures for locating these regions.² Apart from the practical considerations noted above these algorithms are of theoretical import in view of the somewhat controversial history of the noncrossing rule. In 1963 Herzberg and Longuet-Higgins¹ reiterated a result of Teller³ demonstrating that crossings of potential energy surfaces of the same symmetry were possible in *polyatomic* systems. In addition these authors showed that the wavefunctions for these states will change sign when the nuclei make a single pass along a closed path containing this intersection. However their result was questioned in a 1972 paper by Naqvi.⁴ Although Naqvi's contention was subsequently refuted by Longuet-Higgins⁵ the noncrossing 'myth' has persisted. Quite recently Ohrendorf *et al.*⁶ have suggested that the noncrossing rule may hold in an approximate sense when the two states in question differ (principally) by a double excitation.

We have used the algorithm noted above to locate an *actual crossing seam* for the $1^1A'$ and $2^1A'$ potential energy surfaces of the He-H₂ system,⁷ a system which has been the focus of much interest in the HEDM program.^{8,9} The seam we have determined is NOT related to any high symmetry nuclear configuration. *This is the first report of a seam of actual surface crossings for two potential energy surfaces of the same symmetry based on MCSCF/CI wavefunctions.* The actual crossing seam, $R(r)$, is specified by the ordered triple $R(r)=[R(r), \gamma(r), r]$ for which $\Delta E_U(R) = 0$. Here R is the He-H₂ distance, γ is the He-H₂ angle and r is the H₂ distance which is also taken as the seam parameter. This seam defines a region of nuclear coordinate space near which helium can efficiently quench H₂(B $^1\Sigma_u^+$). The locus of the seam [R(r), r, $\gamma(r)$] is pictured below,

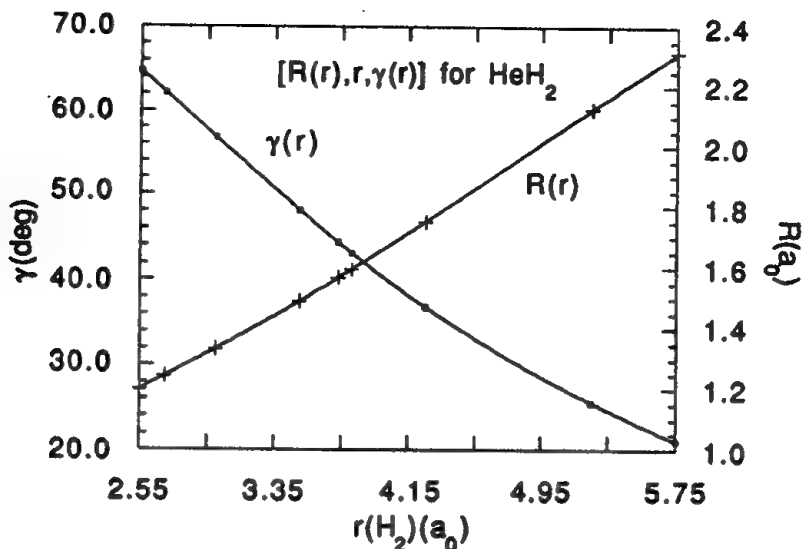


Figure 2

The energy along this seam relative to the $\text{H}_2(\text{B}^1\Sigma_u^+)$ state asymptote is presented below:

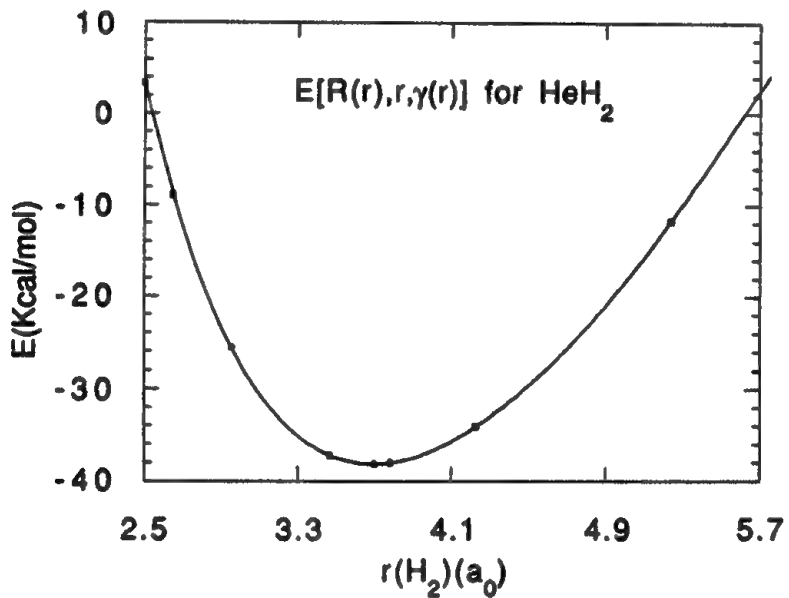
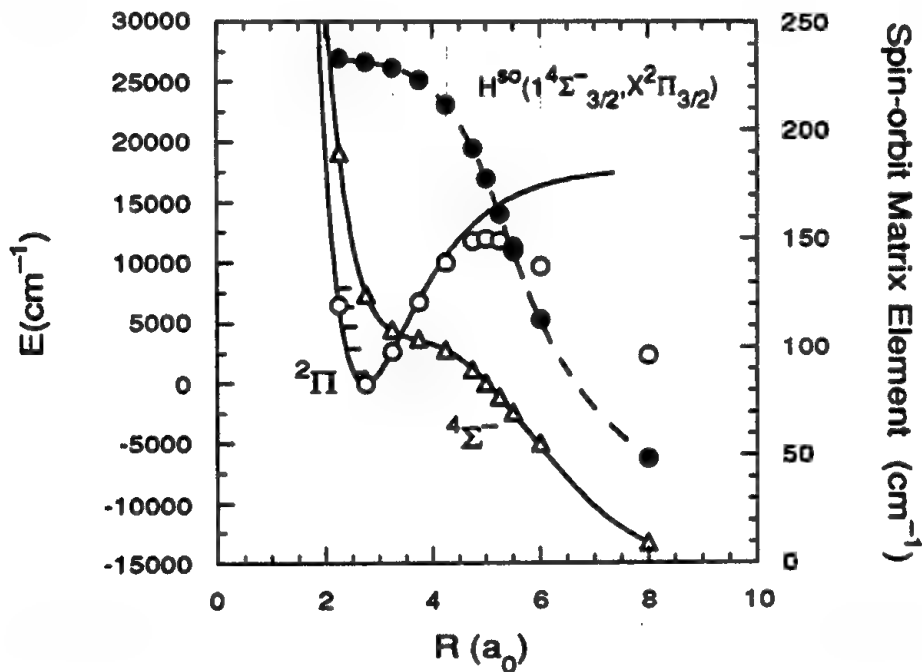


Figure 3

Since this portion of the actual crossing seam is exoergic relative to the $\text{He} + \text{H}_2(\text{B})$ asymptote it is relevant to the low energy scattering experiments recently reported by Moore's group.⁹ Its inclusion in any potential energy surface used in future dynamical studies appears imperative.

In collaboration with the theoretical/experimental group at The University of Colorado at Boulder (S.V. O'Neil, J. Senekowitsch, C. Lineberger, and S. Leone) we have begun a study of the effect of spin-forbidden radiationless decay on the stability of (isolated) dications. In our first such study the lifetimes of the low-lying vibrational levels of the $X^2\Pi$ state of the dication HS^{2+} were considered.¹⁰ This state is formed by the avoided crossing of 2Π states corresponding to $\text{H}^+ + \text{S}^+$ and $\text{H} + \text{S}^{2+}$. However *the lifetimes of the low-lying vibrational levels are controlled entirely by the spin-orbit induced perturbation, $1^4\Sigma^- - X^2\Pi$* , and the corresponding allowed crossing of the $X^2\Pi$ potential energy curve by the dissociative $1^4\Sigma^-$ potential energy curve which correlates with the ground state asymptote $\text{H}^+ + \text{S}^+(4S)$. The relevant potential energy curves and spin-orbit induced coupling, $H''(1^4\Sigma_\Omega^-, X^2\Pi_\Omega) = \langle \Psi^0(1^4\Sigma_\Omega^-) | H'' \Psi^0(X^2\Pi_\Omega) \rangle$ are displayed in the following figure¹⁰



The lifetimes of the individual vibrational levels of the $X^2\Pi$ state are presented in the following table¹⁰

Lifetimes^a of the Vibrational Levels of the $X^2\Pi$ State of HS^{2+}

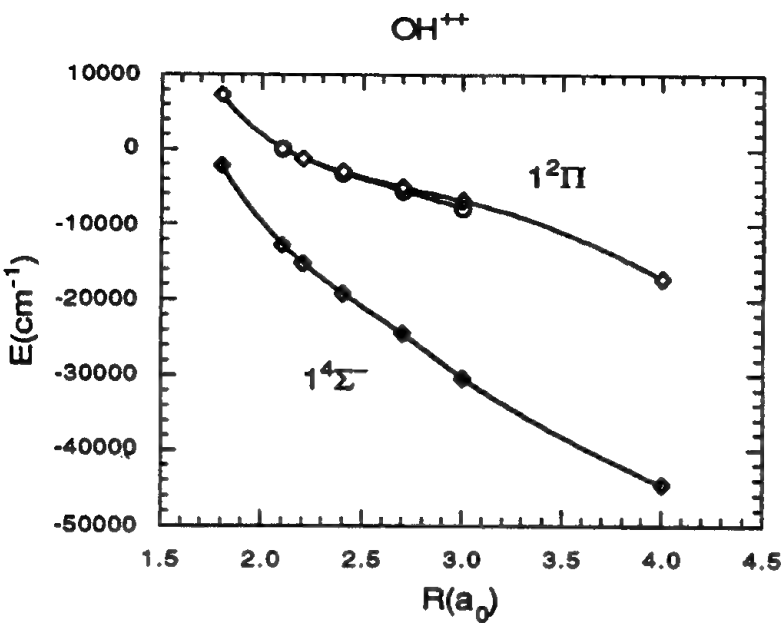
v	G_v	τ^{GR}	τ^{QM}	τ^{SA}
0	997.15	55.0 (-6) 9.85 (-3)	(b) (b)	∞
1	2905.35	106. (-12) 22.3 (-9)	99.0 (-12) (b)	∞
2	4698.75	67.8 (-15) 365. (-15)	64.4 (-15) 334. (-15)	∞
3	6377.35	142. (-15) 81.6 (-12)	131. (-15) 34.2 (-12)	11.1 (+6)
4	7941.15	206. (-15) 44.7 (-12)	189. (-15) 22.3 (-12)	11.8

^aThe vibrational energies G_v (from a Morse curve) are given in cm^{-1} . The lifetimes τ^{GR} (golden rule), τ^{QM} (quantum calculations) and τ^{SA} (spin-allowed) are expressed in seconds, with the characteristic, base 10, given parenthetically. Results from shifted $1^4\Sigma^-$ potential energy curve are below those for unshifted curve. τ^{SA} represents the lifetimes of the vibrational levels on the isolated $X^2\Pi$ potential energy curve from Ref. 11

^bThe width of these levels is too small to be calculated by the lifetime matrix method.

In the absence of the spin-orbit induced coupling to the dissociative $1^4\Sigma^-$ state the $X^2\Pi$ $v=0-4$ levels would be extremely stable (column τ^{SA}). However the presence of this interaction renders these vibrational levels metastable (columns τ^{GR} and τ^{QM}). It is particularly interesting to note that although the crossing of the $X^2\Pi$ and $1^4\Sigma^-$ potential energy curves occurs at an energy greater than that of $X^2\Pi, v=1$ the lifetime of the $X^2\Pi, v=0,1$ levels is significantly shortened. For these levels the radiationless decay is due to spin-orbit induced tunneling.

Since the comparatively short lifetimes of $X^2\Pi, v=0,1$ are due to the large spin-orbit coupling matrix element it is interesting to ask whether these levels would be longer lived in the isovalent first row species OH^{2+} for which the spin-orbit coupling would be weaker. Unfortunately as the following figure shows the corresponding $1^2\Pi$ state is not bound in OH^{2+} .



References

1. G. Herzberg and H. C. Longuet-Higgins, Disc. Faraday Soc. **35**, 77 (1963).
2. D. R. Yarkony, J. Chem. Phys. **92**, 2457 (1990).
3. E. Teller, J. Phys. Chem. **41**, 109 (1937).
4. K. R. Naqvi, Chem. Phys. Lett. **15**, 634 (1972).
5. H. C. Longuet-Higgins, Proc. R. Soc. Lond. A **344**, 147 (1975).
6. E. Ohrendorf, L. S. Cederbaum, and H. Koppel, Chem. Phys. Lett. **151**, 273 (1988).
7. R. Manaa and D. R. Yarkony, J. Chem. Phys. **93**, 4473 (1990).
8. J. K. Perry and D. R. Yarkony, J. Chem. Phys. **89**, 4945 (1988).
9. C. D. Pibel, K. L. Carlton, and C. B. Moore, J. Chem. Phys. **93**, 323 (1990).
10. G. Parlant, J. Senekowitsch, S. V. O'Neil, and D. R. Yarkony, J. Chem. Phys. **xx**, yyyy (1991), in press.
11. P. J. Miller, S. A. Rogers, J. Senekowitsch, S. V. O'Neil, S. R. Leone, H.-J. Werner, and P. J. Knowles, Int. J. Mass Spectrom. Ion Processes **100**, 505 (1990).

LASER AND FOURIER TRANSFORM SPECTROSCOPY OF NOVEL PROPELLANT MOLECULES

Grant F04611-90-K-0031

Peter Bernath
Department of Chemistry
University of Waterloo
Waterloo, Ontario, Canada N2L 3G1

In our continuing study of energetic and metastable molecules, we have recorded spectra of C₃, C₆₀, CH and BeF₂. These molecules were all observed by Fourier transform emission spectroscopy.

A. C₃

A new infrared electronic transition of C₃ was discovered near 6500 cm⁻¹ (Figure 1). The $\tilde{b}^3\Pi_g - \tilde{a}^3\Pi_u$ system of C₃ was detected by infrared Fourier transform emission spectroscopy of a microwave discharge plasma containing CH₄, He and P₄. The $\tilde{b} - \tilde{a}$ transition was also detected at the National Research Council (Ottawa) by diode laser absorption spectroscopy of a hollow cathode discharge of hydrocarbons in the He¹. The $\tilde{a}^3\Pi_u$ state of C₃ is metastable with a lifetime of 20 msec in a solid Ne matrix.²

The excited $\tilde{b}^3\Pi_g$ state was found to be extensively perturbed, probably by the excited vibrational levels of the $\tilde{a}^3\Pi_u$ state. Molecular constants were extracted for the 000-000 vibrational band and are reported in Table 1. The r_0 bond lengths were calculated to be 1.286 Å in the $\tilde{b}^3\Pi_g$ state and 1.298 Å in the $\tilde{a}^3\Pi_u$ state.

B. C₆₀

The recent discovery of a synthetic route to macroscopic quantities of C₆₀ has aroused great interest.³ Pure carbon molecules have potential applications as propellants, although it turns

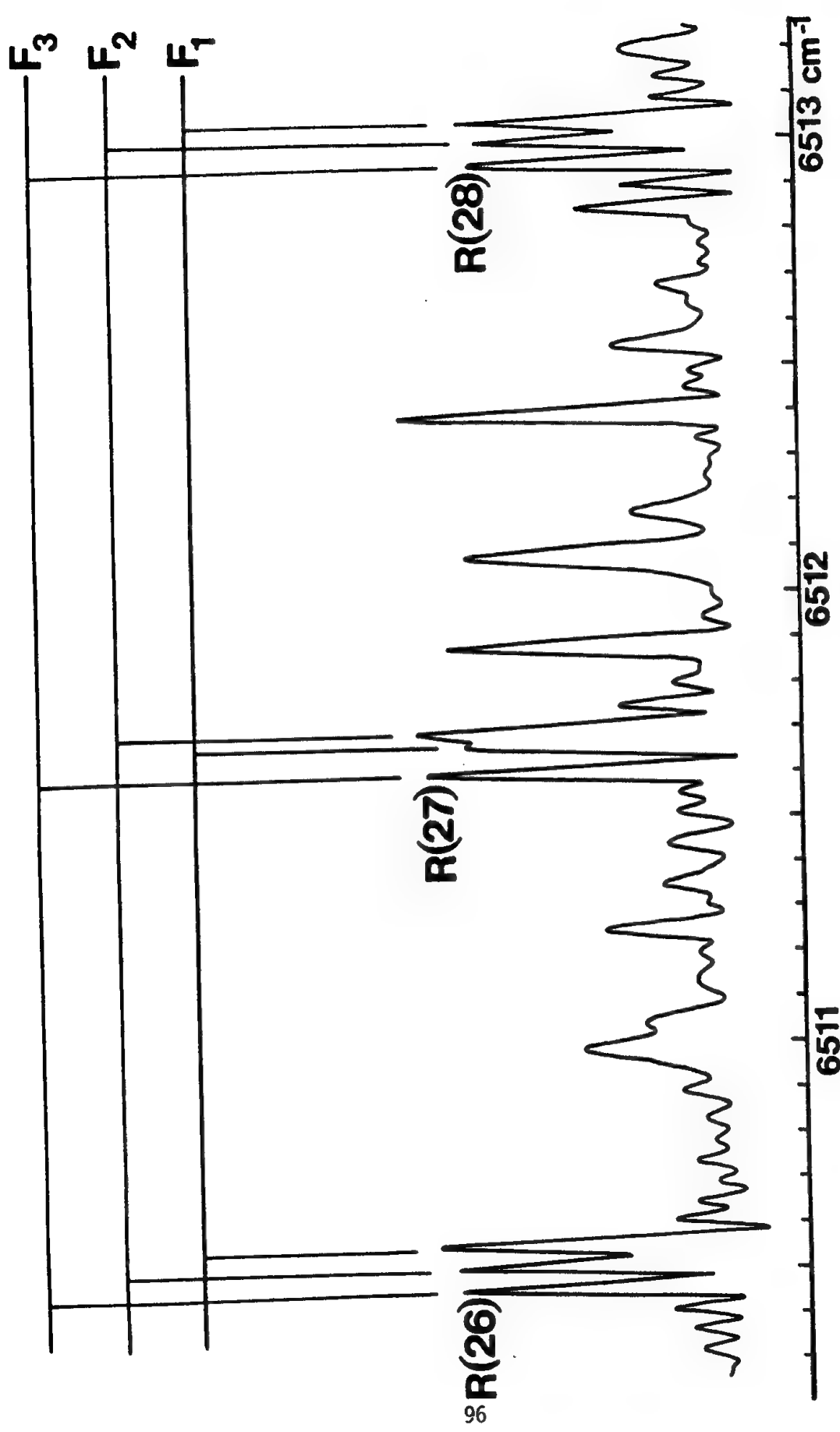


Figure 1
Infrared Emission Spectrum of C_3

out that pure C₆₀ is relatively difficult to ignite. Advanced propellants based on light metals trapped in the C₆₀ cage are also of interest.

We recorded the first gas-phase spectra⁴ of C₆₀ by heating the solid in a tube furnace to 950°C. The infrared emission spectra were recorded with the Kitt Peak Fourier transform spectrometer (Figure 2). In agreement with the condensed phase spectra, four strong bands⁴ were found at 527, 570, 1169 and 1407 cm⁻¹.

C. BeF₂

Infrared emission spectroscopy is proving to be a valuable tool for the characterization of small metal-containing molecules. The conventional wisdom is that high resolution emission is not suitable for long wavelength spectroscopy. In order to test our tube furnace and explore the utility of emission spectroscopy, we recorded⁵ the spectrum of BeF₂.

BeF₂ was heated to 1000°C in an alumina tube furnace and the emission was focussed into the entrance aperture of the Kitt Peak Fourier transform spectrometer. Strong emission was observed at 6.5 μm, corresponding to the antisymmetric stretching vibration, ν₃. The ν₃ fundamental and seven hot bands were rotationally analysed. BeF₂ was confirmed to be a linear molecule with an equilibrium Be-F bond length of 1.3729710(95) Å.

D. CH

CH is one of the most important free radicals because it occurs in a wide variety of environments. In particular, CH emission is prominent when most conventional propellants are burned. We have combined⁶ the infrared vibration-rotation data with a new set of Fourier transform measurements of the A²Δ-X²Π and B²Σ-X²Π electronic transitions to provide an improved set of molecular constants for the X²Π, A²Δ and B²Σ states.

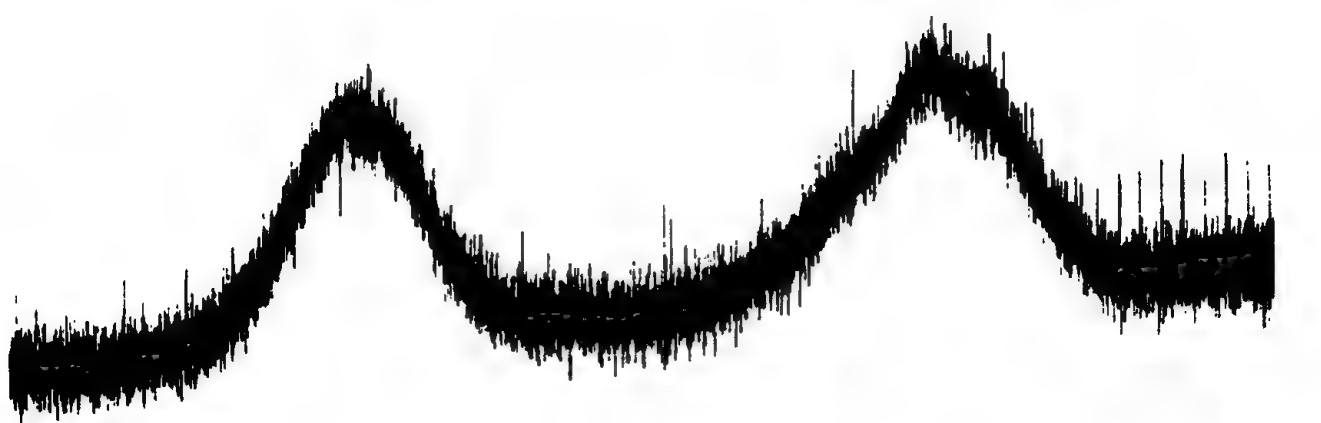


Figure 2
 C_{60} Emission
98

References

1. H. Sasada, T. Amano, C. Jarman and P.F. Bernath, *J. Chem. Phys.* (in press).
2. W. Weltner, Jr. and D. McDonald, Jr. *J. Chem. Phys.* **40**, 1305 (1964).
3. W. Krätschmer, L.D. Lamb, K. Fostiropoulos and D.R. Huffman, *Nature* **347**, 354 (1990).
4. C.I. Frum, R. Engleman, Jr., H.G. Hedderich, P.F. Bernath, L.D. Lamb and D.R. Huffman, *Chem. Phys. Lett.* **176**, 504 (1991).
5. C.I. Frum, R. Engleman, Jr. and P.F. Bernath, *J. Chem. Phys.* (submitted).
6. P.F. Bernath, C.R. Brazier, R. Hailey, W.T.M.L. Fernando, C. Woods and J.L. Hardwick, *J. Mol. Spectrosc.* (in press).

Table I Molecular constants of C_3 in lowest triplet states (in cm^{-1}).

	$\tilde{b}^3\Pi_g$	$\tilde{a}^3\Pi_u$
<i>A</i>	13.919 (44)*	13.556 (43)
<i>B</i>	0.424524(22)	0.416957(19)
<i>D</i> $\times 10^6$	0.5755 (73)	0.368 (15)
<i>H</i> $\times 10^{11}$	—	3.60 (43)
λ	.0396 (73)	-.0588 (68)
γ	-.00222 (76)	-.00461 (77)
σ	.581 (54)	.595 (54)
<i>p</i> $\times 10^3$	-2.2 (12)	-2.2 (12)
<i>q</i> $\times 10^3$.174 (11)	.377 (11)
<i>T_v</i>	6482.3903 (32)	—

* One standard error to the last digits of the quoted constants.

EXPERIMENTAL CONFIRMATION OF CLUSTER-IMPACT FUSION

Y. K. Bae, D. C. Lorents, S. Young, and K. Stalder

SRI International
Molecular Physics Laboratory
Menlo Park, CA 94025

ABSTRACT

We proposed that cluster-impact fusion (CIF), the use of cluster ions for igniting nuclear fusion, is a promising way of achieving an extremely high energy density for rocket propulsion. The energy density that can be achieved by CIF with DT fuel is 3.4×10^{14} J/kg, which is eight orders of magnitude larger than the energy density of LOX/H₂ (1.6×10^6 J/kg). We predicted, that for missions with $I_{sp} < 10^5$ s, CIF rocket performance will be essentially identical to that of antimatter. However, production and storage of CIF fuels will be straightforward, because it uses regular matter instead of antimatter.

Under the current project, we have constructed and demonstrated a cluster-impact fusion facility that includes a new high intensity water cluster ion source and a 300-kV electrostatic accelerator. With the facility, we have successfully reproduced and extended the results obtained by BNL scientists. We are now confident that the extreme fusion enhancement observed in cluster-impact fusion is real, and we are ready to investigate means of increasing the fusion yield to a practical level.

INTRODUCTION

The potential of utilizing nuclear fusion for rocket propulsion has been recognized for many decades, since the discovery of nuclear fusion. Fusion rocket engines have the potential of high I_{sp} and thrust comparable with that of antimatter. Conventional fusion devices with magnetic or inertial confinement schemes, however, seem too bulky and heavy to be used for rocket engines. Thus, to realize fusion powered rocket engines, new, innovative fusion schemes that are efficient and simple enough to allow compact fusion reactors must be sought.

We believe that the cluster-impact fusion (CIF) is an ideal candidate for a revolutionary rocket propulsion scheme.^{1,2} Available results of experimental and theoretical studies on CIF suggest that it may be an extremely efficient and simple fusion power source. Thus, CIF will allow much more compact fusion devices than conventional fusion driven by lasers or heavy ions. Rapid development of practical rocket engines with CIF seems possible, because requisite technologies, such as accelerators and ion source technologies, are readily available. Furthermore, CIF can also be used for evolutionary rocket propulsion with the use of the existing thermal heat exchanger concept for a nuclear fission thermal rocket with an I_{sp} of 900 s. Therefore, if it becomes practical, CIF could serve both revolutionary and evolutionary rocket propulsion needs.

Almost at the end of our previous Air Force contract (Contract F04611-87-C-0025), scientists from Brookhaven National Laboratory (BNL)¹ announced the discovery of CIF, and we concluded that CIF is the best candidate for the revolutionary rocket concepts that the Air Force has been seeking. Thus, we changed our research direction to study CIF in the previous contract and proposed a new three-month contract, which became the current contract. Under the previous contract, we began to modify our cluster source system for adapting the new cluster source and acquired and transported a 300-keV accelerator from the Lawrence Berkeley Laboratory (LBL). Under the current contract, we accomplished building and demonstrating a new water cluster ion source and its associated vacuum system and to adapt the 300-keV accelerator. We also accomplished using the new facility to confirm the results of the BNL scientists.

CONSTRUCTION OF THE ION SOURCE VACUUM SYSTEM AND ION OPTICS

Figure 1 shows the schematic diagram of the completed cluster impact fusion facility. We have constructed a vacuum system composed of two sections and adapted it to the existing ion beam facility. The ion source vacuum chamber consists of two sections vacuum-isolated by a skimmer. The first vacuum section contains the ion source and is made of a Lucite tube for electrical insulation. This section is pumped by a 300 L/s Roots Blower pump backed by a 40 cfm mechanical pump. The pressure of the first section is typically 0.1 Torr when the source is operating. The skimmer has a 1.6-mm-ID entrance aperture and is located 1 cm away from the exit of the nozzle. After passing the first skimmer, the ions are accelerated through the second skimmer, which has a 6-mm-ID entrance aperture to ground potential. The vacuum section defined between the first and second skimmers is pumped by a 10-inch diffusion pump backed by a 60-cfm mechanical pump. The pressure of the first section is typically 10^{-4} Torr when the source is operating. After being accelerated to 500 eV, the cluster ions are focused by two sets of symmetric einzel lenses through 3-mm image apertures.

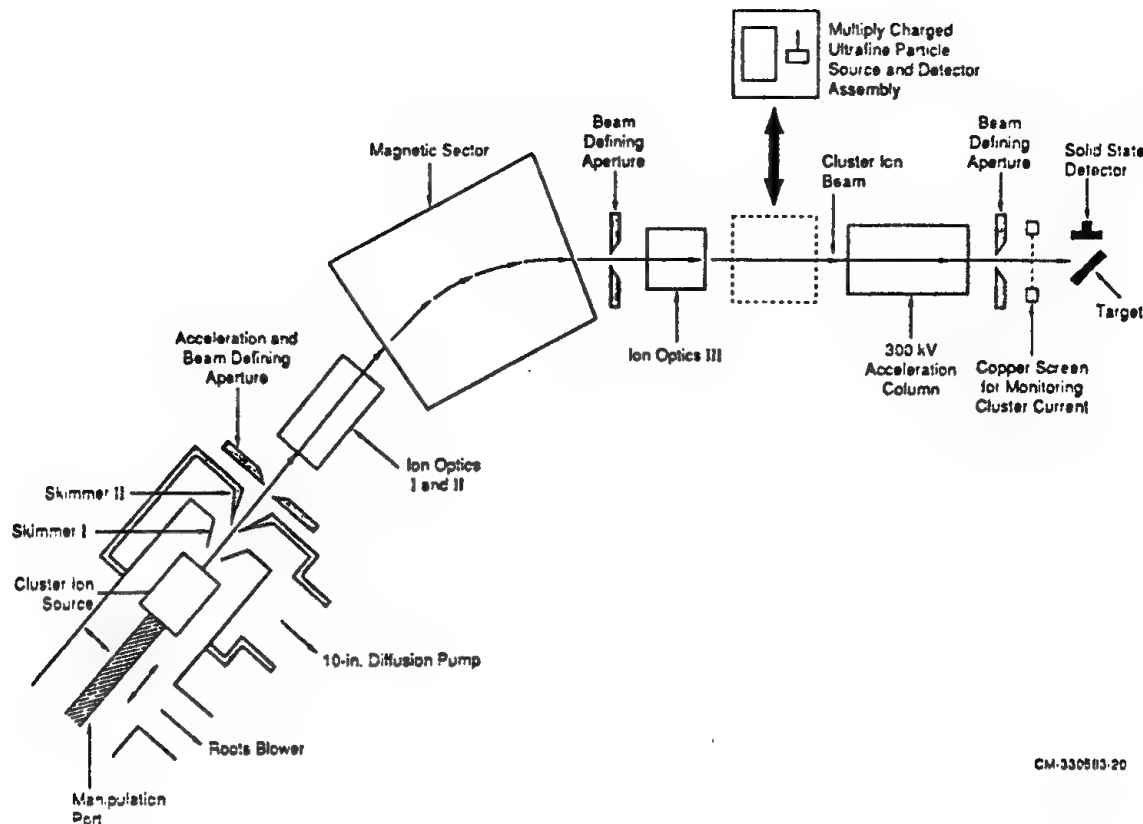


Figure 1. SRI Cluster Impact Facility.

The accelerated and collimated cluster ion beam is mass selected by a 40-cm-radius, 60° electromagnetic sector capable of bending 5500-keV-amu ions, passed through a 2-cm-diameter aperture, and further focused and collimated by the third set of einzel lenses and deflection plates. The beam is then sent to a movable Faraday cup located 65 cm away from the exit of the magnetic sector. The 2-cm aperture yields an effective mass resolution $\Delta M/M$ of ~ 0.05 , which was measured with small cluster ions on the Faraday cup. Moving the Faraday cup out of the beam path allows the beam to pass through another 2-cm-diameter aperture and enter the acceleration column of the 300-keV accelerator. The effective mass resolution of the beam measured in front of the target after acceleration was also 0.05.

DEVELOPMENT OF A NEW HIGH INTENSITY WATER CLUSTER ION SOURCE

We have successfully developed and demonstrated a new high intensity H₂O cluster ion source. The detailed cross sectional drawing of the ion source together with skimmers is shown in Figure 2. The ion source was built by modifying the body of the commercial pulsed valve

(Lasertechnics). The principle of the new cluster ion source is very similar to that described by Beuhler et al.^{1,2} The ion source produces high intensity cluster ion beams by generating abundant seed ions in the cluster source and expanding the ions that nucleate the condensation of neutrals for the growth of the cluster ion in a He and water vapor mixture. The seed ions are produced in a discharge of He and water vapor mixture between a stainless steel tip and the wall of the source near the nozzle. The mixture is produced by bubbling He through water in a gas washing bottle at room temperature. Production of water clusters of 100 molecules requires a He pressure of ~700 Torr. The nozzle-discharge-tip assembly is made of a commercial Lasertechnics nozzle. The tip is held to the nozzle by an adapter made of Macor. The tip holder has holes that allow conductance of the He water vapor mixture.

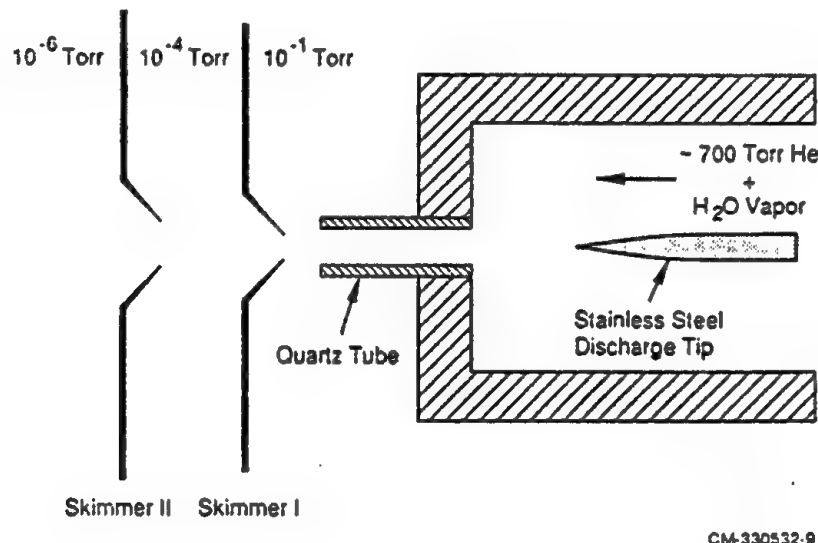


Figure 2. Schematic of the water cluster ion source.

We investigated various ways of reducing the conductance of the nozzle and found that nozzles made of 8-mm-long, 0.5-mm-ID quartz tubes (which have much less conductance than a hole) worked best. The tubes were glued to the nozzle with epoxy. We found that covering the end of the quartz tube facing the discharge tip with metal prevents generation of an intense cluster ion beam. A mass spectrum of the produced $(D_2O)_n^+$ cluster ions measured with the movable Faraday cup is shown in Figure 3. The spectrum has a full width at half maximum (FWHM) of 30% and should represent the mass distribution of the ion source convoluted with the resolution of the magnetic sector. The mean size of the clusters can be readily controlled by tuning the pressure of the source and the discharge current. With the source systems tuned for clusters of

100 molecules, the maximum observed current of cluster ions on the Faraday cup is 7 nA. Higher currents are generated with the source tuned for smaller clusters, and vice versa.

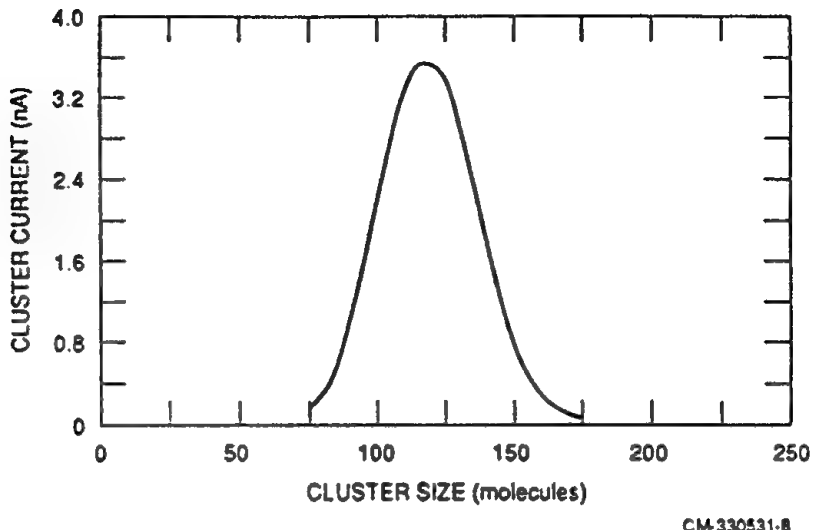
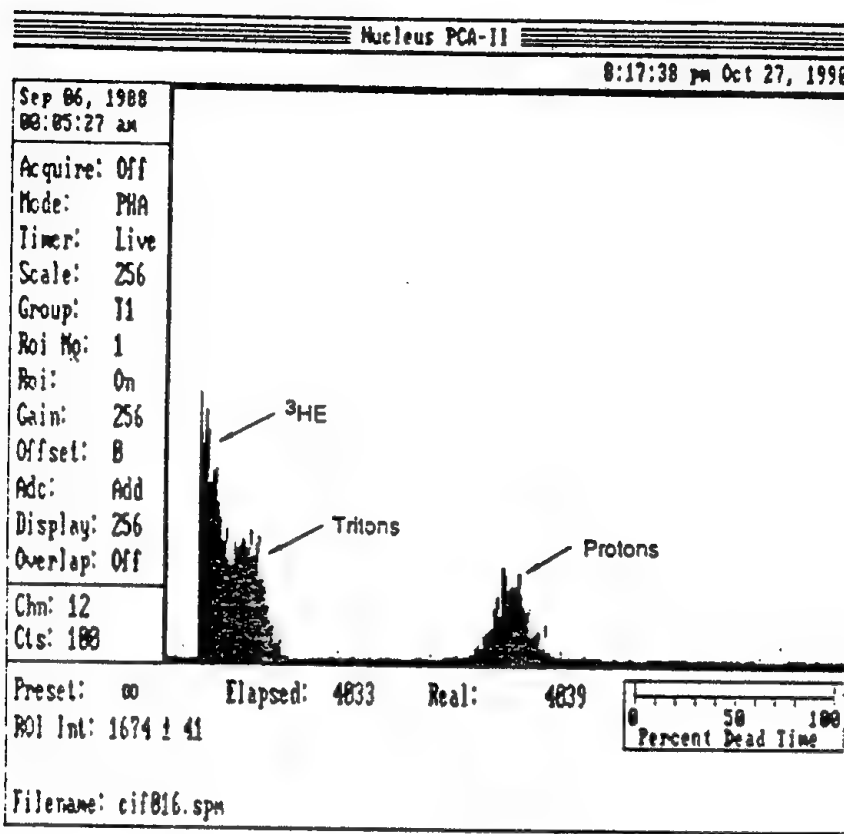


Figure 3. Size distribution of the generation $(D_2O)_n^+$ clusters from the ion source.

INSTALLATION OF A 300-keV ACCELERATOR AND CONSTRUCTION OF FUSION DIAGNOSTICS SYSTEMS

The mass selected and collimated cluster ions are accelerated through a 45-cm-long acceleration column of the 300-keV accelerator and, then enter a chamber that contains the target and the detector which is maintained at the full terminal voltage. The target is a 2-cm-diameter disk made of perdeuteropolyethylene $[(C_2D_4)_n]$ and tilted 45 degrees with respect to the beam axis. The current of the accelerated cluster ions is measured by monitoring secondary electrons from a copper grid upstream of the target. The grid is maintained at 50 V relative to the high voltage terminal, and the loss of the electrons from it is monitored with a DC current amplifier connected through a fiber optic link and monitored by an ADC in a CAMAC crate interfaced with a computer. Fusion product particles are detected by a particle detector, which is a 300-mm² Ortec "ruggedized" silicon solid-state detector. The active surface of the detector is covered with a 50 $\mu g/cm^2$ layer of aluminum. The detector is located 2.5 cm from the center of the target. The amplified detector pulses are sent through a fiber optic link to a pulse height analyzer interfaced with a computer. The detector system, including the fiber optic link, is calibrated with 5.48-MeV α particles from ^{241}Am and with DD fusion particles, protons, tritons, and 3He produced by D⁺ impact on the $(C_2D_4)_n$.

target. Typical fusion signals observed in the collisions of $(D_2O)_n^+$ clusters with a $(C_2D_4)_n$ target in this facility are shown in Figure 4.



CA-330583-16

Figure 4. Typical DD fusion signals observed with the impact of $(D_2O)_n^+$ clusters on a $(C_2D_4)_n$ target.

MEASUREMENT OF FUSION YIELDS

We measured DD fusion yields with $(C_2D_4)_n$ targets. The targets were made by compacting $(C_2D_4)_n$ powder mixed with 1 wt% colloidal carbon under ~1 kbar. Figure 5 shows the energy dependence of the 3-MeV fusion proton yields measured when D_2O clusters impacted on the targets. The incident clusters had a mass distribution with a peak at 115 molecules/cluster and 5% FWHM. In Figure 5, our data are shown as open squares and those of Beuhler et al. are shown as filled-in circles.² Both the magnitude and energy dependence of our data are in excellent agreement with those of Beuhler et al. The agreement is striking considering that our experimental arrangement is very different from theirs.

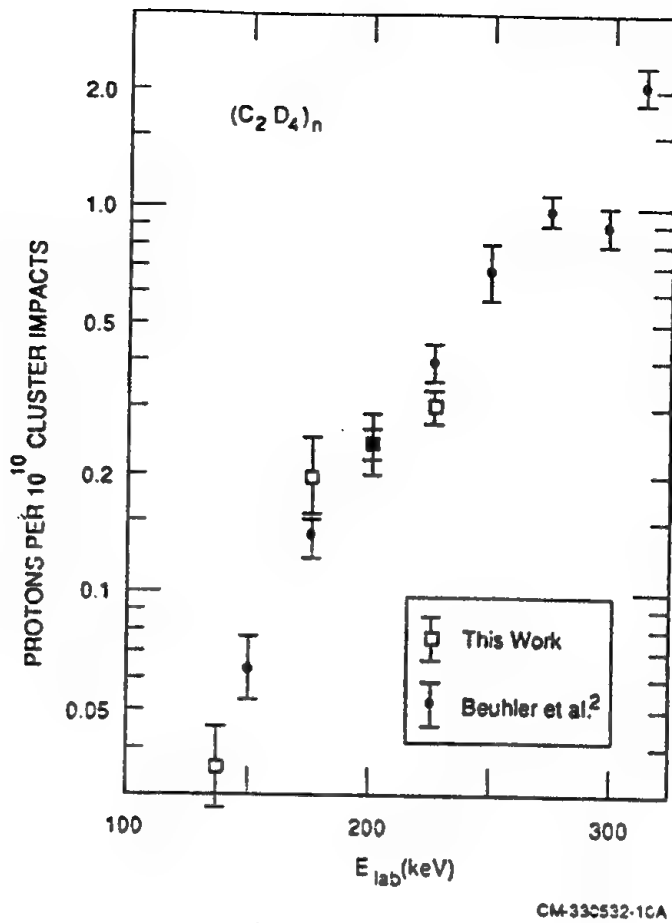


Figure 5. Energy dependence of the observed 3-MeV protons from DD reactions with the impact of $(D_2O)_{115}^+$ clusters on a $(C_2 D_4)_n$ target.

Figure 6 shows the cluster size dependence of the total DD fusion yield measured at a cluster beam energy of 225 keV. A log-log scale is used for this plot. Beuhler et al.² obtained the cluster size dependence at 300 keV using clusters with a mass distribution of 38% FWHM. Their yield has a peak at $n = 200$ and decreases by a factor of three at $n = 100$ and 350. Our measured yield at 225 keV has a less pronounced size dependence and seems to have a peak near $n = 100$. Carraro et al.³ have obtained analytical formulas for fusion yields using several different models. So that general trends and orders of magnitude can be compared, Figure 6 also shows the results of theoretical calculations by various models of the fusion yield of D_2O clusters impacting on a TiD target. In Figure 6, the TT curve represents the thick-target model, which assumes that deuterons in the projectile clusters undergo fusion reactions with the target deuterons while slowing down in the target as a function of the stopping power. The KO curve represents the knock-on model, which considers substrate deuterons knocked on by oxygen atoms in incident clusters. This curve was obtained by dividing Eq. (8) in Reference 4 by a factor of 10 to compensate for the

deficiencies of the parameterization in the universal cross section, Eq. (7) of this reference, used in their modeling. The TN curve represents a thermonuclear model that assumes thermalization of the atomic degrees of freedom upon impact of clusters.

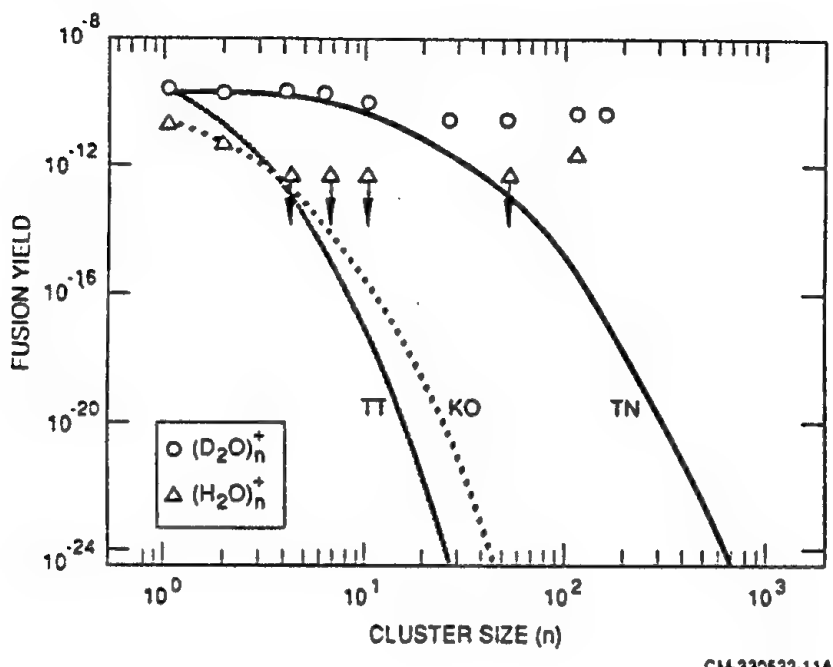


Figure 6. The total DD fusion yield at the impact energy of 225 keV as a function of the cluster size n .

It is interesting that our measured data on D_2O clusters follow the TN model curve for clusters up to 10 molecules in size. However, for $n > 10$, our data deviate rapidly from the TN curve as n increases; this deviation indicates the existence of some unknown cluster size effects. The difference between thermonuclear model of Carraro et al.³ and the model of Echenique et al.³ is the existence in the latter of a temperature enhancing mechanism caused by the correlated, coherent collisions. Echenique et al.⁴ qualitatively explain that the observed size dependence of the yield results from two effects: The decrease observed in the larger clusters is due to the same amount of translational energy being distributed over a larger region of the target, which results in a lower effective temperature of the localized impact spot. However, if the cluster becomes substantially smaller than 100 molecules, the impact region has dimensions comparable with the mean free path between collisions; here too, the energy is dispersed, resulting in a lower temperature of the localized impact spot. Thus, one might wonder if the deviation appearing above $n = 10$ results from the triggering of correlated collisions.

Fusion reactions were also observed for H₂O clusters impacting on the (C₂D₄)_n targets. Both the magnitude and cluster size dependence of the fusion yield of H₂O clusters are much different from those of D₂O clusters. The fusion yields of (H₂O)_n⁺ clusters with n = 1 and 2 seem to agree with the value based on the knock-on (KO) model. No fusion event was observed for (H₂O)_n⁺ clusters with n between 4 and 50 during the integration times of 3 hours for each datum. For comparison, the upper bounds (which were obtained by setting the observed counts at 0.5) are shown in Figure 6 as arrows. However, n = 115 clusters produced an observable fusion yield, i.e., 5 ± 2% of the yield of D₂O clusters. This observed ratio is in excellent agreement with the ratio of ~5% observed by Beuhler et al. The difference between the fusion yields of D₂O and H₂O clusters is very intriguing. One might wonder whether the difference indicates that thermalization of projectile D atoms is different from thermalization of target D atoms.

REFERENCES

1. R. J. Beuhler, G. Friedlander, and L. Friedman, Phys. Rev. Lett. **63**, 1292 (1989).
2. R. J. Beuhler, Y. Y. Chu, G. Friedlander, L. Friedman, and W. Kunmann, J. Phys. Chem. **94**, 7665 (1990).
3. C. Carraro, B. Q. Chen, S. Schramm, and S. E. Koonin, Phys. Rev. A **42**, 1379 (1990).
4. P. M. Echenique, J. R. Manson, and R. H. Ritchie, Phys. Rev. Lett. **64**, 1413 (1990).

Inorganic Halogen Oxidizers

W.W. Wilson and K.O. Christe

Rocketdyne Division of Rockwell International Corporation
Canoga Park, California 91303

During the past year, our efforts were devoted to the following three main areas: (i) nitrogen fluoride chemistry, (ii) the synthesis and characterization of anions at the limits of coordination and oxidation, and (iii) the development of a quantitative oxidizer strength scale.

In the area of nitrogen fluorides, the synthesis of catenated nitrogen fluorides, i.e., of higher molecular weight nitrogen fluorides containing several N-N bonds, was pursued. These catenated nitrogen fluorides would be earth-storable while having the performance of a space-storable liquid propulsion system. In this manner the specific impulse of the best presently known earth-storable system, i.e. $\text{ClF}_5\text{-N}_2\text{H}_4$, could be improved by about 20 seconds.

The synthesis of catenated nitrogen fluorides requires nitrogen fluoride anions as a starting material. Since at the present time no nitrogen fluoride anions are known, a systematic search for these anions was undertaken. Using the same approach as the one which we have recently successfully demonstrated for the syntheses of numerous novel high oxidizer anions, the reactions of anhydrous $\text{N}(\text{CH}_3)_4\text{F}$ in either CH_3CN at -30°C or CHF_3 at -80°C with N_2F_2 , N_2F_4 , FNO , or FNO_2 were studied. In all cases no stable anions were observed. The most promising anion would be the N_3F_2^- anion which is analogous to the NO_2^- anion. By analogy with the known chemistry of the nitro group, one could envision a similar,

but more energetic family of $\begin{array}{c} \text{NF} \\ | \\ -\text{N}-\text{NF} \\ | \\ \text{NF} \end{array}$ substituted compounds. The required precursor for an

N_3F_2^- anion is fluorine azide, FN_3 . Since the latter is extremely shock sensitive, attempts were made to generate and react FN_3 in solution. For this purpose, the fluorination of $\text{N}(\text{CH}_3)_4\text{N}_3$ with either XeF_2 or F_2 in CH_3CN or CHF_3 solution was studied. In all reactions, the N_3^- anion was oxidized to N_2 but the desired N_3F_2^- anion was not isolated. In connection with this study, an improved synthesis for $\text{N}(\text{CH}_3)_4\text{N}_3$ from $\text{N}(\text{CH}_3)_4\text{F}$ and $(\text{CH}_3)_3\text{SiN}_3$ was developed, and a crystal structure determination of $\text{N}(\text{CH}_3)_4\text{N}_3$ is in progress in collaboration with Prof. Bau from USC. In view of these unsuccessful attempts in solution, the direct synthesis of $\text{N}(\text{CH}_3)_4^+\text{N}_3\text{F}_2^-$ from $\text{N}(\text{CH}_3)_4\text{F}$ and gaseous FN_3 will be attempted.

Another subject of interest to us in nitrogen fluoride chemistry was that of the N_2F^+ cation and N_2F_2 chemistry. Based on previous force field computations it had been predicted that N_2F^+ either had a very short NF bond or was a rare exception to Gordy's Rule which correlates force constants with bond lengths. For this reason, a knowledge of the exact NF bond length in N_2F^+ was desirable. Single crystals of $\text{N}_2\text{F}^+\text{AsF}_6^-$ were grown and a crystal structure determination was carried out in collaboration with Prof. Bau's group at USC. Since disorder problems allowed the determination of only the sum of the NF + NN bond lengths, Dr. Dixon from DuPont carried out local density functional calculations which permitted the partitioning of this sum into the individual bond lengths. It was shown that in N_2F^+ both the NF (1.225 Å) and the NN (1.106 Å) bonds are unusually short and that this shortening must be due to the high s-character of the σ-bonds (sp hybridization).

Several mysteries in the chemistry of N_2F_2 were elucidated. Plausible explanations were found for: (i) the fact that only cis- N_2F_2 and not trans- N_2F_2 forms N_2F^+ salts with Lewis acids, (ii) why Lewis acids do not catalyze the cis-trans isomerization, and (iii) why only the cis-isomer is formed in displacement reactions between N_2F^+ salts and stronger Lewis bases.

The second area of interest had to do with anions at the limits of coordination and oxidation. During the previous contract year we had discovered a synthesis for truly anhydrous $\text{N}(\text{CH}_3)_4\text{F}$ and that this compound is highly soluble in either CH_3CN or CHF_3 solution. Furthermore, it was found that these solutions exhibit a surprising kinetic stability toward strong halogen oxidizers, and numerous $\text{N}(\text{CH}_3)_4^+$ salts with halogen fluoride counterions were prepared in this manner. This potential of $\text{N}(\text{CH}_3)_4\text{F}$ has now been exploited to carry out a systematic effort toward the synthesis and characterization of complex fluoro anions at the limits of oxidation and coordination. This study is being carried out in collaborations with Prof. Schrobilgen's group at McMaster University and Dr. Dixon from Du Pont who provide invaluable expertise in NMR spectroscopy and crystal structure determination and theoretical computations, respectively. This study is aimed at coordination numbers exceeding six and structures with either zero, one, or two free valence electron pairs on the central atom. Our particular interest in this context is the steric activity of these free valence electron pairs and the fluxionality of these highly crowded structures. The following progress has been achieved to date: (i) the novel XeF_5^- anion, a seven coordinated rigid structure with two free valence electron pairs has been prepared and shown to be the first known example of an AX_5 species in which all six atoms lie within the same plane, i.e. the structure is derived from a pentagonal bipyramidal in which the two axial positions are occupied by two free valence electron pairs; (ii) the novel IF_6O^- anion was prepared and characterized and is the first known example of a pentagonal bipyramidal AX_5YZ species in which five fluorines and one

fluorine and one oxygen atom occupy the five equatorial and the two axial positions, respectively; (iii) the IF_8^- and TeF_8^{2-} anions were shown to have an antiprismatic structure of symmetry D_{4d} and not a cubic O_h structure; and (iv) the XeF_5O^- anion which has one sterically active free valence electron pair has a pentagonal bipyramidal C_{5v} structure with five equatorial fluorine and an oxygen atom and a free valence electron pair in the two axial positions. Other anions under investigation include TeF_7^- , TeF_6O^- , and XeF_7^- .

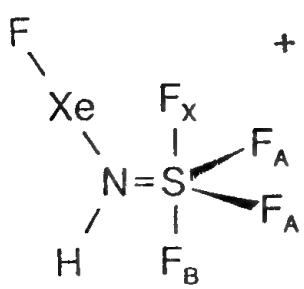
The third area of interest deals with the development of a quantitative oxidizer strength scale. Strong oxidizers can be divided into two categories: one-electron oxidizers, such as PtF_6^- ; and oxidative fluorinators, such as KrF^+ , XeF^+ , ClF_6^+ , N_2F^+ or NF_4^+ . Of these, the second category is much more important. The oxidizer strength of one-electron oxidizers is given by their electron affinities; however, the latter values are generally not known and in the past have been crudely estimated from go, no-go reactions with substrates of known ionization potentials. The case of oxidative fluorinators is much more complex and previously had not been analyzed. We have now in collaboration with Dr. Dixon from Du Pont developed a reliable quantitative oxidizer-strength scale by calculating total energies for all components in typical oxidative fluorination reactions and extracting from these total energy values the corresponding reaction enthalpies. From these reaction enthalpies, a relative oxidizer strength scale was developed which correlates the oxidizer strength to the F^+ detachment energy of a compound. Selecting F^+ itself which has a zero F^+ detachment energy as the zero point of the scale and anchoring the remaining F^+ detachment energies to this F^+ value by local density functional calculations, a quantitative oxidative fluorinator strength scale was developed. Since the formation enthalpy of F^+ is experimentally known, the oxidizer strength scale can be readily converted, if desired, into a thermodynamic formation enthalpy scale. Values for many known and unknown oxidizers are presently being computed. This oxidizer strength scale will be invaluable for future synthetic efforts because, for the first time, it is now possible to predict which oxidizers are strong enough to oxidize a given substrate and which new oxidizers can be prepared by means of the presently known oxidizers. It will also be of great help in the search for new more powerful oxidizers.

LEWIS ACID BEHAVIOR OF XENON(II) CATIONS AND THE SYNTHESIS AND CHARACTERIZATION OF THE HYPERVALENT ANIONS XeF_5^- , XeF_7^- , XeOF_5^- , IOF_6^- , TeF_6^- , TeF_8^{2-} and IF_6^- .

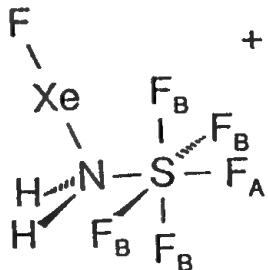
Neil T. Arner, Hélène P. Mercier, Michael Rokoss, Jeremy C.P. Sanders, Gary J. Schrobilgen Joseph S. Thrasher; Department of Chemistry, McMaster University, Hamilton, Ontario L8S 4M1, Canada

By taking advantage of the Lewis acid properties of the XeF^+ and KrF^+ cations, it has been possible to prepare a diverse range of noble-gas adduct cations; F-Xe-L^+ , $\text{F-Kr-N}\equiv\text{CH}^+$ and $\text{F-Kr-N}\equiv\text{CR}_r^+$ ($\text{L} = \text{HC}\equiv\text{N}$, $\text{RC}\equiv\text{N}$, $\text{R}_2\text{C}\equiv\text{N}$, $\text{C}_5\text{F}_5\text{N}$, $\text{s-C}_3\text{F}_3\text{N}_3$). The adduct salts, whose stabilities range from explosive at -60°C for $\text{F-Kr-N}\equiv\text{CH}^+\text{AsF}_6^-$, the first example of a Kr-N bond, to stable at room temperature for $\text{s-C}_3\text{F}_3\text{N}_3\text{-Xe-F}^+\text{AsF}_6^-$; have been characterized by multi-NMR spectroscopy and Raman spectroscopy. We have also extended this work to the related noble-gas cations XeOTeF_5^+ and XeOSeF_5^+ , to yield the first examples of O-Xe-N linkages.

More recently, we begun to investigate chalcogen nitrogen fluorides as potential bases and precursors to energetic materials. The adduct cation $\text{F-Xe-N}\equiv\text{SF}_5^+$ has been prepared and characterized as its AsF_6^- salt. The cation has been shown by ^{129}Xe and ^{19}F NMR spectroscopy to undergo successive additions of HF to the N=S bond in anhydrous HF to give the adduct cations $\text{F-Xe-N(H)}=\text{SF}_5^+$ (Structure I) and $\text{F-Xe-N(H}_2\text{)-SF}_5^+$ (Structure II). The $\text{F-Xe-N(H}_2\text{)-TeF}_5^+$ cation has also been synthesized by the direct reaction of F_5TeNH_2 and $\text{XeF}^+\text{AsF}_6^-$ in HF and BrF_5 solvents and has been shown by ^{19}F , ^{125}Te and ^{129}Xe NMR to possess to be isostructural with the sulfur analog (Structure II).

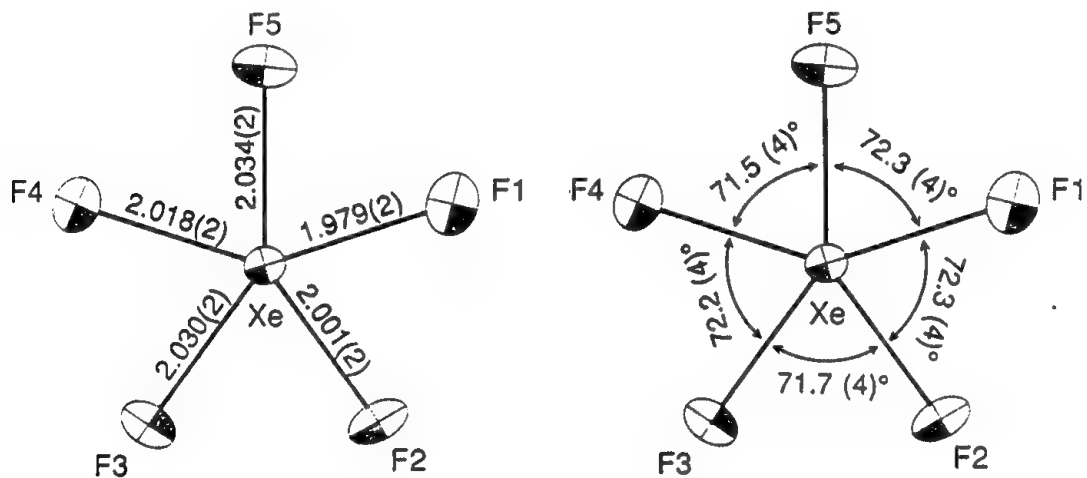


Structure I



Structure II

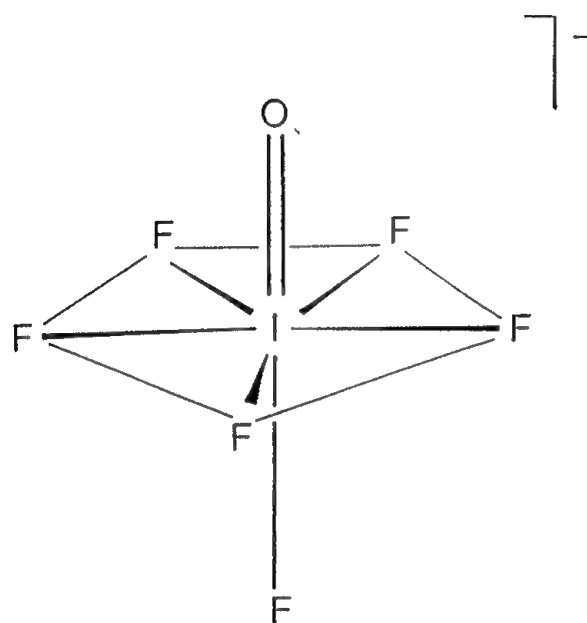
The syntheses and structural characterization of high-coordination number, high oxidation state hypervalent fluoro- and oxofluoro- anions has recently been undertaken in our laboratory in collaboration with Dr. K.O. Christe's group at Rocketdyne Division, Rockwell International. We have recently synthesized $(CH_3)_4N^+XeF_5^-$ by the reaction of stoichiometric amounts of XeF_4 and $N(CH_3)_4^+F^-$ in dry CH_3CN . The salt was characterized by ^{19}F and ^{129}Xe NMR spectroscopy and X-ray crystallography. The XeF_5^- anion has a pentagonal planar (D_{5h}) structure (Structure III) with five equivalent fluorines and is of considerable significance as it represents the first example of an AX_5E_2 (E = valence electron lone pair) system.



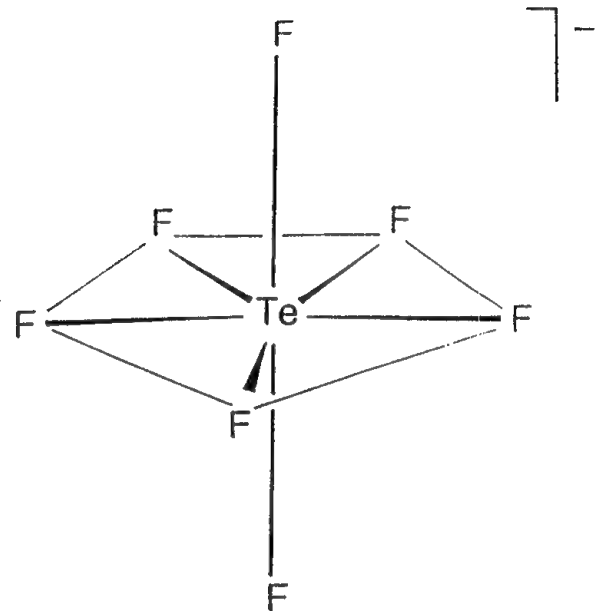
Structure III

Further examples of hypervalent anions possessing five-fold symmetries have been synthesized which include the novel isoelectronic pair of anions IF_5O^- (C_{5v} , Structure IV) TeF_5O^{2-} (C_{5v} , cf. Structure IV) and the previously ill-defined $XeOF_5^-$ (structure appears to be C_{5v} in which the oxygen and lone pair are located on the C_5 -axis) TeF_5^- (D_{5h} , Structure V, fluxional on the NMR time scale). The anions have been synthesized as the $N(CH_3)_4^+$ salts by the reaction of anhydrous $N(CH_3)_4^+F^-$ with IF_5O , $N(CH_3)_4^+TeF_5O^-$, XeF_5O or TeF_6 at low temperature in CH_3CN . The isoelectronic pair of anions TeF_5^{2-} (D_{4h} , Structure VI) and IF_5^- anions and the XeF_5^- anion have also been prepared as their $N(CH_3)_4^+$ salts using the method outlined above by the reaction of $N(CH_3)_4^+TeF_5^-$, IF_5^- , IF_6^- and XeF_6^- with $N(CH_3)_4^+F^-$. The XeF_5^- anion has been shown to be fluxional on the NMR

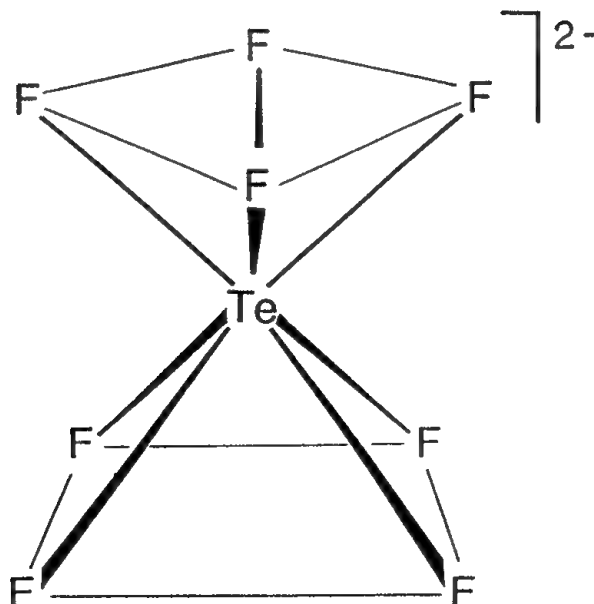
time scale and its structure appears to be based on a square antiprism in which one vertex is occupied by the xenon valence electron lone pair (C_{2v} symmetry). Structural characterization in our laboratories has been achieved using X-ray crystallography and multi-NMR spectroscopy, and vibrational spectroscopy.



Structure IV



Structure V



Structure VI

The formation of the F₅TeO⁻ analog of XeF₅⁻ was also investigated, namely Xe(OTeF₅)₅⁻, as well as the mixed F/F₅TeO species, XeF_{5-n}(OTeF₅)_n⁻. The non-linearity of the Xe-O-Te angle in these anions ought to afford relief of steric congestion by allowing the F₅Te⁻ groups to lie out-of-plane while maintaining an approximately pentagonal arrangement of oxygens/fluorines bonded to xenon. The reactions of N(CH₃)₄⁺F₅TeO⁻/N(CH₃)₄⁺F⁻ with Xe(OTeF₅)₅/XeF₄ at -40 °C in CH₃CN do not lead to the formation of the proposed anions, but rather result in the formation of the novel neutral xenon(IV) species, O=Xe(OTeF₅)₂ and O=XeF(OTeF₅) and previously known O=XeF₂ according to the following reactions:



The mixed anions, which are expected to be structurally related to TeF₇⁻ (Structure V), are currently being characterized.

CHARACTERIZATION OF HNIW AT THE NAVAL WEAPONS CENTER

M. P. Nadler, A. T. Nielsen, R. A. Nissan,
D. J. Vanderah and R. Y. Yee

Chemistry Division, Research Department
Naval Weapons Center
China Lake, CA 93555

Arnold T. Nielsen's pioneering work resulted in the synthesis of hexanitrohexaaazaisowurtzitane (HNIW) in February 1987. HNIW is the first known caged nitramine explosive and it is being examined by many organizations for use in propellants and explosives. This paper will concentrate on the initial characterization of HNIW by the Chemistry Division at the Naval Weapons Center (NWC).

The first ^1H nuclear magnetic resonance (NMR) of HNIW was obtained in February 1987 (Figure 1) and within a week R. Gilardi of the Naval Research Laboratory (NRL) confirmed the caged structure by X-ray diffraction (Figure 2). Several interesting side products and impurities of the synthesis of HNIW have been identified by NMR. High performance liquid chromatography (HPLC), Fourier transform infrared (FTIR) and NMR techniques have been developed to analyze HNIW and aid in making significant improvements in the synthesis. Ring-oxygen substituted (oxa), dioxa, trioxa, tetraoxa, mono-substituted and amine impurities have been confirmed (Figure 3 shows 2-oxa-HNIW).

Diffuse reflectance infrared Fourier transform spectroscopy (DRIFTS) is used to identify the crystalline forms or polymorphs of HNIW. Two new polymorphs were discovered in 1989 by differential scanning calorimetry (DSC) (γ -HNIW) and DRIFTS (ϵ -HNIW) and confirmed by X-ray diffraction at NRL. Figure 4 shows the molecular conformations and crystal space groups of the four known stable polymorphs. Quantitative analysis of polymorph mixtures is performed using DRIFTS and a partial least squares (PLS) program. Vibrational assignments have been made from comparisons with other nitramines and isotopic labelling.

The α -, β - and ϵ -HNIW transition to γ -HNIW at about 160 - 170°C. Thermal decomposition of HNIW occurs at 250 - 255°C. All four HNIW polymorphs appear to be stable at ambient temperature and pressure, unlike HMX (1,3,5,7-tetranitro-1,3,5,7-tetraazacyclooctane) which has unstable high temperature forms (δ -HMX and strained γ -HMX). Drop weight impact shows HNIW is slightly more sensitive than HMX and RDX. HNIW exhibits a small increase in impact sensitivity with particle size and a possible change with different polymorphs.

Alpha-HNIW has eight HNIW molecules and four cavities per unit cell and can trap small molecules thereby forming clathrates. DRIFTS has proven the existence of H_2O , CO_2 and CH_3OH clathrates. Table 1 shows the observed frequencies for the three

clathrates as ν (guest), the gas phase absorption [ν (gas)], the frequency shift [ν (guest) - ν (gas)] and vibrational assignments. The small shifts from gas phase frequencies and the lack of rotational structure indicate that the guest molecules behave as matrix isolated molecules or non-rotating gas phase molecules. There is some distortion of the HNIW cavities and little hydrogen bonding. Clathrates are quite stable and in some cases require crystal lattice destruction by either recrystallization or phase transformation to release the guest molecule.

The slow thermal decomposition of HNIW is being studied by DSC, examination of residues from isothermal decompositions at known time intervals by FTIR and isotopic labelling with deuterium. Figure 5 shows that HNIW ν_a (NO₂) and ν (CH) decrease at about the same rate at 205°C in 1 atm argon and the resulting residue contains a carbonyl group that peaks when the HNIW is exhausted. HNIW does not burn clean and the residue structure will be discussed using the FTIR data. The deuterium isotope effect and other evidence shows that cleavage of the -N-NO₂ bond dominates the slow thermal decomposition in the temperature range studied (190 - 215°C).

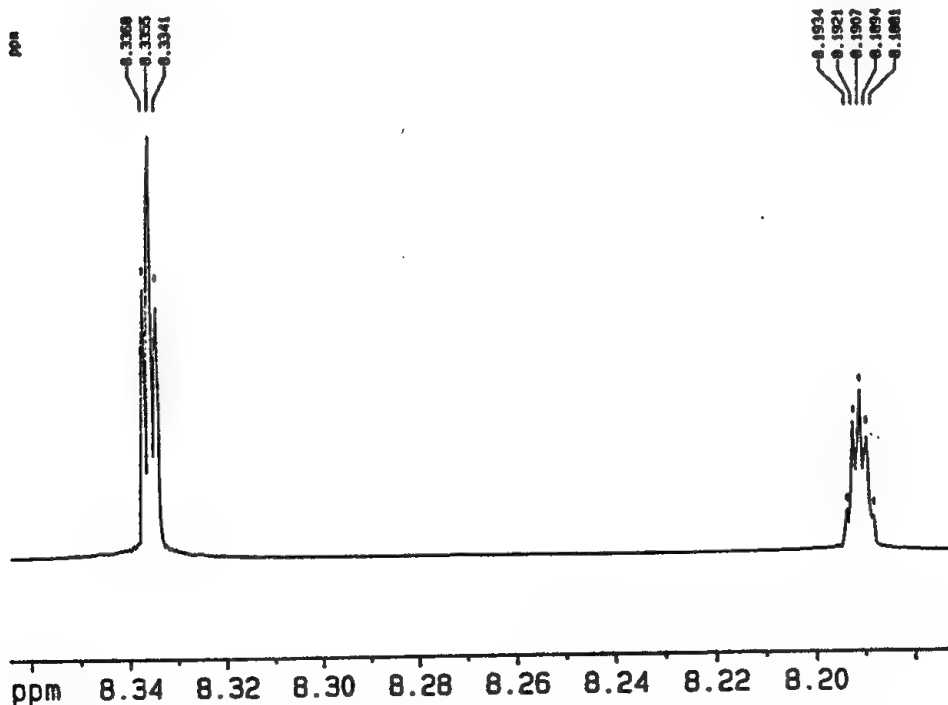


Figure 1. HNIW ^1H NMR Spectrum, 400 MHz, Gaussian Multiplication

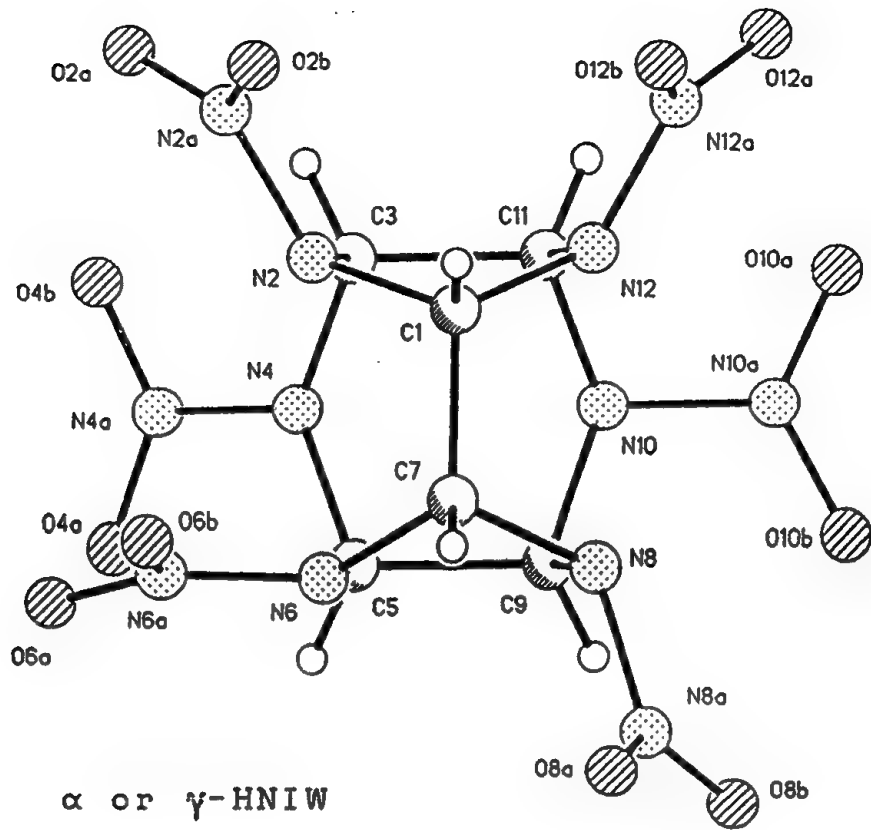


Figure 2. X-ray Diffraction Structure of HNIW (R. Gilardi, NRL)

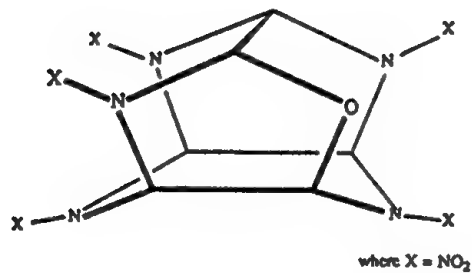


Figure 3. 2-Oxa-HNIW

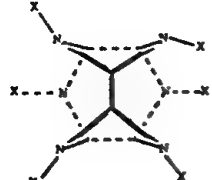
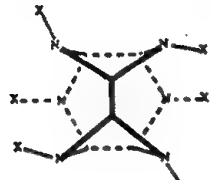
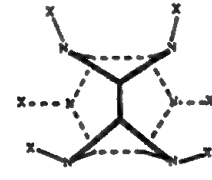
Molecular Structure ^b	Polymorph	Space Group	Z
	alpha ^c	P _{bca}	8
	gamma	P _{2₁/n}	4
	beta	P _{b2₁a}	4
	epsilon	P _{2₁/n}	4

Figure 4. X-ray Data of HNIW Polymorphs (R. Gilardi, NRL)

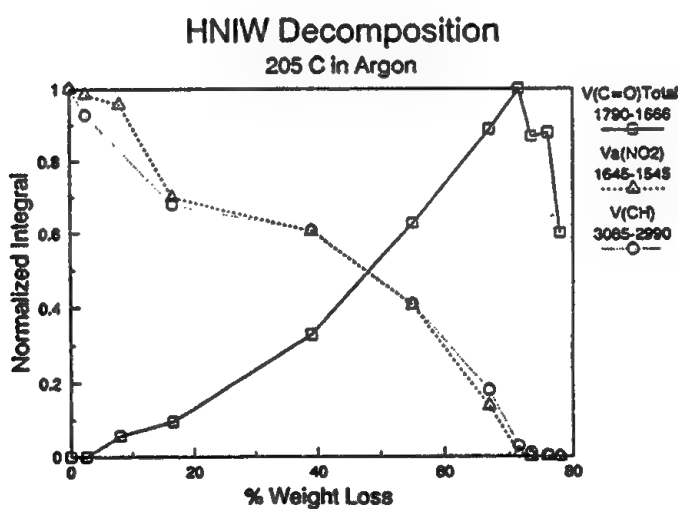


Figure 5. HNIW Decomposition. 205°C in 1 atm Argon

	Vibration	v(gas), cm-1	v(guest), cm-1	v(guest) - v(gas)
H ₂ O	V _a (OH),V ₃ (B1)	3756	3695	-61
	V _s (OH),V ₁ (A1)	3652	3607	-45
	bending,V ₂ (A1)	1595		
CH ₃ OH	V ₁ (OH) (a')	3682	3621	-61
	V ₅ (CH) (e)	2977	2951	-25
	V ₂ (CH) (a')	2844	2849	5
	V ₄ (CO) (a')	1034	1022	-12
CO ₂	V _a ,V ₃	2349	2344	-5
	bending,V ₂	667	648	-19

Table 1. FTIR Data on HNIW Clathrates

Extended Abstract: Metastability in Molecules*
Rodney J. Bartlett, Walter J. Lauderdale, John
F. Stanton, Jürgen Gauss, and Kim Ferris
Quantum Theory Project
University of Florida
Gainesville, Florida 32611

In our efforts in investigating metastability in molecules and their high energy content, we have focused primarily on nitrogen based species. Some of the metastable molecules that have been of interest to us include N₄, N₈, and various isomers of HNCBH and N₃H₃. In all cases, the molecules are not known experimentally, but high level predictive, *ab initio*, correlated quantum mechanical methods demonstrate that these are local minima on the global potential energy surface for the system. We have determined structures, relative energetics, and predicted vibrational spectra for identification purposes. N₈, for example, has an I_{sp}=539. Some recent work has also considered other types of materials like cubane (C₈H₈), LiBe(BH₄)₃ and Al₂B₄H₁₈. To obtain *ab initio* results using coupled-cluster theory that accurately includes electron correlation, for such large molecules as Al₂B₄H₁₈ requires the development of new methods and highly efficient implementations. This extended abstract summarizes these developments.

"Metastability" is usually defined as a thermodynamically unstable form of some molecule that, nonetheless, has a reasonable lifetime in that form. Molecules in electronic excited states that are prohibited by selection rules from decaying to lower states, exhibiting phenomena like phosphorescence, offer one example of metastability. Another, which we can term geometric, achieves its metastable status via a particular geometric arrangement of the atoms in a molecule. In a sense, nearly all endothermic molecules are "metastable" relative to their simpler components, which means they have a local minimum on the potential energy surface where some other atomic arrangement constitutes the global minimum. Typically, however, such known molecules have a long lifetime and are described by conventional chemical bonding concepts. A more extreme category of geometrically metastable molecules is those that have some electronic basis for their existence, but because of other factors, have never been observed. Given a local minimum and a barrier to unimolecular dissociation, such a molecule may be found to have a reasonable lifetime while trapped in its local potential well.

The potential existence of the more exotic metastable species offers us insight into the nature of the chemical bond. For example, we teach that the normal form of P is P₄ while that of N is N₂, despite that N₄ would have an equally attractive conceptual valence bond description. Nuclear repulsion and bond length considerations lead to the fact that since P₂ is a relatively weak bond, P₄ is more stable than 2P₂. On the other hand, the N₂ bond is one of the strongest known. This does not invalidate N₄ as a possible molecule, but does imply that if it exists, it could be metastable. Other examples would include the benzene analog hexatriene N₆, and

* Supported by the AFOSR, Chemical and Atmospheric Sciences Division, Grant No. AFOSR-89-0207.

March 27, 1991

particularly the cubane analog N₈. Other forms containing N include the three forms of N₃H₃, which although analogous to propene, cyclopropene, and ozone are experimentally unknown, but have been thoroughly characterized [1] in our prior work for this grant.

An investigation of such metastable species is made possible by the existence of accurate *ab initio* theoretical methods that include electron correlation and permit the efficient search of potential energy surfaces via analytical gradient techniques. Furthermore, such techniques provide vibrational spectroscopic information that can be used to identify the species. Unknown molecules require predictive accuracy since unlike well-known species, there will be no existing experimental data for comparison. This places severe demands on the level of *ab initio* treatment. Today, it is generally considered that coupled-cluster methods are among the most accurate available for reliable studies of comparatively large molecules. We have introduced such methods like CCSD, CCSD+T(CCSD), CCSDT-n, and CCSDT over the last several years (see [2] for a review). However, the necessity of analytical gradient methods to effectively search energy surfaces requires some additional methodological developments for CC theory. We presented the relaxed density based theory of CC analytical gradients some years ago [3-5], and an efficient implementation of CCSD restricted to closed shells (RHF reference) was accomplished by Scheiner, et al. [6]. However, many metastable species of interest are open-shell systems, or have low-lying open shell electronic states that are critical to an assessment of the viability of a species. Hence, in the developmental portion of this project, besides writing a new and very efficient RHF-CCSD analytical gradient program, we have derived and implemented the first open-shell CCSD analytical gradient method [7,8] where the reference functions may either be an unrestricted Hartree Fock (UHF) reference [7] or a restricted open shell (ROHF) reference [8]. As a byproduct, analytical gradients for all MBPT approximations from second order MBPT(2) to MBPT(4) are also available. Since these are non-iterative, for many large problems they can often offer excellent answers in typically a tenth of the time of the corresponding CC method. These are also the first such ROHF-MBPT methods for the energy or the gradient [9].

Besides the essential methodological developments outlined above, we have also implemented these methods into a new, very efficient and flexible program, Advanced Concepts in Electronic Structure, II (ACES II). This is the first CC/MBPT program that fully uses Abelian symmetry in all (inner and outer) loops [10]. This gives us a potential improvement of h² (h is order of group) in every step of a calculation after the molecular integrals. Furthermore, our new formulation of the CC equations makes it very easy to vectorize the program to gain typically factors of two to three over other such programs like GAUSSIAN 90, even with no symmetry. Consequently, for large D_{2h} examples like cubane (C₈H₈), and for the approximate CCSD method, QCISD, implemented into GAUSSIAN 90, ACES II does the calculation 115 times faster, and does the *entire* C₈H₈ calculation (integrals, SCF, transformation, and QCISD) in only 539 seconds on a CRAY-YMP. Since many metastable molecules will necessarily exhibit high symmetry, as already discussed for T_dN₄ or O_hN₈, a symmetry based many-body program system is an essential tool in providing the results we require in our predictive, *ab initio* investigation of metastable species.

The following summarizes results for N_n metastable species we have investigated, including I_{sp} evaluation via the formula, $I_{sp} = 265(Q/M)^{1/2}$. Q is the heat of the reaction in kcal/mol and M is the molar mass of the reaction products. All N_n species are assumed to be monopropellants.

March 27, 1991

Table I. Geometries (in Angstroms) for the $N_4(T_d)$, $N_6(D_{6h})$, and $N_8(O_h)$ structures, optimized at the SCF level (several bases for N_4 ; see text for detail), and with the DZP basis at the MBPT(2) level.

	SCF			MBPT(2)
	MNI1	DZ	DZP	DZP
N_4	1.534	1.471	1.394	1.476
N_6			1.287	1.334
N_8			1.459	1.525

Table II. MBPT(2) and CCSD results on N_x ($x=2,4,6,8$) molecules using the DZP and TZ2P basis sets; all values reflect dropping the core (1s) orbitals. Energies are in hartrees; differences relative to separated N_2 molecules are in kcal/mol; specific impulse in seconds.

	N_2	N_4	N_6	N_8
MBPT(2)				
DZP	-109.2690191	-218.2567240	-327.4701388	-436.3375652
TZ2P	-109.3295234	-218.3704557	-327.6444814	-436.5816492
Differences				
DZP	0.0	176.5	211.3	463.2
TZ2P	0.0	181.1	215.8	461.9
CCSD				
DZP	-109.2685064	-218.2447322	-327.4684083	-436.3644593
TZ2P	-109.3251890	-218.3465673	-327.6259758	-436.5834961
Differences				
DZP	0.0	183.3	211.4	445.1
TZ2P	0.0	190.6	219.3	461.9
I_{sp} ^a				
DZP		479	b	528
TZ2P		489	b	531

^aThe reactions used are $N_4 \rightarrow 2N_2$ and $N_8 \rightarrow 4N_2$

^b N_6 is unstable, hence there is no specific impulse.

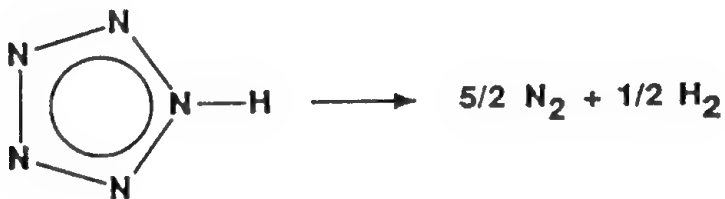
Frequency determinations have been made for all species at the SCF and MBPT(2) level. This demonstrates that T_dN_4 and O_hN_8 are, indeed, local minima on their potential energy

March 27, 1991

surface. However, while the benzene analog, N₆, is found to be a minimum at the SCF level, in agreement with other studies [11] at the correlated MBPT(2) level the e_{2μ} mode becomes imaginary (208i). Following through this point, some potentially interesting structures of N₆ seem to be possible minima. These will be characterized in the future.

The definitive predictions of the decomposition barrier to 2N₂ and 4N₂ molecules for T_dN₄ and O_hN₈ is complicated by severe changes in orbital occupation in the transition region. These crossings, of course, are the reason that the barrier to decomposition was predicted to exist prior to any calculation. The correct resolution of the barrier height requires a multi-reference calculation, and such studies have been pursued. However, all calculations point unambiguously to a barrier on the order of 40–50 kcal/mol for T_dN₄ and ~60–80 kcal/mol for O_hN₈. Consequently, the possibility of stabilizing either of these structures in a matrix isolation experiment is a good one. If so, with the aid of our predicted MBPT(2) frequencies and interactions, expected to fall within about 5% of experiment, the molecule could be identified. Clever synthetic methods should succeed in making these two molecules.

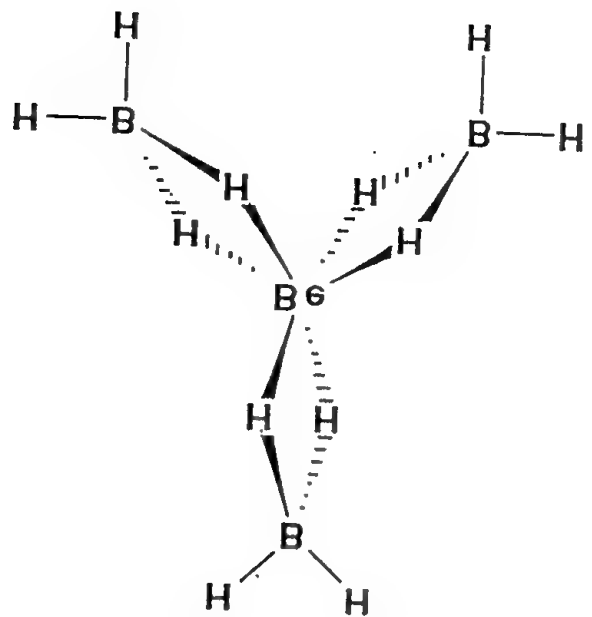
Our interest in high energy nitrogen structures that are potentially more readily synthesized has led us to pentazole,



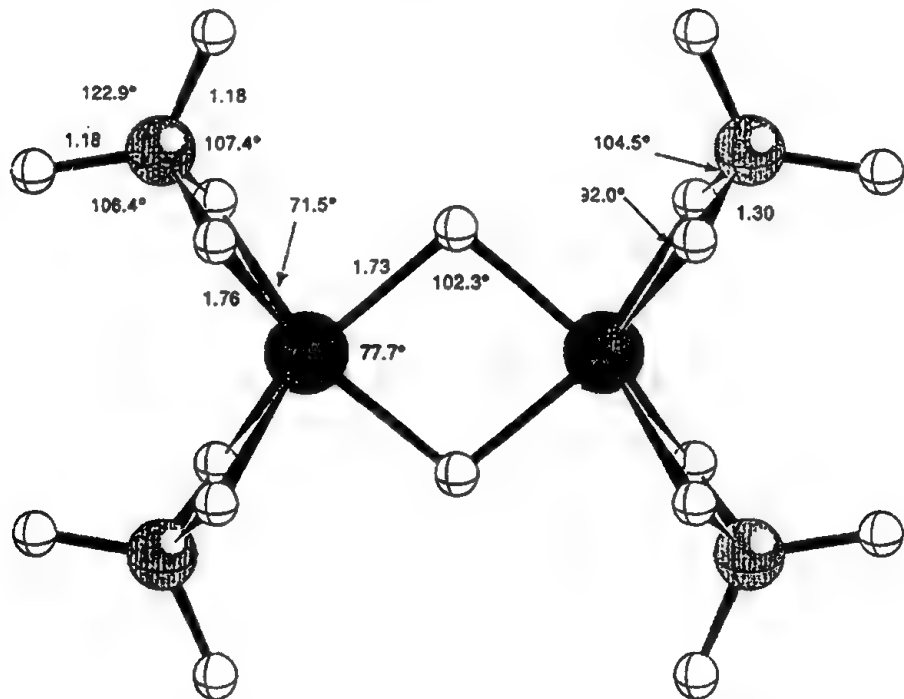
Despite reports of attempted synthesis of A_gN₅ and other derivatives that date back to 1910, no derivative of pentazole had been made until 1957, when Huisgen and Uzi reported the synthesis of phenyl pentazole in their paper entitled, "Pentazoles I. The Solution of the Classical Problem of Organic Nitrogen Chemistry." Only with a stabilizing group like the phenyl group has the N₅, five membered ring form been synthesized. In particular, HN₅ is unknown. In analogy with the above N₄ and N₈ systems, there is reason to believe that HN₅ would be metastable. Our calculations demonstrate that fact, obtaining all positive frequencies. As a monopropellant, HN₅ is also competitive giving an I_{sp} of 346 seconds. Derivatives will be considered soon.

The third objective of our study were certain "all fuel" molecules, namely LiBe(BH₄)₃ and Al₂B₄H₁₈. Be(BH₄)₂ is known to have among the highest heats of formation of any molecule. However, it would appear to be possible to add a third (BH₄)₂ group along with the Li counter ion. We investigated the anion Be(BH₄)₃⁻ (Figure 1) and found it to be stable with all positive frequencies, and to have a very high heat of formation.

March 27, 1991



In a related study, we considered $\text{Al}_2\text{B}_4\text{H}_{18}$,



Assuming complete combustion, $\text{Al}_2\text{B}_4\text{H}_{18} + 9\text{O}_2 \rightarrow \text{Al}_2\text{O}_3 + 2\text{B}_2\text{O}_3 + 9\text{H}_2\text{O}$ $\Delta H_{rxn} = -1600$ kcal/mol, resulting in an $I_{sp} = 528$ seconds.

More detailed studies of such "all fuel" species will be reported in the future.

March 27, 1991

References

1. D.H. Magers, E.A. Salter, R.J. Bartlett, C. Salter, B.A. Hess and L.J. Schaad, J. Am. Chem. Soc. **110**, 3435 (1988).
2. R.J. Bartlett, J. Phys. Chem. **93**, 1697 (1989).
3. R.J. Bartlett, in *Geometrical Derivatives of Energy Surfaces and Molecular Properties*, eds. P. Jørgensen and J. Simons (Reidel, Dordrecht, The Netherlands), p. 179, 1986.
4. G.B. Fitzgerald, R.J. Harrison and R.J. Bartlett, J. Chem. Phys. **85**, 5143 (1986).
5. E.A. Salter, G.W. Trucks and R.J. Bartlett, J. Chem. Phys. **90**, 1752 (1989).
6. A. Scheiner, G. Scuseria, J.E. Rice, T.J. Lee and H.F. Schaefer, III, J. Chem. Phys. **87**, 5361 (1987).
7. J. Gauss, J.F. Stanton and R.J. Bartlett, J. Chem. Phys., in press.
8. J. Gauss, W. Lauderdale, J.F. Stanton, J.D. Watts and R.J. Bartlett, Chem. Phys. Lett., in press.
9. W. Lauderdale, J.F. Stanton, J. Gauss, J.D. Watts and R.J. Bartlett, Chem. Phys. Lett., submitted.
10. J.F. Stanton, J.D. Watts, J. Gauss and R.J. Bartlett, J. Chem. Phys., in press.
11. P. Saxe and H.F. Schaefer, III, J. Am. Chem. Soc. **105**, 1764 (1983).
12. K. Ferris and R.J. Bartlett, J. Am. Chem. Soc., submitted.

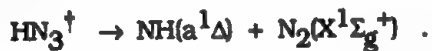
March 27, 1991

Potential Surface Control of the Dynamics of the Decomposition of HN₃

Millard H. Alexander, Department of Chemistry
University of Maryland, College Park, Maryland 20742
Paul J. Dagdigian, Department of Chemistry
The Johns Hopkins University, Baltimore, Maryland 21218

The distribution of the products of molecular photodissociation among accessible fine-structure levels can provide considerable insight into the photolysis or reaction mechanism. Much attention has been focussed on fragments in $^2\Pi$ electronic states, where the preferential production of a given $^2\Pi$ state Λ -doublet level can be interpreted by analysis of the evolution of the molecular orbitals of the precursor species which correlate with the unfilled π molecular orbital in the diatomic fragment. In the most sophisticated models^{1, 2} the relative populations of the $\Pi(A')$ and $\Pi(A'')$ Λ doublets³ can be predicted by projection of a transition state of constrained geometry onto the asymptotic fragments. In this way a purely planar transition state becomes increasingly associated with one or the other product Λ doublet level as the final state rotational angular momentum increases, since the definite reflection symmetry of these states becomes increasingly pronounced.⁴

We have extend this type of argument to the photodissociation of HN₃ producing NH in the $a^1\Delta$ electronic state. Our theoretical modelling was prompted by the work at NIST by Casassa *et al.*⁵ who characterized the NH($a^1\Delta$) v=0 product state distribution from the decomposition of HN₃ excited to the $7v_{NH}$ overtone level:



They report that the preference for the $\Delta(A')$ state rises from 1:1 at J=2 (the lowest level) to 4:1 at J=7 (the highest level probed).

It is possible to understand qualitatively the preference for the $\Delta(A')$ levels of NH formed in reaction (1a).⁶ This reaction proceeds through a planar transition state at a NN - NH separation of about 4.5 bohr, which lies $\sim 1,500$ cm⁻¹ above the product channel.^{6, 7} Because the wavefunction of the undissociated HN₃(X^1A') molecule is

symmetric with respect to reflection in the molecular plane and the wavefunction of the N₂ fragment is also symmetric with respect to reflection in any plane containing the internuclear axis, then if the HN₃ molecule remains planar during this spin-allowed dissociation, the wavefunction of the NH fragment must be symmetric with respect to reflection in the initial molecular plane. Further, if the dissociation occurs through a planar geometry, the plane of rotation of the NH fragment will be coincident with the initial molecular plane. Thus we anticipate that the electronic wavefunction of the NH(a¹Δ) fragment will be symmetric with respect to reflection in the plane of rotation of the NH molecule. Since the *e*-labelled levels of a ¹Δ state are symmetric (A') with respect to reflection of the electronic coordinates in the plane of rotation of the NH molecule,⁶ it is not surprising that the Δ(A') levels of NH are found to be preferentially populated in reaction (1b).

We have developed a simple, Franck-Condon like model to predict quantitatively the distribution of population among the product NH electronic-rotational states from a consideration of the transition state and the wavefunctions of the separated NH fragment. This involves the projection of the electronic-vibrational wavefunction of the NH moiety of the HN ... NN system at the transition state onto the electronic-rotational wavefunction of the free NH rotor. We assume that the probability of populating a final state is given by the square of the overlap between the initial and final NH wavefunctions (including both the nuclear coordinates and the coordinates of the two outer electrons), in other words

$$P_{JM\epsilon} = | \langle \psi_i | \psi_f \rangle |^2. \quad (1)$$

Here ψ_f is just the NH(a¹Δ) electronic-rotational wavefunction subsequent to dissociation, namely,^{6, 8}

$$\psi_f = | JM\epsilon \rangle = \left[\frac{2J+1}{8\pi} \right]^{1/2} [| \Lambda=2 \rangle D_{M,2}^{J*}(\phi, \theta, 0) + \epsilon | \Lambda=-2 \rangle D_{M,-2}^{J*}(\phi, \theta, 0)]. \quad (2)$$

where $D_{M\Lambda}^J$ is a rotation matrix element.

In a simple two-electron picture⁹ the three valence singlet states of HN₃ can be represented as the solution of a 3×3 Hamiltonian in the basis $\psi_1 = N_2(X) \cdot NH(\pi_X^2)$, $\psi_2 =$

$N_2(X) \cdot NH(\pi_y^2)$, and $\psi_3 = N_2(X) \cdot NH(^1\pi_x\pi_y)$. Asymptotically, we have

$$\lim_{R \rightarrow \infty} \Psi [N_2(X) \cdot NH(a^1\Delta_{A'})] = \Phi_1 = 2^{-1/2} (\psi_1 - \psi_2). \quad (3a)$$

$$\lim_{R \rightarrow \infty} \Psi [N_2(X) \cdot NH(a^1\Delta_{A''})] = \Phi_2 = \psi_3. \quad (3b)$$

$$\lim_{R \rightarrow \infty} \Psi [N_2(X) \cdot NH(b^1\Sigma^+)] = \Phi_3 = 2^{-1/2} (\psi_1 + \psi_2). \quad (3c)$$

where R designates the NN - NH separation coordinate. At the barrier in the singlet NN - NH dissociation channel, the electronic wavefunction of the ground X^1A' state is nearly exactly $\psi_1 (\dots \pi_x^2)$. We assume that this configuration ... π_x^2 is maintained even when the NH fragment tilts out of plane. From the known transformation properties of π orbitals, we can write

$$R(\phi) \pi_x = \cos \phi \pi_x + \sin \phi \pi_y. \quad (4)$$

where $R(\phi)$ is a rotation of the orbital (or, equivalently, of the NH fragment) through an azimuthal angle of ϕ . It can be shown that the effect of the rotation on the doubly filled π orbital is

$$R(\phi) \pi_x^2 = 2^{-1/2} [-\Phi_3 + \cos 2\phi \Phi_1 - i \sin 2\phi \Phi_2]. \quad (5)$$

The contribution of the $b^1\Sigma^+$ (Φ_3) component in the electronic wavefunction at the barrier in the NN - NH decomposition channel poses a problem here. In reality, as the NN - NH distance increases, the contribution of this component will adiabatically decrease to zero since formation of $NH(b^1\Sigma^+) + N_2$ is not energetically allowed in the experiments of Casassa *et al.*⁵ The reduction of the $^1\Sigma^+$ component must be compensated by an increase in the $^1\Delta$ components (Φ_1 and Φ_2). To take this redistribution of the $^1\Sigma^+$ component into account we assume that the $b^1\Sigma^+$ (Φ_3) component in Eq. (5) becomes transferred into the $\Delta(A')$ state. Thus, in determining the overlap in Eq. (1), we will rewrite Eq. (5) as

$$R(\phi) \pi_x^2 = 2^{1/2} \{ \frac{1}{2} [\cos 2\phi - 1] \Phi_1 - \frac{1}{2} \sin 2\phi \Phi_2 \}. \quad (6)$$

The electronic-vibrational wavefunction of the parent HN_3 molecule can be written as

$$\psi_1 = R(\phi) \pi_x^2 f(\theta, \phi). \quad (7)$$

where $f(\theta, \phi)$ is the librational wavefunction of the NH group. To proceed further, let us assume that the librational wavefunction $f(\theta, \phi)$ is separable and can be written as a product of two gaussians:

$$f(\theta, \phi) = \exp[-\alpha(\theta - \pi/2)^2] \exp[-\beta(\phi - \pi/2)^2]. \quad (8)$$

centered about a planar transition state.

Our earlier *ab initio* calculations⁷ determined that the geometry of the HN_3 molecule at the barrier in the singlet dissociation channel (1a) corresponds to the following geometry $R_{\text{N}_1\text{N}_2} = 2.074$ bohr, $R_{\text{N}_2\text{N}_3} = 4.45$ bohr, $R_{\text{N}_3\text{H}} = 1.958$ bohr, $\theta_{\text{NNN}} = 163^\circ$, $\theta_{\text{NNH}} = 90^\circ$, and $\phi = 90^\circ$. To obtain a more accurate picture of the saddle point region we have carried out additional complete active space self-consistent field (CASSCF) calculations. Figure 1 shows a contour plot of the energy of the HN_3 system as a function of the in-plane and out-of-plane NNH angles. We observe that the barrier to torsion is much less than the barrier to in-plane NNH wagging. From our previous polynomial fit,³⁷ we estimate that the harmonic oscillator exponential parameters [Eq. (16)] for the torsion and in-plane

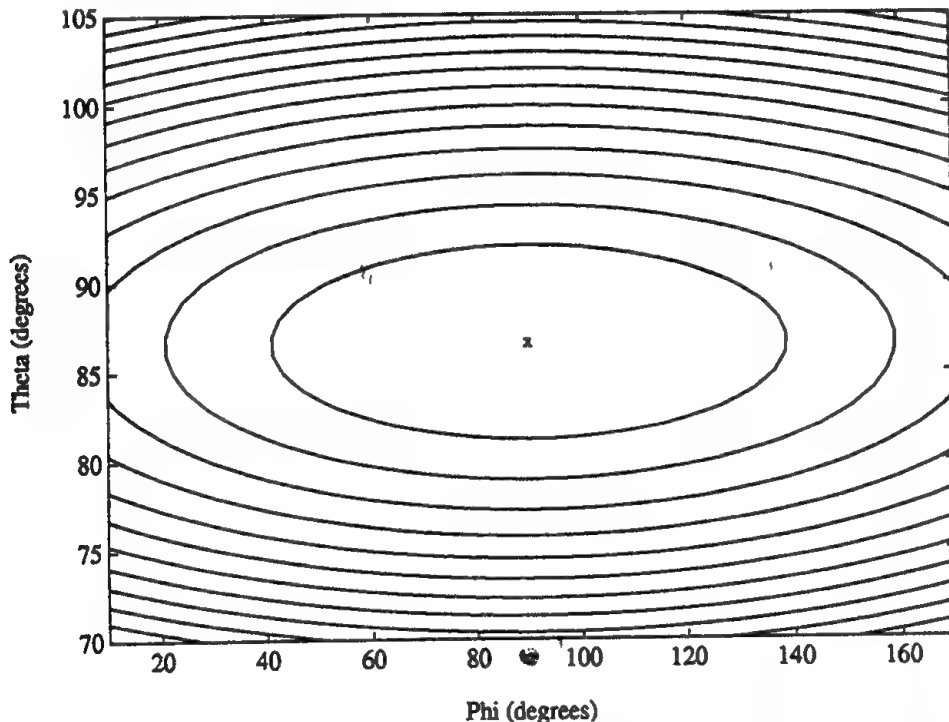


Fig. 1. Contour plot of the lowest HN_3 singlet potential energy surface in the region of the barrier in the singlet dissociation channel from CASSCF calculations with the atomic orbital basis described in the text. The two coordinates θ and ϕ correspond to the in-plane NNH wag and out-of-plane NNH torsion, with $\phi=90^\circ$ denoting planar geometry. The remaining coordinates are fixed at the values appropriate to the singlet barrier, namely $R_{\text{N}-\text{NNH}} = 2.074$ bohr, $R_{\text{N}-\text{H}} = 1.958$ bohr, $R_{\text{NN}-\text{NH}} = 4.45$ bohr, $\theta_{\text{NNN}} = 163^\circ$. The terminal NN bond is *trans* to the NH bond. Contours are indicated at every 50 cm^{-1} . The minimum (indicated by the 'x') lies at $(\theta, \phi) = (86.6^\circ, 90^\circ)$. The zero point frequencies at the barrier are 139 cm^{-1} for the torsional mode and 771 cm^{-1} for the bending mode most directly comparable to the in-plane NNH wag

NNH wagging will be $\alpha = 11.82 \text{ degrees}^{-2}$ and $\beta = 0.6552 \text{ degrees}^{-2}$. This corresponds to a full width at half maximum of the gaussians in Eq. (8) of 27.8° for the in-plane angle θ and 119.8° for the torsional angle ϕ .

Table 1 displays calculated values of the Λ doublet ratios $R(J)$ determined for these values of the exponential parameters α and β . As expected from the symmetry argument we gave earlier,⁶ the $\Delta(A')$ levels are always found to be preferentially formed. We also see that the ratio $R(J)$ increases as a function of increasing J for those cases where this ratio differs significantly from unity. Such a variation in $R(J)$ is consistent with the semiclassical picture that the plane of rotation of the NH fragment becomes better defined the higher the value of J . The comparison with the experimentally observed⁵ Λ doublet ratios is entirely satisfactory.

Table 1. Ratio of population in the $\Delta(A')$ as compared to $\Delta(A'')$ levels of the $\text{NH}(a^1\Delta)$ molecule subsequent to the spin-allowed decomposition of HN_3 , as a function of the final state rotational quantum number.

	N=2	3	4	5	6	7
experiment a:	1.0 ± 0.3		1.2 ± 0.3	1.7 ± 0.3	2.1 ± 0.3	4 ± 1
theory:	1.14	1.46	1.97	2.62	2.83	3.41

a) Ref. 5.

References

1. M. J. Bronikowski and R. N. Zare, *Chem. Phys. Lett.* **166**, 5 (1990).
2. P. Andresen, G. S. Ondrey, B. Titze, and E. W. Rothe, *J. Chem. Phys.* **80**, 2548 (1984).
3. M. H. Alexander, P. Andresen, R. Bacis, R. Bersohn, F. J. Comes, P. J. Dagdigian, R. N. Dixon, R. W. Field, G. W. Flynn, K.-H. Gericke, B. J. Howard, J. R. Huber, D. S. King, J. L. Kinsey, K. Kleinermanns, A. C. Luntz, A. J. MacCaffery, B. Pouilly, H. Reisler, S. Rosenwaks, E. Rothe, M. Shapiro, J. P. Simons, R. Vasudev, J. R. Wiesenfeld, C. Wittig, and R. N. Zare, *J. Chem. Phys.* **89**, 1749 (1988).
4. M. H. Alexander and P. J. Dagdigian, *J. Chem. Phys.* **80**, 4325 (1984).
5. M. P. Casassa, B. R. Foy, J. C. Stephenson, and D. S. King, *J. Chem. Phys.* **94**, 250 (1991).
6. M. H. Alexander, H.-J. Werner, and P. J. Dagdigian, *J. Chem. Phys.* **89**, 1388 (1988).
7. M. H. Alexander, T. Hemmer, H.-J. Werner, and P. J. Knowles, *J. Chem. Phys.* **93**, 3307 (1990).
8. D. G. Sauder, D. Patel-Misra, and P. J. Dagdigian, *J. Chem. Phys.* **91**, 5316 (1989).
9. V. Bonacic-Koutecky, J. Koutecky, and J. Michl, *Angew. Chem. Int. Ed. Engl.* **26**, 170 (1987).

THE REACTION OF METAL ATOMS WITH HN₃ AND HNCO

Paul J. Dagdigian

*Department of Chemistry
The Johns Hopkins University
Baltimore MD 21218*

Hydrazoic acid (HN₃) and the azide radical (N₃) are very interesting reagents because of the extremely small energies required for their decomposition. The reaction of the azide radical with a number of nonmetallic atomic reagents has been studied by observation of the chemiluminescence from highly excited product states formed. By contrast, the reactions of N₃ with metal atoms have received little attention. We have extended our previous investigation¹ of the H + N₃ reaction to the study of such metal atom reactions.

As a first step in this program, we have carried out chemiluminescence and laser fluorescence studies of the reactions of Ca and Sr atoms with HN₃, and also HNCO. These molecular reagents were chosen for initial study because they are used as chemical precursors for the corresponding radicals N₃ and NCO. These particular atomic reactants have been investigated initially because of our laboratory's considerable experience with alkaline earth atom reactions. These reactions can proceed along two possible pathways:



where XY = N₂ or CO and M = Ca or Sr. The exothermicity of pathway (1) is expected to be substantial, while pathway (2) is thermoneutral or endothermic. The metal imides (MNH) are isoelectronic with the well known alkaline earth oxides.

Our experiments have been carried out in a beam-gas arrangement, in which metal atoms produced in a high-temperature oven housed in a differentially pumped chamber pass through a collimating slit and impinge on the molecular reagent in the scattering chamber at low pressure ($\leq 10^{-3}$ Torr). Our atomic beam source is designed so that both ground state (¹S) atoms, or metastable excited (³P, ¹D) atoms, can be produced, the latter by striking a dc discharge in the source. Chemiluminescence from the electronically excited species, or laser excited fluorescence from nonemitting species, can be recorded in these experiments. Figure 1 illustrates a chemiluminescence spectrum for the reaction of ground state Ca(¹S) atoms with HN₃ at low pressure. Visible in this spectrum are emissions from excited Ca atomic states and CaH*, as well as several unidentified molecular features near 550 and 600-620 nm. In order to identify the mechanism of excitation and the identity of the

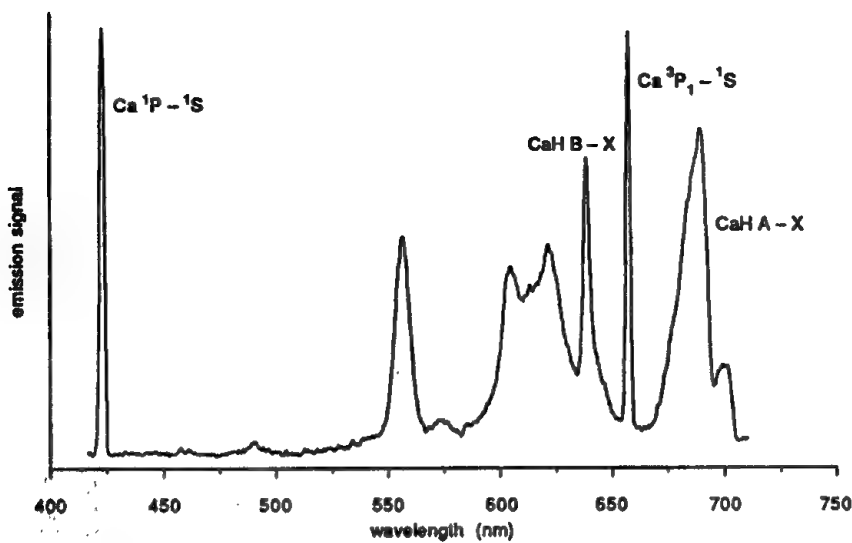


FIG. 1. Chemiluminescence spectrum from $\text{Ca}(^1\text{S}) + \text{HN}_3$ ($p = 5 \times 10^{-4}$ Torr).

unknown emitter, the dependence of the emission intensity of the various features upon the HN_3 pressure was determined. The Ca^* lines and CaH^* bands displayed a nonlinear pressure dependence, consistent with a multiple-collision mechanism. By contrast, the new molecular features were found to vary linearly with the HN_3 pressure. We tentatively assign these features to chemiluminescence from CaNH formed by reaction (1). We note that the wavelengths of these bands corresponds very closely with those of the well known green and orange arc bands of the isoelectronic CaO molecule.² We have also investigated the reaction of $\text{Sr}(^1\text{S})$ atoms with HN_3 and find similar emission features. In particular, bands assigned to SrNH are observed at wavelengths near to those of the known SrO arc bands.³

It is interesting to speculate on the multi-step reaction mechanism which can explain the production of excited Ca^* , and also CaH^* . For the former, reaction (2), with $M = \text{Ca}$ and $XY = \text{N}_2$, can be followed by



The combination of reactions (2) and (3) can be described as the Ca -catalyzed decomposition of HN_3 :



The energy liberated in reaction (4) is sufficient to explain the production of excited Ca atoms in reaction (3). Electronically excited CaH can be produced by the following reaction:



We have also conducted laser fluorescence excitation experiments in order to probe the nonemitting species produced in the reactions of Ca with HN_3 and HNCO . For the former molecular reagent, we observe strong laser fluorescence excitation of the CaN_3 , whose spectrum has been previously analyzed by Brazier and Bernath.⁴ We also have observed several band systems in the green and orange-red (at 536, 555, 598, 602, and 625 nm) when electronically excited metastable Ca atoms react with HN_3 or HNCO under multiple-collision conditions at pressures greater than 6×10^{-4} Torr. Careful comparison of these spectra with previously reported spectra of Ca-containing molecules reveals that the identity of this molecule is CaOH .⁵ The mechanism of production of CaOH in this system is not clear as the addition of H_2O , instead of HN_3 or HNCO , does not yield any CaOH bands. Perhaps trace water in the presence of HN_3 allows production of CaOH .

We have also been investigating the chemiluminescence produced by the reaction,



previously investigated by Coombe and coworkers,⁶ as well as several other investigators, at a total pressure of several Torr. This reaction is of importance in the pumping scheme for the chemical laser proposal involving the detonation of lead azide currently under study by Rosenwaks and coworkers.⁷ The $\text{N} + \text{N}_3$ reaction yields electronically excited $\text{N}_2(\text{B}^3\Pi_g)$, which emits in the visible in the nitrogen first positive B – A band system. With the above quoted exothermicity, population up to $v'=12$ is possible. Spin conservation arguments suggest that the excited nitrogen molecules should be formed in triplet electronic states. David and Coombe⁶ give an orbital correlation argument to provide a rationalization of why the B state should be exclusively formed in reaction (6). As the radiative lifetime of the B state is fairly long ($5\text{-}10 \mu\text{s}$,⁸ depending on v'), collisional effects could be perturbing the chemiluminescence spectrum. It is known, in particular, that the B state is collisionally coupled strongly to the long-lived $\text{W}^3\Delta_u$ state,⁹ as well as also to the $\text{A}^3\Sigma_u^+$ and $\text{B}'^3\Sigma_u^-$ states. Unfortunately, direct observation of the W state is possible only through the infrared B – W bands, which have relatively small transition probabilities.

We have recorded the $\text{N} + \text{N}_3$ chemiluminescence spectrum as a function of added argon gas for total pressures of 0.3 to 3 Torr. The nitrogen atoms were produced by a 2450 MHz microwave discharge in nitrogen gas; the N_3 reagent was derived from HN_3 precursor. Figure 2 displays the B – A $\Delta v=+3$ and +4 sequences at several pressures. It can be seen that the emission intensity from higher v' levels is markedly enhanced at the higher pressure. The marked rise in the chemiluminescence signal with increasing pressure

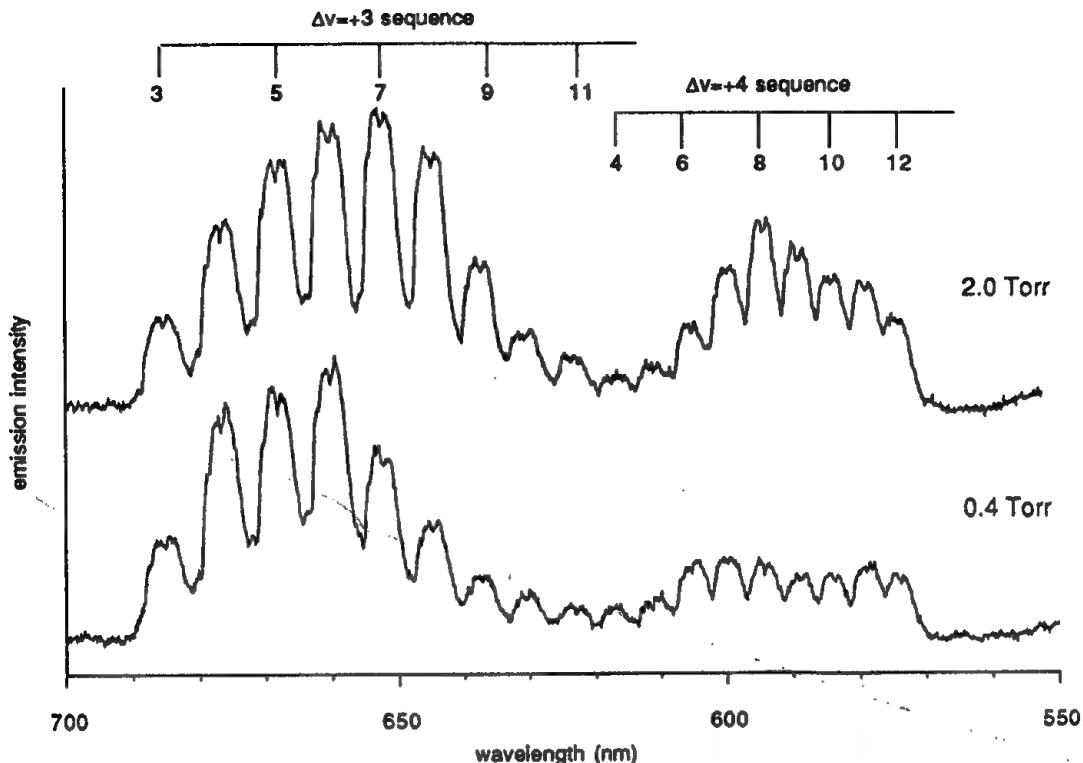


FIG. 2. Chemiluminescence spectrum from the $N(^4S) + N_3$ reaction at several total pressures with Ar added. The v' levels of the $\Delta v = +3$ and $+4$ B - A sequences are indicated.

implies the existence of a significant population in a nonemitting reservoir state, taken to be $W^3\Delta_u$. Two-photon laser fluorescence detection was employed to verify that the $N(^4S)$ concentration did not change when Ar gas was added. Rate constants for transfer between the B and W vibrational levels induced by collisions with Ar have been derived from time-resolved laser excitation experiments.⁹ From the vibrational dependence of these transfer rates, it is clear that $N_2(W)$, as well as $N_2(B)$, is directly produced in reaction (6). We are attempting to extract the nascent B to W state branching ratio in this reaction by fitting the pressure-dependent steady-state B state vibrational populations derived from the chemiluminescent spectra.

1. J. Chen, E. Quiñones, and P. J. Dagdigian, *J. Chem. Phys.* **93**, 4033 (1990).
2. J. B. Norman, K. J. Cross, H. S. Schweda, M. Polak, and R. W. Field, *Mol. Phys.* **66**, 235 (1989), and references therein.
3. See J. W. Cox and P. J. Dagdigian, *J. Phys. Chem.* **86**, 3738 (1982).
4. C. R. Brazier and P. F. Bernath, *J. Chem. Phys.* **88**, 2112 (1988).

5. P. F. Bernath and C. R. Brazier, *Astophys. J.* **288**, 373 (1985), and references therein.
6. S. J. David and R. D. Coombe, *J. Phys. Chem.* **89**, 5206 (1985); **90**, 3260 (1986).
7. I. Bar, A. Cohen, D. Heflinger, Y. Tsuk, and S. Rosenwaks, *Appl. Phys. Lett.* **58**, 322 (1991).
8. L. G. Piper, K. W. Holtzclaw, B. D. Green, and W. A. M. Blumberg, *J. Chem. Phys.* **90**, 5337 (1989).
9. N. Sadeghi and D. W. Setser, *J. Chem. Phys.* **79**, 2710 (1983); A. Rotem and S. Rosenwaks, *Opt. Eng.* **22**, 564 (1983).

State-Resolved Dynamics of Intramolecular Relaxation in Superexcited Molecules: Isoelectronic Analogies of BH_2 and AlH_2 with NO_2

K. S. Haber, Y. Jiang, G.P. Bryant, Y.-F. Zhu, R. Shehadeh and E. R. Grant

Department of Chemistry

Purdue University

West Lafayette, IN 47907

Introduction

While advanced propellants are most often measured against H_2/O_2 , most practical propulsion systems, for reasons of convenience and increased density, use other fuel/oxidizer combinations that provide less specific impulse. Such propellant alternatives are often aided by additives, which can augment specific energy density and I_{sp} . One well established such practice utilizes metallized propellants. The main benefit in this case is increased specific energy density. For example, in the Space Shuttle liquid engine the I_{sp} of H_2/O_2 is 406 seconds, but its density $\times I_{sp}$ product is only 4. Ammonium perchlorate + aluminum under comparable conditions is limited to a specific impulse of 264, but offers a density $\times I_{sp}$ product of 17.¹

Improvements in both I_{sp} and specific energy density can be envisioned for a fuel composed of metallized hydrogen.² Other factors aside, lighter atomic weights are to be favored. Lithium, however, appears to have low solubility, beryllium is toxic, particularly in its oxidized form, and boron tends to oligomerize. Experiments have successfully jelled aluminum with H_2 ,³ and diatomic aluminium lithium has come under theoretical and experimental scrutiny as a potential additive of low mobility in solid hydrogen.⁴ Other possibilities include immobilized fragment molecules or complexes of an atomic additive such as boron or aluminum with hydrogen itself.

Experimental and theoretical progress on promising new high-energy-density materials will continue to rely on solid fundamental information on the structural, thermochemical and kinetic properties of novel molecules and complexes. Current efforts along these lines in our laboratory are focussed on the electronic spectroscopy and radiationless dynamics of Group III hydride fragments, notably BH_2 and AlH_2 . Work thus far has produced several promising new free-jet sources of these molecules, together with distinctive spectroscopic diagnostics. Sections below report progress on these sources. We then describe experiments presently underway to investigate the low- and high-energy electronic spectroscopy of these molecules, and explore the dynamics of energy flow and fragmentation in their highly excited states. An informative electronic analogy exists between the Group III dihydride radicals and the extra-electron dioxide, NO_2 . We illustrate the scope of experimental information accessible for BH_2 and AlH_2 by presenting selected new results on NO_2 .

Evaporative and Pyrolysis Filament Pulsed-Jet Source

An evaporative, aluminum-coated tungsten-filament nozzle can form an intense jet of aluminum atoms. When attached to a pulsed source of helium, the exhaust from such a nozzle produces an aluminum mirror on a glass substrate in a matter of minutes. If hydrogen is used in place of helium, no mirror is produced, indicating an efficient conversion to hydrides. Monitoring

the output of the aluminum-filament nozzle by nonresonant multiphoton ionization mass spectrometry, we find the Al^+ signal observed with He carrier replaced by one assignable to molecular hydride cations, including AlH and AlH_2 as well as heavier ion fragments derived apparently from dilane, Al_2H_6 . Figure 1 shows a diagram of our pulsed evaporative filament aluminum hydride source, together with a laser-induced fluorescence spectrum of AlH .

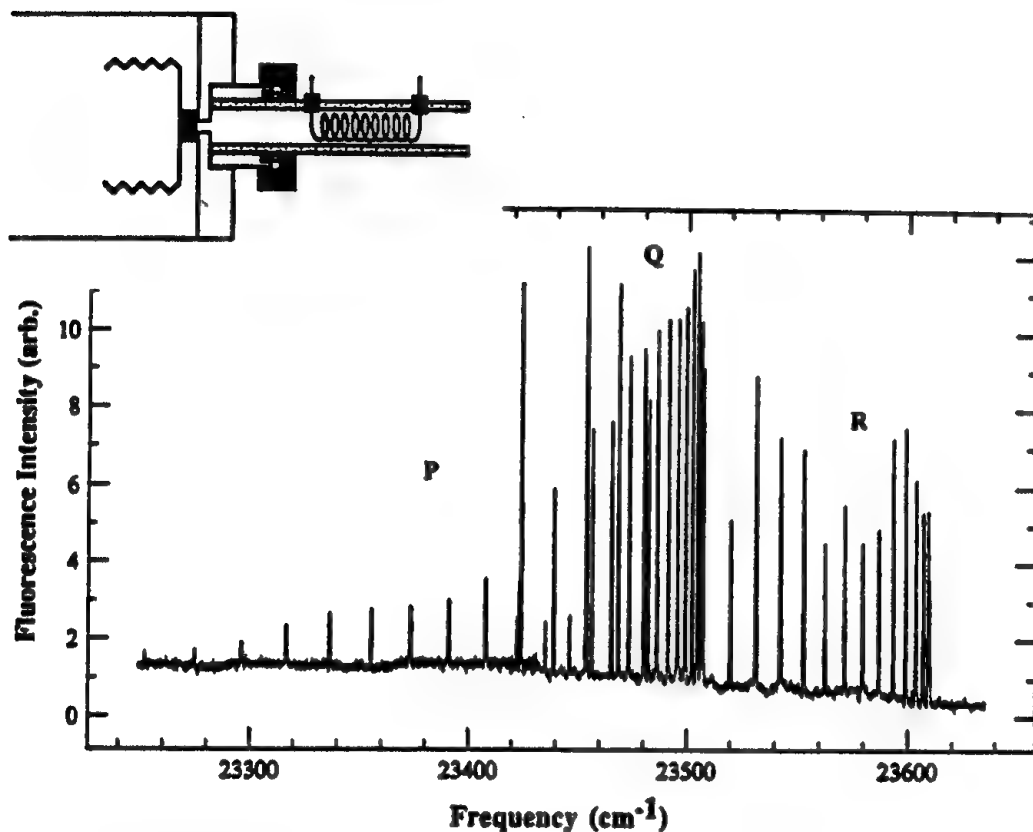


Figure 1 Schematic diagram of the pulsed evaporative aluminum hydride source. Laser induced fluorescence spectrum of AlH .

Electric Discharge Source

Another productive source of aluminum hydrides is our pulsed-valve electric discharge source. To form this source, a DC potential of around 1.5 KV is applied across an assembly comprised of a pair of electrodes spaced by a ceramic disk, which forms the orifice plate of a pulsed nozzle. Under vacuum, the electrode assembly holds off the high voltage, so that no current flows. When the valve opens, the pressure in the orifice rapidly rises to the breakdown threshold, and a glow discharge forms. Normally, with inert gas or hydrogen and stainless steel electrodes, emission of light from this discharge is weak. However, when the combination of hydrogen gas with aluminum electrodes is used, an intense afterglow forms which exhibits the rich emission spectrum pictured below.

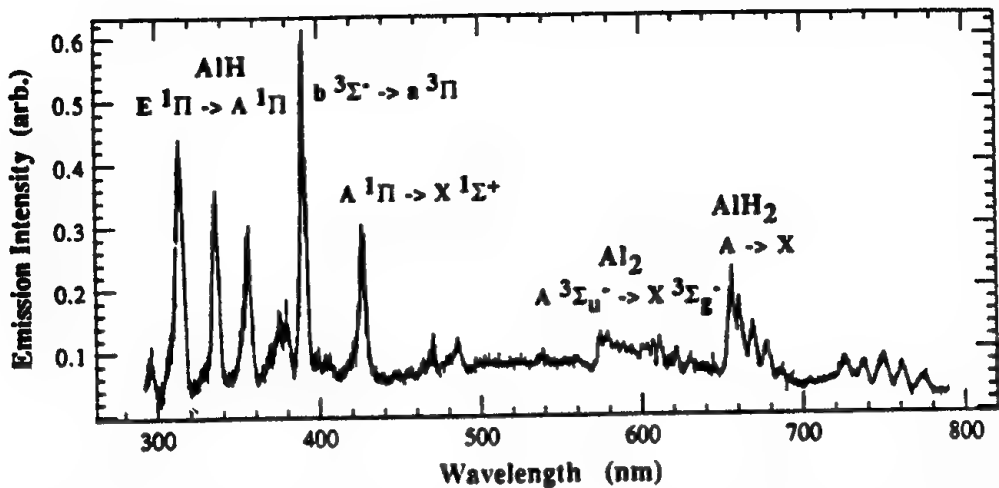


Figure 2 Emission spectrum of the flowing afterglow formed in H_2 pulsed through aluminum electrodes.

Emission in the red has been seen before in aluminum-hydrogen discharges. Herzberg and Johns⁵ have suggested that light in this spectral region can be attributed to AlH_2 . The frequency of this emission together with its broad structure is consistent with ab initio calculations as well as a simple physical picture based on Walsh orbital arguments. Available MCSCF calculations predict absorption in long progressions of $^2\text{A}_1$ to $^2\text{B}_1$ bent-to-linear transitions.⁶ Inspection of the Walsh diagram for five-electron dihydrides such as AlH_2 and BH_2 shows that the situation is more complicated than this. These extra-electron molecules have higher occupied orbital populations entirely analogous to NO_2 , which give rise to a set of low-lying transitions to bent $^2\text{B}_2$ in addition to $^2\text{B}_1$. B_1 is coupled by quadratic terms in the bending mode to the A_1 ground state. B_2 is coupled linearly in asymmetric stretch to A_1 . A dark A_2 state can also be predicted, which is coupled vibronically to both B_1 and B_2 .

We are interested in studying these transitions in AlH_2 and BH_2 to learn more about electronic structure and bonding in these energetic fragments. We are also interested in probing higher, where after promoting an electron to a diffuse orbital, we are left with a well-defined closed shell cation core which is isoelectronic with linear $^1\Sigma_g$ BeH_2 and MgH_2 . We wish to probe the dynamics of energy flow between this approximately separable cationic framework and the diffuse electronic degree of freedom. To illustrate the approach we are taking and the level of detail we expect for AlH_2 and BH_2 , we turn now to some new results in a parallel program on a highly analogous system NO_2 .

Electronic Structure of NO_2

Like AlH_2 and BH_2 , NO_2 presents a set of electronic properties which is ideal for a spectroscopic exploration of the dynamics of energy flow between vibrational and electronic degrees of freedom in a highly excited polyatomic molecule. Because NO_2 is a seventeen-valence-electron triatomic molecule, its low lying manifold of electronic states is dense, while its cation, which is isoelectronic with sixteen electron CO_2 , has a closed-shell $^1\Sigma$ electronic ground state, with no low-lying excited states. For this reason, while low-lying electronic states can be expected to

be strongly coupled, the higher-lying excited states of the neutral molecule are Rydberg in nature, each with a potential surface that, for small displacements, closely parallels that of the ion, making Rydberg-Rydberg and Rydberg-cation transitions highly vertical. The near-continuum of strongly coupled valence states, which extends from the red to the near UV, facilitates transitions from the bent ground state to both vibronically symmetric and asymmetric linear Rydberg states in two steps of resonant absorption, that specify rotational and vibrational quantum numbers. From this highly selected Rydberg vantage point, third-color scans can probe vibrationally and rotationally accessible Rydberg states near and above the adiabatic ionization threshold.

Triple-Resonant Selection of Vibrational-Rotational States

Using such stepwise excitation methods, we have undertaken an extensive examination of specific factors that affect the dynamics of competitive channels of decay in superexcited NO₂.⁷ We characterize these dynamics by analyzing patterns of intensity and lineshape in ionization-detected absorption spectra of vibrationally autoionizing states, reached in transitions from selected rovibrational levels of double-resonantly prepared levels of the gateway 3pσ $^2\Sigma_g^+$ Rydberg state. Figure 3 shows an energy level diagram.

Two-color double-resonant scans establish suitable transitions to the 3pσ $^2\Sigma_g^+$ state. We tune the dye laser providing the first excitation step to an arbitrary wavelength near 482 nm and then scan the second laser, which is doubled, over the transition from this intermediate level to the selected 3pσ vibrational state. Absorption of a second ultraviolet photon promotes ionization. We find intermediate states with large cross sections for particular overall transitions by locking the energy of $\omega_1 + \omega_2$ and scanning one laser up and the other down in energy.

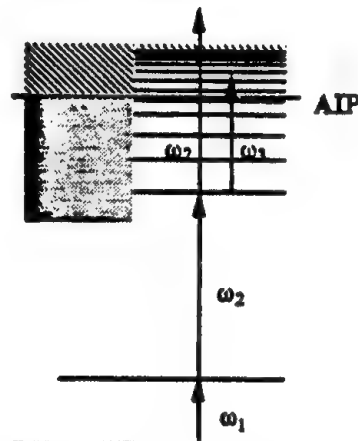


Figure 3 Energy level diagram.

Vibrational Autoionization Dynamics in Single Rotational States Converging to NO₂⁺ (100)

Scanning third laser with $\omega_1 + \omega_2$ fixed on the P(2) transition to 3pσ (100) N = 1, yields the spectrum of the (100) vibrationally autoionizing Rydberg states shown in Figure 4, which displays the entire region between the adiabatic IP and the (100) limit. Most features observed can be assigned to σ, dσ, and dπ series converging to the vertical threshold. Identified transitions extend over principal quantum numbers ranging from n=10 to more than 50. Also evident are modulations or dips in ionization-detected absorption that form an interloping series converging the (110) threshold. Discrete states in the (100) series autoionize efficiently, as evidenced by the continuity of ionization-detected oscillator strength across the vertical threshold. The periodic mixing of bending character via coupling with (110) apparently interferes with ionization, presumably by diverting radiationless decay through neutral fragmentation channels.

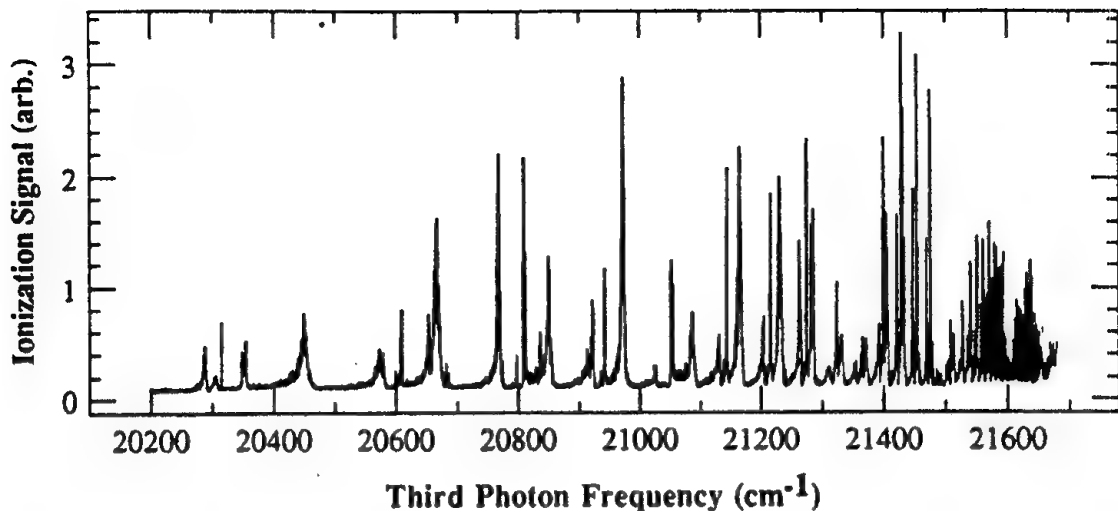


Fig. 4. Manifold of autoionizing states converging to NO_2^+ (100).

Autoionization via Loss of One Quantum of Bend

The behavior evidenced in the spectrum of autoionizing states reached in vertical transitions from the $3\text{p}\sigma$ (010) state confirms this hypothesis. Figure 5 shows the vibrational autoionization spectrum scanned from $3\text{p}\sigma$ (010), $N' = 1$. Here we see a weak spectrum of sharp lines, evidencing slower decay times and diminished yield from autoionization, together with a definite step of increased ion production at the vertical threshold. Evidently, autoionization is less efficient from core-bending excited Rydberg states.

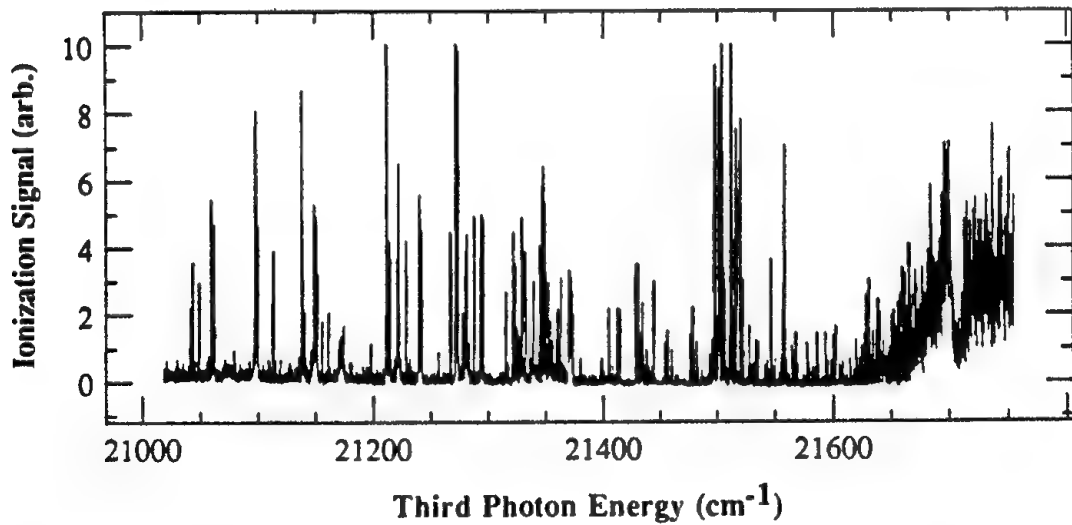


Fig. 5. Manifold of autoionizing states converging to NO_2^+ (010).

Basis for Mode-Specific Autoionization

We can conclude, from patterns of linewidths and intensities in respective vibrational autoionization spectra, that, in states with total energies near 80,000 cm⁻¹, the presence of one quantum of excitation in symmetric stretch is sufficient to direct radiationless decay strongly toward electron ejection, while a similarly small increment of the total energy deposited in bending excitation channels relaxation much more efficiently toward neutral fragmentation. This mode specificity can be explained within the context of MQDT by assuming bend-stretch differences in the normal coordinate dependence of quantum defects.⁸ It can also be viewed as consistent with the simple long-range interaction picture developed some time ago by Berry and Neilsen to first describe the process of vibrational autoionization.⁹ In Berry and Neilsen's model, coupling is factored into vibrational overlaps and Rydberg-continuum electronic matrix elements of the dynamic multipole, dU_{lm}/dR , corresponding to the vibrational motion of the core charge distribution. Their calculations for H₂ suggest that the sum over dU_{lm}/dR is dominated by its leading terms, associated with the oscillating monopole. Within this latter picture it appears possible that the apparent mode specificity of vibrational autoionization described thus far might be explained simply by taking note of differences in the dynamic multipole potential of the core associated with motion in different normal modes. In such a picture we would say that symmetric stretch autoionizes efficiently by virtue of a large dynamic monopole term; the vibrational motion consists purely of lengthening and shortening the molecule. Bending states live longer and are lost to dissociation, because in this normal coordinate the charge distribution oscillates, but its volume remains approximately constant as the oxygens move roughly on the surface of a sphere.

The Dynamics of Vibrational Autoionization from Asymmetric Stretch Excited States

The dynamics of vibrational autoionization from Rydberg states built on asymmetric stretch excited cores supply a critical test of this simple long-range picture. As with bending, the volume of the electronic charge distribution changes little with motion asymmetric stretch. Also like bending, asymmetric stretch produces a substantial dynamic dipole, directed in this case along the internuclear axis. On the other hand, asymmetric stretch substantially differs from bending in at least one respect which is not reflected in the low-order components of the dynamic multipole: In contrast with bending and more like symmetric stretch, displacement along the asymmetric stretch coordinate is accompanied by large individual N-O bond length changes.

To probe asymmetric stretch in autoionization, we must establish a gateway transition to the (001) vibronic level in the 3pσ $^2\Sigma_u^+$ Rydberg state, relying on state mixing in a vibronically distorted first-photon intermediate state. The fundamental frequency of asymmetric stretch in the NO₂⁺ core is unknown, but by analogy with CO₂ we can expect it to be high, in the neighborhood of 2500 cm⁻¹. This region of core vibrational energy is congested by overtones and combinations of symmetric stretch and bend. Fortunately, however, transitions to the asymmetric stretch fundamental in the 3pσ $^2\Sigma_u^+$ Rydberg state are readily isolated at our laser resolution, and identified by their unique rotational structure. (001) is the only level within 5000 cm⁻¹ to have vibronic symmetry Σ_g^+ . It is therefore uniquely distinguished by the fact that nuclear spin statistics exclude all of its odd-numbered rotational states, and two-photon selection rules allow transitions originating only from the all-even ground rotational levels of the K = 0, 2, ... stacks.

A third-laser scan across the complete vibrational autoionizing interval, originating from double-resonantly prepared 3pσ $^2\Sigma_u^+$ (001) N = 0, is shown in Figure 6. This interval, which is 1000 cm⁻¹ longer than that for symmetric stretch, is dominated by a single series that extends

uniformly across the range. This continuity of structure provides an immediate confirmation of the assignment made on the basis of rotational structure; autoionization from overtones or combinations of lower frequency modes would exhibit linewidth and/or intensity steps at succeeding thresholds. The only candidate single mode of such a large frequency is asymmetric stretch.

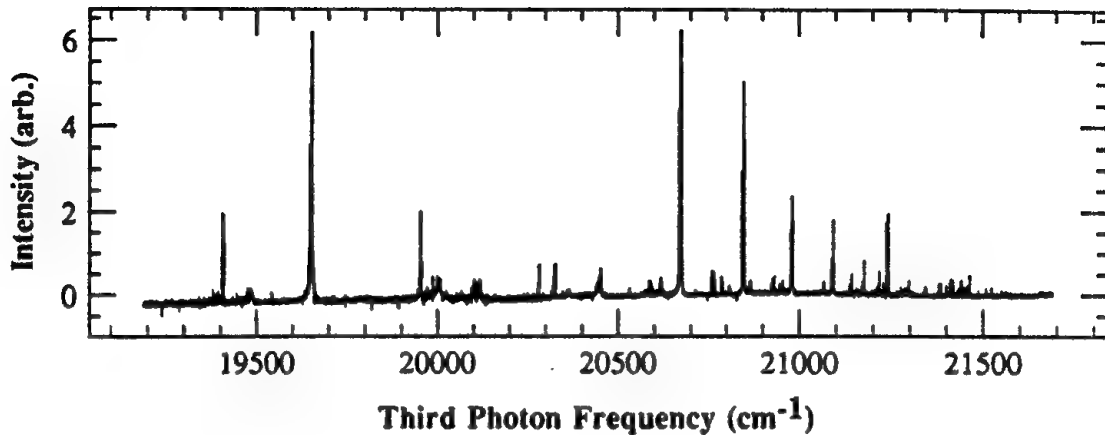


Fig. 6. Manifold of autoionizing states converging to NO_2^+ (001).

Comparison of Figure 6 with Figures 4 and 5 establishes clearly that the dynamics of autoionization via asymmetric stretch differ substantially from those associated with relaxation in either symmetric stretch or bend. The single prominent series has a quantum defect of about 0.7. This matches a strong series in symmetric stretch that we have designated $n\sigma$. Here, however, the linewidths are uniformly narrower; autoionization lifetimes are apparently longer. The resonances in this series are intense, and by comparison the ionization detected absorption signal rises little across the vertical threshold, so we can also conclude that autoionization in this series is at the same time efficient, competing effectively with neutral fragmentation.

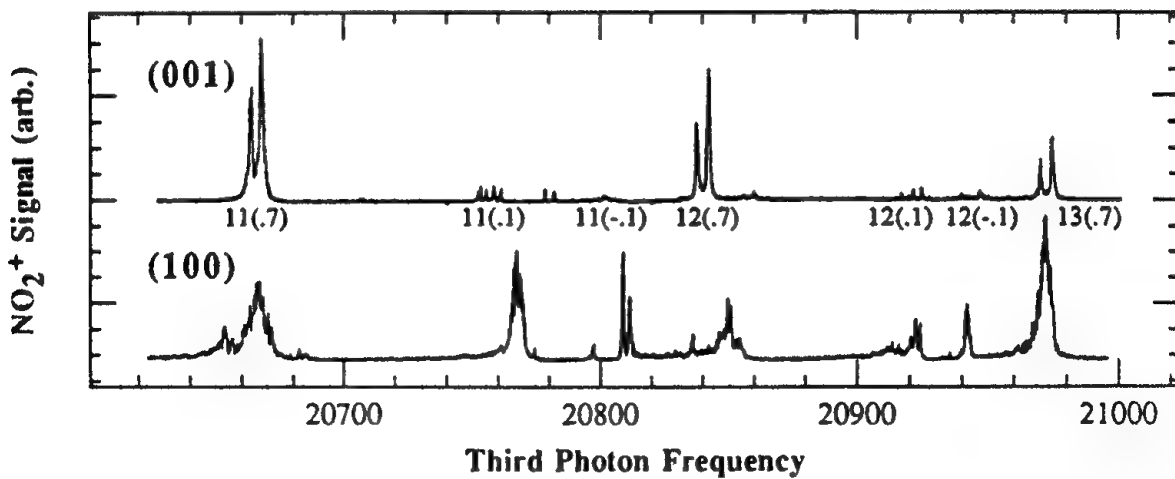


Fig 9. Spectra comparing series converging to (001) and (100) for principal quantum numbers $n = 11$ and 12

Thus in summary, for asymmetric stretch we see autoionization decay times intermediate between symmetric stretch and bend. This is at least qualitatively consistent with the nature of the long range dynamic potentials associated with the vibrational motion in each case, assuming that we can associate efficient autoionization with a large dynamic monopole. Patterns in dissociation, on the other hand, seem more subtly controlled by vibronic dynamics. Symmetric stretch is resistant to dissociation, bend is highly dissociative, while in asymmetric stretch the relative efficiencies of dissociation versus autoionization vary with the nodal properties of the Rydberg orbital.

This work was supported by the Air Force Office of Scientific Research under Contract F49620-87-C-0092 and by a grant from the National Science Foundation (CHE-8920555). GPB gratefully acknowledges fellowship support from NASA under the Graduate Student Researchers Program.

References

1. R. Carpenter, *Proceedings of the High Energy Density Materials (HEDM) Conference*, L. Burgraff ed., Long Beach, CA, February 1990.
2. B. Palaszewski, *Proceedings of the High Energy Density Materials (HEDM) Conference*, L. Burgraff ed., Long Beach, CA, February 1990.
3. *Systems analysis of Jelled Space-Storable Propellants*, Aerojet General Corporation, Propulsion Division, Contract NAS7-473, SA1, Summary Report 1038 02S, July 1968.
4. M. E. Rosenkrantz, *Proceedings of the High Energy Density Materials (HEDM) Conference*, L. Burgraff ed., Albuquerque, NM, February 1991.
5. G. Herzberg and J. W. C. Johns, unpublished
6. B. Nestman and M. Peric, *Chem. Phys.* **89**, 257 (1984)
7. F. X. Campos, Y. Jiang and E. R. Grant, *J. Chem. Phys.* **93**, 2308 (1990);
F. X. Campos, Y. Jiang and E. R. Grant, *J. Chem. Phys.* **93**, 7731 (1990)
8. G. Herzberg and Ch. Jungen, *J. Mol. Spec.* **41**, 425 (1972).
9. R. S. Berry, *J. Chem. Phys.* **45**, 1228 (1966); R. S. Berry and S. E. Nielsen, *Phys. Rev. A* **1**, 395 (1970).

Photodynamics in Solids Under High Pressure

Ellen Sekreta and V. A. Apkarian

Department of Chemistry

University of California

Irvine, California 92717.

Extended Abstract

It is rather clear that pressure can have a profound effect on all aspects of molecular dynamics in compressible solids -- the category of all existing and projected solid state propellants. Of particular interest is the possibility of stabilizing high densities of radical and ion dopants by application of pressure in such solids. Experimental evidence to this effect can be found in our previous studies on chlorine doped xenon contained in a diamond anvil cell, in which issues of molecular photodissociation, thermal and photo-induced atomic mobility were probed in some detail.¹ One of the most dramatic demonstrations of the profound effect of pressure on dynamics in compressible solids was the demonstration that Cl atoms at a doping density of 1:250 could be maintained for weeks in room temperature solid Xe without any appreciable recombination.² We have extended this observation window, by keeping the same sample under 56 kbar of pressure, at room temperature, for two years. In figure 1, the emission spectrum of the sample when excited at 308 nm is shown. The emission is strictly from Xe₂Cl, i.e due to atomic Cl in Xe. In the same spectral range, 750-850 nm, occurs the molecular Cl₂(A' → X) emission, of which there is no trace. The conclusion is quite clear: even at room temperature, under 56 kbar of pressure, *Cl radicals in solid Xe are perfectly stable with respect to recombination!* It should however be noted, that we have no direct measurement of the radical number density in this sample, other than the initial molecular doping concentration of Cl₂:Xe of 1:500. There is no reason to believe that there has been any significant loss of chlorine concentration in the sample.

While storage of radicals in high pressure solids is of obvious value, an important question is also the methods for their generation. *In situ* photodissociation is an attractive scheme. In the case of Cl₂ in Xe, it was noted that at pressures above 20 kbar, direct dissociation by optical access of repulsive potentials did not occur at any

temperature. We have since verified this observation by Molecular Dynamics simulations.³ A constant pressure MD algorithm was developed for this purpose. Simulations at T=100 K indicate that at an excess energy of 1.5 eV (dissociation wavelength of 308 nm), the dissociation quantum yields drop dramatically with pressure: 35% at 0 kbar, 2% at 12.5 kbar, 0% at 25, 50 and 100 kbar. In effect, where experiment and simulation overlap, the two agree. A more rigorous test of the validity of simulations is suggested by measurements of depolarization of recombinant emissions -- at high pressures, molecular axis remains fixed during the entire dissociation-recombination process. Simulations are clearly of great value in feasibility tests prior to experimentation in such systems.

Our more recent high pressure studies have been carried out on a sample of Xe:F₂:Ar, which is rather well understood at zero pressure.⁴ There are several motivations for the choice of this system for study:

a) F/Ar represents a lighter system, and as such of greater relevance to propellant applications. Moreover, the photodissociation of F₂ in Ar and Kr have been studied in depth by both simulation^{5,6} and experiment^{7,8} at zero pressure, and therefore a clear evaluation of the effect of pressure on photodissociation, photomobility, and thermal mobility of atoms is possible. As far as these questions are concerned, the role of Xe in these solids is strictly for detection purposes: the XeF emission intensity can be used to probe for the presence of F atoms at Xe trap sites.

b) The spectroscopic investigation of XeF in solid Ar is of direct interest. Among rare gas halide exciplexes, XeF is the most stable in both ionic and covalent states. The closing of the gap between ionic and covalent manifolds with pressure is of relevance to the possibility of designing an entirely metastable solid, which may remain so after release of pressure due to the many-body nature of the ionic/covalent solid-state potentials. It is possible to estimate for instance that, due to the Madelung summation of Coulombic interactions, even at zero-pressure, an ionic XeF solid is nearly isoenergetic with its covalent counterpart.

The photodissociation probability of F₂ in Ar at zero pressure is near unity, moreover the F atoms generated at this excess energy of 2.4 eV undergo long-range migration.⁴⁻⁶ As such, the photodissociation process can be followed by monitoring the density of XeF centers. While this process can be clearly observed in the diamond anvil cell at 0 pressure, it is completely quenched at pressures above 25 kbar. The longest investigated wavelength, at which photogeneration is observed, is 265 nm (3 eV of excess

energy). It is clear that 25 kbar, has a profound effect on photodissociation dynamics in Ar, however at present it is not possible to ascertain whether dissociation probabilities are quenched, or whether the subsequent impulsive mobility of atoms is blocked. An added complication of these studies, which are carried out in a single sample subjected to numerous irradiation and thermal cycles, is the possibility that we are strongly effected by the photodynamics of XeF_2 , which is a stable covalently bonded molecule. XeF_2 undergoes efficient photodissociation when excited to its first continuum in the gas phase⁷ and also in rare gas solids.⁸ However, our prior studies at zero-pressure indicate that the formation of XeF_2 from XeF and F is activated, and hence not significant at cryogenic temperatures. It may, however become an important sink of F atoms in the high pressure studies, which are also conducted at high temperatures. These uncertainties could be clarified if we were to monitor F atom concentrations in the bulk of Ar. However, the ultraviolet cutoff of the diamond windows does not allow such a determination. Such studies are however entirely feasible in solid Kr, in which both F atoms scavenged by Xe and those in the bulk of Kr can be probed at wavelengths longer than 280 nm.^{4,6} Such studies are now in progress.

The thermal mobility of F atoms in these solids is probed by monitoring the loss of XeF emission during warm-up cycles. Two examples are shown in figure 2. In figure 2a, the warm-up cycle of a sample under 20 kbar of pressure is shown, the emission intensity initially grows (at $\sim 60\text{K}$) and subsequently disappears. The initial growth can clearly be ascribed to mobile F atoms finding the Xe trap sites. Note, F atoms recombine at 25 K in zero-pressure Ar.⁶ There are two possible mechanisms for the decay of emission with intensity: a) detrapping of F atoms from the Xe sites, and their subsequent diffusion controlled recombination, b) reaction of XeF with F to form XeF_2 . We prefer the former argument, since complete disappearance of emission by XeF_2 formation would require an exact stoichiometric reaction, which is rather doubtful. First order kinetics for an activated rate process, $k=k_0 \exp(-E_a/kT)$, should then be sufficient to fit the data. Such a fit is shown in figure 2b, it was also verified that second order kinetics yield much poorer fits. While it is possible to reproduce the data with an activation energy that can be rationalized ($E_a \sim 0.04\text{eV}$), the preexponents required for the fit of $\sim 1\text{s}^{-1}$, are difficult to justify. Clearly, a more sophisticated treatment, which includes correlated dynamics of the trapped atom and the lattice are necessary for the interpretation of the dynamics of atomic thermal mobilities. Such models are now being developed, taking

into account the dynamic distribution of barrier heights, which can be rather broad in compressible solids. The studies in solid Kr should greatly help in the elucidation of these considerations. We expect these studies will lead to develop a realistic model for thermal atomic mobilities as a function of pressure. As far as practical considerations are concerned, we note that at 130 kbar, we have been able to stabilize F atoms in our system for several minutes at a temperature of 230 K -- an order of magnitude increase in recombination temperature!

Emission spectra showing the D \rightarrow X and D \rightarrow A emissions are illustrated in figure 3. The spectra are partially obscured in the 430 nm region due to fluorescence of the diamond windows. The D \rightarrow X emission clearly broadens and undergoes a red shift of over 1 eV in this range of pressures. In figure 4 we summarize the observed spectral shift data for all transitions: D \rightarrow X, D \rightarrow A, B \rightarrow X, and C \rightarrow A. Note that at pressures above 60 kbar, the B and C state emissions disappear. In fact prior to this disappearance, strong mixing between states is observed as evidenced by domination of the spectrum by the C \rightarrow X transition. This could be possible by environment induced spin-orbit mixing between the nested ionic potentials. The drop in emission quantum yields from the B/C states, would imply a strong mixing between the ionic and covalent states as well. In effect, by lowering the ionic potentials, a crossing between the covalent A, and ionic B/C states is created which at 60 kbar already leads to efficient predissociation. This is the very effect sought in these studies, and rather encouraging to note that the onset to ionic/covalent crossing occurs at such relatively low pressures. Spectral analyses also indicates that the difference between potential minima of the ionic and covalent X states is reduced as a function of pressure. This would also signify stabilization of the ionic potentials at high pressure. These effects are expected to be even more dramatic in solid Kr, due to the higher polarizability and compressibility. At present, experiments are in progress in a XeF₂/Xe solids, in which we expect to form ionic crystallites generated by a novel photo-induced phase transition.

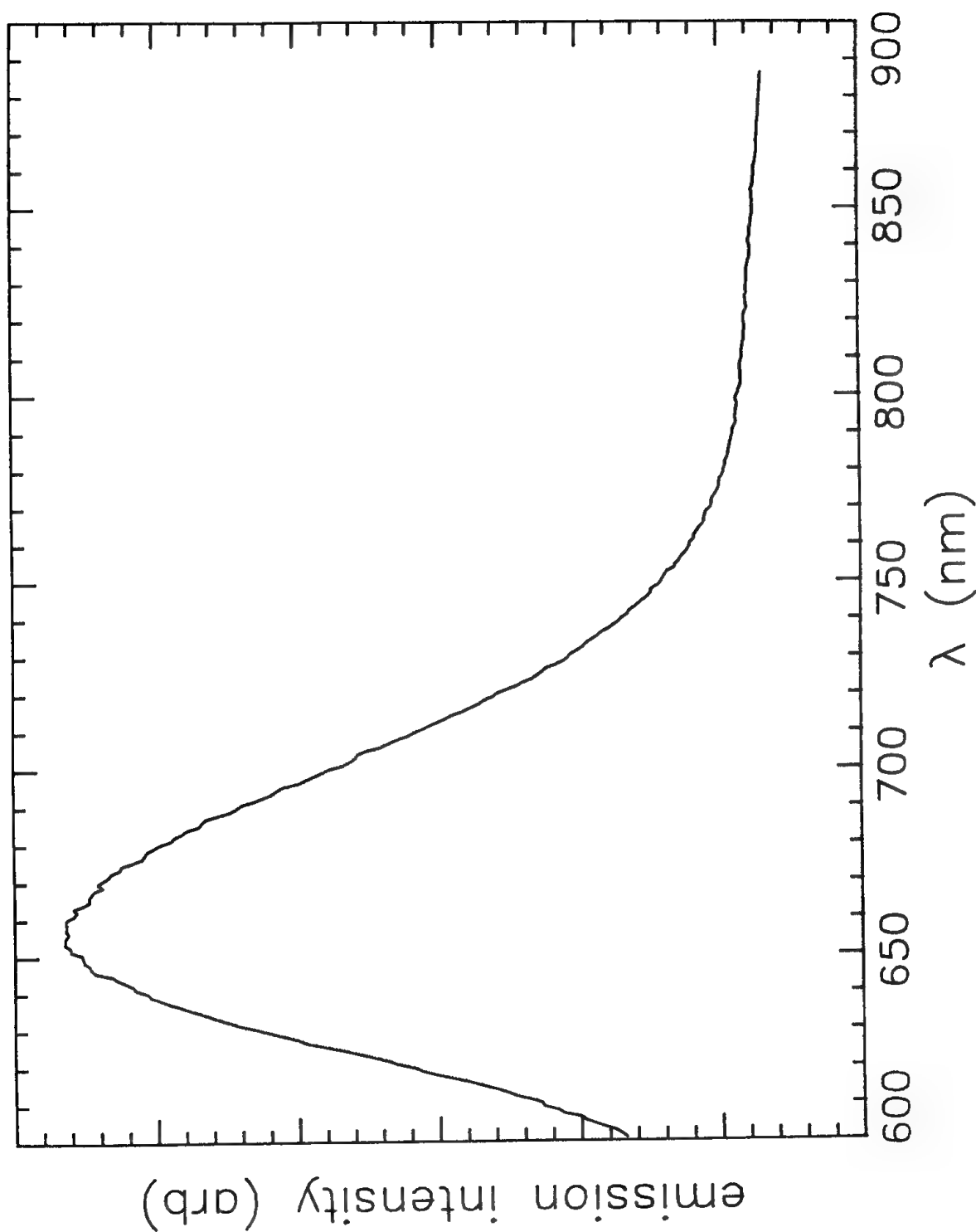
References:

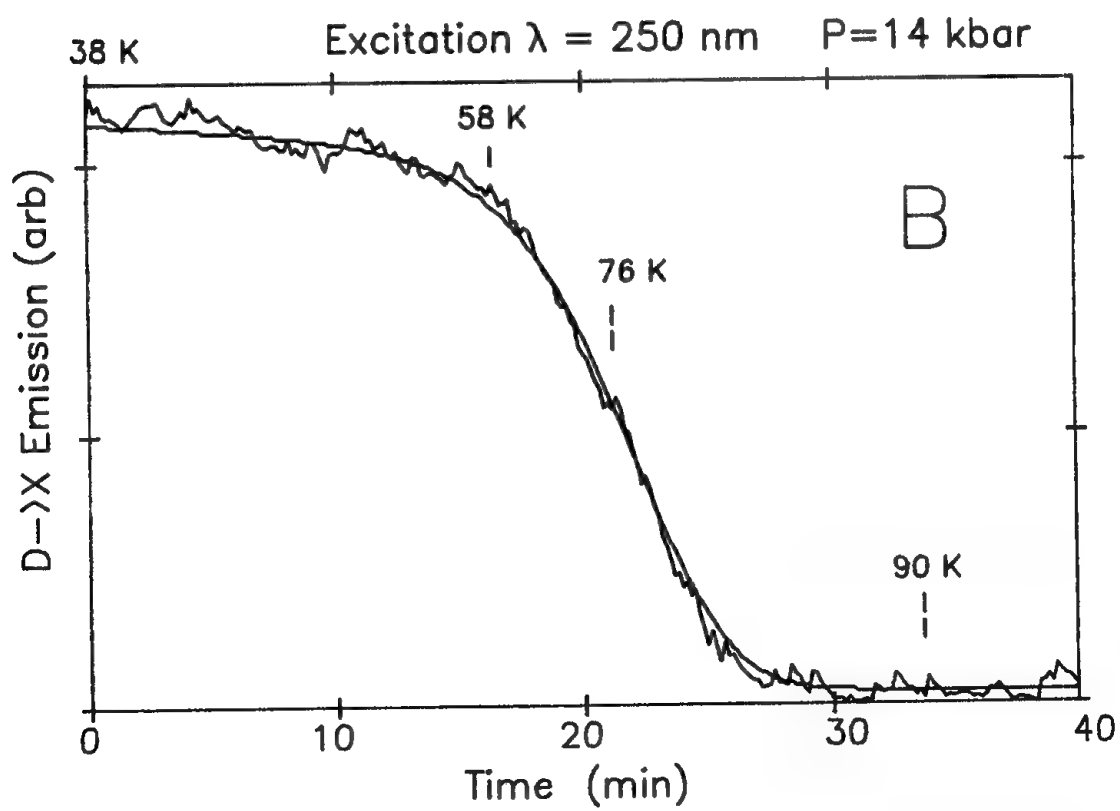
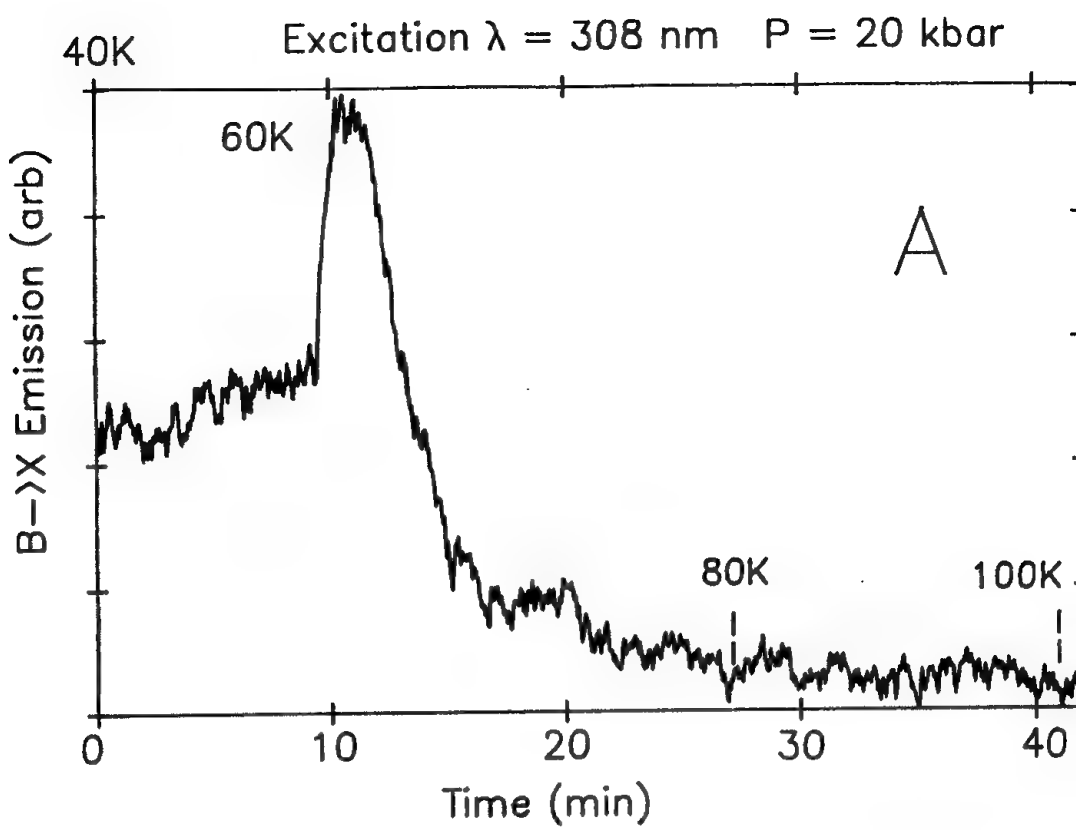
- 1 A. I. Katz and V. A. Apkarian, J. Phys. Chem. 94, 6671(1990).

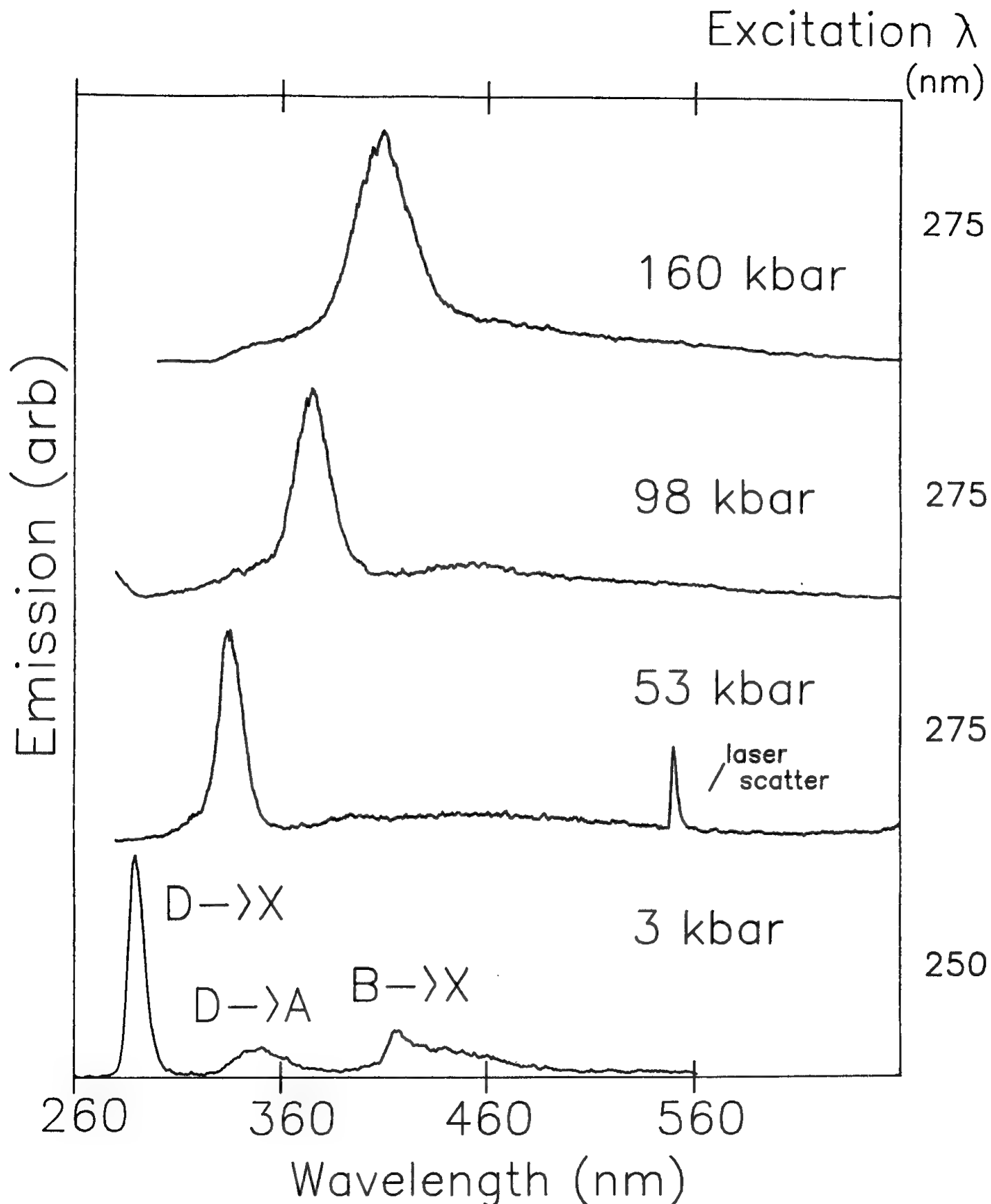
- 2 V. A. Apkarian, "Photogeneration and Storage of Atomic
Radicals in Van der Waals Solids", in the Proceedings of HEDM
conference, (Long Beach, 1990.)
- 3 R. Alimi, R. B. Gerber, and V. A. Apkarian, (to be published).
- 4 a) N. Schwentner and V. A. Apkarian, Chem. Phys. Lett., 154,
413(1989).
b) H. Kunttu, J. Feld, R. Alimi, A. Becker, and V. A. Apkarian, J.
Chem. Phys. 92, 4856(1989).
- 5 a) R. Alimi, R. B. Gerber, and V. A. Apkarian, J. Chem. Phys., 92,
3551(1990).
b) R. Alimi, R. B. Gerber, and V. A. Apkarian, Phys. Rev. Lett. (in
press).
- 6 a) J. Feld, H. Kunttu and V. A. Apkarian, J. Chem. Phys., 93,
1009(1990).
b) H. Kunttu and V. A. Apkarian, J. Chem. Phys. (in press).
- 7 H. Helm, D. L. Huestis, M. J. Dyer, and D. C. Lorents, J. Chem.
Phys., 79, 3220(1983); J. F. Bott, R. F. Heidner, J. S. Holloway,
and J. B. Koffend, Chem. Phys. 148, 411(1990).
- 8 K. M. Monahan, V. O. Jones, and V. Rehn, J. Chem. Phys., 71,
2360(1979).

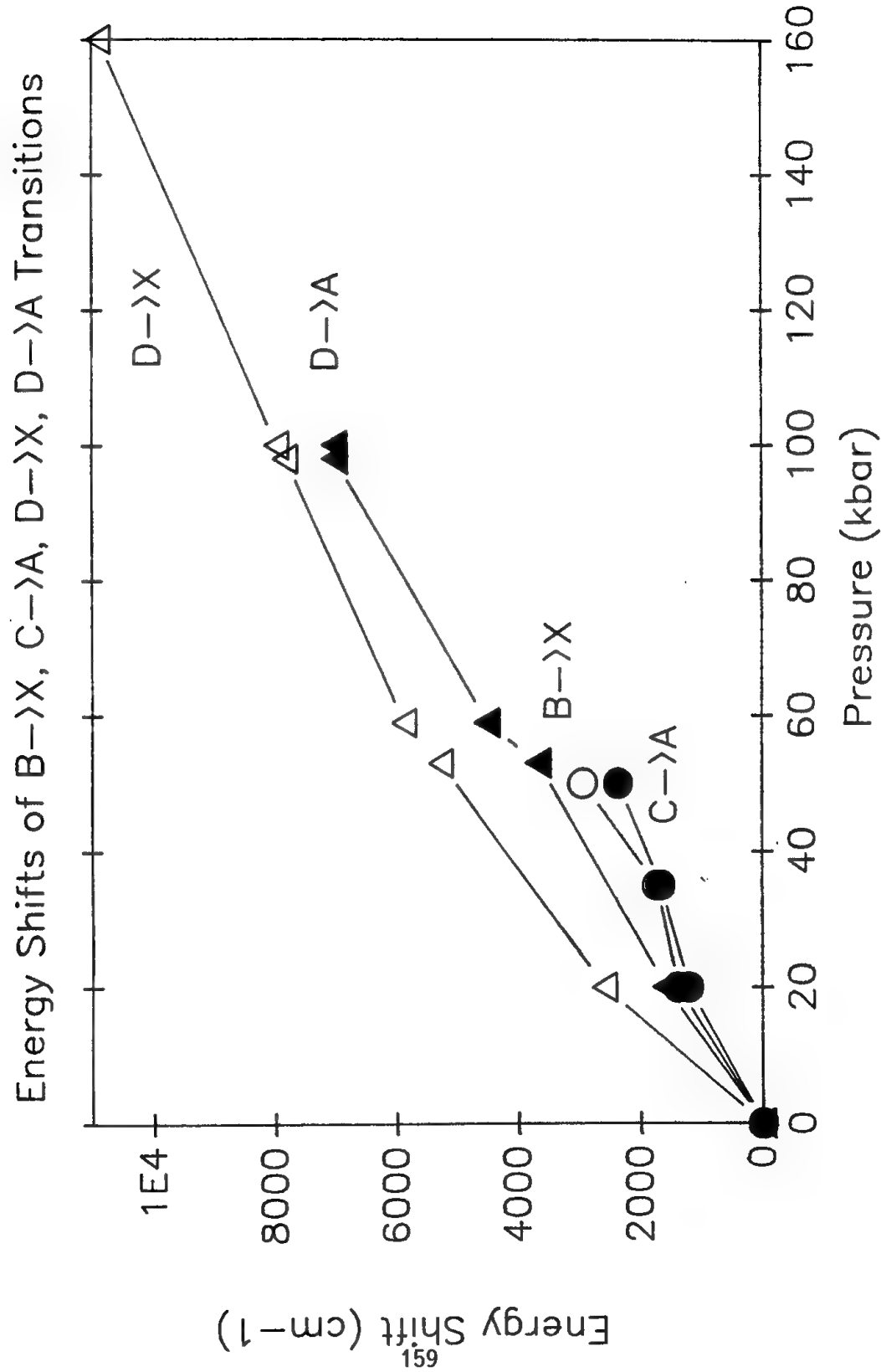
Figure Captions:

- 1 Xe₂Cl emission in from 1:250 Cl:Xe sample, at room
temperature and 56 kbar, two years after initial storage. There
is no evidence for Cl₂ emission, i.e. no evidence for
recombination.
- 2 Emission of XeF during warm-up of a sample at 20 kbar. a)
shows an initial increase due to diffusion controlled trapping of
F atoms at Xe sites, and subsequent decay. b) shows the warm-
up cycle fitted to first order kinetics. Time is indicated on the
ordinate, temperatures are annotated on the curves. The
temperature ramp is nearly linear in time.
- 3 Emission spectra of XeF in solid Ar, as a function of pressure.
- 4 Spectral red-shifts of the different XeF emissions as a function
of pressure. Emission from B and C states disappears above 60
kbar.







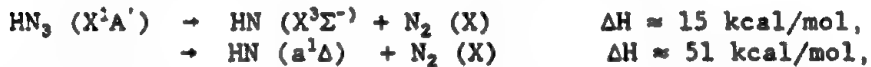


PHOTODISSOCIATION OF HN₃ AND (NO)₂

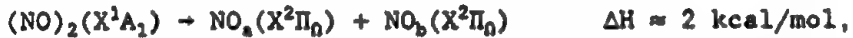
M.P. Casassa, B.R. Foy, J.R. Hetzler, D.S. King, and J.C. Stephenson
National Institute of Standards and Technology
Molecular Physics Division
Gaithersburg, Md 20899

State-to-state studies of the unimolecular decomposition of energetic molecules from their ground electronic states are enabled by direct excitation of metastable vibrational levels. Measurements of the photodissociation spectra, product state distributions, and lifetimes provide information on the energies and topologies of potential energy surfaces which are key to bonding and stability in energetic molecules.

We have studied the decomposition reactions



by direct pumping of 12 different NH stretching overtone and combination states in the range $5\nu_{\text{NH}}$ (1512cm^{-1}) to $7\nu_{\text{NH}}$ (20070cm^{-1}).¹ We have also studied the decomposition reaction



by excitation of the NO symmetric (ν_1) and antisymmetric (ν_5) fundamentals, and the v=2 overtone and combination states.² The nascent NH($\text{X}^3\Sigma^-$), NH($\text{a}^1\Delta$) or NO fragments were detected by laser-induced fluorescence (LIF). The experiments were performed with molecules cooled to 3 to 8K in a free-jet expansion, simplifying the photodissociation spectra, and precluding intermolecular interactions which perturb nascent product state distributions. Picosecond and nanosecond laser systems were used to measure photodissociation rates in real time. High-resolution nanosecond lasers were used to measure detailed product state distributions and the photodissociation spectra. Together these measurements provide an unusually comprehensive view of the unimolecular dissociation processes.

In this report we emphasize measurements of correlations among the fragment states produced in these decompositions, and implications for the potential energy surfaces. These include correlations among the vector and scalar quantities which specify the state of a given fragment, and correlations among geminate fragment states. In particular we present results for the decomposition of HN₃, $7\nu_{\text{NH}}$, and $(\text{NO})_2$, $\nu_1+\nu_5$ (3626cm^{-1}).

HN₃, $7\nu_{\text{NH}}$

Dissociation of HN₃ from the $7\nu_{\text{NH}}$ level produces exclusively NH($\text{a}^1\Delta, v=0$). Only the lowest rotational states of NH($\text{a}^1\Delta$) are populated, giving an average fragment rotational energy $\langle E_R(\text{NH}) \rangle \approx 220\text{cm}^{-1}$. A-doublet propensities, which reflect the organization of electronic structure upon dissociation, are found to depend upon J_{NH} . The ratio of populations, $\Delta(\text{A}')/\Delta(\text{A}'')$ ranges from 1 to 4 for $J_{\text{NH}} = 2$ to 7. Figure 1 shows fragment Doppler profiles measured in two pump-

probe geometries. The difference in the appearance of these profiles is mainly due to a significant recoil anisotropy (i.e. the μ - v vector correlation). Note also the propensity to form the $\Delta(A')$ Λ -doublet.

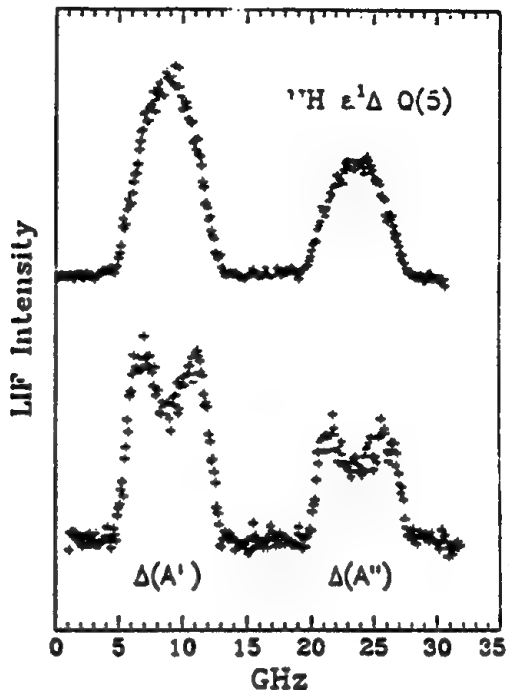


Figure 1. $\text{NH}(a^1\Delta)$ Doppler profiles following $7\nu_{\text{NH}}$ excitation. In the upper trace the pump polarization vector and the probe Poynting vector are perpendicular. They are parallel in the lower trace.

Profiles like those shown in figure 1 were measured for several NH lines in various pump-probe geometries. Weighted sums of these profiles were used to construct hybrid profiles which accentuate certain vector correlations in the NH fragment. These in turn were fitted with a Doppler profile of the form,

$$g(\nu) = \frac{1}{2\Delta\nu} (1 + B_{\text{eff}} P_2((\nu - \nu_0)/\Delta\nu)),$$

(which corresponds to a δ -function speed distribution centered at $v - c\Delta\nu/\nu_0$ and a transition with rest frequency ν_0) convoluted with a fragment kinetic energy distribution function.

One parameter determined in this analysis is the recoil anisotropy, $B_{\mu\nu}=0.31\pm0.03$. The positive value indicates fragments are scattered preferentially in directions parallel to the near-linear NNN backbone (i.e., the a -axis). For HN_3 , $7\nu_1$, the recoil anisotropy is not influenced by the dissociation lifetime. It is instead determined by the spatial form of the excited rotational wavefunction, and by the distribution of body-fixed recoil angles. Taking the former effect into account, we find that the average body-fixed recoil angle is $23\pm7^\circ$, measured from the a -axis.

Figure 2 shows hybrid profiles with only the v - J anisotropy (B_{vJ} , left panel), and with all anisotropy removed ($B_{\text{eff}}=0$, right panel). The difference in P and Q lines is due to a significant positive v - J correlation. The positive value B_{vJ} obtained (0.17 ± 0.06) indicates that J is tilted slightly toward v ($\theta_{vJ}=48^\circ$), corresponding to helicopter-like motion about v , and as a result also about the a -axis. The sloping wings of the $B_{\text{eff}}=0$ profile (Fig. 2, right) are

a consequence of the correlated N₂ cofragment rotational state distribution (a narrow distribution would give a square shaped profile). The essential form of this distribution was extracted from the Doppler in the fitting procedure. The result indicates that the J(N₂) distribution is peaked at high J, with J(N₂) \geq 20.

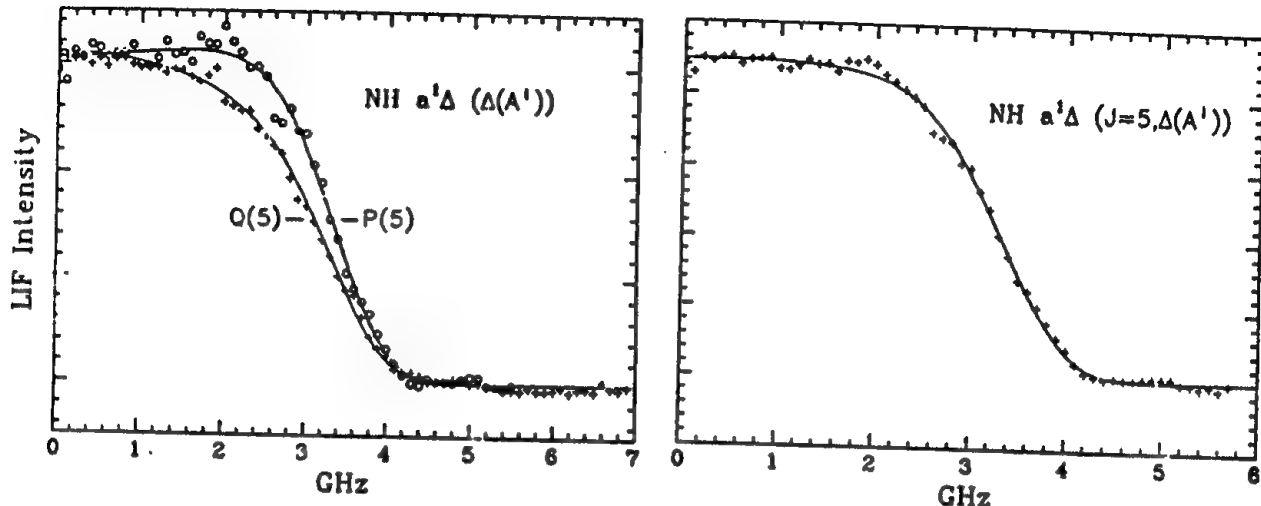


Figure 2. NH(a¹Δ) hybrid Doppler profiles following 7ν_{NH} excitation, showing the v-J anisotropy (left), and with all anisotropy removed (right).

These results can be compared with expectations based on ab initio potential energy surfaces.³ The J_{NH}-dependent A-doublet propensities are quantitatively reproduced by a quantum mechanical calculation which projected the transition state bending and torsional vibronic wavefunctions onto the vibronic coordinates of the fragments. The disparate N₂ and NH rotational state distributions are qualitatively explained by a classical model which transforms vibrational motion in the transition state, as determined in ab initio calculations, into fragment rotational motion.

(NO)₂ ν₁+ν₅

The NO dimer is of special interest because the ²Π configurations of the fragments give rise to 16 electronic surfaces as they are brought together to form (NO)₂. Certain of these surfaces are thought to be important for the collisional quenching of NO(v=1), which has unusually large cross sections. Dramatic mode specificity observed for decomposition of (NO)₂ excited in the ν₁ and ν₅ fundamentals has also been attributed to nonadiabatic transitions among these surfaces. Little is known about the positions of these surfaces, and there has been no determination of which excited electronic surfaces (if any) are actually involved. We used the techniques developed to study HN₃, as described above, to gain some insight into the role of excited electronic surfaces in the decomposition of (NO)₂.

Figure 3 shows the (NO)₂ ν₁+ν₅ photodissociation spectrum obtained in a molecular beam, along with a fit using the known ground state constants. In addition to giving the excited state constants, this spectrum proves that the

photolysis signals we observe arise from the dimer.

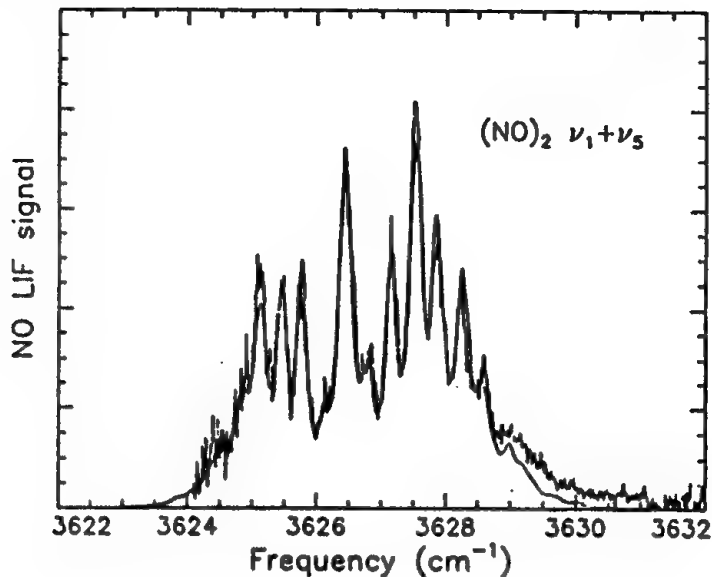


Figure 3. $(NO)_2 \nu_1 + \nu_5$ photodissociation spectrum.

Product state measurements show that essentially all of the dissociations produce the correlated vibrational products $(v_a=1)+(v_b=0)$. This $\Delta v=1$ propensity is consistent with energy gap laws developed for other vibrational energy transfer processes. The remaining available energy ($\approx 1000\text{cm}^{-1}$) is partitioned as follows into the fragment translational, rotational, and spin-orbit degrees of freedom: $f_{\text{trans}}=.87$, $f_{\text{rot}}=.03$, $f_{\text{so}}=.10$. These results give an improved value for the bond energy, $D_0=710\pm 40\text{cm}^{-1}$.

The minimal energy appearing as rotation in the fragments must be mainly due to zero-point motion in the parent molecule. A transition state vibration-to-rotation model, similar to that mentioned for HN_3 , qualitatively reproduces the observed rotational distributions. Because the bending and torsional motions in $(NO)_2$ are of comparable frequency, their transformation into rotations should not give rise to a pronounced v - J correlation, or to a particular Λ -doublet propensity. In fact, we observe $B_{vJ}=0$ for the NO fragments, and equal population in the Λ -doublets.

Unlike the HN_3 experiments, the NO internal state distributions are too narrow to affect the wings of the NO Doppler profiles observed with 0.2GHz resolution. Still, product state correlations are revealed in the widths of the profiles, given by Δv . Determinations of the maximum Doppler shift, Δv , as a function of quantum state are collected in Figure 4. When plotted vs J , the shifts lie on the same straight line. From the slope of this line, one can show that the cofragment rotations, J_a and J_b , are uncorrelated, i.e., each J_a has a cofragment distribution $P(J_b)$ given by the rotational state distribution measurements.

In contrast, figure 4 shows that cofragment spin-orbit states are highly correlated. We distinguish between four channels: $(\Omega_a, \Omega_b) = (1/2, 1/2)$,

(1/2,3/2), (3/2,1/2), and (3/2,3/2). The Ω -3/2 state carries 123cm^{-1} as internal energy, so channels involving this fragment give smaller Doppler shifts than Ω -1/2 channels. The solid line in Fig. 4 is a linear fit to the shifts measured for Ω -1/2 fragments. If the (1/2,3/2) channels operate exclusively, the Ω -3/2 points should fall on the same line, and they appear to do so. The other lines in the figure represent other limiting correlations which clearly don't reproduce the data as well as the (1/2,3/2) correlation. Modelling the data of figure 4, together with measured spin-orbit populations, shows that about 75% of the decompositions occur via the (1/2,3/2) channel, and 20% occur via the (1/2,1/2) channel. Less than 5% occurs via the (3/2,3/2) channel.

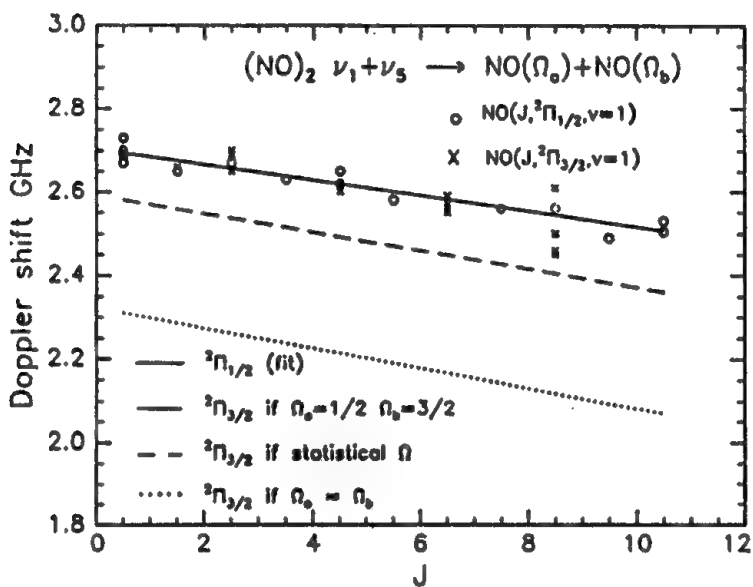


Figure 4. NO fragment Doppler shifts following $(\text{NO})_2 \nu_1 + \nu_5$ dissociation.

The spin-orbit results prove that a nonadiabatic transition occurs at some point during the dissociation. The dimer $^1\text{A}_1$ ground state correlates adiabatically to (1/2,1/2), which is evidently not the major channel for decomposition from $\nu_1+\nu_5$. Correlation diagrams drawn using the non-crossing rule to connect the separated fragment states to dimer states determined in ab initio calculations⁴ indicate that spin-orbit coupling can induce transitions from the (1/2,1/2) to (1/2,3/2) surfaces.

1. B.R. Foy, M.P. Casassa, J.C. Stephenson and D.S. King, *J. Chem. Phys.* 89, 608 (1988); 90, 7073 (1989); 92, 2782 (1990); M.P. Casassa, B.R. Foy, J.C. Stephenson and D.S. King, *J. Chem. Phys.* 94, 250 (1991).
2. M.P. Casassa, J.C. Stephenson and D.S. King, *J. Chem. Phys.* 89, 1966 (1988); J.R. Hetzler, M.P. Casassa and D.S. King, to be published.
3. M.H. Alexander, H.J. Werner, and P.J. Dagdigian, *J. Chem. Phys.* 89, 1388 (1988); M.H. Alexander, T. Hemmer, H.J. Werner and P.J. Knowles, *J. Chem. Phys.* 93, 3307 (1990) M.H. Alexander, P.J. Dagdigian and H.J. Werner, *Faraday Discuss. Chem. Soc.*, in press.
4. T.K. Ha, *Theor. Chim. Acta* 58, 125 (1981).

TRAPPED ATOMS IN CRYOGENIC MATRICES--CORRELATIONS BETWEEN TRAPPING SITES AND MCD SPECTRA

John W. Kenney, III
Department of Physical Sciences--Chemistry
Eastern New Mexico University
Portales, New Mexico 88130

Rocket performance can be boosted significantly by trapping reactive, low mass metal atoms in cryogenically cooled rocket fuels. This promise of enhanced performance underscores a need to understand more fully the nature of the interactions between the trapped metal atoms and the host cryogenic fuel matrices. Recent advances in using the technique of metal laser ablation (1,2) to prepare high concentrations of metal atoms in unusual tight matrix trapping sites need to be followed up with careful experimental studies of these sites. Magnetic Circular Dichroism (MCD) spectroscopy, particularly when used in conjunction with UV-visible absorption spectroscopy, provides unique and otherwise inaccessible insights into how an absorbing chromophore (e.g., a reactive alkali metal atom) is perturbed when it is trapped in a cryogenic matrix environment (3,4).

Many matrix isolated alkali metal atoms exhibit fine structure in their absorption and MCD spectra. Typically the single sharp gas phase absorption line is broken up into three closely spaced peaks near the atomic transition, the red "triplet", and three other closely spaced peaks blue shifted from the atomic transition, the blue triplet. One of the key results to emerge from the recent MCD studies using Knudsen generated alkali metals (3,4) and absorption studies based upon laser ablated alkali metals (1,2) is the clear realization that many of the observed spectra arise from metal atoms trapped in multiple sites. For example, matrices prepared from Knudsen oven generated Li atoms and lighter Rg hosts exhibit predominantly red sites (multiple Rg vacancy sites) with a lesser percentage of Li atoms in blue sites (single Rg vacancy sites); laser ablated Li sites are predominantly blue sites in the same lighter Rg matrices (1). The Xe host is a special case since Li and Xe atomic radii are approximately equal. Annealing of Li/Xe matrices can produce single vacancy "blue" sites whose triplet absorption spectra are not significantly blue shifted from the atomic Li transition (3,4). In the Li/Rg systems, MCD data analysis and MCD based theoretical interpretations--to date limited to Knudsen oven generated Li --have therefore been restricted to only the blue sites of Xe matrices. MCD spectroscopy of matrices prepared from laser ablated metal atoms promises to open up a number of new--and essentially unambiguous--metal atom/blue Rg trapping site combinations to the powerful theoretical formalism of MCD theory.

The origin of the triplet structure as well as the underlying reasons for the observations of both blue and red triplets in M/Rg matrices continue to be lively areas of experimental focus and theoretical debate. A number of experimentally challenging and theoretically sophisticated MCD and absorption studies by Schatz, O'Brien and co-workers (3,4) strongly suggest a spin-orbit/Jahn-Teller interpretation of these phenomena but the question is by no means fully resolved since the spin-orbit/Jahn-Teller models invariably assume that the matrix isolated metal atom is trapped in a single substitutional site. Although this appears to be the case for the blue triplet of Li/Xe, it is not generally true for the red triplet in any Rg matrix other than Xe (1-4). Another potential problem with the Schatz-O'Brien model is that the excited state spin orbit coupling constant derived from the model as applied to Li/Rg MCD data is several orders of magnitude larger than the free atom value. Can the interaction of closed shell Rg atoms with the Li 2p electron reasonably be expected to produce such a large shift? Since laser ablation provides a way to selectively access blue sites in high concentration and to prepare metals exclusively in blue sites in those matrices where blue trapping sites have not been observed previously, this technique needs to be applied as a starting point for MCD analysis. ^{6}Li vs. ^{7}Li isotopic substitution provides a way to test the Jahn-Teller interpretation. If the Schatz-O'Brien Jahn-Teller component of the model is valid, metal-lattice phonon modes should shift in energy with the ~8 % reduced mass change. This should give

rise to a measurable change in the MCD spectra of $^6\text{Li}/\text{Rg}$ vs. $^7\text{Li}/\text{Rg}$ matrices. Moreover, if the spin orbit aspects of the Schatz-O'Brien model are valid we would predict that the large excited state spin orbit coupling constant calculated for Li/Xe will diminish in Li/Kr and Li/Ar. Here the ability of the laser ablation technique to produce blue triplet sites in the lighter Li/Rg matrices will be crucial for testing this aspect of the Schatz-O'Brien model. Interestingly enough, the extant MCD theory can accommodate a multiple host vacancy trapping site model of red triplet sites suggested by laser ablation absorption data (1-4).

In summary, the combination MCD spectroscopy with the laser ablation technique for preparing matrix isolated metal atoms promises to shed significant new insights into the problem of understanding metal--matrix interactions. Metal/Rg matrices prepared by laser ablation are the proper and indeed often the only reasonable experimental starting point for testing models of M/Rg interactions. The recent report by Fajardo of the trapping of laser ablated Li in Ne and H₂ matrices provides further impetus for doing follow up MCD studies to elucidate the nature of the trapping in these systems (2).

1. Fajardo, M. E.; Carrick, P. G.; Kenney, J. W., III, Matrix Isolation Spectroscopy of Metal Atoms Generated by Laser Ablation: the Li/Ar, Li/Kr, and Li/Xe Systems, *J. Chem. Phys.* accepted for publication.
2. Fajardo, M. E., Metal Atoms in Solid Rare Gases, AFOSR-HEDM Conference Proceedings, Albuquerque, NM , 1991.
3. Rose, J; Smith, D.; Williamson, B. E.; Schatz, P. N.; O'Brien, M. C. M., Magnetic Circular Dichroism and the Jahn-Teller Effect in the $^2\text{S} \rightarrow ^2\text{P}$ Transition of Sodium and Lithium Atoms Isolated in Xenon Matrices, *J. Phys. Chem.* 1986, 90, 2608-2615.
4. Lund, P. A.; Smith, D.; Jacobs, S. M.; Schatz, P. N., Magnetic Circular Dichroism Study of the $^2\text{S} \rightarrow ^2\text{P}$ Transition of Lithium Atoms in Noble Gas Matrices, *J. Phys. Chem.* 1984, 88, 31-42.

Theoretical Study of HEDM Materials: a-N₂O₂ and LiNe

Extended Abstract: 1991 Air Force HEDM Contractors Meeting

Byron H. Lengsfeld III

Theoretical Atomic and Molecular Physics Group / L-446
Lawrence Livermore National Laboratory
Livermore, CA 94550

Multireference configuration interaction (MRCI) studies of the heat of dissociation and stability of a-N₂O₂ have been undertaken. The results of these studies will be reported and compared to earlier coupled-cluster and single reference CI calculations. Preliminary MRCI studies of a-N₂O₂ indicated that a low-lying non-azide isomer might exist and give rise to a low-energy dissociation channel not previously investigated.

The Li-Ne interaction potential has been determined as part of an effort to model the spectroscopy of Li in rare gas matrices and ultimately Li in H₂. The addition of metals to H₂ is a common means of increasing the specific impulse of certain classes of propellants and efforts are underway to develop diagnostics for these systems. In this study, the Interacting Correlated Fragments method was used to obtain the interaction potential. The polarizability of Li and Ne must be accurately described in order to a reliable interaction potential for this system. A polarized-orbital-ltransformation was used to obtain a compact Gaussian basis set capable of producing accurate polarizabilities. A figure which summarizes this technique is included in this abstract.

Ne-Li Potential

The addition of Li and other metals to H₂ has been shown to increase the specific impulse obtained from a broad class of fuels which employ liquid H₂. The spectroscopy of Li and other metal atoms in H₂ is of interest as a diagnostic that can be used to characterize this class of fuels. In order to develop an understanding of this spectroscopy, studies of simpler systems, such Ne-Li, have been undertaken. In order to model this system an accurate Ne-Li potential energy curve is needed. To date, the well depth but not the equilibrium internuclear separation of the ²Π state has been determined experimentally (Balling, Wright and Havey, Phys Rev A 26,1426(1982)).

Ab Initio calculations, using the Interacting Correlated Fragments (ICF) method of Liu and Mclean (JCP 72,3418(1980); JCP 91,2348(1989)), have been used to obtain the ²Σ⁺ and ²Π potential energy curves. Earlier studies by Mclean et al. on Ar₂ (JCP 89,6339(1988)) have indicated that approximations are needed to study systems as large as Ne-Li. Natural Orbital truncation and a Polarized-Orbital-Transformation have been used to reduce the size of the CI expansions employed in the ICF calculations. A Polarized-Orbital-Transformation produces a small set of virtual orbitals which are optimized for a molecular property, in this case polarizability. A figure which summarizes the arguments used to obtain this transformation has been appended to this abstract.

First order interaction potentials have been computed and compare well with the experimental well depth. Orbital truncation was not needed in these calculations. Orbital truncation schemes are currently being investigated at this level of theory so that a manageable second order calculation can be undertaken.

THEORETICAL STUDIES OF N₂O₂

Theoretical studies of N₂O₂ were conducted at both the multiconfiguration-self-consistent-field (MCSCF) and the multi-reference configuration interaction (MRCI) level. These studies employed a DZP quality basis set. Earlier studies, which were undertaken with SCF and single-reference CI methods, indicated that the barrier to dissociation to N₂ + O₂ was on the order of 15 kcals/mole. This reaction was first studied at the MCSCF level of theory. The initial MCSCF orbitals were obtained from the natural orbitals of a single-reference CI conducted at a molecular geometry in which the N-O bond was stretched to about twice the equilibrium value. The natural orbital occupation numbers indicated that a 4in4 Complete-Active-Space (CAS) wavefunction was needed to study the MCSCF dissociation of this molecule. The equilibrium and transition state structures were then located with analytic gradient techniques. At this level, the barrier was found to be 2.5 kcals/mole. This calculation was then repeated with second-order CI wavefunctions based on these 4in4 CAS calculations. In order to make these calculations more manageable, the high-lying virtual orbitals were excluded in the second-order CI calculations. The structures were reoptimized with these larger wavefunctions. These more accurate calculations indicated that the dissociation barrier was 1 kcals/mole. These calculations produced a non-azide equilibrium structure (a bent N-N-O bond) and additional calculations are being undertaken to determine the relative energy of the azide and non-azide structures at this level of theory.

Dissociation barriers of this size would indicate that this molecule would not be long-lived. If the equilibrium structure is indeed bent, then one would conclude that the uncertainties associated with the DZP basis and the truncation of the virtual orbitals (errors on the order of 7 kcals/mole) are not large enough to alter this conclusion. This molecule might be synthesized and stored in a solid-state matrix but these calculations indicate that the gas-phase lifetime of this molecule would be small.

Figure 1.

Polarized Virtual Orbitals

Use Perturbation Theory to Truncate the Virtual Orbitals Used in the Configuration Interaction Calculation (ICF Calculation)

Coupled-Perturbed-Hartree-Fock (CPHF) Theory Produces the Response of Each Occupied Orbital to an External Field

Independent Orbital Approximation to CPHF Theory - Use Perturbation Theory and IVO Virtual Orbitals to Generate Polarized Virtual Orbitals

$$\phi_1 = \sum_i^{\text{virtuals}} \frac{\langle \phi_i | \mu | \phi_0 \rangle}{\epsilon_i - \epsilon_0}$$

μ = dipole operator, ϕ_i = IVO orbital , ϕ_0 = HF orbital
 ϵ_i = IVO eigenvalue and ϵ_0 = HF eignevalue

or Diagonalize a PVO Operator

$$\rho_{ij} = \frac{\langle \phi_i | \mu | \phi_0 \rangle \langle \phi_0 | \mu | \phi_j \rangle}{(\epsilon_i - \epsilon_0) (\epsilon_j - \epsilon_0)}$$

Example: Singles CI For CH₄ Polarizability

17.85 PVO

17.98 Full Virtual Space

17.50 Experiment

FUNCTIONALIZED PENTACYCLO[5.4.0.0^{2,6}.0^{3,10}.0^{5,9}]UNDECANES (NON-PHOTOCHEMICALLY)

**Suresh Chander Suri* and Ngo Q. Vu
University of Dayton Research Institute
c/o Philips Laboratory-Propulsion Directorate
Edwards Air Force Base, CA 93523 U.S.A.**

Summary: Substituted pentacyclo[5.4.0.0^{2,6}.0^{3,10}.0^{5,9}]undecanes are synthesized non-photochemically via samarium(II) iodide promoted intramolecular ketone-olefine reductive coupling.

INTRODUCTION:

For the last decade, attention has been focused upon potential military applications of cage molecules because of their inherent high strain energy and compact structure. The strain energy content is released upon combustion. The compactness provides maximum net volumetric heat of combustion. Accordingly, such compounds are of interest as a potential high density/high energy fuels.

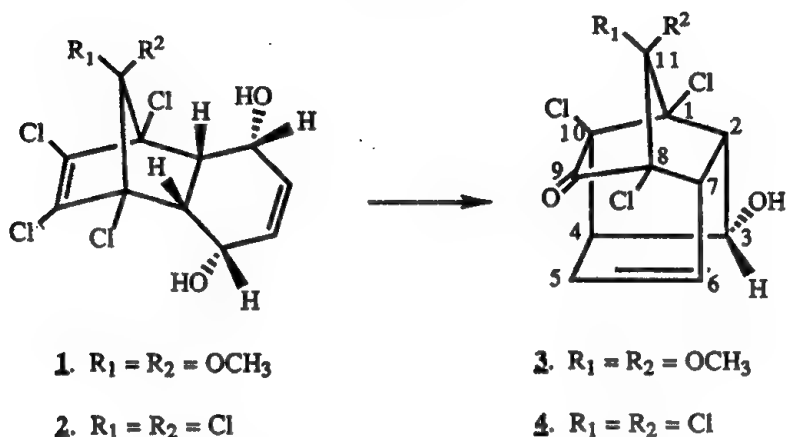
In recent years, substituted pentacyclo[5.4.0.0^{2,6}.0^{3,10}.0^{5,9}]undecanes (PCUD) have been extensively explored as intermediates in the synthesis of polycyclic cage molecules and naturally occurring cis-syn-cis fused linear triquinanes¹. Cookson and co-workers² first synthesized the carbon frame of functionalized PCUD by Diels-Alder reaction of cyclopentadiene and benzoquinone followed by intramolecular [2+2] photocyclization of the resulting endo-cycloadduct. Since then, this methodology has been used for the synthesis of functionalized PCUD by employing substituted cyclopentadiene and/or substituted benzoquinones. In this preliminary communication, we report a non-photochemical synthesis of functionalized PCUD via intramolecular ketone-olefine reductive coupling reaction using an efficient one electron system, SmI₂-THF.

BASE-PROMOTED ELIMINATIVE CYCLIZATION:

It has been established that when 1,8,9,10-tetrachloro-3 α ,6 α -dihydroxy-11,11-dimethoxytricyclo[6.2.1.0^{2,7}]undec-4,9-diene³ (1) and 1,8,9,10,11,11-hexachloro-3 α ,6 α -dihydroxytricyclo[6.2.1.0^{2,7}]undec-4,9-diene³ (2) are treated with potassium-t-butoxide/t-

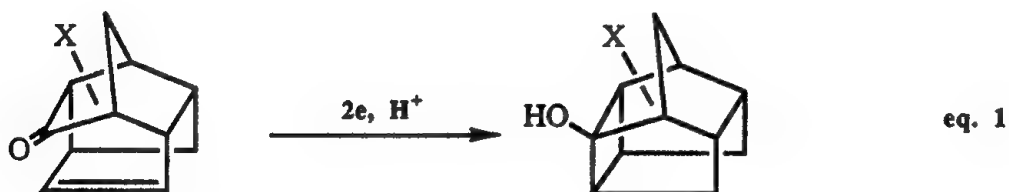
butanol, it furnishes 1,8,10-trichloro-11,11-dimethoxy-3 α -hydroxy-tetracyclo[6.2.1.0^{2,7}.0^{4,10}]undec-5-ene-9-one⁴ (3) and 1,8,10,11,11-pentachloro-3 α -hydroxytetracyclo[6.2.1.0^{2,7}.0^{4,10}]undec-5-ene-9-one⁵ (4) respectively (Scheme-1).

Scheme-1



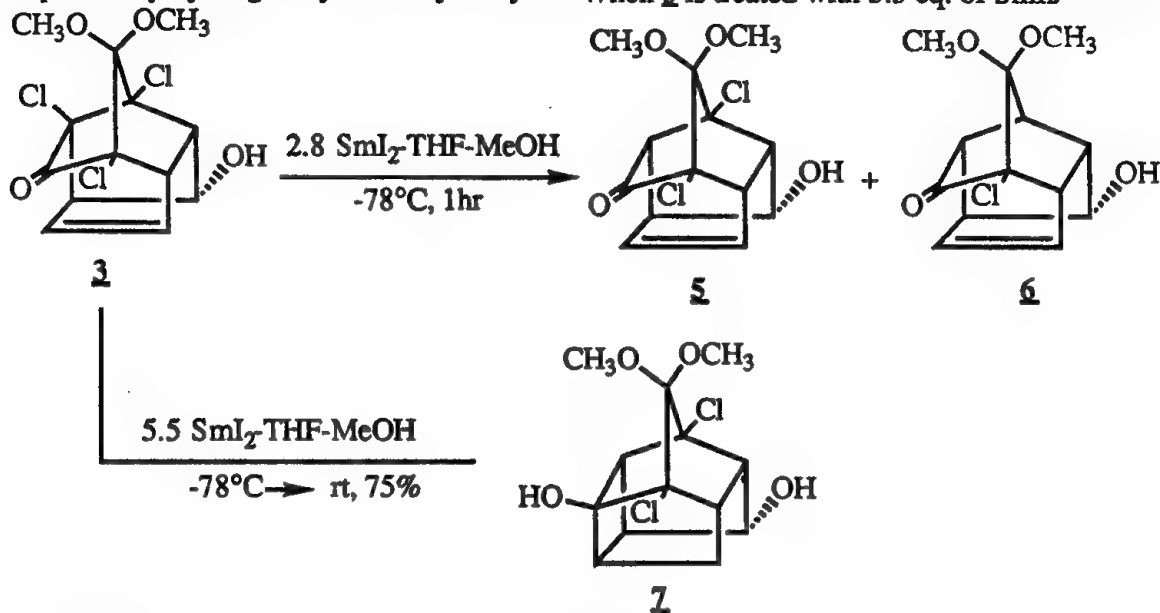
REDUCTIVE DEHALOGENATION AND INTRAMOLECULAR KETONE-OLEFINE REDUCTIVE CYCLIZATION:

The topology of **3** & **4** reflects close proximity of ketone and C-5 olefine π -bonds. It is envisaged that intramolecular ketone-olefine reductive coupling should lead to functionalized pentacyclo[5.4.0.0^{2,6}.0^{3,10}.0^{5,9}]undecanes (eq. 1). Many chemical methodologies⁶ have been reported to generate ketyls that are subsequently trapped by olefins. Samarium (II) iodide is one

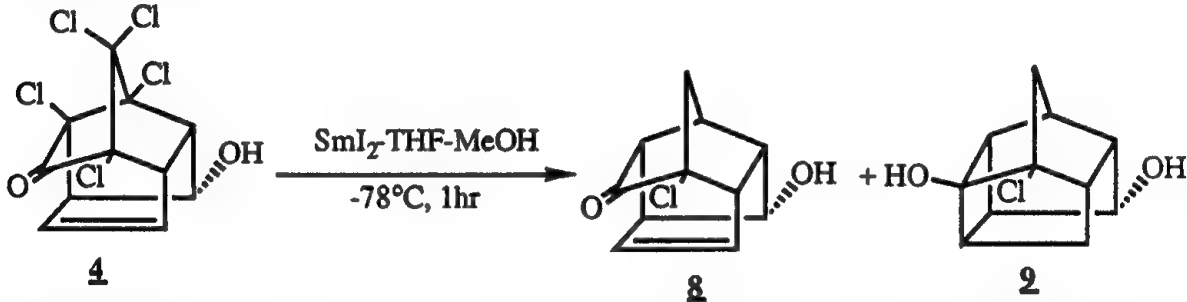


of the reagents which has gained wide popularity in various synthetic transformation in inter- as well as intramolecular fashion. Furthermore, under proper conditions Samarium (II) iodide provides a mild and convenient method⁷ for the reduction of organic halides and α -haloketones to the corresponding alkane and ketone.

Treatment of 3 with 2.5 eq. of Samarium (II) iodide at -75°C furnishes two products. At first glance their spectral data reveals that both products have the same carbon skelton as 3. The major compound (65%) is dichlorinated and is assigned structure 5 on the basis of its spectral data and elemental analysis. The mass spectrum and elemental analysis data of the minor compound (4%) shows the presence of only one chlorine. The structure, 6, for the minor compound is determined unequivocally by single-crystal x-ray analysis. When 3 is treated with 5.5 eq. of SmI₂ at -70°C,



it furnished functionalized PCUD 7 in 75% yield. In preliminary experiments, when 4 was treated with different quantities of Samarium (II) iodide, partial dechlorinated product 8 and



functionalized PCUD 9 are isolated. The experimental conditions are being optimized to isolate higher yield of functionalized PCUD.

CONCLUSION:

For the first time it has been demonstrated that functionalized pentacyclo[5.4.0.0^{2,6}.0^{3,10}.0^{5,9}]undecanes can be synthesized non-photochemically via Samarium (II) iodide promoted intramolecular ketone-olefine reductive coupling.

REFERENCES

1. Marchand, A. P., In Advances in Theoretically Interesting Molecules; Thummel, R. P., Ed., JAI: Greenwich, CT, 1989, Vol 1, 357-399
2. Cookson, R. C., Grundwell, E.; Hudec, J., J. Chem. Ind. (London) 1958, 1003.
3. Marchand, A. P., LaRoe, W. D., Sharma, G. V. M., Suri S. C., Reddy, D. S., J. Org. Chem. 1986, 51, 1622
4. Suri, S. C., Tetrahedron Lett., 1990, 31, 3695.
5. Suri, S. C. and Vu, N. Q., Unpublished results.
6. Pradhan, S. K., Kadam, S. R., Kolhe, J. N., Radhakrishnan, T. V., Sohani, S. V. and Thaker, J. Org. Chem., 1981, 46, 2622; Corey, E. J. and Pyne, S. G., Tetrahedron Lett., 1983, 24, 2821.
7. Girard, P., Namy, J. L., and Kegan, H. B., J. Am. Chem. Soc., 1980, 102, 2693; Molander, G. A., Hahn G., J. Org. Chem., 1986, 51, 1135.

Theoretical Studies of the Spectroscopy of Alkali Metal Atoms in Condensed Phases: Inert Gases and Hydrogen

Neil R. Kestner, Jia-an Yang, Nate Brener,
and Sumnesh Gupta

Departments of Chemistry, Physics
and Chemical Engineering
Louisiana State University
Baton Rouge, LA 70803

Extended Abstract

In order to study real materials, especially impurity states of various types, it is essential to be able to handle fairly complex systems but it is also essential to introduce temperature and disorder systematically. During the past few years a number of new interrelated techniques have been developed. We have applied the Fast Fourier Transform methods coupled to Molecular Dynamics to the case of alkali atoms in an inert gas fluid and have done preliminary work when molecular hydrogen is the medium.

In order to get the electronic absorption spectrum of a molecule or atom in some condensed phase, the Franck Condon Principle requires that we obtain the excitation energy for that molecule in all of the thermally accessible configurations of the medium, but in particular for all thermally accessible configurations of the solvent around the molecule since the effect of the medium is usually rather short range. If we could calculate this we would then have the inhomogeneously broadened line shape as the configurational average of the excitation energy for each of the possible configurations. We can use one of the standard statistical mechanical methods to find these configurations knowing the correct interactions between the molecules. But since the molecules are often not spherically symmetric we will need the complete coordinates of all molecules, not only the radial distribution function around the impurity. Furthermore the wave functions are drastically distorted by the medium. Since ab initio calculations are too time consuming, especially when excited states are needed we must use alternative methods. We need a fast way to obtain the electronic energy level and yet have the results be accurate for the weak interactions which take place between the many molecules. If these interactions were purely classical then one could treat the electronic part of the calculation separately and consistently. That procedure was first used by Rossky, Friesner, and Schnitter¹ on the hydrated electron, more formal procedures have been developed by Nitzan, Landman, and Barnett² as well as Car and Parinello³ for the general case. We need a method capable of yielding several excited states as well as the ground state in tens of seconds, at most, since good statistics require that we have several hundred to a thousand molecular configurations.

To solve this problem we will use the Fast Fourier Transform(FFT) method, originally developed by Feit, Fleck, and Kosloff⁴. It has been applied to a variety of one electron or quasi one electron problems by many groups.⁵ We were interested primarily in the low lying excited states of an effective one electron atom, the alkali, imbedded in a fluid. Such systems are difficult

to treat by standard quantum chemistry procedures using basis sets since our impurity would be changing position and could be altered significantly by the media as well as by temperature. We also wanted to allow the electron density distribution to respond in any way, unbiased by a particular basis set. The FFT method is also capable of yielding the lower excited states to sufficient accuracy, by an orthogonalization technique.

Various methods were tested for typical harmonic and effective one electron pseudopotentials. Using an IBM 3090/600E and subroutine calls to the highly vectorized ESSL (Engineering and Scientific Subroutine Library), the FFT method appeared to be very fast. We typically use sixteen grid points per dimension. In order to get the answers in quantum chemical problems, it is necessary to do a number of FFT's for each configuration and then propagate these in time (or imaginary time) to achieve a converged answer. This means that we need to do something of the order of 200 steps with about 3 FFTs and 2 Inverse FFT's at each time step. Nevertheless this can be done sufficiently fast. The excited states are then found as the next orthogonal member of the solutions, repeating the entire process. Thus for two excited states we can obtain them in roughly 20-30 seconds. This means that even for 500 or 100 configurations the three electronic states can be determined in a reasonable amount of computer time.

The program we use was originally written by U. Landman and R. Barnett at the Georgia Institute of Technology for a CDC Cyber machine but we modified it for use on our IBM 3090/600VF and to use IBM ESSL routines. Our older version was slightly less efficient. The speed comes from the use of the highly vectorized FFT routines, in which 256 FFTs are done at one time, and all arithmetic functions are calculated only once. This is possible since we always use the same grid. To give an example of the timings, we ran some typical cases. The 8x8x8 case took 2.4 sec, the 16 case took 25.9 sec, while the 32 grid point run took 322 seconds. These scale as roughly $n \ln n$ as they should while the finite difference runs were worse than n^3 .

We will now describe some details of the actual calculations. To begin we must model the Hamiltonian of an alkali in the medium. We have chosen to consider a simple one electron model. The alkali metal's valence electron is modeled by a simple pseudopotential composed of the Coulombic interaction with a plus one charge and an exponential repulsive term which has been fit to yield the lower excited states of the metal. In particular we use the parameterizations of Preuss⁶, although we have modified those parameters for lithium to yield better agreement with experiment. In that case the energy levels of an exact finite difference calculation were matched with the excitation energies as closely as possible. For some reason lithium data is harder to fit than sodium results. The electron inert gas potential is also represented by a pseudopotential, which for the electron xenon and electron helium was taken from work of Berne, Coker and Thirumalai⁷, although the electron helium result is very similar to the more elaborate earlier studies by Kestner, Jorner, Cohen and Rice⁸. We will report here only some of the early studies of sodium and lithium in xenon under various experimental conditions. Our procedure in this case is to use the previously fit inert gas-inert gas and inert gas-alkali atoms interactions (the latter by Baylis⁹) in a molecular dynamics program. For the lithium hydrogen calculations we have only done some initial work in which we have used the electron rare gas potentials as models for the electron hydrogen pseudopotentials. The hydrogen hydrogen parameters were taken from the literature and the lithium hydrogen parameters were from our ab initio calculations which compare approximately with those of Konowalow. However, we have approximated, in these first trials, the hydrogen by a spherical model. This is not extremely serious as the hydrogen molecule electronic wavefunction is almost spherical.

We have been fortunate to have the MIXNVT program written by S. Gupta at Louisiana

State University. After running the program long enough to establish equilibrium, we dump sample configurations at every tenth time step until we have collected 500 to 1000 representative solvent configurations around the impurity. These configurations are then put into the FFT program and three or four excited states are obtained for each configuration of the molecules. The results are then expressed in terms of a histogram of the energies using either 50 or 100 bins, typically, with the range covering the absorption peak.

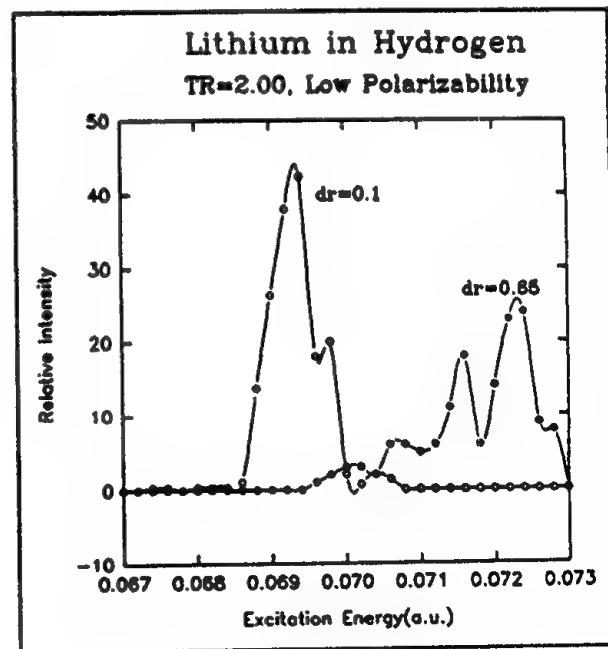
We show some typical results in attached figures. In order to understand these results it is important that one realize that we have used a Lennard Jones 6-12 potential for the atomic interactions and thus all results are expressed relative to those parameters. In particular the relative temperature, T_r , is expressed in terms of the well depth for the inert gas reactions. Typically a liquid or solid has T_r near one. The densities are expressed relative to the zero of the potential cubed, or sigma cubed as it is usually expressed. It is a number density with low numbers being low densities. Only at low temperatures is the liquid state reached for relative densities, D_r , below about 0.7. The figures included in this paper represent only a hint at the capabilities of this method to tackle complex issues in condensed matter physics.

This method has a unique capability of then going back to find out what type of configurations contribute to what features. In early work we were able to see that one case involving three distinct peaks corresponded to three distinct sets of nearest neighbor distances. Thus this method can be used to really understand some specific spectral features in molecular terms.

In conclusion, we have been developing a new method which is particularly suited to new computer architectures and which allows one to study in detail, effects of temperature, density and various degrees of disorder on electronic and vibrational energies. It can study a range of densities and temperatures. It can also be applied to solid state studies and clusters. Now we can study those systems of relevance to the Air Force and provide diagnostic guides for studies of doped fuels.

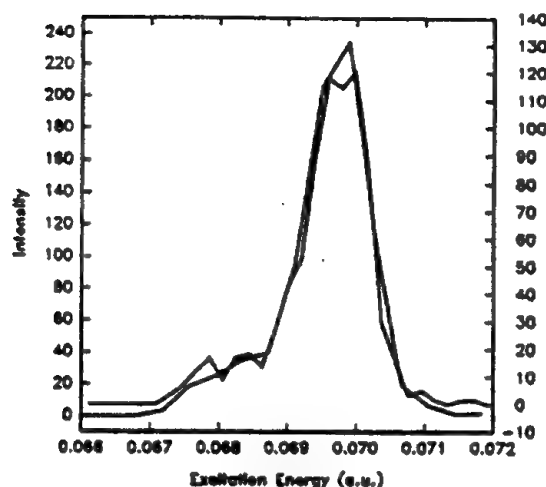
Work partly supported by DOE Grant FG05-87ER13674 and Astronautics Lab Contract (F04611-87-C-0026)

Figures:



Low Density

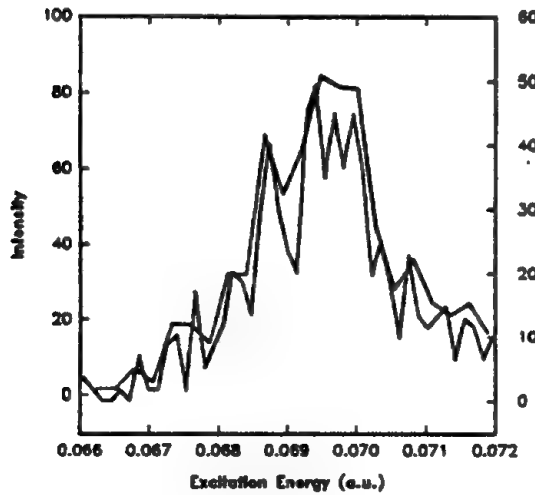
Lithium in Xenon ($Tr = 2.8$, $Dr = .1$)
2s - 2p Transition



The dotted line is the more jagged one (100 bins vs 50).

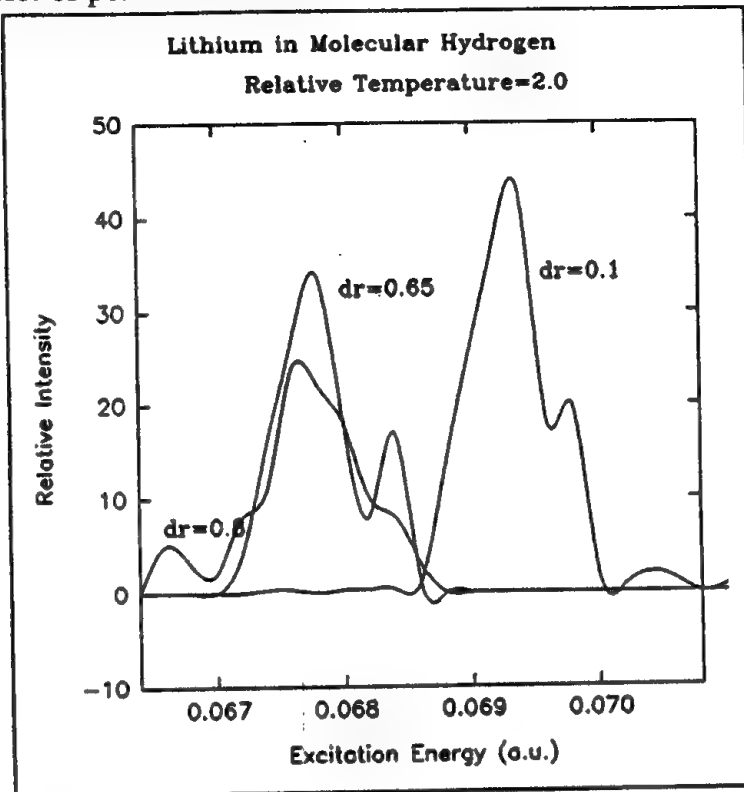
Higher Density

Lithium in Xenon ($Tr = 2.0$, $Dr = .7$)
2s - 2p Transition



Lithium in Hydrogen

Using highly polarizable hydrogen molecules (like xenon)
as test of polarization effects.



References

1. Schnitker, J.; Motakabbir, K.; Rossky, P.J.; Friesner, R., Phys. Rev. Letters, **60**, 456(1988).
Schnitker, J.; Rossky, P.J., J. Chem. Phys., **86**, 3471(1987).
2. Barnett, R.N.; Landman U.; Cleveland C.L.; Jortner, J., Phys. Rev. Letters, **59**, 811(1987).
Barnett, R.N.; Landman U.; Cleveland C.L.; Jortner, J., J. Chem. Phys. **88**, 4429(1988).
3. Car, R.; Parrinello, M., Phys. Rev. Letters, **55**, 478(1985).
4. Feit, M.D.; Fleck, Jr. J.A., J. Chem. Phys. **80**, 2578(1984).
Feit, M.D.; Fleck, J.A.; Steiger, A., J. Comput. Phys. **47**, 412(1982).
Feit, M.D.; Fleck, Jr. J.A., J. Chem. Phys. **78**, 301(1983).
Bisseling, R.; Kosloff R., J. Comput. Phys. **59**, 136(1985).
Kosloff, R., J. Phys. Chem. **92**, 2087(1988).
5. Helling, B.; Nitzan, A.; Metiu, H., Chem. Phys. Letters, **123**, 523(1986).
Martyna, G.J.; Berne, B.J., J. Chem. Phys. **88**, 4516(1988).
Coker, D.F.; Berne, B.J., J. Chem. Phys. **89**, 2128(1988).
6. Preuss, H.; Stoll, H.; Wedig, U.; Kruger, TH., International J. Quant. Chem. **19**, 113(1981).
Flad, J.; Stoll, H.; Preuss, H., J. Chem. Phys. **71**, 3042(1979).
7. Coker, D.F.; Berne, B.J.; Thirumalai, D., J. Chem. Phys. **86**, 5689(1987).
8. Kestner, N.R.; Jortner, J.; Cohen, M.H.; Rice, S.A., Phys. Rev. A, **56**, 140(1965).
9. Baylis, W.E., J. Chem. Phys. **51**, 2665(1969)
Watts, R.O.; McGee, I.J., Liquid State Chemical Physics, John Wiley & Son, 1976.

Infrared Spectroscopy of SF₆ In and On Argon Clusters: New Results for an Extended Range of Cluster Sizes

S. Goyal, G.N. Robinson, D.L. Schutt and G. Scoles

Department of Chemistry, Princeton University, Princeton, NJ 08544

Molecular beams are the ideal medium for the production and study of finite size particles (clusters). Using infrared laser spectroscopy, it is possible to study the evolution of the cluster's properties as they approach the bulk matter limit. We have recently built a new infrared photodissociation spectrometer of improved sensitivity in which we can study clusters in a wide range of sizes (upto approximately n=10⁴). Using this apparatus, we have remeasured the infrared spectrum of the v₃ stretching mode of SF₆ molecules seeded in or deposited on argon clusters at very low concentrations (the lowest being three parts in 10⁵) and extended its study to include larger cluster sizes. While in the lower cluster size range we confirm the previous results, the data obtained in the larger cluster regime are quite different. The range of pressures is between 6.8-80 atm using a 50μ nozzle.

A series of spectra taken by coexpanding a mixture of 0.025 % SF₆/Ar is shown in figures a-h (solid line) The spectrum of clusters produced by a 6.8 atm beam (fig.a) shows two absorptions at 937.5 cm⁻¹ and 938.4 cm⁻¹ that bracket a feature recorded at 937.9 cm⁻¹ in the spectrum of SF₆ in an argon matrix by Swanson et al.. This corresponds to the largest matrix red shift experienced by the v₃ mode of an SF₆ molecule due to it's interaction with an unannealed or moderately annealed (at 30 K) argon environment. However, the peak with the largest shift at 937.5 cm⁻¹ is clearly to the red of the matrix feature. This suggests that the argon atoms in the clusters formed at this pressure can pack around the chromophore more densely than in the bulk matrix. The spectrum at 13.6 atm (fig.b) shows one principal absorption at 937.9 cm⁻¹ and two other broader features. This absorption is also very prominent in the spectra taken at 20.4 atm but fades away when the stagnation pressure reaches 27.2 atm. We conclude that in the pressure region up to 20 atm. the matrix-like features of the SF₆/Ar cluster spectra are very close to those found in the unannealed bulk matrix.

However, in general agreement with the previous work, at 20.4 atm three additional peaks located at 940.0 cm⁻¹, 941.1 cm⁻¹, 942.6 cm⁻¹ are resolved. The absorption at 941.1 cm⁻¹ (comparable in intensity to the matrix-like absorption) and the one at 942.6 cm⁻¹ are, as explained below, due to the chromophore residing in the surface of the cluster. The identity of this feature was previously established by comparing spectra obtained by coexpansion with those obtained using the pick-up technique, since in the latter, the peak at 941.1 cm⁻¹ was greatly enhanced. What is new in the present results is that, as the pressure is increased above 20 atm, the surface features gain intensity at the expense of the unannealed matrix peak which almost totally disappears at 40.8

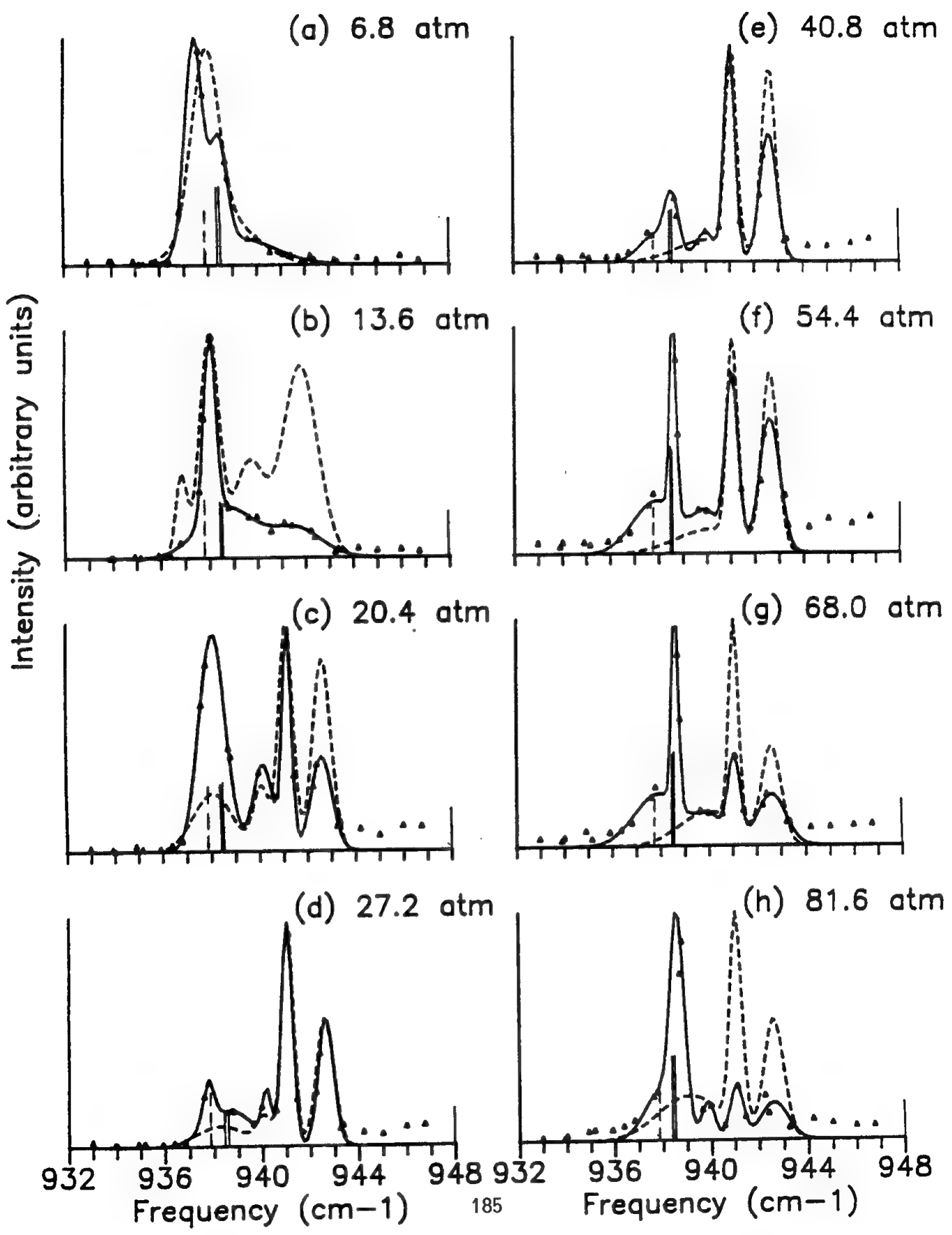
atm. At this pressure (fig.e) a previously unobserved peak is resolved at 938.6 cm^{-1} . This peak gains prominence at the still higher pressure of 54.5 atm and becomes the dominant peak at 68.0 atm and 81.6 atm.

We believe that this observation is important for several reasons. Swanson and Jones have reported two principal absorptions in a SF_6/Ar matrix spectra, annealed at temperatures below 30K. These are a doublet at 938.6 cm^{-1} and 938.45 cm^{-1} caused by a splitting of the three v_3 modes of SF_6 residing at a single site and the absorption at 937.9 cm^{-1} discussed above. Upon annealing the matrix at higher temperatures (39K and 42K), the peak at 937.9 cm^{-1} loses prominence with respect to the doublet because of the disappearance of unstable matrix sites. This indicates that the 938.6 cm^{-1} and 938.45 cm^{-1} doublet can be used as an infrared signature of bulk-solid argon. In light of these observations, it is natural to conclude that the appearance of the peak at 938.6 cm^{-1} , first observed in clusters produced at a stagnation pressure of 40.8 atm, signifies the point at which the transition to the bulk fcc solid argon structure occurs.

The above assignments made on the basis of coexpansion spectra, are further supported by contrasting these with the pick-up spectra taken at the same stagnation pressures figures a-h (dashed line). At the lower pressures (6.8-27.2 atm) the differences in the spectra produced by the two techniques are minor and similar features are seen. However, starting at 27.2 atm, the chromophore has a higher probability of residing on the surface of the cluster when it is deposited there by pick-up as compared to co-expansion. At higher pressures (40.8 - 81.6 atm), the matrix peak at 938.60 cm^{-1} is almost entirely absent in the pick-up spectra .

The occurrence of two resolved surface peaks at 941.1 cm^{-1} and 942.6 cm^{-1} , both in the pick-up and the co-expansion spectra at pressures above 20.4 atm is significant. These peaks maintain an intensity ratio of 2:1 at pressures above 20 atm., leading to the suggestion that they might be due to a site asymmetry splitting of the triply degenerate v_3 mode. Eichenauer and LeRoy have calculated the magnitude of such a splitting for SF_6 interacting with a bulk argon surface modeled as a polarizable continuum with the same density as the solid. For an SF_6 molecule more than half embedded in the surface of the cluster, their model predicts that the two v_3 modes which are perpendicular to the normal to the cluster surface experience a greater shift than the parallel mode, the difference attaining a maximum value of approximately 1.5 cm^{-1} . Since the peak with the larger red shift has the larger intensity, our results are consistent with the assumption that these "surface" chromophores are indeed in such a buried location.

We are also interested in the infrared spectrum of molecules solvated in clusters which are expected to exhibit a high degree of quantum behaviour (ie. hydrogen and helium). We have demonstrated that it is possible to produce clusters containing approximately 1000 hydrogen molecules which "pick-up" a variety of infrared active molecules and have measured their preliminary photodissociation spectrum when SF_6 is embedded in them.



Short Version

**MULTICENTER MOLECULAR INTEGRALS OVER SLATER-TYPE ORBITALS:
MOMENTUM SPACE AND THE FOCK HYPERSPHERE**

by

Charles A. Weatherford
 Physics Department
 and
 Institute For Molecular Computations
 Florida A&M University
 Tallahassee, FL 32307, USA

I. PRELIMINARIES

The problem of performing multicenter integrals over Slater-Type Orbitals is one of the classic problems of Quantum Chemistry.¹ Two of the most successful techniques for the evaluation of such integrals are the Löwdin α -function method²⁻⁵ and the Fourier Transform technique.⁶⁻⁸ An interesting variant of the Fourier Transform technique is based on the Fock hyperspherical projection of the momentum space hydrogenic orbitals onto a four dimensional hypersphere.^{9,10} Some important applications of the Fock projection to the Slater integral problem are given in references 11 and 12.

We are interested in performing the following 4-center electron repulsion integral:

$$\begin{aligned} E_{(n_l m_l) \alpha (n_l m_l) \beta}^{(n_l m_l) \alpha (n_l m_l) \beta} (\alpha_a, \alpha_b, \alpha_c, \alpha_d; \vec{A}, \vec{B}, \vec{C}, \vec{D}) \equiv \\ \int d\vec{r}_1 S_{(n_l)}^{m_l}(\alpha_a, \vec{r}_1 + \vec{A}) S_{(n_l)}^{m_l}(\alpha_b, \vec{r}_1 + \vec{B}) \\ \times \int d\vec{r}_2 \frac{1}{|\vec{r}_1 - \vec{r}_2|} S_{(n_l)}^{m_l}(\alpha_c, \vec{r}_2 + \vec{C}) S_{(n_l)}^{m_l}(\alpha_d, \vec{r}_2 + \vec{D}) \end{aligned} \quad (1)$$

The S -functions are Coulomb Sturmians (CSs).¹³ The CSs are defined by⁷

$$S_{nl}^m(\alpha, \vec{r}) \equiv (-1)^{n+l-1} \alpha^{3/2} N_{nl} e^{-\alpha r} L_{n-l-1}^{(2l+1)}(2\alpha r) Y_l^m(2\alpha \vec{r}) \quad (2)$$

where the phase factor $(-1)^{n+l-1}$ has been introduced in the manner of Koga and Matsuhashi.¹⁴

The E integral is the most general integral which is encountered when non-correlated basis functions are used in an LCAO procedure for CI calculations. In the present work, addition theorems (which separate integration variables) are derived for Coulomb Sturmian functions and modified Coulomb Sturmian functions (Ψ),

$$\Psi_{nl}^m(\alpha, \vec{r}) \equiv \frac{n}{\alpha r} S_{nl}^m(\alpha, \vec{r}) \quad (3)$$

in coordinate and momentum space. The Coulomb Sturmians and their Fourier Transforms, are complete in the sense of distributions in Sobolev space⁷ $W_2^{(1)}(\mathbf{R}^3)$, which is a proper subset of Hilbert space $L^2(\mathbf{R}^3)$. In this regard, a standard Slater Type Orbital (STO) (χ) may be expanded in a finite linear combination of Coulomb Sturmians and vice versa.¹⁷

$$\chi_{(n_l l_i)}^{m_i}(\alpha, \vec{r}) = \alpha^{1/2} \sum_{n_f=l_i+1}^{n_i} b_{n_f}^{(n_l)} S_{n_f l_i}^{m_i}(\alpha, \vec{r}) \quad (4)$$

and vice versa

$$S_{(nl)_i}^{m_i}(\alpha, \vec{r}) = \alpha^{-1/2} \sum_{n_f=l_i+1}^{n_i} a_{n_f}^{(nl)_i} \chi_{n_f l_i}^{m_i}(\alpha, \vec{r}) \quad (5)$$

The CSs satisfy a partial differential equation⁷ given by

$$[\nabla_r^2 - \alpha^2] S_{nl}^m(\alpha, \vec{r}) = -\frac{1}{2\alpha^2} \Psi_{nl}^m(\alpha, \vec{r}) \quad (6)$$

This can be contrasted with the partial differential equation satisfied by the STOs

$$[\nabla_r^2 - \alpha^2] \chi_{nl}^m(\alpha, \vec{r}) = V_{nl}(\alpha, r) \chi_{nl}^m(\alpha, \vec{r}) \quad (7)$$

where

$$V_{nl}(\alpha, r) = -\frac{2\alpha n}{r} - \frac{l(l+1) - n(n-1)}{r^2} \quad (8)$$

It can be easily demonstrated that the CSs satisfy a homogeneous Fredholm integral equation of the second kind¹⁵

$$S_{nl}^m(\alpha, \vec{r}) = \frac{1}{2\alpha^2} \int d\vec{x} G(\alpha, |\vec{r} - \vec{x}|) \Psi_{nl}^m(\alpha, \vec{x}) \quad (9)$$

where G is the Green's function (same as for the modified Helmholtz equation) and is given by

$$G(\alpha, |\vec{r} - \vec{x}|) = \frac{e^{-\alpha|\vec{r} - \vec{x}|}}{4\pi|\vec{r} - \vec{x}|} \quad (10)$$

The Green's function satisfies the partial differential equation

$$[\nabla_r^2 - \alpha^2] G(\alpha, |\vec{r} - \vec{x}|) = -\delta(\vec{r} - \vec{x}) \quad (11)$$

The CSs satisfy the orthonormality conditions⁷

$$\int d\vec{r} \Psi_{(nl)_1}^{*m_1}(\alpha, \vec{r}) S_{(nl)_2}^{m_2}(\alpha, \vec{r}) = \delta_{(nl)_1(nl)_2} \quad (12)$$

and

$$\int d\vec{r} S_{(nl)_1}^{*m_1}(\alpha, \vec{r}) \Psi_{(nl)_2}^{m_2}(\alpha, \vec{r}) = \delta_{(nl)_1(nl)_2} \quad (13)$$

and the closure conditions¹⁹

$$\hat{\mathbf{I}} = \sum_{nlm} |S_{nl}^m\rangle \langle \Psi_{nl}^m| \quad (14)$$

and

$$\hat{\mathbf{I}} = \sum_{nlm} |\Psi_{nl}^m\rangle \langle S_{nl}^m| \quad (15)$$

and the single-center (equal screening constant), coordinate-space overlap of two CSs is given by^{7,18}

$$\begin{aligned} O_{(nl)_1(nl)_2}^{m_1 m_2} &\equiv \int d\vec{r} S_{(nl)_2}^{*m_2}(\alpha, \vec{r}) S_{(nl)_1}^{m_1}(\alpha, \vec{r}) \\ &= \delta_{(lm)_1(lm)_2} [\gamma_{n_1 l_1}^+ \delta_{n_2, n_1+1} + \delta_{n_2, n_1} + \gamma_{n_2 l_2}^- \delta_{n_2, n_1-1}] \end{aligned} \quad (16)$$

where

$$\gamma_{nl}^\pm = \left[\frac{(n \mp l)(n \pm l \pm 1)}{4n(n \pm 1)} \right]^{1/2} \quad (17)$$

II. FOCK HYPERSPHERE AND ADDITION THEOREMS

The symmetric definition of the three-dimensional Fourier transform is first applied to a CS so that

$$S_{nl}^m(\alpha, \vec{r}) = (2\pi)^{-3/2} \int d\vec{p} e^{i\vec{r}\cdot\vec{p}} \bar{S}_{nl}^m(\alpha, \vec{p}) \quad (18)$$

$$\bar{S}_{nl}^m(\alpha, \vec{p}) = (2\pi)^{-3/2} \int d\vec{r} e^{-i\vec{p}\cdot\vec{r}} S_{nl}^m(\alpha, \vec{r}) \quad (19)$$

where \bar{S}_{nl}^m is the Fourier transform of the CS (CSFT). Thus, it can be shown⁷ that the single-center (equal screening constant), momentum-space overlap of two CSs is

$$\begin{aligned} O_{(nl)_1(nl)_2}^{m_1 m_2} &= \int d\vec{p} \bar{S}_{(nl)_2}^{m_2}(\alpha, \vec{p}) \bar{S}_{(nl)_1}^{m_1}(\alpha, \vec{p}) \\ &= \delta_{(lm)_1(lm)_2} [\gamma_{n_1 l_1}^+ \delta_{n_2, n_1+1} + \delta_{n_2, n_1} + \gamma_{n_2 l_2}^- \delta_{n_2, n_1-1}] \end{aligned} \quad (20)$$

The Fourier transform of Ψ can also be taken. Weniger⁷ demonstrated the relationship between a CSFT and a four-dimensional spherical harmonic (the FDSH is the one used by Judd, Ref. 23) given by

$$Y_{nl}^m(\tau, \theta, \phi) = \frac{(\alpha^2 + p^2)^2}{4\alpha^{5/2}} \bar{S}_{nl}^m(\alpha, \vec{p}) \quad (21)$$

where the relationship between τ (hyperangle) and α (screening parameter) is defined by

$$\xi = \frac{2\alpha p_x}{\alpha^2 + p^2} = \sin(\tau) \sin(\theta) \cos(\phi) \quad (22a)$$

$$\eta = \frac{2\alpha p_y}{\alpha^2 + p^2} = \sin(\tau) \sin(\theta) \sin(\phi) \quad (22b)$$

$$\zeta = \frac{2\alpha p_z}{\alpha^2 + p^2} = \sin(\tau) \cos(\theta) \quad (22c)$$

$$\chi = \frac{\alpha^2 - p^2}{\alpha^2 + p^2} = \cos(\tau) \quad (22d)$$

Thus α is a scaling parameter and

$$\xi^2 + \eta^2 + \zeta^2 + \chi^2 = 1 \quad (23)$$

It is clear then that a point \vec{p} of three-dimensional space is mapped (one-to-one) onto a surface of a four-dimensional unit sphere described by the angular variables ξ, η, ζ, χ . The following relationships are then determined.

$$\sin^l(\tau) = \left[\frac{2\alpha p}{\alpha^2 + p^2} \right]^l \quad (24)$$

$$d\hat{\Omega}_\alpha(\vec{p}) \equiv \sin^2(\tau) \sin(\theta) d\tau d\theta d\phi = \left[\frac{2\alpha}{\alpha^2 + p^2} \right]^3 d\vec{p} \quad (25)$$

The orthonormality conditions for the CSFTs and FDSHs are given by

$$\begin{aligned} &\int_0^\pi d\tau \sin^2(\tau) \int_0^\pi d\theta \sin(\theta) \int_0^{2\pi} d\phi Y_{(nl)_1}^{m_1}(\tau, \theta, \phi) Y_{(nl)_2}^{m_2}(\tau, \theta, \phi) \\ &= \int d\vec{p} \bar{S}_{(nl)_1}^{m_1}(\alpha, \vec{p}) \bar{Y}_{(nl)_2}^{m_2}(\alpha, \vec{p}) \\ &= \int d\vec{p} \bar{Y}_{(nl)_1}^{m_1}(\alpha, \vec{p}) \bar{S}_{(nl)_2}^{m_2}(\alpha, \vec{p}) \\ &= \delta_{(nlm)_1(nlm)_2} \end{aligned} \quad (26)$$

where

$$\begin{aligned}\bar{\Psi}_{nl}^m(\alpha, \vec{p}) &= \frac{(\alpha^2 + p^2)}{2\alpha^2} \bar{S}_{nl}^m(\alpha, \vec{p}) \\ &= \frac{2\alpha^{1/2}}{(\alpha^2 + p^2)} Y_{nl}^m[\hat{\Omega}_\alpha(\vec{p})]\end{aligned}\quad (27)$$

The Shibuya and Wulfman¹⁰ expansion of a plane wave in terms of CSs and FDSHs is given by

$$e^{i\vec{p}\cdot\vec{r}} = [\alpha 2^6 \pi^3]^{1/2} \sum_{nlm} \frac{1}{(\alpha^2 + p^2)} S_{nl}^m(\alpha, \vec{r}) Y_{nl}^{-m}[\hat{\Omega}_\alpha(\vec{p})] \quad (28)$$

Eq. (28) may be compared with the expansion of a plane wave in terms of CSs and CSFTs given by

$$e^{i\vec{p}\cdot\vec{r}} = (2\pi)^{3/2} \sum_{nlm} \bar{\Psi}_{nl}^{-m}(\alpha, \vec{p}) S_{nl}^m(\alpha, \vec{r}) \quad (29)$$

or

$$e^{i\vec{p}\cdot\vec{r}} = (2\pi)^{3/2} \sum_{nlm} \bar{S}_{nl}^{-m}(\alpha, \vec{p}) \Psi_{nl}^m(\alpha, \vec{r}) \quad (30)$$

The derivation of the addition theorem begins by applying the translation operator to both sides of Eq. (18). The result is

$$S_{nl}^m(\alpha, \vec{r} \pm \vec{R}) = (2\pi)^{-3/2} \int d\vec{p} e^{i\vec{p}\cdot\vec{r}} e^{\pm i\vec{p}\cdot\vec{R}} \bar{S}_{nl}^m(\alpha, \vec{p}) \quad (31)$$

The Shibuya and Wulfman plane wave expansion of Eq. (29), is used for the \vec{r} -containing plane wave term in the integrand of Eq. (31). The result is

$$S_{(nl)i}^{m_i}(\alpha, \vec{r} \pm \vec{R}) = \sum_{(nlm)_j} Q_{(nlm)_i(nlm)_j}(\alpha, \pm \vec{R}) S_{(nl)_j}^{m_j}(\alpha, \vec{r}) \quad (32)$$

where

$$Q_{(nlm)_i(nlm)_j}(\alpha, \pm \vec{R}) = \int d\vec{p} e^{\pm i\vec{p}\cdot\vec{R}} \bar{\Psi}_{(nl)_j}^{-m_j}(\alpha, \vec{p}) \bar{S}_{(nl)_i}^{m_i}(\alpha, \vec{p}) \quad (33)$$

Then Eqs. (25) and (27) along with

$$\frac{1}{\alpha^2 + p^2} = \frac{\pi}{2^{3/2} \alpha^2} [2Y_{10}^0[\hat{\Omega}_\alpha(\vec{p})] + Y_{20}^0[\hat{\Omega}_\alpha(\vec{p})]] \quad (34)$$

is used to transform the volume integral over \vec{p} to an integral over the surface of a four-dimensional unit sphere with the result

$$Q_{(nlm)_i(nlm)_j}(\alpha, \pm \vec{R}) = \int d\hat{\Omega}_\alpha(\vec{p}) e^{\pm i\vec{p}\cdot\vec{R}} Y_{(nl)_j}^{-m_j}[\hat{\Omega}_\alpha(\vec{p})] Y_{(nl)_i}^{m_i}[\hat{\Omega}_\alpha(\vec{p})] \quad (35)$$

Note that $Y_{10}^0(\Omega) = [\pi 2^{1/2}]^{-1/2}$ and $Y_{20}^0(\Omega) = [\pi 2^{1/2}]^{-1/2} \cos(\tau)$. The explicit evaluation of the integral in Eq. (35) proceeds by using Eq. (27), (29), and (34) and a very important linearization property of FDSHs.²³ This is a property of the FDSHs which allows the product of two FDSHs on the same hypersurface, to be written as a finite linear combination of a single FDSH on the same surface, and is central to the present strategy. This expression was earlier by Shibuya and Wulfman¹⁰ and used to great advantage by Alper.¹¹ Actually, the result is probably most directly attributable to Biedenharn²². It may be expressed as

$$Y_{(nl)_1}^{m_1}[\hat{\Omega}_\alpha(\vec{p})]Y_{(nl)_2}^{m_2}[\hat{\Omega}_\alpha(\vec{p})] = \\ \times \sum_{n_3=|n_1-n_2|+1,2}^{n_1+n_2-1} \sum_{l_3=|l_1-l_2|,2}^{l_1+l_2} C(n_1 l_1 m_1, n_2 l_2 m_2; n_3 l_3, m_1 + m_2) Y_{n_3 l_3}^{m_1+m_2}[\hat{\Omega}_\alpha(\vec{p})] \quad (36)$$

The '2' on the sum indicates every other term is used. The C is defined by

$$C(n_1 l_1 m_1, n_2 l_2 m_2; n_3 l_3 m_3) = \left[\frac{(2l_1 + 1)(2l_2 + 1)n_1 n_2 n_3}{2\pi^2} \right]^{1/2} \\ \times (l_1 m_1, l_2 m_2 | l_3, m_1 + m_2) \begin{Bmatrix} \frac{(n_1 - 1)}{2} & \frac{(n_1 - 1)}{2} & \frac{l_1}{2} \\ \frac{(n_2 - 1)}{2} & \frac{(n_2 - 1)}{2} & \frac{l_2}{2} \\ \frac{(n_3 - 1)}{2} & \frac{(n_3 - 1)}{2} & \frac{l_3}{2} \end{Bmatrix} \quad (37)$$

The efficient evaluation of the $9j$ symbol is critical to the ultimate computational success of the present program. However, present and projected computer technology offers great encouragement in this regard. Even now, textbooks have reasonably adequate computer codes included in the appendices.²⁵

The direct evaluation of Q is now straightforward, resulting in

$$Q_{(nlm)_1(nlm)_2}(\alpha, \pm \vec{R}) = \\ \times \alpha^{-3/2} \sum_{n=\max(|n_1-n_2|,1)}^{n_1+n_2} \sum_{l=|l_1-l_2|,2}^{\min(n-1, l_1+l_2)} \Lambda_{nl}^{(nlm)_1(nlm)_2} S_{nl}^{m_1-m_2}(\alpha, \vec{R}) \quad (38)$$

where in general

$$\Gamma[(nlm)_1(nlm)_2(nlm)_3(nlm)_4] \equiv \\ \int d\hat{\Omega}_\alpha(\vec{p}) Y_{(nl)_1}^{m_1}[\hat{\Omega}_\alpha(\vec{p})] Y_{(nl)_2}^{m_2}[\hat{\Omega}_\alpha(\vec{p})] Y_{(nl)_3}^{m_3}[\hat{\Omega}_\alpha(\vec{p})] Y_{(nl)_4}^{m_4}[\hat{\Omega}_\alpha(\vec{p})] \quad (39)$$

Now, an addition theorem for Ψ can be derived, in an analogous fashion to the one given in Eq. (32) for S with the result of

$$\Psi_{(nl)_i}^{m_i}(\alpha, \vec{r} \pm \vec{R}) = \sum_{(nlm)_j} Q_{(nlm)_i(nlm)_j}(\alpha, \pm \vec{R}) \Psi_{(nl)_j}^{m_j}(\alpha, \vec{r}) \quad (40)$$

Note that the coefficient matrix Q is the same as in Eq. (32).

In a very similar manner, an addition theorem can be given for \bar{S} . It is

$$\bar{S}_{(nl)_i}^{m_i}(\alpha, \vec{p} \pm \vec{p}) = \sum_{(nlm)_j} R_{(nlm)_i(nlm)_j}(\alpha, \beta, \pm \vec{p}) \bar{S}_{(nl)_j}^{m_j}(\beta, \vec{p}) \quad (41)$$

with

$$R_{(nlm)_i(nlm)_j}(\alpha, \beta, \pm \vec{p}) = \int d\vec{r} e^{\mp i \vec{p} \cdot \vec{r}} \Psi_{(nl)_j}^{m_j}(\beta, \vec{r}) S_{(nl)_i}^{m_i}(\alpha, \vec{r}) \quad (42)$$

The explicit evaluation of R is then possible and results in

$$R_{(nlm)_1(nlm)_2}(\alpha, \beta, \pm \vec{p}) = \\ \times \sum_{n=\max(|n_1-n_2|,1)}^{n_1+n_2} \sum_{l=|l_1-l_2|,2}^{\min(n-1, l_1+l_2)} G_{nl}^{(nlm)_1(nlm)_2}(\alpha, \beta) \bar{\Psi}_{nl}^{m_1-m_2}(\alpha + \beta, \vec{p}) \quad (43)$$

and

$$G_{nl}^{(nlm)_1(nlm)_2}(\alpha, \beta) = (2\pi)^{3/2} \frac{n_2(\alpha + \beta)}{n\beta} P_{nl}^{(nlm)_1(nlm)_2}(\alpha, \beta) \quad (44)$$

Finally, an addition theorem can be given for $\bar{\Psi}$. The result is

$$\bar{\Psi}_{(nl)_i}^{m_i}(\alpha, \vec{p} \pm \vec{p}) = \sum_{(nlm)_j} T_{(nlm)_i(nlm)_j}(\alpha, \beta, \pm \vec{p}) \bar{\Psi}_{(nl)_j}^{m_j}(\beta, \vec{p}) \quad (45)$$

where it can be easily shown that

$$T_{(nlm)_i(nlm)_j}(\alpha, \beta, \pm \vec{p}) = Q_{(nlm)_j(nlm)_i}^*(\beta, \alpha, \mp \vec{p}) \quad (46)$$

The R and Q matrices can be shown to be unitary. This can be accomplished using closure relations. The closure relations for the FDSHs were given by Schwinger²⁶

$$\delta(\Omega - \Omega') = \sum_{nlm} Y_{nl}^{*m}(\Omega') Y_{nl}^m(\Omega) \quad (47)$$

The following completeness relations can then be derived to give

$$\delta(\vec{r}_1 - \vec{r}_2) = \sum_{nlm} \Psi_{nl}^{*m}(\alpha, \vec{r}_2) S_{nl}^m(\alpha, \vec{r}_1) = \sum_{nlm} S_{nl}^{*m}(\alpha, \vec{r}_2) \Psi_{nl}^m(\alpha, \vec{r}_1) \quad (48)$$

$$\delta(\vec{p}_1 - \vec{p}_2) = \sum_{nlm} \bar{\Psi}_{nl}^{*m}(\alpha, \vec{p}_2) \bar{S}_{nl}^m(\alpha, \vec{p}_1) = \sum_{nlm} \bar{S}_{nl}^{*m}(\alpha, \vec{p}_2) \bar{\Psi}_{nl}^m(\alpha, \vec{p}_1) \quad (49)$$

The unitarity of Q and R can then be readily demonstrated. Therefore

$$\sum_{(nlm)_3} [Q(\alpha, \vec{R})]_{(nlm)_1(nlm)_3} [\tilde{Q}^*(\alpha, \vec{R})]_{(nlm)_3(nlm)_2} = \delta_{(nlm)_1(nlm)_2} \quad (50)$$

and similarly for R

$$\sum_{(nlm)_3} [R(\alpha, \beta, \vec{P})]_{(nlm)_1(nlm)_3} [\tilde{R}^*(\alpha, \beta, \vec{P})]_{(nlm)_3(nlm)_2} = \delta_{(nlm)_1(nlm)_2} \quad (51)$$

III. MULTICENTER INTEGRALS OVER COULOMB STURMIANS

The addition theorems are useful for application to problems which involve the evaluation of multicenter integrals over exponentially decaying orbitals. Thus, applications to the calculation of molecular wavefunctions for discrete and continuum processes can be considered. In particular, the general 4-center electron repulsion integral, defined in Eq. (1), will be analytically evaluated. Now, introducing the Fourier transform of the Coulomb potential into Eq. (1) results in

$$E_{(nlm)_c(nlm)_d}^{(nlm)_a(nlm)_b}(\alpha_a, \alpha_b, \alpha_c, \alpha_d; \vec{A}, \vec{B}, \vec{C}, \vec{D}) = \frac{1}{2\pi^2} \int d\vec{P} \frac{1}{P^2} e^{+i\vec{P}\cdot\vec{R}_{AB}} \\ \times F_{(nlm)_a(nlm)_b}^*(\alpha_a, \alpha_b; \vec{R}_{AB}; \vec{P}) F_{(nlm)_d(nlm)_c}(\alpha_d, \alpha_c; \vec{R}_{DC}; \vec{P}) \quad (52)$$

where F is called a 2-center form factor and is given by

$$F_{(nlm)_1(nlm)_2}(\alpha_1, \alpha_2; \vec{R}; \vec{P}) \equiv \int d\vec{r} S_{(nl)_2}^{*m_2}(\alpha_2, \vec{r}) S_{(nl)_1}^{m_1}(\alpha_1, \vec{r} + \vec{R}) e^{-i\vec{P}\cdot\vec{r}} \quad (53)$$

or, by introducing the appropriate Fourier transforms,

$$F_{(nlm)_1(nlm)_2}(\alpha_1, \alpha_2; \vec{R}; \vec{P}) \equiv \int d\vec{\rho} \bar{S}_{(nl)}^{m_2}(\alpha_2, \vec{\rho} - \vec{P}) \bar{S}_{(nl)}^{m_1}(\alpha_1, \vec{\rho}) e^{-i\vec{R}\cdot\vec{\rho}} \quad (54)$$

It is important to realize that E in Eq. (52) depends only on the differences between internuclear vectors and not on the vectors themselves. Also, the efficient evaluation of the 2-center form factors (F) is of critical importance.

In order to evaluate the form factors, the 2-center overlap of two CSs in coordinate and momentum space needs to be defined and evaluated. Thus

$${}^r O_{(nl)_i(nl)_j}^{m_i m_j}(\alpha, \beta; \vec{R}) \equiv \int d\vec{r} S_{(nl)_j}^{m_j}(\beta, \vec{r}) S_{(nl)_i}^{m_i}(\alpha, \vec{r} + \vec{R}) \quad (55)$$

and

$${}^p O_{(nl)_i(nl)_j}^{m_i m_j}(\alpha, \beta; \vec{P}) \equiv \int d\vec{\rho} \bar{S}_{(nl)_j}^{m_j}(\beta, \vec{\rho}) \bar{S}_{(nl)_i}^{m_i}(\alpha, \vec{\rho} + \vec{P}) \quad (56)$$

Then, in terms of Q , the form factor becomes

$${}^Q F_{(nlm)_1(nlm)_2}(\alpha_1, \alpha_2; \vec{R}; \vec{P}) = \sum_{(nlm)_3} Q_{(nlm)_1(nlm)_3}(\alpha_1, \vec{R}) {}^p O_{(nl)_3(nl)_2}^{m_3 m_2}(\alpha_1, \alpha_2; \vec{P}) \quad (57)$$

where a pre-superscript has been added to indicate that F has its internuclear dependence expressed in terms of the Q function. In terms of R , then

$${}^R F_{(nlm)_1(nlm)_2}(\alpha_1, \alpha_2; \vec{R}; \vec{P}) = \sum_{(nlm)_3} {}^r O_{(nl)_3(nl)_2}^{m_3 m_2}(\alpha_1, \alpha_2; \vec{R}) R_{(nlm)_3(nlm)_2}(\alpha_1, \alpha_2, \vec{P}) \quad (58)$$

Using Eqs. (57) and (58) in (52) results in

$$\begin{aligned} {}^Q E &= \frac{1}{2\pi^2} \sum_{(nlm)_2} Q_{(nlm)_0(nlm)_2}^*(\alpha_a, \vec{R}_{AB}) \sum_{(nlm)_1} Q_{(nlm)_4(nlm)_1}(\alpha_d, \vec{R}_{DC}) \\ &\quad {}^Q I_{(nl)_1(nl)_0(nl)_2(nl)_0}^{m_1 m_a m_2 m_b}(\alpha_d, \alpha_c, \alpha_a, \alpha_b; \vec{R}_{CB}) \end{aligned} \quad (59)$$

$$\begin{aligned} {}^R E &= \frac{1}{2\pi^2} \sum_{(nlm)_2} {}^r O_{(nl)_0(nl)_2}^{m_0 m_2}(\alpha_a, \alpha_a, \vec{R}_{AB}) \sum_{(nlm)_1} {}^r O_{(nl)_4(nl)_1}^{m_4 m_1}(\alpha_d, \alpha_d, \vec{R}_{DC}) \\ &\quad {}^R I_{(nl)_1(nl)_0(nl)_2(nl)_0}^{m_1 m_a m_2 m_b}(\alpha_d, \alpha_c, \alpha_a, \alpha_b; \vec{R}_{CB}) \end{aligned} \quad (60)$$

where

$$\begin{aligned} {}^Q I_{(nl)_1(nl)_0(nl)_2(nl)_0}^{m_1 m_a m_2 m_b}(\alpha_d, \alpha_c, \alpha_a, \alpha_b; \vec{R}_{CB}) &= \\ \int d\vec{P} \frac{1}{P^2} e^{+i\vec{P}\cdot\vec{R}_{CB}} {}^p O_{(nl)_2(nl)_0}^{m_2 m_b}(\alpha_a, \alpha_b; \vec{P}) {}^p O_{(nl)_1(nl)_0}^{m_1 m_a}(\alpha_d, \alpha_c; \vec{P}) & \end{aligned} \quad (61)$$

$$\begin{aligned} {}^R I_{(nl)_1(nl)_0(nl)_2(nl)_0}^{m_1 m_a m_2 m_b}(\alpha_d, \alpha_c, \alpha_a, \alpha_b; \vec{R}_{CB}) &= \\ \int d\vec{P} \frac{1}{P^2} e^{+i\vec{P}\cdot\vec{R}_{CB}} R_{(nlm)_2(nlm)_0}^*(\alpha_a, \alpha_b; \vec{P}) R_{(nlm)_1(nlm)_0}(\alpha_d, \alpha_c; \vec{P}) & \end{aligned} \quad (62)$$

It is then easy to see that

$$\begin{aligned} {}^Q I_{(nl)_1(nl)_0(nl)_2(nl)_0}^{m_1 m_a m_2 m_b} &= \sum_{n_4=\max(1, n_2-1)}^{n_2+1} \sum_{n_3=\max(1, n_1-1)}^{n_1+1} {}^R I_{(nl)_1(n_3 l_c)(nl)_2(n_4 l_b)}^{m_1 m_a m_2 m_b} \\ &\quad \times O_{(n_4 l_b)(nl)_0}^{m_b m_b} O_{(n_3 l_c)(nl)_0}^{m_a m_a} \end{aligned} \quad (63)$$

and thus only R^I needs to be considered at this point in the development. Thus, using Eq. (43) in Eq. (62) produces

$$\begin{aligned}
 R^I_{(nl)_1(nl)_2(nl)_3(nl)_4}(\alpha_d, \alpha_e, \alpha_a, \alpha_b; \vec{R}_{CB}) = & \\
 \sum_{\substack{n_4 = \max(|n_3 - n_4|, 1)}}^{n_2 + n_4} \sum_{\substack{l_4 = |l_2 - l_4|, 2}}^{\min(n_4 - 1, l_2 + l_4)} G_{(nl)_4}^{(nl)_2(nl)_3}(\alpha_a, \alpha_b) \\
 \sum_{\substack{n_3 = \max(|n_3 - n_4|, 1)}}^{n_1 + n_3} \sum_{\substack{l_3 = |l_1 - l_3|, 2}}^{\min(n_3 - 1, l_1 + l_3)} G_{(nl)_3}^{(nl)_1(nl)_2}(\alpha_d, \alpha_e) \\
 \times J_{(nl)_3(nl)_4}^{(m_1 - m_e)(m_2 - m_d)}(\alpha_d + \alpha_e, \alpha_a + \alpha_b; \vec{R}_{CB})
 \end{aligned} \tag{64}$$

where

$$J_{(nl)_1(nl)_2}^{m_1 m_2}(\alpha_1, \alpha_2; \vec{R}) \equiv \int d\vec{P} \frac{1}{P^2} e^{+i\vec{P} \cdot \vec{R}} \bar{\Psi}_{(nl)_2}^{m_2}(\alpha_2, \vec{P}) \bar{\Psi}_{(nl)_1}^{m_1}(\alpha_1, \vec{P}) \tag{65}$$

In order to perform the integral in Eq. (65), the modified CSFT ($\bar{\Psi}$) must be explicitly given. This can be done by first relating the CS to the B -function of Steinborn⁸ via

$$S_{nl}^m(\alpha, \vec{r}) = \alpha^{3/2} \sum_{i=1}^{n-l} a_i^{nl} B_{il}^m(\alpha, \vec{r}) \tag{66}$$

Then taking the Fourier transform of Eq. (66) and using Eq. (27), the Fourier transform of $\bar{\Psi}$ is obtained as

$$\bar{\Psi}_{nl}^m(\alpha, \vec{P}) = (-i)^l \frac{2^{1/2}}{\pi} \sum_{i=1}^{n-l} a_i^{nl} \alpha^{2i+l+1/2} \frac{P^l}{[\alpha^2 + P^2]^{l+1}} Y_l^m(\hat{P}) \tag{67}$$

Then, J can be evaluated as

$$\begin{aligned}
 J_{(nl)_1(nl)_2}^{m_1 m_2}(\alpha_1, \alpha_2; \vec{R}) = & 4\pi \sum_{l_2=1}^{n_2 - l_2} a_{l_2}^{(nl)_2} \alpha_2^{2l_2 + l_3 + 1/2} \sum_{l_1=1}^{n_1 - l_1} a_{l_1}^{(nl)_1} \alpha_1^{2l_1 + l_1 + 1/2} \\
 & \times \sum_{\substack{l_3 = |l_1 - l_2| \\ l_3 = l_1 + l_2}}^{l_1 + l_2} \delta_{l_1 + l_2 + l_3 = \text{even}} [(-1)^{l_1 l_1 + l_2 + l_3}] \langle l_2 m_2 | l_1 m_1 | l_3, m_2 - m_1 \rangle \\
 & \times W_{(l_1 + l_1), (l_2 + l_3)}^{l_3, \left[\frac{l_1 + l_2 - l_3}{2} \right]}(\alpha_1, \alpha_2; R) Y_{l_3}^{m_2 - m_1}(\hat{R})
 \end{aligned} \tag{68}$$

where

$$W_{m,n}^{l,j}(\alpha_1, \alpha_2; R) \equiv \frac{2}{\pi} \int dP \frac{P^{l+2j}}{[\alpha_1^2 + P^2]^m [\alpha_2^2 + P^2]^n} j_l(RP) \tag{69}$$

The W integral may be evaluated by the methods developed by Harris and Michels.²⁹

Thus, the evaluation of E , the 4-center electron repulsion integral, has been described. The programming of these results is underway.

This work was supported by the Air Force Office of Scientific Research under Contract No. F49620-89-C-007.

References

1. *Proceedings of the First International Conference on ETO Multicenter Molecular Integrals*, edited by C.A. Weatherford and H.W. Jones, (D. Reidel, Holland, 1982).
2. P.O. Löwdin, *Adv. Phys.* **5**, 1 (1956).
3. M.P. Barnett and C.A. Coulson, *Philos. Trans. R. Soc. London Ser. A* **243**, 221 (1951); M.P. Barnett, in *Methods in Computational Physics*, V. 3, edited by B. Alder, S. Fernbach, and M. Rotenberg, (Academic Press, New York, 1963), p. 95; and references therein.
4. F.E. Harris and H.H. Michels, *J. Chem. Phys.* **43**, S165 (1965).
5. H.W. Jones and C.A. Weatherford, *Int. J. Quant. Chem.* **S12**, 483 (1978).
6. H.J. Silverstone, *J. Chem. Phys.* **48**, 4098 (1986); and references therein.
7. E. J. Weniger, *J. Math. Phys.* **26**, 276 (1985).
8. E.J. Weniger, J. Grotendorst, and E.O. Steinborn, *Phys. Rev. A* **33**, 3688 (1986).
9. V. Fock, *Z. Phys.* **98**, 145 (1935).
10. T-I. Shibuya and C. Wulfman, *Proc. R. Soc. London Ser. A* **286**, 376 (1965).
11. J.S. Alper, *J. Chem. Phys.* **55**, 3770 (1971); **55**, 3780 (1971).
12. B.K. Novosadov, *Int. J. Quant. Chem.* **24**, 1 (1983).
13. M. Rotenberg, *Ann. Phys. (NY)* **19**, 262 (1962).
14. T. Koga and T. Matsuhashi, *J. Chem. Phys.* **88**, 1110 (1988).
15. G. Arfken, *Mathematical Methods For Physicists*, Third Edition, (Academic Press, New York, 1985).
16. I.N. Sneddon, *Special Functions of Mathematical Physics and Chemistry*, (Oliver and Boyd, Edinburgh, 1966).
17. C.A. Weatherford, Ref. 1, p. 29.
18. C.A. Weatherford, unpublished.
19. R. Shakeshaft, *Phys. Rev. A* **34**, 244 (1986).
20. E. Filter and E.O. Steinborn, *J. Math. Phys.* **21**, 2725 (1980).
21. H.H. Kranz and E.O. Steinborn, *Phys. Rev. A* **25**, 66 (1982).
22. L.C. Biedenharn, *J. Math. Phys.* **2**, 433 (1961).
23. B.R. Judd, *Angular Momentum Theory For Diatomic Molecules*, (Academic Press, Inc., New York, 1975).
24. A.R. Edmunds, *Angular Momentum in Quantum Mechanics*, (Princeton U.P., Princeton, New Jersey, 1957).
25. R.N. Zare, *Angular Momentum*, (Wiley, Princeton, New York, 1988).
26. J. Schwinger, *J. Math. Phys.* **5**, 1606 (1964).
27. T. Koga, *J. Chem. Phys.* **83**, 2328 (1985).
28. T. Koga and T. Matsuhashi, *J. Chem. Phys.* **87**, 4696 (1987).
29. F.E. Harris and H.H. Michels, *Adv. Chem. Phys.* **13**, 205 (1967).

Interacting Correlated Fragments Treatment of Li_n-H₂ van der Waals Interaction

(Long abstract of paper presented at the HEDM Conference, 24-27 February 1991 in
Albuquerque N.M.)

Daniel D. Konowalow

**Phillips Laboratory OLAC
Edwards Air Force Base, CA 93523-5000**

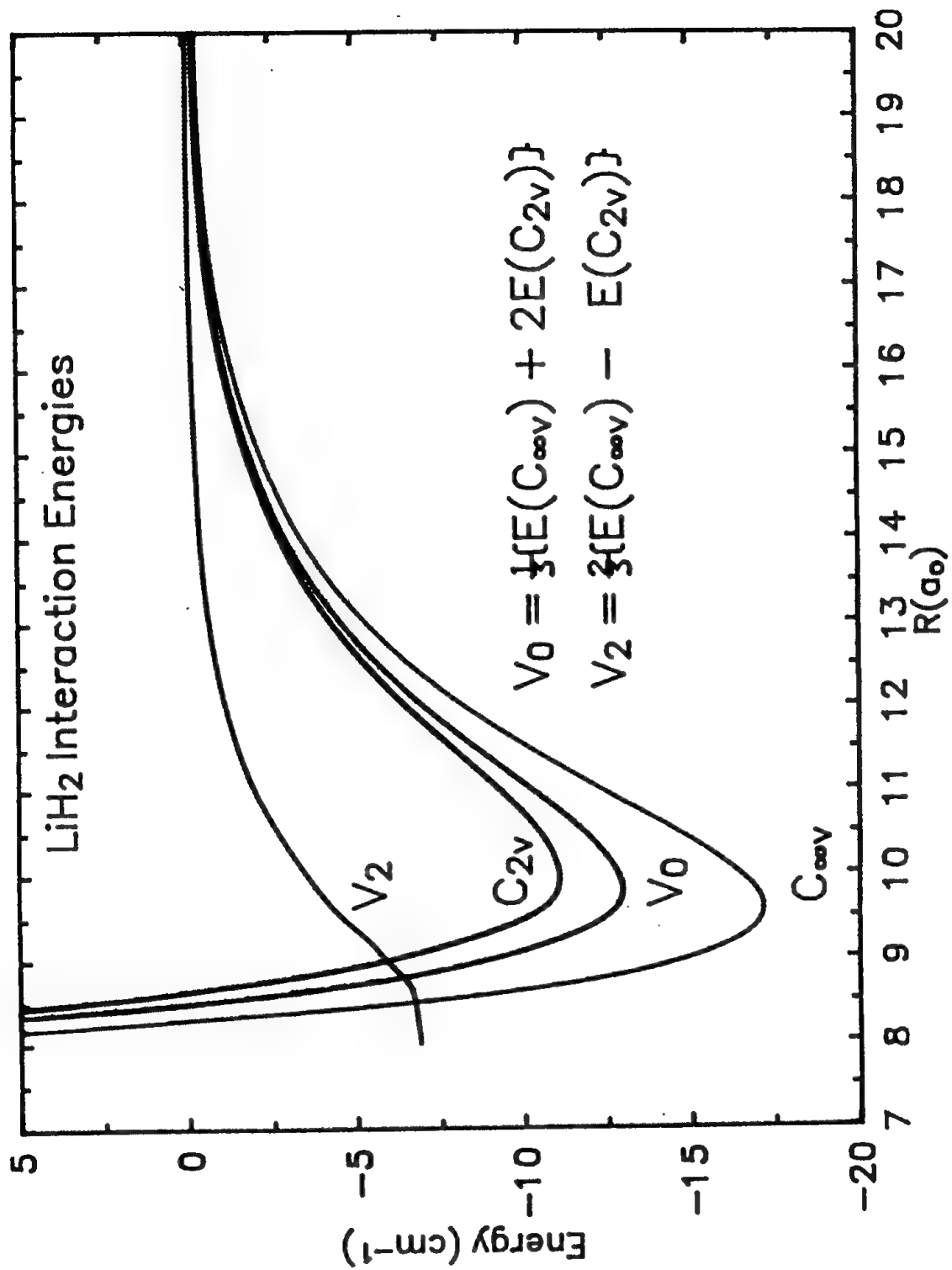
For an introduction to this subject see my previous HEDM reports.

I use the Interacting Correlated Fragments method of Liu and McLean [J. Chem. Phys., 91 2348 (1989)] to describe the weakly bound systems Li-H₂ and Li₂-H₂. The molecules are held rigidly fixed at essentially their equilibrium internuclear separations and allowed to interact. Interfragment distances are measured between the centers of mass of the interacting fragments. I take the molecular energy at some large interfragment separation (usually 30 a₀) to be the zero of energy; thus these results are size consistent.

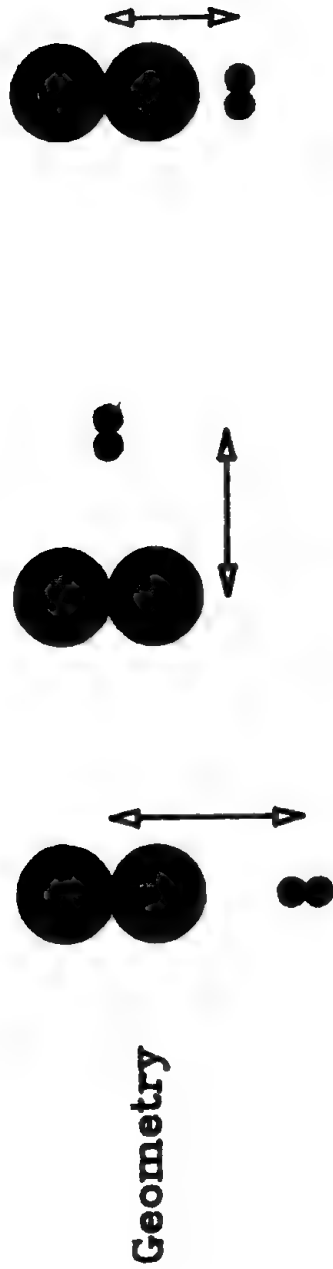
The basis sets are optimized for the dipole, quadrupole, and octupole polarizability of the Li atom and the dipole polarizability of the H₂ molecule by means of finite-field calculations at the SCF level. No basis set superposition corrections have been incorporated.

Figure 1 shows the Li-H₂ binding energy curves for the linear and C_{2v} (T) approaches. These results can be recast to give a spherically symmetric part and an anisotropic part. These results are being used by Voth and Klein to model the dynamics of Li in condensed H₂.

Figure 2 gives certain characteristic constants of the van der Waals molecules Li₂-H₂ in three symmetries. Clearly, the weak binding is highly anisotropic. This reflects the combination of the quadrupole-quadrupole interaction (which is repulsive for the C_{oo} symmetry, but attractive in C_{2v}) and the dispersion interactions (which are all attractive but are also anisotropic). By comparison with the H₂-H₂ interaction, whose binding energy D₀ is about 2.9 cm⁻¹, these Li₂-H₂ interactions are quite attractive.



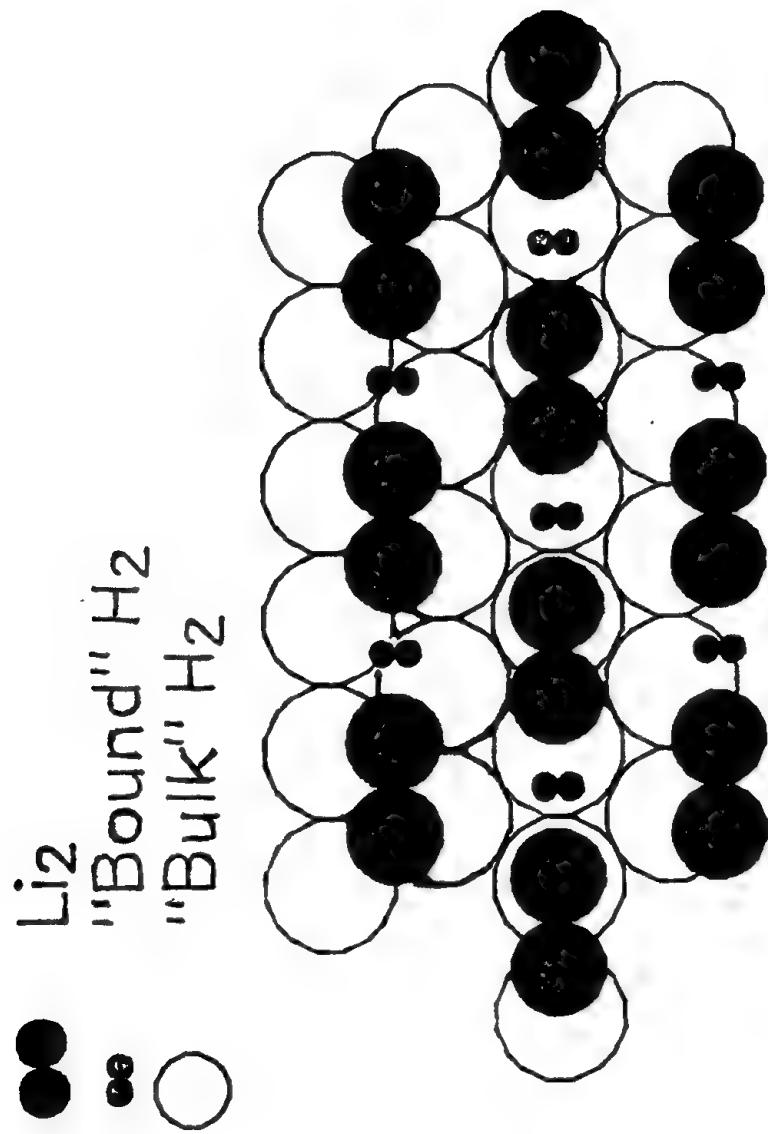
Name	t	T
$R_e (a_0)$	10.43	8.80
$D_0 (\text{cm}^{-1})$	16.9	61.2
		116.1



Geometry

Figure 3 shows how a number of Li_2 molecules might pack with H_2 molecules in solid H_2 . In this picture I show the “unbound” H_2 molecules of the solid matrix as a large open circle. Li_2 molecules are shown as a solid, medium sized figure eight and the H_2 molecules (which are “bound” by quadrupole and dispersion forces to neighboring Li_2) are shown as a small, solid figure eight. In this picture I’ve cheated by that H_2 and Li_2 the most favorable two-body interactions and ignoring the possibility that less favorable interactions like linear $\text{Li}_2\text{-H}_2$ would be important at equilibrium, and ignoring all interactions where I have no data. This picture does suggest where additional data is needed. It also suggests that one might be able to attain the 10% doping of Li_2 in H_2 that one needs to achieve a large increase in I_{sp} .

Hypothetical Placement of Li₂ in Solid H₂ Matrix



NOVEL BONDING IN MOLECULES: METASTABLE MOLECULAR FUELS[†]

Roberta P. Saxon
Molecular Physics Laboratory, SRI International
Menlo Park, California 94025

Species which show promise as high energy density materials may exhibit novel bonding mechanisms which distinguish them from conventional stable molecules. The goal of this program is to theoretically evaluate compounds composed of first row-atoms that might serve as the basis of new propulsion schemes. Two, possibly overlapping, categories are under current consideration: (1) electron deficient compounds, certain compounds of B and Be which do not have sufficient valence electrons to distribute two per chemical bond, and (2) mixed metal clusters of the form $\text{Li}_n\text{B}_m\text{H}_k$. Preliminary I_{sp} estimates, using approximate or guessed heats of formation, for compounds of these types indicate they may potentially improve performance as additives to liquid oxygen and liquid hydrogen. Results obtained to date for optimized geometries and predictions of heats of formation and theoretical I_{sp} values are reported here for the electron-deficient BH_4 and Li_3Be systems. Calculations exploring the concept of "superalkalis" and "superhalogens", extraordinarily stable cations and anions that might combine to give species unusually resistant to charge transfer, undertaken in the early part of this work, are also reported.

Calculations of BH_4

Compounds of boron have long been considered as potential fuels because the heat of reaction of boron to form oxides and fluorides is relatively large.¹ Furthermore, a hypervalent compound of boron may be expected to have a relatively high heat of formation and the hypervalency could possibly counteract the tendency of electron-deficient compounds of boron to dimerize. The only information on energy of BH_4 in the literature prior to this work was based on calculations at the approximate MNDO level.² Use of this value in theoretical specific impulse calculations indicated BH_4 is potentially advantageous as an additive to liquid hydrogen and liquid oxygen.

Geometry optimizations and frequency calculations for BH_4 and for the asymptotes $\text{BH}_3 + \text{H}$ and $\text{BH}_2 + \text{H}_2$ were performed using MCSCF analytic second derivatives.³ For these complete active space calculations, 7 electrons were distributed in 8 orbitals resulting in 2352 configurations in C1 symmetry. A double zeta basis set was used.

Optimized geometries are given in Table 1; comparison with literature values shows reasonable agreement. We find the global minimum of BH_4 to be of C_{2v} symmetry in agreement with the report of Claxton et al.⁴ We also investigated the D_{2d} symmetry isomer reported in Ref. 4 but found it to have a doubly degenerate imaginary frequency. We were unable to locate any additional stable isomers.

Energies were calculated by multi-reference single and double CI calculations (MRSDCI) using the B(4s3p2d) H(3s2p) basis reported by Lengsfeld.⁷ In the MRSDCI calculations, 5-7 reference configurations resulted in CI expansions of 100,000 to 175,000 configurations.

Table 1.
 BH_4 Geometries

	Present Work MC/DZ	UHF/4-31G*	Claxton et al. ⁴ UHF/6-311G**
BH1	1.3278	1.275	1.288
BH2	1.2072	1.182	1.182
θ_1	51.48	55.0	48.4
θ_2	128.73	125.8	128.4
		1.2072 Å	

Relative energies for the BH_4 system are reported in Table 2. The general approach in these theoretical studies is to determine the heat of formation of a previously unknown compound by computing the energy difference with respect to fragments whose heat of formation is known reliably. Unfortunately, there is little accurate information for the small boron hydrides. For example, as pointed out by Adams and Page,⁶ the JANAF⁸ value for BH_2 is completely wrong.

We have chosen to base the values reported in Table 2 on the heat of formation of BH_3 , $\Delta H_f^{298} = 20.95$ kcal/mol derived from the careful study of the dimerization energy of borane by Page et al.⁵ (The JANAF⁸ value for BH_3 is 25.5 kcal/mol). Using our calculated zero point energies and assuming classical equipartition of energy for rotation and translation to compute temperature effects gives ΔH_f^{298} (BH_4) of 53.2 kcal/mol. This is precisely the same as the MNDO value² originally used to estimate the expected I_{sp} . The agreement should be attributed to coincidence. The heat of formation for BH_2 of 73.2 kcal/mol reported in Table 2 is in excellent agreement with the value of 73.6 given by Adams and Page.⁶

Calculations of Li_3Be

The design of the calculations of Li_3Be was analogous to that described above for BH_4 . The complete active space for geometry optimization included 5 electrons distributed in 4 orbitals. For MRSDCI calculations of energies, the active space was enlarged to 10 orbitals to include the most important part of the 2p space, as determined by testing of the full 2p space.

Optimized geometries are reported in Table 3. The equilibrium geometry of Li_3Be is a planar, symmetric species in agreement with the previous report of Pewestorf et al.⁹ Energies for the Li_3Be system are listed in Table 4. The heat of formation, $\Delta H_f^0 = 138$ kcal/mol reported here is referenced to the heat of formation of gaseous atomic Be from the JANAF tables⁸ and the experimentally derived Li_3 heat of formation given by Wu¹².

Theoretical I_{sp} Calculations

Estimated I_{sp} values for BH_4 and Li_3Be considered as additives to liquid oxygen and liquid hydrogen were calculated with the AFAL Theoretical I_{sp} program using the heats of formation predicted in

Table 2.
BH₄ Results Energies^a

	BH ₄	BH ₃ + H	BH ₂ + H ₂
Relative Electronic Energy	-22.4	0.0	-0.7
Zero Point Energy	19.0	15.8	15.2
ΔH _f ²⁹⁸ This work	53.2 ^b	73.0 ^b	73.2 ^b
Other values	53.2 ^c		73.6 ^d

^a Energies in kcal/mol

^b Assuming ΔH_f²⁹⁸(BH₃) = 20.95 kcal/mol from Page, et al., Ref. 5.

Temperature effects calculated assuming classical equipartition of energy for rotation and translation

^c MNDO calculation Symons et al. Ref. 2

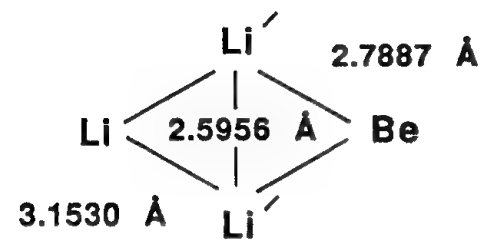
^d Adams and Page, Ref. 6

this work. They are compared in Table 5 with liquid hydrogen and oxygen under the same conditions. Both of the compounds studied here theoretically represent performance improvement as additives. Note that use of the present calculated heat of formation of Li₃Be of 138 kcal/mol rather than the previously guessed values of 175 and 150 makes a very modest difference. Further calculations should be directed toward predicting synthetic pathways and stability, including with respect to dimerization, of these compounds.

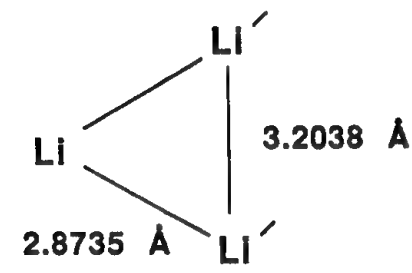
"Superalkalis" and "Superhalogens"

In the early part of this program, the qualitative ideas underlying the concept of "superalkalis" and "superhalogens", extraordinarily stable cations and anions that should combine to give species unusually resistant to charge transfer, were investigated. The property of resistance to charge transfer, in order to enhance charge separation, was originally considered desirable. While the prediction of exceptional ionic stability was substantiated, these ideas appear to lead to compounds with heats of formation too low to allow formation of charge-separated species of sufficient energy to be of interest here. In addition, the recent model study of Fajardo¹³ points out possible limitations on the densities that could theoretically be achieved for charge separated species.

Table 3.

Li₃Be Results Geometries^a**Li₃ Be Minimum****Li₃ Be**⁹**Present Work****MC/DZ****Pewestorf et al.****HF/3-21G**

Li Be	2.7787	2.61
Li Li	3.1530	3.13
Li Li	2.5956	3.02

Li₃ + Be**Li₃ (²B₂)**¹⁰**Present Work****MC/DZ****Talbi & Saxon****MC/(5s2p1d)**

Li Li	2.8735	2.820
Li Li	3.2038	3.271

Li₂ + Li Be

$$\text{Li}_2 \left(^1\Sigma_g^+ \right) R_e = 2.9820$$

Experiment (Verma, Koch, Stwalley)¹¹

2.673

$$\text{Li Be} \left(^2\Sigma^+ \right) R_e = 2.5640$$

^a Distances in Å

Table 4.
Li₃Be Results Energies^a

	Li ₃ Be	Li ₃ + Be	Li ₂ + Li Be
Relative Electronic Energy	-12.4	0.0	8.5
Zero Point Energy	1.9	1.0	0.9
ΔH _f ⁰	137.9	149.5 ^b	157.9

^a Energies in kcal/mol

^b Assuming ΔH_f⁰(Be) = 76.5 kcal/mol from JANAF tables.

ΔH_f⁰(Li₃) = 73.0 kcal/mol from C.H Wu, Ref. 12.

Table 5.

Estimated Theoretical I_{sp}^a

Additive	ΔH _f (kcal/mol)	Additive	Mole Fraction		I _{sp} (sec)
			O ₂ (liq)	H ₂ (liq)	
none			1	4	421
BH ₄	53	2	1	9	488
		2	1	8	490
		2	1	7	490
Li ₃ Be	175	1	1	10	525
		1	1	13	532
		150	1	13	532
		138	1	13	513
		138	1	14	512

^a Calculated with AFAL Theoretical I_{sp} Program (Micro Version). Density of additives taken as 1.5 grams/cc. Chamber pressure 1000 psia. Exhaust pressure 14.696 psia.

[†]Supported by contract No. F04611-90-K-0012

1. S. F. Sarner, Propellant Chemistry (Reinhold, New York, 1966).
2. M.C.R. Symons, T. Chen, and C. Glidewell, J. Chem. Soc. Chem. Commun. 326 (1983).
3. ALCHEMY 2 program system.
4. T. A. Claxton, T. Chen, M. C.R. Symons, and C. Glidewell, Faraday Discuss. Chem. Soc. 78, 121 (1984).
5. M. Page, G. F. Adams, J. S. Binkley, and C. F. Melius, J. Phys. Chem. 91, 2675 (1987).
6. G. F. Adams and M. J. Page, Technical report BRL-TR-3027 (1989).
7. B. H. Lengsfield, Final Report FY89 "Theoretical Studies of HEDM Molecules"
8. JANAF Thermochemical Tables, Third Edition, J. Phys. Chem. Ref. Data, 14, Supplement No. 1 (1985).
9. W. Pewestorf, V. Bonacic-Koutecky, and J. Koutecky, J. Chem. Phys. 89, 5794 (1988).
10. D. Talbi and R. P. Saxon, Chem. Phys. Lett. 157, 419 (1989).
11. K. K. Verma, M. E. Koch, and W. C. Stwalley, J. Chem. Phys. 78, 3614 (1983).
12. C. H. Wu, J. Chem. Phys. 65, 3181 (1976).
13. M. Fajardo, "Limitations on Stored Energy Densities in Systems of Separated Ionic Species," to be published.

OPTICAL AND THERMAL ENERGY DISCHARGE FROM TRITIATED SOLID HYDROGEN

Frank Magnotta, Evan R. Mapoles, Gilbert W. Collins and P. Clark Souers
Lawrence Livermore National Laboratory, Livermore, CA 94551

We are investigating mechanisms of energy storage and release in tritiated solid hydrogens, by a variety of techniques including ESR, NMR and thermal and optical emission. The nuclear decay of a triton in solid hydrogen initiates the conversion of nuclear energy into stored chemical energy by producing unpaired hydrogen atoms which are trapped within the molecular lattice. The ability to store large quantities of atoms in this manner has been demonstrated and can serve as a basis for new forms of high energy density materials.¹ This paper presents preliminary results of a study of the optical emission from solid hydrogen containing tritium over the visible and near infrared (NIR) spectral regions. Specifically, we have studied optical emission from DT and T₂ using CCD, silicon diode and germanium diode arrays.

The visible emission spectrum of tritium gas at room temperature has been observed previously² and consists of atomic lines due to ³He and ³H transitions. Figure 1 shows that the emission of tritiated solid hydrogen is considerably different displaying no ³H lines and comparatively few ³He lines. Instead, very strong emission is seen from various excited state transitions in He₂ and one transition due to HeD(T). In addition, we have observed a strong, broad emission feature centered at 800 nm with a width of about 100 nm (0.19eV), which has not been seen previously and is currently unidentified. These features are virtually identical in samples of either DT or T₂ in sapphire or crystalline quartz sample cells. Figure 2 shows little or no isotopic shift in the 800nm feature in DT verses T₂. We have measured the emission spectrum out to 1.7 um as shown in Figure 3. Two more bands originating from helium dimer states are observed. By a combination of both spatially resolved spectroscopy and visible and infrared photography, we have determined that the helium emission lines originate mainly from the gas phase above the solid hydrogen whereas the broad 800 nm line derives from the solid sample itself. There is no short wavelength emission observed down to 250 nm.

The temperature dependence of the emission was investigated in low resolution spectra taken between 6K and 18K, part of which is shown in Figure 4. The atomic helium lines persist out to 15K whereas the helium dimer peak is gone at 9K. The broad 800 nm peak emission decreases rapidly over this temperature range remaining centered at 800nm, going to zero at 10.5K. A broadband bluish background emission from the quartz containment sphere itself is present (not shown) and is unchanged with temperature.

Between 2.5 and 6.5 K, the release of stored energy, in these systems can be triggered by slightly raising the temperature. We observe both light and heat pulses as shown in Figures 5a and 5b. The duration of the evolution of optical energy can be varied from 1.0 msec to 0.1 sec by varying the storage temperature.³ The recovery time during which the atom concentration builds back up to a steady state concentration is 8 to 10 minutes. After a flash, the sample temperature drops as the radiation from the triton decay is stored as unpaired atoms. The steady state stored atom density increases rapidly with decreasing temperature

such that at temperatures below ~ 2 K spontaneous thermal and optical pulses are observed.¹ We have demonstrated that these pulses occur 'simultaneously'.

We have studied the pulsed emission spectroscopically and observe that from 250 nm to 1.7 μm , the entire emission is due to the 800 nm peak. Figure 6 shows a sequence of CCD frames captured at 2.5 second intervals. The peak of the flash emission has red shifted about 50 nm. Following an optical flash, the cell goes 'dark'. The atomic helium emission lines remain unchanged but the helium dimer emission is initially quenched but returns rapidly after about 5 - 10 seconds as witnessed by the peaks around 920 nm in both figures 3 and 6. The slower buildup of the 800 nm peak is also evident. It is shown from broadband photodiode response data that the peak pulse emission can be two to three orders of magnitude higher than the steady state emission (at low temperatures) but this is not evident in figure 6 due to the millisecond timescale of the pulse versus the long integration time of the frame. About 4 KJ/m^3 ³ is radiated as pulsed emission between 710 and 1100nm.³

Tritium decays to form ${}^3\text{He}$, a beta particle and an antineutrino.



While the antineutrino carries off ~70% of the energy,⁴ the beta particle is left with the remaining mean energy of about 5.7 keV (neglecting nuclear recoil), generating ~ 10^5 W/m^2 . We have found that in the solid phase, tritium produces about 150 ion pairs per triton decay resulting in about 800 atoms, similar to that in the gas phase.⁵ When a tritium nucleus decays, the ${}^3\text{HeT}^+$ daughter may remain bound since it is stable by 1.84eV. However, the ion is unstable to electron recombination leaving HeT on a repulsive wall with a 10 ns lifetime. Kinetically, the ion should be unstable in hydrogen as well and can react by



Despite this, there is speculation that HeT^+ is stable in solid hydrogen and may form ion clusters rather than reacting with it.⁴ Unfortunately, the known energetics of such species (as well as other obvious excited states of hydrogen, helium hydrides etc), do not suggest the origin of the 800 nm emission.

The absorption spectra of tritiated hydrogens have been measured from the near UV to the mid IR⁶. Two interesting features occur only in the irradiated solid below about 7 K and disappear upon warming. A broad UV band appears at ~ 345 nm (1.5eV FWHM) and a narrower (0.3 eV FWHM) IR peak at 1.6 μm in tritium doped D_2 and 1.9 μm in doped H_2 . A similar absorption is seen in solid T_2 with the onset, blue shifted ~100 nm compared with doped D_2 . There is no apparent absorption in the region between these features. Both absorption peaks have been observed in samples irradiated with tritium beta particles as well as external proton bombardment.⁷ It is currently thought that both transitions are due to electron bubbles, ie a free electron trapped in the crystal lattice. Such a state would possess a spherical square-well potential, with the IR line assigned to the $1s \rightarrow 1p$ transition (analogous to the Coulombic $1s \rightarrow 2p$ transition) and the UV feature, the $1s$ to continuum transition. Considering the similarity of the bandwidth of the 800nm transition.

emission to that of the IR absorption, one might conjecture its origin as related to such a bubble state perhaps the $1s \rightarrow 2p$ or $1s \rightarrow 1d$ transition. Another possibility would be that the emission is from transitions from the continuum, coupling first to high lying discrete states. Calculations of electron bubble states in liquid helium show increasing displacement in the equilibrium configuration coordinate curves of states with increasing energy such that large energy differences (ie factors of two or more) between absorption and emission are likely. Emission spectra of proton bombarded solid hydrogen doped with helium have been observed and are remarkably similar to that of tritiated hydrogen except that apparently no emission is seen at 800 nm.⁸ Experiments to study the emission spectra of tritiated hydrogen further out into the IR are currently underway and promise a wealth of further information in detailing the energy storage and disposal mechanisms and dynamics in these systems.

References:

- ¹G.W. Collins, P.C. Souers, J.L. Maienschein, E.R. Mapoles and J.R. Gaines, "Atom Densities in Tritiated Solid Hydrogens", submitted to Phys. Rev. B (1991).
- ²R.W. Schmieder, J. Opt. Soc. Am. 72, 593 (1982).
- ³E.R. Mapoles, F. Magnotta, G.W. Collins and P.C. Souers, Phys. Rev. B 41, 11653 (1990).
- ⁴P.C. Souers, *Hydrogen Properties for Fusion Energy*, University of California Press, Berkeley, Ca (1986).
- ⁵G.W. Collins, P.C. Souers, E.R. Mapoles and F. Magnotta, *Proceedings of the HEDM Contractors Conference*, (1991).
- ⁶(a) J.H. Richardson, S.B. Deutscher, P.C. Souers, R.T. Tsugawa and E.M. Fearon, Chem. Phys. Lett. 81, 26 (1981). (b) E.M. Fearon, R.T. Tsugawa and P.C. Souers, Fusion Tech. 8, 2239 (1985).
- ⁷J.A. Forrest, J.L. Hunt, R.L. Brooks, Can. J. Phys. 68, 1247 (1990).
- ⁸R.L. Brooks and J.L. Hunt, J. Chem. Phys. 88, 15 (1988).

This work was performed under the auspices of the U.S. Department of Energy by Lawrence Livermore National Laboratory under contract No. W-7405-Eng-48.

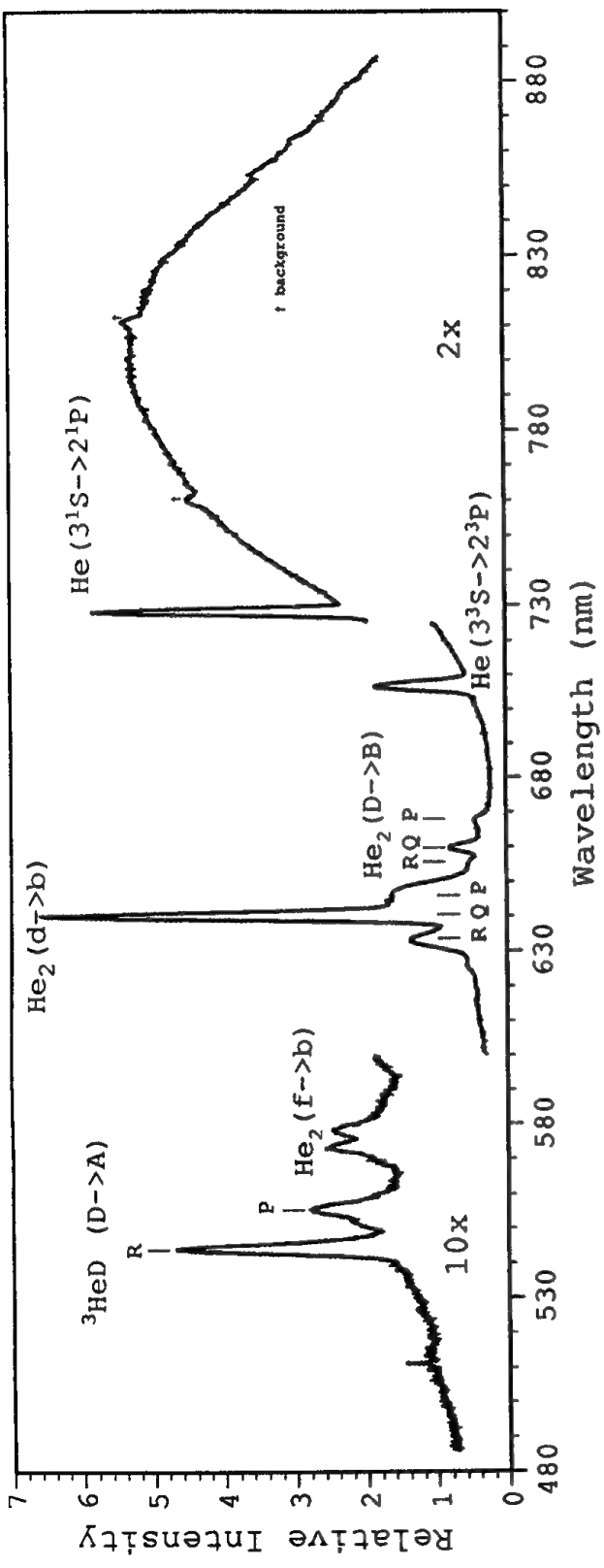


Figure 1: Low resolution emission survey spectrum of DT at 4.2 K.

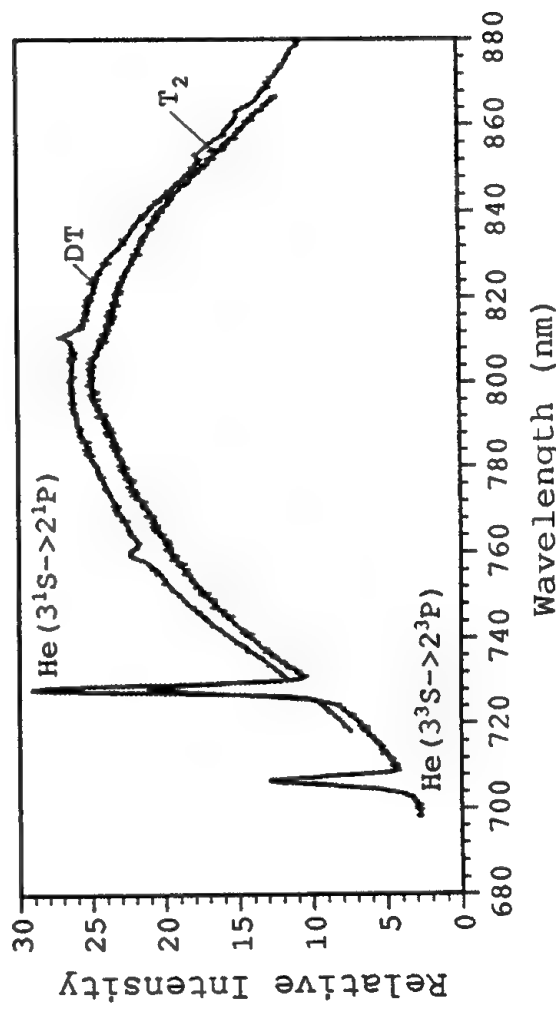


Figure 2: Comparison of NIR features in DT and T_2

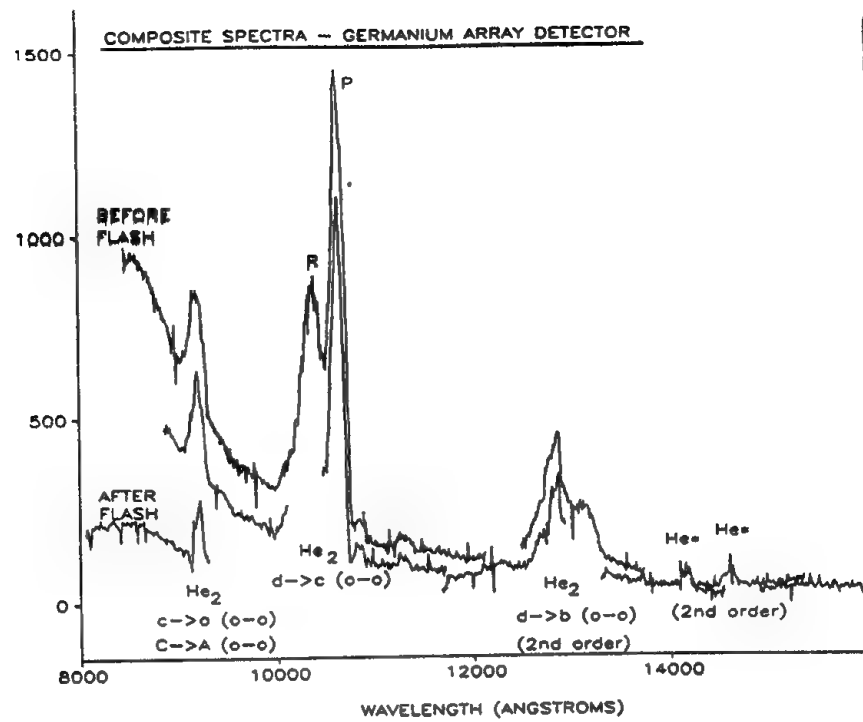


Figure 3: Infrared emission from DT at 4.2 K

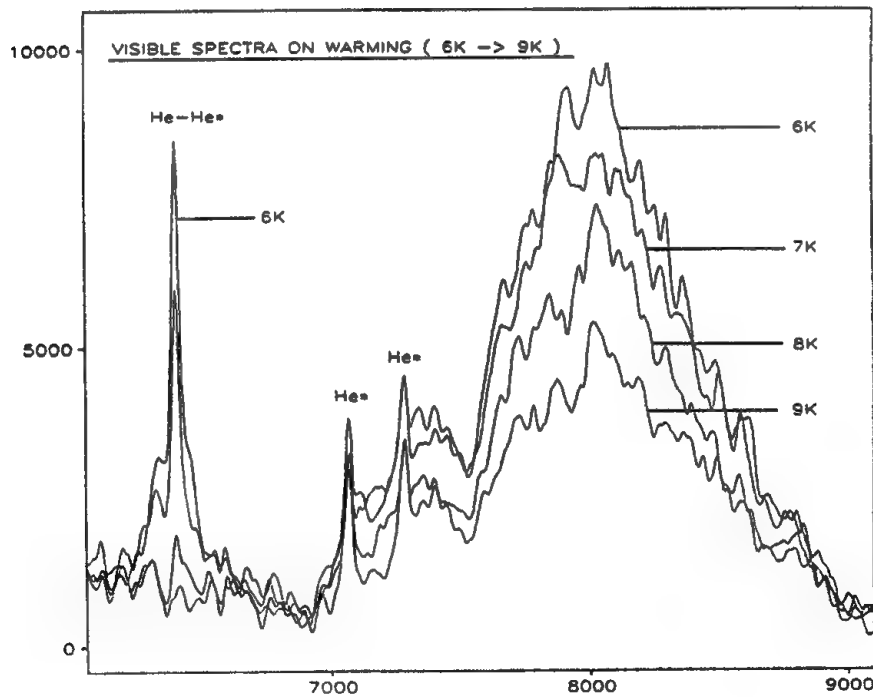


Figure 4 :Temperature dependence of NIR features in solid DT

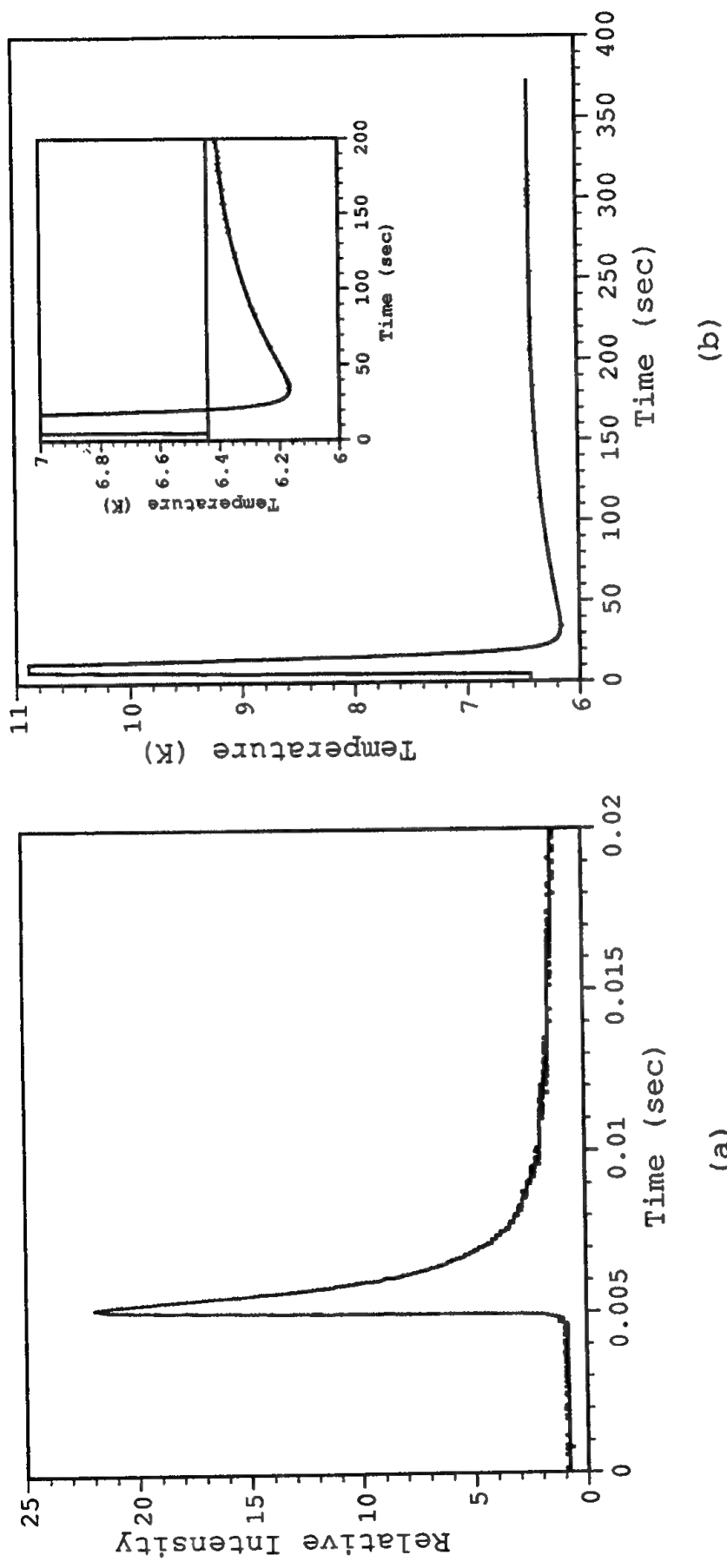


Figure 5: Time resolved triggered optical (a) and thermal (b) pulses.
Note difference in time scales.

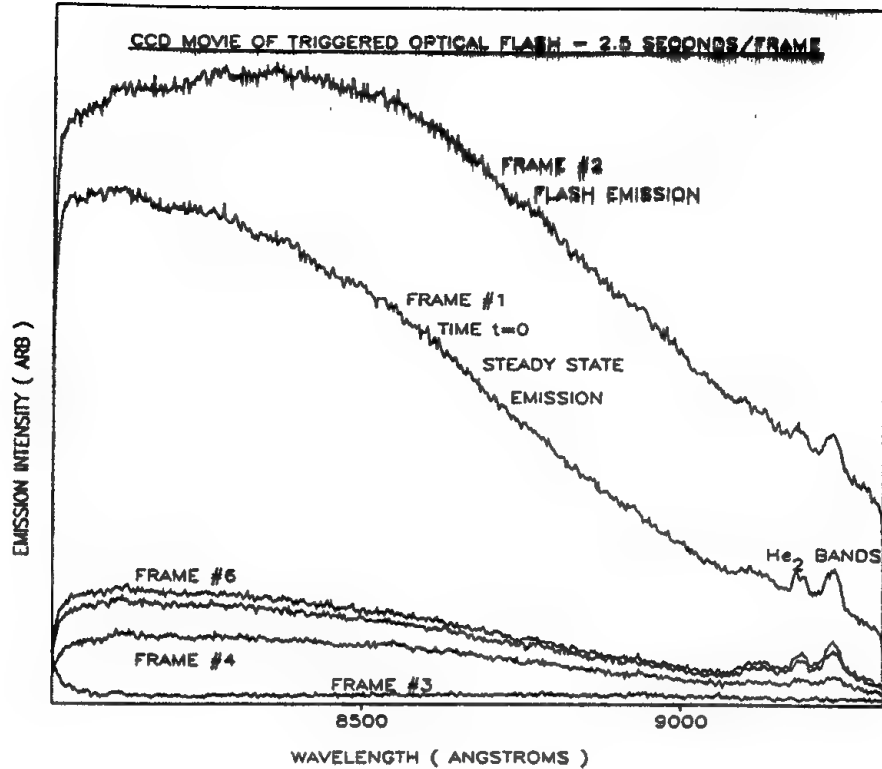


Figure 6 : CCD spectra of 800 nm peak, before, during and after a triggered flash, taken at 2.5 seconds / frame

VARIABLE ENERGY PHOTOELECTRON SPECTROSCOPY OF VOLATILE FLUORIDES

Ronald G. CAVELL

Dept of Chemistry, University of Alberta,
Edmonton, Alberta, Canada T6G 2G2

INTRODUCTION

In collaboration with G. M. Bancroft of the University of Western Ontario, we have installed a very high resolution photoelectron spectrometer on the Aladdin storage ring at the Synchrotron Radiation Center, University of Wisconsin, Madison, Wisconsin. The facility is comprised of two monochromators on two beam lines and is named the Canadian Synchrotron Radiation Facility (CSR). This combination has provided excellent resolution for gas phase photoelectron spectroscopy of both valence (20 - 50 eV) and core (50 - 2000 eV) regions. There is also a facility for gas phase absorption spectroscopy throughout the energy range. Facilities are also available for solid state and surface studies with these monochromators but this area will not be covered in this presentation.

EQUIPMENT

Monochromators:

Low Energy (20 - 800 eV) Grasshopper grazing incidence
High Energy (1500 - 2000 eV) Double Crystal Monochromator

Electron Spectrometer:

36 cm mean radius electrostatic deflection (0.02% resolution)
with heated sample cell

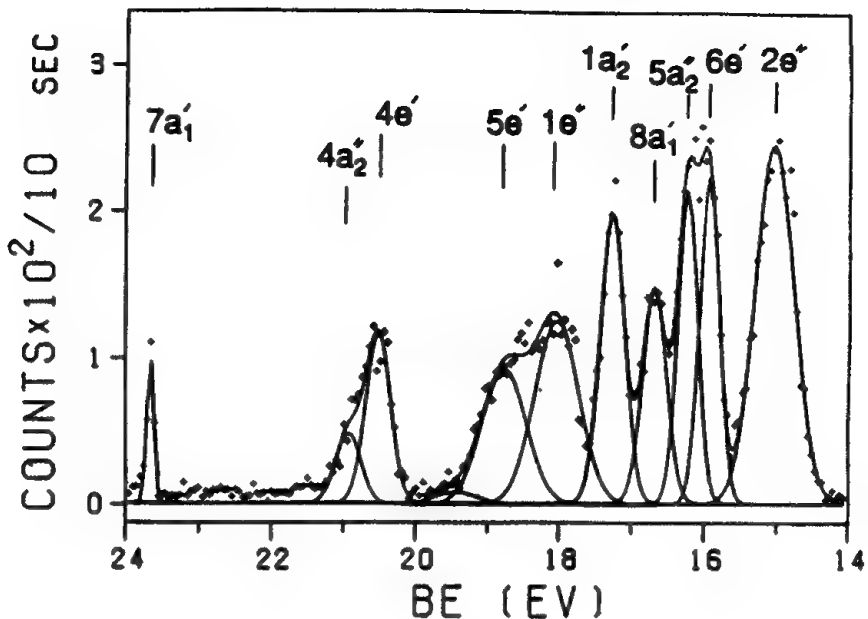
RESULTS

As illustrations of the capabilities of the system a few examples of studies on phosphorus compounds will be described.

Valence Photoelectron Spectroscopy of PF₅:

Figure 1 shows the valence region photoelectron spectrum of PF₅ obtained with a photon energy of 35eV. Resolution is excellent because the intensity of the photon beam is sufficient to allow minimal slit widths to be used at this photon energy. (The evaluation of the resolution is discussed further below.) The full valence spectrum is obtained for the first time and almost all of the bands are clearly resolved. The assignment is obtained from X α and ab initio calculations of the energy levels and is further aided by an analysis of the variation of the photoelectron branching ratio (Fractional Cross-Sections) with photon energy, a property which is sensitive to the atomic orbital composition of the molecular orbital. The calculated cross sections were determined by Dr. John Tse of the National Research Council of Canada.

FIGURE 1
The Valence Band Spectrum of PF₅
Photon energy = 35 eV



Some valence spectra determined at different photon energies are shown in Figure 2. The assignment of the valence band spectrum of PF₅ incorporating the insights provided by the branching ratio behaviour is given in the table. Note that the calculated energies are not in regular increasing order as would be predicted from an energy calculation only.

To illustrate the resolution capability in the valence region, the inner valence orbital peak (7a₁') is expanded in Figure 3. The full width of the plot is 1 eV. The monochromator resolution, determined by the slit width setting, was about 50 meV. The width of the peak then represents a convolution of the photon bandwidth, the natural lifetime contribution of the ionic state and the analyzer contribution. The latter contribution is thought to be about 5 to 10 meV so the major contributions are the monochromator and lifetime contributions. This is a highly symmetric state made up of mostly P(3s) and Fσ bonding orbitals so the band is narrow. The narrow band shows some structure with a spacing of 100 meV which we tentatively assign to P-F vibrational splitting. The value of 800 cm⁻¹ is an appropriate value for a PF ion.

Core (P2p) Spectroscopy of PH₃:

The resolution capabilities of the system are further illustrated by the phosphorus 2p spectrum of PH₃ shown in Figure 4. The spectrum was excited with a photon energy of 190 eV and the slits were set to provide a photon bandwidth of 220 meV. The main spin orbit component peaks are clearly separated, a situation which

is unprecedented for normal laboratory photoelectron exciting sources (soft X-ray Mg or Al tubes). The band width is almost exclusively determined by the photon bandwidth. There is also clearly resolved a small shoulder on each main peak at a spacing of 300 meV (2400 cm^{-1}) which is due to the P-H vibrational component on this core state. This assignment is reinforced by data obtained for SiH_4 and SiD_4 by Bancroft and his students. The vibrationally excited components comprise about 25% of the intensity of the main line, a much smaller fraction than in the case of SiH_4 .

FIGURE 2

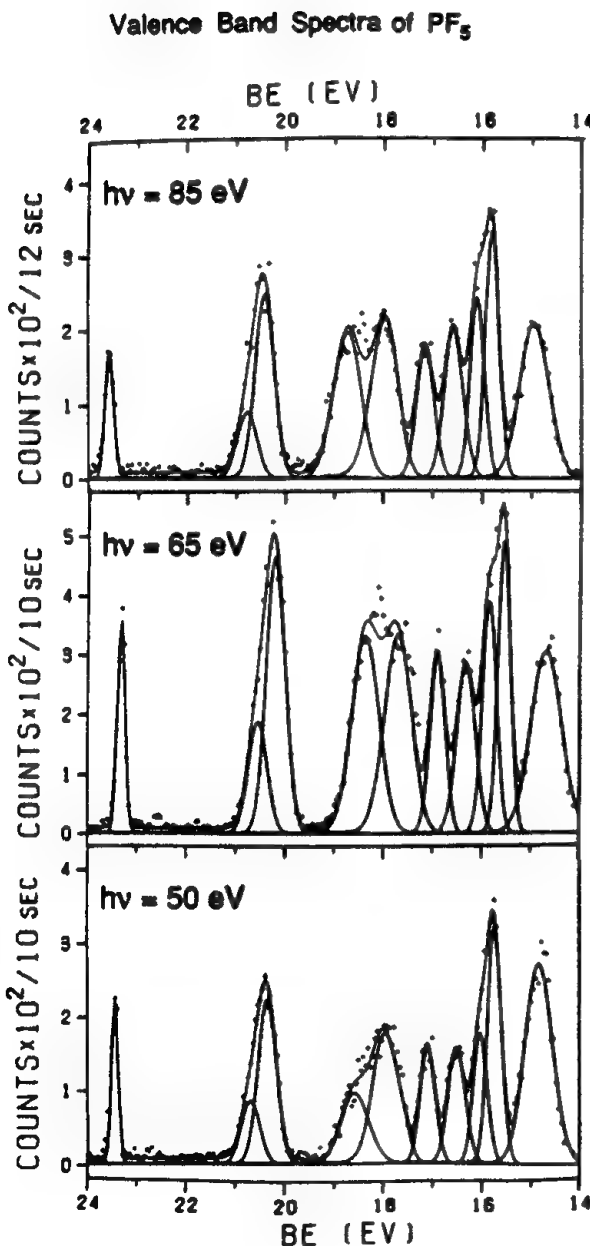


FIGURE 3

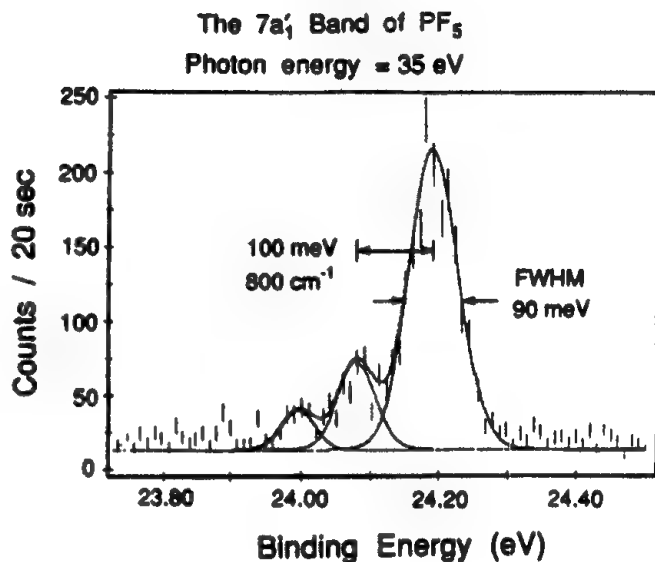
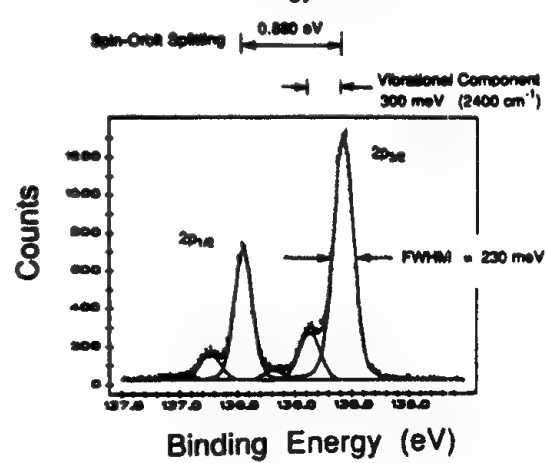


FIGURE 4

The 2p Core Level Spectrum of PH_3

Photon energy = 190 eV



PHOTOELECTRON SPECTRUM OF PF₅

Molecular Orbital	E _B (calc) (eV)	E _B (expt) (eV)	Dominant Character	Lit*
2e"	17.5	15.6	ax F(lone pair)	15.6 (6e', 8a ₁ ')
6e'	18.1	16.5	ax F(lone pair)	16.5 (2e'')
5a ₂ "	18.4	16.8	σPF(ax+eq)	(16.8)(not resol) (5a ₂ " or 8a ₁ ')
8a ₁ '	18.7	17.2	σPF(axial)	(17.2) (not resol) (8a ₁ ')
1a ₂ '	19.1	17.8	lp eq F no P	17.8 (1a ₂ ')
1e"	21.3	18.6	σPF eq	(19.5)(sh)
5e'	20.3	19.4	P + lp F eq	18.6 } (1e'', 5e'')
4e'	22.9	21.0	σPF eq	>20 br } (4a ₂ "', 4e')
4a ₂ "	22.7	21.6	σPF ax	19.1 }
7a ₁ '	25.9	24.2	P _{3g} + Fσ	not observed

*Cox et al., Disc. Faraday Soc. 1972 No. 54 p.126.

ACKNOWLEDGEMENTS:

Co-Workers: Kim Tan at CSRF
 I. J. Vayrynen at The University of Turku, Finland
 John Tse at the National Research Council of Canada

I also thank Ouwen Zhang (Univ of Alberta) for assistance with the fitting of the spectra.
 and the staff of the Synchrotron Radiation Centre (SRC), Univ of Wisconsin,
 for general assistance to The Canadian Synchrotron Radiation Facility (CSRF)

Financial Assistance:

National Science Foundation for support of Aladdin at SRC
 at the University of Wisconsin
 National Research Council of Canada for support of J. Tse
 The Finnish Academy of Sciences for support of I. J. Vayrynen
 The Natural Sciences and Engineering Research Council of
 Canada for support of CSRF
 The University of Alberta for assistance to R. Cavell

Photochemical Synthesis of N₆

Thomas Seder
Molecular Dynamics
Rockwell International Science Center
1049 Camino Dos Rios
Thousand Oaks, CA 91360

The N₆ molecule is a potentially useful monopropellant owing to its high heat of formation ($\Delta H_f > 200$ kcal/mole). Since Vogler¹ has previously claimed to have observed an N₆ photoproduct, and the results of recent ab initio calculations^{2,3,4} indicate that at least two of the many possible structural forms of this highly energetic species may have a lifetime of days at cryogenic temperatures, we have initiated a company funded IR&D program to synthesize and characterize N₆. The two most likely structures are the D_{6h} 'benzene' structure² and trans open structure of C_{2h} symmetry^{3,4}. Our synthetic approach involves preparation of these structures of the pseudo-dihalide as products of photoinduced reductive elimination reactions of azido-metal systems. This approach is based on both Vogler's results for the (PPh₃)₂Pt(N₃)₂ system, as well as the results for analogous halide-metal systems⁵ where upon excitation of ligand-to-metal charge transfer (LMCT) band the central metal experiences a two electron reduction and a dihalide product is eliminated via a concerted mechanism that does not involve formation of halide radicals;



We have been elucidating the charge transfer photochemistry of the analogous [Pt(N₃)₆]²⁻ system in our IR&D program. To date we have synthesized gram sized quantities of the [As(C₆H₅)₄]₂Pt(N₃)₆ precursor. This precursor compound was chosen for a variety of reasons. First, it does not exhibit the explosive behavior which is characteristic of many metal azides. Its stability results from physical separation of the energetic ligands of the neighboring metal azide anions by the exceedingly large size of the As(Ph)₄⁺ cations⁶. Second, this compound undergoes the required reductive elimination process upon charge transfer excitation⁷, and it exhibits a CT band at 308 nm, the wavelength of the XeCl excimer laser⁸. Finally, it is soluble in desirable glass forming organic solvents. The synthesized [As(C₆H₅)₄]₂Pt(N₃)₆ precursor has been characterized using uv-vis and infrared spectroscopy, and melting point determinations have demonstrated that the prepared solid samples are of high purity. The solid has been found to be stable indefinitely when stored in the dark under an argon atmosphere. However, CH₂Cl₂ and CH₃CN solutions of the azido-platinato complexes are unstable, lasting only a few hours in a undarkened room.

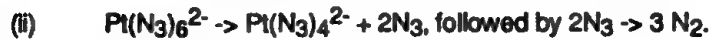
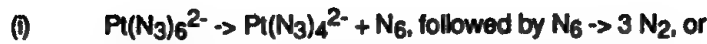
Flash photolysis experiments on de-aerated room temperature CH_2Cl_2 solutions of the hexaaazidoplatinate complex have been performed to verify that single photon irradiation of a MTLCT band^{6,7} induces the redox process,



Photolysis of 10^{-5} molar solution was conducted in a uv grade quartz cuvette using a single 50 mJ/cm² pulse (15 ns) from a 308 nm XeCl excimer laser. The rectangularly shaped output from the excimer laser was rotated with a periscope so that the entire solution was irradiated with the single pulse. Approximately 7% of the platinate complexes absorb a single photon under these conditions. Changes in the uv-vis (220-420 nm) absorption spectrum were detected with a spectrometer consisting of a gated optical multichannel analyzer (100 ms integration time, 0 ms delay) and a deuterium lamp source. Absorption spectra that were obtained under these conditions are displayed in Fig. 1. The heavy lined spectrum was obtained with the excimer laser blocked and the other spectrum was obtained upon 308 nm photolysis. The stationary bands at 225-, 259-, 265- and 271-nm are those of the $[\text{As}(\text{C}_6\text{H}_5)_4]^+$ cation. The band at 308 nm that diminishes upon photolysis is that of the hexaaazidoplatinate(IV) precursor, while the band that grows in at 250 nm is assignable to the tetraazidoplatinate(II) product. Thus, we have demonstrated that 308 nm excimer laser photolysis induces the above reductive elimination process.

The quantum yield of the $\text{Pt}(\text{IV}) \rightarrow \text{Pt}(\text{II})$ process has also been deduced from the transient spectrum. Subtraction of the spectrum having the excimer laser blocked from the flash photolysis spectrum produces the difference spectrum shown in Fig. 2. There are a couple of observations of importance. First, the magnitude of the Pt(IV) band is as expected on the basis of a calculation that considers the initial absorber concentration, the extinction coefficient of the absorber and the photolysis laser fluence. Thus, each absorbing molecule decomposes. Second, the ratio of the Pt(IV) to Pt(II) band intensity is 1.8, while the ratio of the Pt(IV) to Pt(II) band extinction coefficient^{8,8} is 1.9. Thus, the quantum yield of $\text{Pt}(\text{IV}) \rightarrow \text{Pt}(\text{II})$ is unity within experimental error. We note that the potential Pt(III) intermediate could not be detected via ESR upon photolysis of $\text{Pt}(\text{CN})_4(\text{N}_3)_2$ in ethanol glasses⁸, and is not expected to be formed in our experiments. This type of reductive elimination reaction has been shown in the past to proceed via simultaneous two electron transfer to the metal center^{7,9}.

Two other important observations were noted while conducting the above experiments. First, bubbles of N_2 , were observed to be evolved from the solution subsequent to each excimer laser pulse. This indicates that one of the two following processes is occurring:



The second important observation noted while conducting the above experiments is that colloidal platinum metal is formed upon prolonged photolysis. This has been previously observed⁷ and has been ascribed to a second single photon two-electron reductive elimination pathway,



We are currently in the process of distinguishing between the two pathways by attempting ESR detection of the N_3^\cdot radical.

1. Vogler, A., Wright, R.E. and Kunkely, H. *Angew. Chem. Int. Ed. Engl.* 19, 717 (1980).
2. Saxe, P. and Schaefer, H. F. *J. Am. Chem. Soc.* 105, 1760 (1983).
3. Ha, T-K., Cimiraglia, R. and Nguyen, M. T. *Chem. Phys. Lett.* 83, 317 (1981).
4. Brener, N., LSU, personal communication.
5. Penkett, S. A. and Adamson, A. W., *J. Am. Chem. Soc.* 87, 2514 (1965).
6. Beck, W., Fehlhammer, W. P., Pollman, P., Schulerer, E. and Feldl, K., *Chem. Ber.* 100, 2335 (1967).
7. Vogler, A. and Hlavatsch, J., *Angew. Chem. Int. Ed. Engl.* 22, 154 (1983).
8. Schmidke, H-H. and Gartoff, D., *J. Am. Chem. Soc.* 89, 1317 (1967).
9. Vogler, A., Kern, A. and Huttermann, J., *Agnew. Chem. Int. Ed. Engl.* 17, 524 (1978).

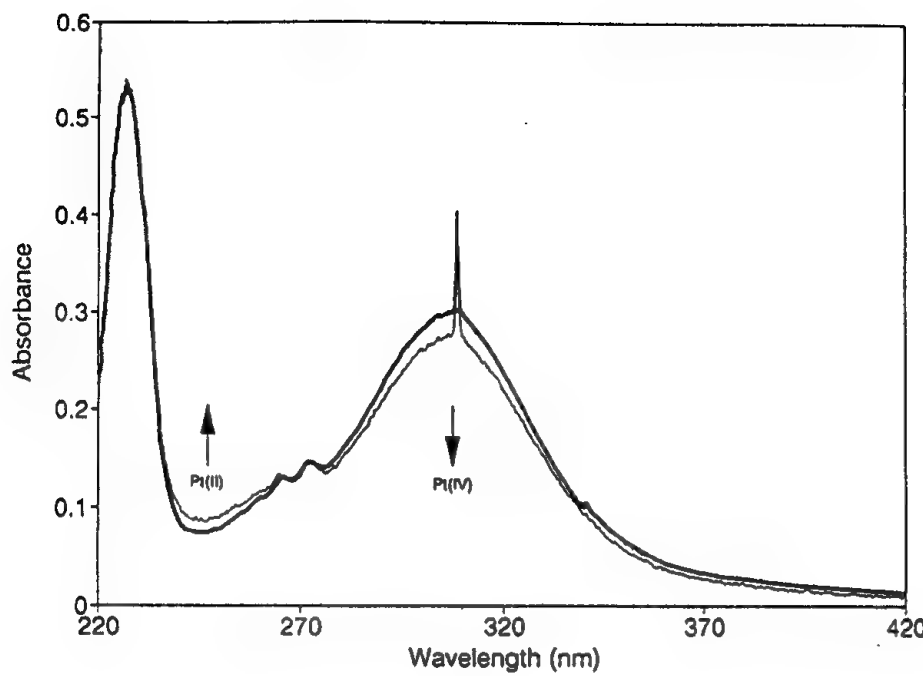


Fig.1 Gated OMA Spectra

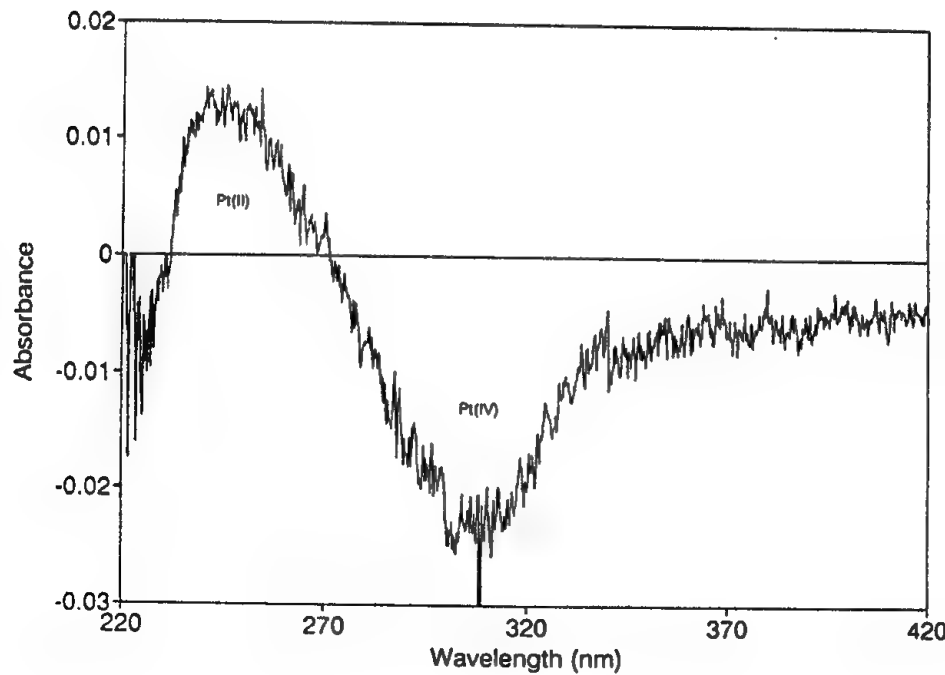


Fig.2 Difference spectrum

**Matrix Reactions of Boron Atoms with Molecular Oxygen: Infrared Spectra of
BO, BO₂, B₂O₂, B₂O₃ and BO₂⁻ in Solid Argon**

Thomas R. Burkholder, G. Dana Brabson and Lester Andrews

*Chemistry Department, University of Virginia,
McCormick Rd., Charlottesville, VA 22901*

Boron atoms, generated by Nd:YAG laser ablation, were codeposited with dilute O₂/Ar mixtures onto a CsI window at 12K and the FT-IR spectra of the reaction products were recorded. A schematic diagram of the apparatus used for boron atom reactions is shown in Figure 1. The concentration of O₂ in Ar was 1:200 O₂:Ar, while the boron concentration was kept in the 1:1000 to 1:3000 B:Ar range.

Figure 2 shows a typical series of spectra obtained; upon deposition, the strongest absorptions were observed in the B-O stretching region at 1299.3, 1282.8 and 1274.6 cm⁻¹ with a corresponding set of bands at 1347.6, 1331.0 and 1322.3 cm⁻¹. These bands have an intensity ratio of 4:1 indicative of natural ¹¹B and ¹⁰B isotopic absorptions for a species containing a single boron atom. The use of a ¹⁰B sample confirmed this interpretation. Mixed ¹⁶O/¹⁸O experiments give triplets for each band with 1:2:1 intensity ratios consistent with a species containing two oxygen atoms and allow assignment of the frequencies to ¹¹BO₂ and ¹⁰BO₂ respectively. The observed bands bracket the 1278.3, 1326.1 cm⁻¹ gas phase absorptions¹ for BO₂ and are assigned to different argon matrix packing effects. The boron and oxygen isotopic shifts are

appropriate for a linear molecule with substantial quartic anharmonicity in the v_3 coordinate. The present observation of BO_2 is in agreement with earlier matrix work where BO_2 was generated from a $\text{ZnO}/\text{B}_2\text{O}_3$ mixture.²

Also observed upon deposition were absorptions at 1930.9 cm^{-1} and 2000.0 cm^{-1} displaying the same isotopic patterns as BO_2 for $^{11}\text{B}/^{10}\text{B}$ and $^{16}\text{O}/^{18}\text{O}$ experiments. Literature values for metaborate ions in alkali halide pressed disks show that the v_3 frequency of BO_2^- decreased as the polarity of the matrix decreased, from 1995 cm^{-1} in NaCl to 1948 cm^{-1} in CsBr and infrared spectra of alkali metaborates in an argon matrix show that the v_3 stretching frequency shifts from 1975.8 cm^{-1} for LiBO_2 to 1945.6 cm^{-1} for CsBO_2 .^{3,4} Extrapolation to the low polarity argon matrix showed that the observed frequencies are appropriate for $^{11}\text{BO}_2^-$ and $^{10}\text{BO}_2^-$ ions isolated in solid argon. The observed isotopic data are in accord with a linear anion which is consistent with the isoelectronic CO_2 molecule.

Based on gas phase measurements and ^{10}B and $^{18}\text{O}_2$ data it was possible to assign the band at 1854.8 cm^{-1} to the diatomic species BO . The gas phase fundamental⁵ of BO comes at 1862.1 cm^{-1} and the matrix shift is remarkably small, only 7.3 cm^{-1} ; these characteristics imply that the molecule has a small dipole moment compared to a more ionic species such as LiO which shows a larger matrix shift.^{6,7} The BO absorption is weak when compared to BO_2 and BO_2^- even though it should be a major component in the product mixture.

On annealing of the matrix to 25K, the BO band decreased and absorptions at 1898.9, 1920.3 and 1955.5 cm^{-1} increased. These bands had intensity ratios of 16:8:1 which is appropriate for the $^{10}\text{B}/^{11}\text{B}$ isotope pattern for a species containing two equivalent boron atoms. Mixed $^{16}\text{O}/^{18}\text{O}$ isotope experiments showed a triplet with the intensity ratio of 1:2:1; the molecule possesses two equivalent oxygen atoms. B_2O_2 was previously observed in the argon matrix from the high temperature reaction of a $\text{B}_2\text{O}_3/\text{B}$ mixture, and the present B_2O_2 observations are in agreement.²

Spectra taken after annealing of the matrix to 25K showed several new absorptions, one set at 2061.2 and 2130 cm^{-1} and one at 1512.3 cm^{-1} . The absorption at 2061.2 splits into a doublet of doublets in the mixed $^{16}\text{O}/^{18}\text{O}$ experiment and is in good agreement with literature reports for B_2O_3 .²

The observed band at 1512.3 cm^{-1} becomes a triplet with mixed isotopic oxygen showing a 1:2:1 intensity ratio. These bands are in good agreement with predicted shifts for diatomic O_2 ; an experiment with alternating layers containing B atoms with Ar and O_2 with Ar showed small amounts of the normally observed products but annealing produced the 1512.3 cm^{-1} absorption in good yield. This evidence supports a complex of B atoms with molecular oxygen. The band decreased about 10% on 254 nm irradiation, which suggests that the complex reacts to give BO_2 .

Matrix isolation techniques were used, successfully, to trap intermediates of boron atom-oxygen reactions; an unreacted $\text{B}^{\cdot\cdot}\text{O}_2$ complex was observed as well as a number of small boron oxides including BO , BO_2 , BO_2^- , B_2O_2 and B_2O_3 .

References:

- (1) Kawaguchi, K.; Hirota, E.; Yamada, C.; *Mol. Phys.* **1981**, *44*, 509.
- (2) Sommer, A.; White, D.; Linnevsky, M.J.; Mann, D.E. *J. Chem. Phys.* **1963**, *38*, 87.
- (3) Hisatsune, I.C.; Suarez, N.H. *Inorg. Chem.* **1964**, *112*, 3332.
- (4) Teghil,R.; Janis,B.; Bencivenni,L. *Inorg. Chim. Acta.* **1984**, *88*, 115.
- (5) Huber, K.P.; Herzberg, G. *Constants of Diatomic Molecules* VanNostrand Rinehold: N.Y., 1979.
- (6) Buchler, A.; Stauffer, J.L.; Klemperer, W.; Warton, L. *J. Chem. Phys.* **1963**, *39*, 2299.
- (7) Spiker, Jr., R.C.; Andrews, L. *J. Chem. Phys.* **1973**, *58*, 702.

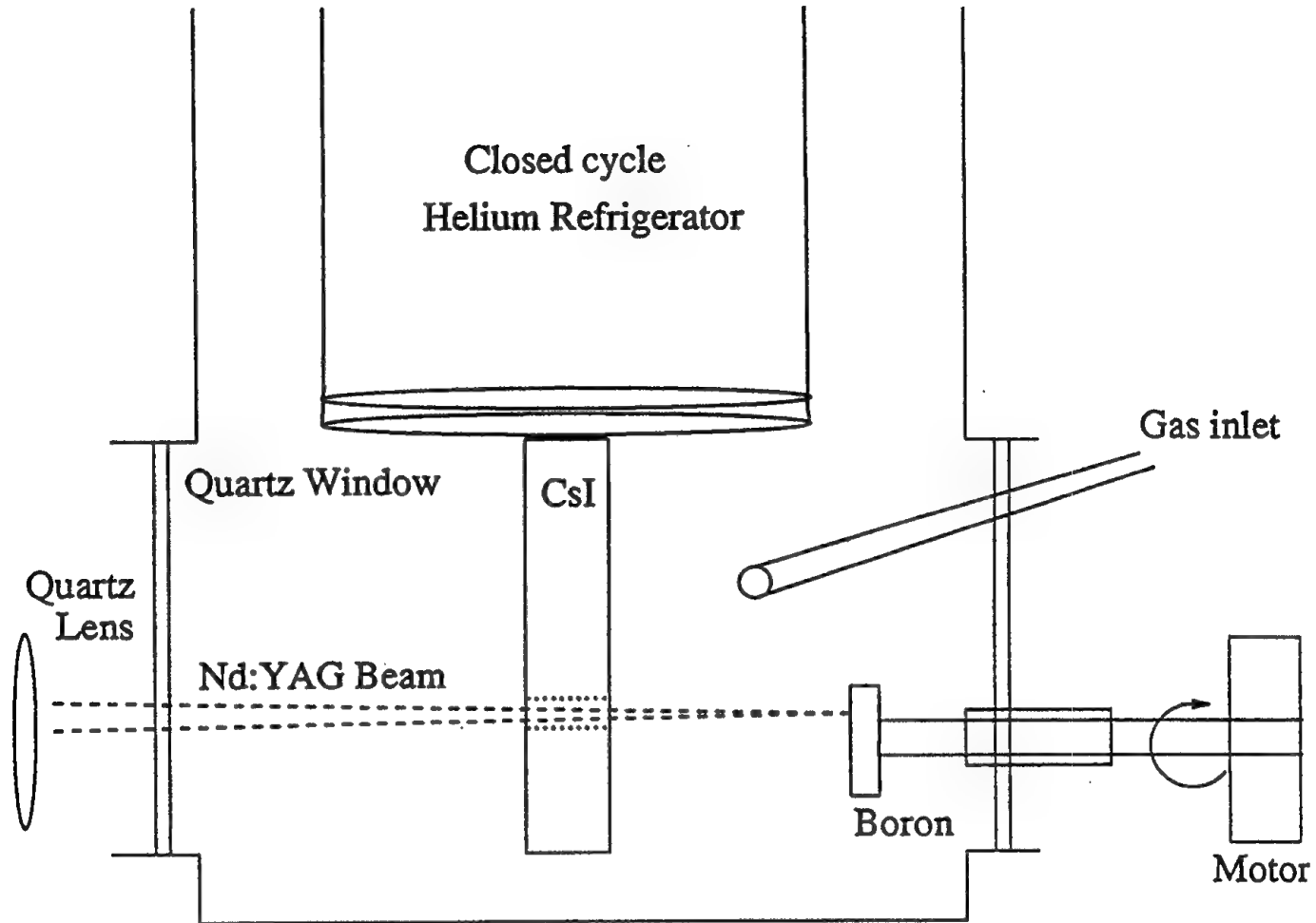


Figure 1. Schematic diagram of matrix-isolation apparatus used for boron atom reactions. Boron is mounted on a rotatable rod for ablation with the YAG laser beam and codeposition with a stream of argon gas on a 12K CsI window. Reagent molecules can be directed into the laser plume or separately into the matrix. The center cold window is rotated to record spectra.

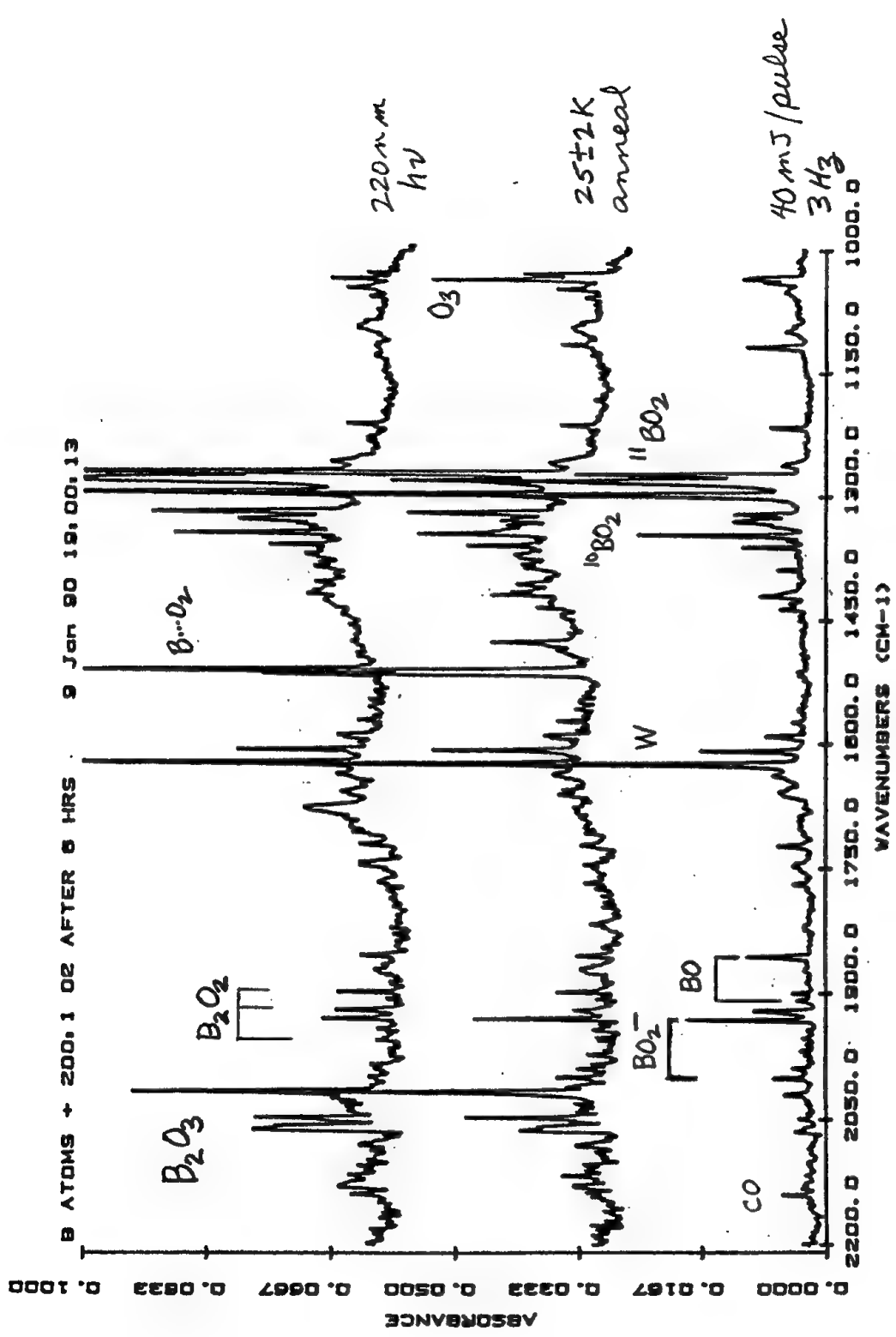


Figure 2. Infrared spectra in the 1000-2200 cm⁻¹ region for B atoms codeposited with O₂ molecules in excess argon.

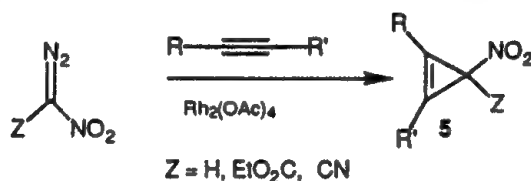
**SYNTHESIS AND PROPERTIES OF NOVEL NITROCYCLOPROPENES AND
AB INITIO CALCULATIONS ON POTENTIAL HIGH ENERGY DENSITY
MATERIALS**

William P. Dailey, Department of Chemistry
University of Pennsylvania, Philadelphia, PA 19104-6323

Recently there has been considerable interest in strained ring nitro compounds as high-energy density materials.¹ Our work in this area has focused on nitrocyclopropanes. While there are several methods for nitrocyclopropane formation,² the addition of a nitrocarbene to an alkene has only recently been described by us.³

Because of the high strain energy associated with the cyclopropene skeleton (55 kcal/mol), cyclopropenes offer promise as potential energetic materials. Here we describe the formation of nitrocyclopropenes **5** from nitrodiazo compounds **1-3** and alkynes (Scheme I). These results are presented in Table 1 along with the corresponding data for ethyl diazoacetate (**4**).⁴

Scheme I



5a	R₁	R₂	Z
5b	<i>n</i> -Pentyl	H	H
5c	Me	Me	H
5d	TMS	H	H
5e	Ph	H	CN
5f	<i>n</i> -Bu	H	CN
5g	Et	Et	CN
5h	TMS	H	CN

Table 1. Yields of Cyclopropenes from Alkynes and Diazo Compounds using $\text{Rh}_2(\text{OAc})_4$.

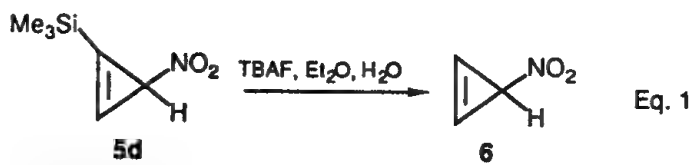
	1	2	3	4^a
PhCCH	60	65	b	0
<i>n</i> -ButylCCH	33 ^c	35	84	84
RCCR	35 ^d	35 ^e	0	68 ^d
TMSCCH	30	28 ^f	0	86
PhCCPh	0	0	0	-

^a Taken from ref 4. ^b Product was formed but could not be purified beyond 60% purity.

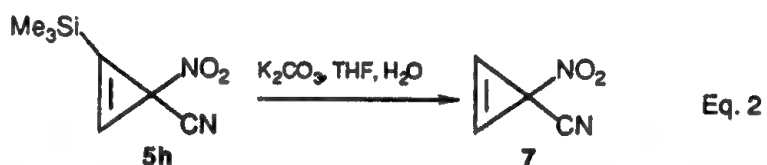
^c Reaction was carried out with 1-heptyne. ^d Reaction was carried out with 2-butyne.

^e Reaction carried out with 2-hexyne. ^f This compound was not purified but was converted directly to 3-cyano-3-nitrocyclopropene in 28% overall yield.

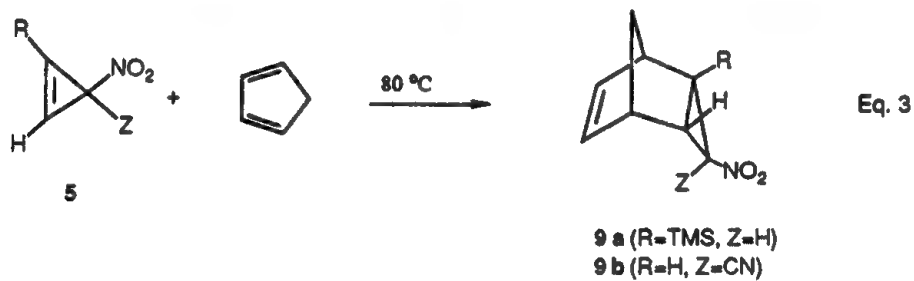
The parent 3-nitrocyclopropene (**6**) and 3-cyano-3-nitrocyclopropene (**7**) can be obtained from the corresponding trimethylsilyl substituted cyclopropenes **5d** and **5h**. In the case of nitrocyclopropene, deprotection with TBAF in wet diethyl ether affords a ca. 5% solution of nitrocyclopropene (Eq. 1). This material can be detected by NMR and by TLC. Our attempts to isolate **6** have been unsuccessful.



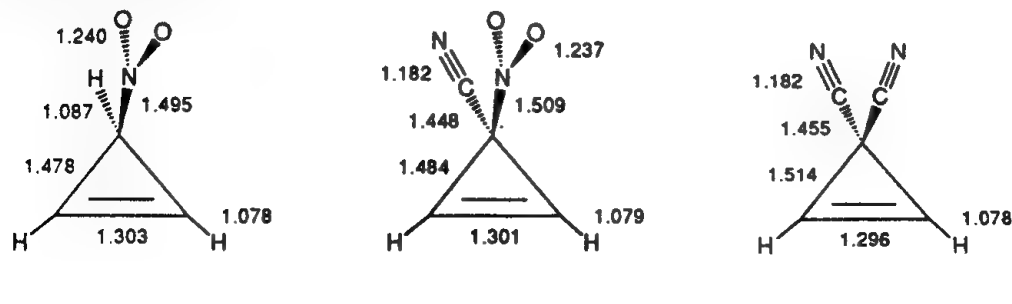
3-Cyano-3-nitrocyclopropene (**7**), on the other hand, is a relatively stable compound as a neat liquid at room temperature. It is prepared by potassium carbonate hydrolysis of the trimethylsilyl derivative **5h** (Eq 2).



With the exception of **6**, all of these compounds are stable to air at room temperature for several days. On heating or stirring with acid they do decompose to give uncharacterizable polar materials. Nitrocyclopropenes derived from **1** solvolyze readily in hydroxylic solvents while those derived from **2** are stable to solvolysis. These compounds undergo a Diels-Alder reaction with cyclopentadiene to afford stable adducts **9** which may be fully characterized. For instance, heating nitrocyanocyclopropene (**7**) with cyclopentadiene afforded a single isomer **9b** (Eq. 3). In this case the stereochemistry of the adduct was determined by x-ray crystallography. As further proof of structure we have determined the crystal structure of 1-nitro-2-phenylcycloprop-2-enecarbonitrile (**5e**).



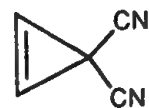
Ab initio calculations were carried out on several cyclopropenes at the MP2/6-31G* level. The results are shown below.



Using Schleyer's group equivalent method⁵ for converting total energies to heats of formation, we calculate $\Delta H_f = 90$ and 135 kcal/mol for 3-cyano-3-nitrocyclopropene and 3,3-dicyanocyclopropene, respectively. Both of these compounds are excellent candidates as novel high energy fuels.



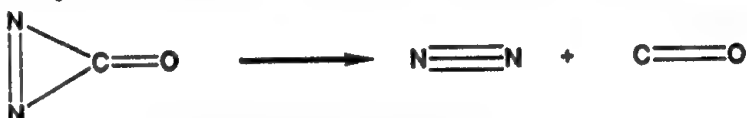
$$\Delta H_f = 90 \text{ kcal/mol}$$



$$\Delta H_f = 135 \text{ kcal/mol}$$

Diazirinone - a Potential High Energy Density Material

Diazirinone (diazacyclopropenone) is an unknown compound. Because of the potentially large driving force for its decomposition to dinitrogen and carbon monoxide, diazirinone is a potential candidate as a high energy material. We have undertaken a computational study of diazirinone to determine its potential stability.⁶



The structure of diazirinone was calculated with the 6-31G* basis set at the HF, MP2 and CISD levels of theory using the Gaussian 82, 86, 88 and 90 series of programs

Calculated Structure, Energy, and Dipole Moment of Diazirinone using the 6-31G* Basis Set.

	HF	MP2	CISD
Dipole Moment	1.35	0.73	1.07
r(N-N)	1.267	1.349	1.295
r(C-N)	1.347	1.395	1.368
r(C-O)	1.173	1.197	1.185
Total Energy	-221.5179	-222.14732	-222.06559

Bond lengths in angstroms, dipole moments in debye and total energy in hartrees.

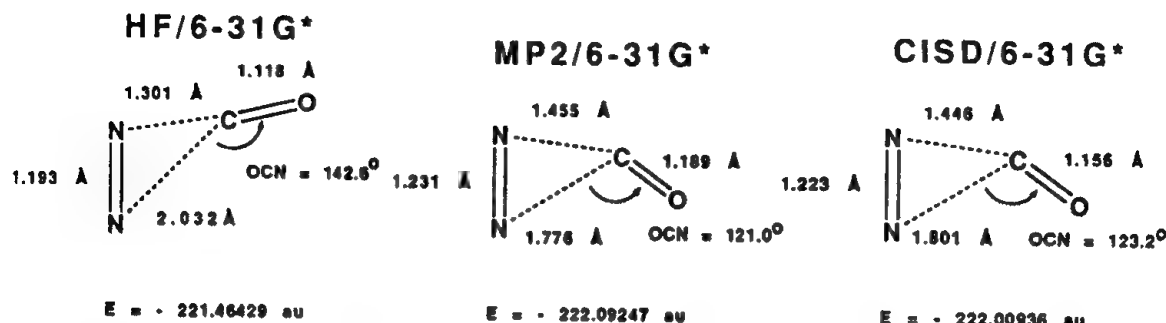
Frequency calculations were carried out at each level and are shown below. Characterization of diazirinone by IR spectroscopy may be somewhat difficult because the only intense band in the IR spectrum, corresponding to the C=O stretch, will be very close to that for carbon monoxide. The N=N stretch is predicted to have little intensity.

Calculated IR Spectrum for Diazirinone

HF/6-31G*		MP2/6-31G*		CISD/6-31G*	
freq	int	freq	int	freq	int
2250	682	2085	353	2179	514
1686	16	1242	2	1549	4
1170	6	1048	39	1113	12
1072	4	913	5	1007	5
653	50	570	28	607	38
617	24	535	11	578	19

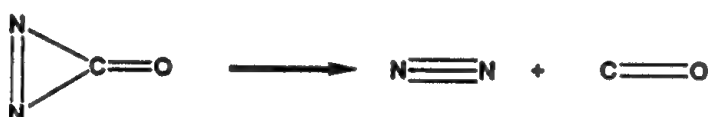
Frequencies in cm^{-1} , intensities in km/mol .

Transition structure calculations were performed for the decomposition of diazirinone to dinitrogen and carbon monoxide. The calculated structures at the HF, MP2 and CISD levels are shown below.



The activation barrier and energy of reaction for decomposition of diazirinone to dinitrogen and carbon monoxide were calculated at various levels of theory and the results are shown in the table. Thus diazirinone should have a reasonable barrier to decomposition and the reaction should be exothermic by about 90 kcal/mol.

Calculated Activation Barriers and Energies of Reaction (kcal/mol) for the Decomposition of Diazirinone Using the 6-31G* Basis Set



method	$\Delta E^\ddagger + \text{ZPE} =$	$\Delta E =$
HF	31.6	-102
MP2	32.4	-75
MP3 ^a	31.9	-80
CISD	33.2	-93
MP4SDTQ ^a	27.8	-75
QCISD(T) ^b	25.2	-90

^a Single point calculation employing MP2 optimized geometries. ^b Single point calculation employing CISD optimized geometries. Energies in kcal/mol. All correlated wavefunctions employed all electrons and all virtual orbitals

Conclusion: Diazirinone will have a reasonable barrier to decomposition and may be a useful high energy material.

References

1. (a) Review: Marchand, A. P. *Tetrahedron* **1988**, 2377. (b) Eaton, P. E.; Ravi Shankar, B. K.; Price, G. D. Pluth, J. J.; Gilbert, E. E.; Alster, J.; Sandus, O. *J. Org. Chem.* **1984**, *49*, 185. (c) Archibald, T. G.; Baum, K. *J. Org. Chem.* **1988**, *53*, 4645. (d) Shen, C.-C.; Paquette, L. A. *J. Org. Chem.* **1989**, *54*, 3324. (e) Murray, R. W.; Rajadhyaksa, S. N. Mohan, L. *J. Org. Chem.* **1989**, *54*, 5783.
2. (a) Asunsakis, J.; Shechter, H. *J. Org. Chem.* **1968**, *33*, 1164. (b) Lampman, G. M. Horne, D. A. Hager, G. D. *J. Chem. Eng. Data* **1969**, *14*, 396. (c) Russell, G. A.; Makosza, M.; Hershberger, J. *J. Org. Chem.* **1979**, *44*, 1195.
3. (a) O'Bannon, P.E.; Dailey, W. P. *Tetrahedron Lett.* **1988**, 987. (b) O'Bannon, P. E.; Dailey, W. P. *J. Org. Chem.* **1989**, *54*, 3096. (c). O'Bannon, P. E.; Dailey, W. P. *Tetrahedron Lett.* **1989**, 4197.
4. Petinot, N.; Anciaux, A. J.; Noels, A. F.; Hubert, H. J.; Teyssie, P. *Tetrahedron Lett.* **1978**, 1239.
5. Ibrahim, M. R.; Schleyer, P. v. R. *J. Comput. Chem.* **1985**, *6*, 157.
6. Portions of these results have been published: J. A. Berson, D. M. Birney, W. P. Dailey and J. F. Lieberman "Ethylenedione, Its Ions and Isoelectronic Analogs" in "Molecular Structure and Energetics", J. F. Lieberman and A. Greenberg, Eds., VCH Publishers, Vol. 6, 1988.

Weak Interactions at Metal Atoms and Clusters Studied with
Electronic Spectroscopy in Supersonic Beams

Michael A. Duncan

Department of Chemistry

University of Georgia

Athens, GA 30602

Light metals such as lithium, magnesium or aluminum are interesting as additives to pure component fuels to achieve advanced heterogeneous propellants. The high exoergicity of oxidation for metals such as these enhances propellant efficiency relative to the respective pure component systems. There is a significant interest, therefore, in the preparation of highly dispersed metal systems and in the fundamental chemical interactions in these systems. In our laboratory, fundamental interactions in highly dispersed metal systems are studied in the gas phase using molecular beam laser spectroscopy and mass spectroscopy methods. These techniques make it possible to study weak interactions at small metal particle surfaces.

Metal atoms and small clusters are produced in a supersonic molecular beam with pulsed-nozzle laser vaporization. van der Waals complexes are formed by seeding the supersonic expansion with rare gas atoms or small molecules (e.g., Ar, N₂, CO₂). Downstream from the source, the neutral species in the molecular beam are probed with resonant two-photon photoionization electronic

spectroscopy (R2PI), while ion complexes are probed with resonant two-photon photodissociation spectroscopy (R2PD). These experiments are performed in a reflectron time-of-flight mass spectrometer system.

Weakly bound complexes of silver dimer have been the subject of prior work in our laboratory,^{1,2} and these systems illustrate the methods to be applied to more relevant metal systems in ongoing work. Complexes of silver dimer with the rare gases argon and krypton are produced by laser vaporization at 308 nm in mixed expansions in helium. R2PI spectra are obtained near the B<-X Ag₂ electronic transition (near 280 nm), with a red-shifted origin band observed for both complex spectra. These spectra are shown in Figures 1 and 2. Analysis of these spectra provide vibrational constants for each of the three coordinates in these two complexes (the solvated metal dimer stretch, the metal dimer-rare gas stretch, and the metal-rare gas bend). The vibrational constants obtained are given in Table 1. Surprisingly, the rare gas stretch and bend frequencies are nearly identical in both complexes. Potential surface analysis provides binding energies for these complexes in their ground and excited states, which are also given in Table 1. Both complexes are significantly more strongly bound in their excited state, with the krypton complex more strongly bound in both its states than the argon complex, as expected.

Ongoing experiments in this area, begun under a new AFOSR contract, will probe weak interactions in lighter metals (lithium, aluminum, magnesium).

References

1. P.Y. Cheng, K.F. Willey and M.A. Duncan, Chem. Phys. Lett. **163**, 469 (1989).
 2. K.F. Willey, P.Y. Cheng, D.L. Robbins, C.S. Yeh, D.K. Hines and M. A. Duncan, J. Chem. Phys., to be submitted.
-

Table 1. Spectroscopic constants for $\text{Ag}_2\text{-Ar}$ and $\text{Ag}_2\text{-Kr}$ complexes.
All entries are given in cm^{-1} units.

	$\text{Ag}_2\text{-Ar}$	$\text{Ag}_2\text{-Kr}$	$^{107,109}\text{Ag}_2$
0-0	35,329	34,998	35,808.7
ω_1'	156.3	157.7	151.3
x_1'	0.71	0.64	0.70
ω_2'	28.3	27.9	-
x_2'	2.73	1.76	-
ω_3'	73.9	72.6	-
x_3'	1.72	1.06	-
$D_0'(\text{Ag}_2\text{-RG})$	755	1205	-
$D_0''(\text{Ag}_2\text{-RG})$	275	394	-
B.E.	808	1258	-

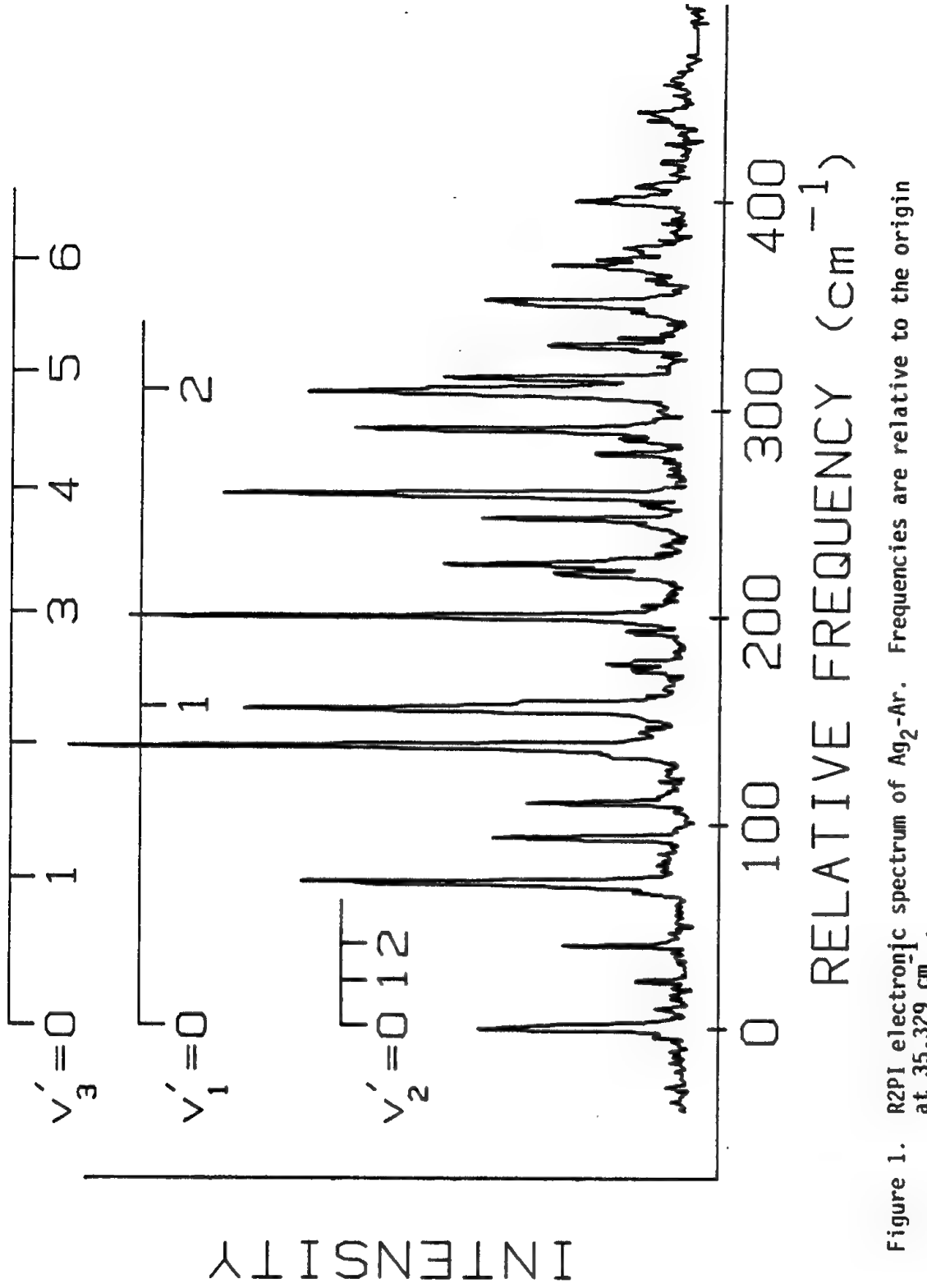


Figure 1. R2PI electronic spectrum of $\text{Ag}_2\text{-Ar}$. Frequencies are relative to the origin at $35,329 \text{ cm}^{-1}$.

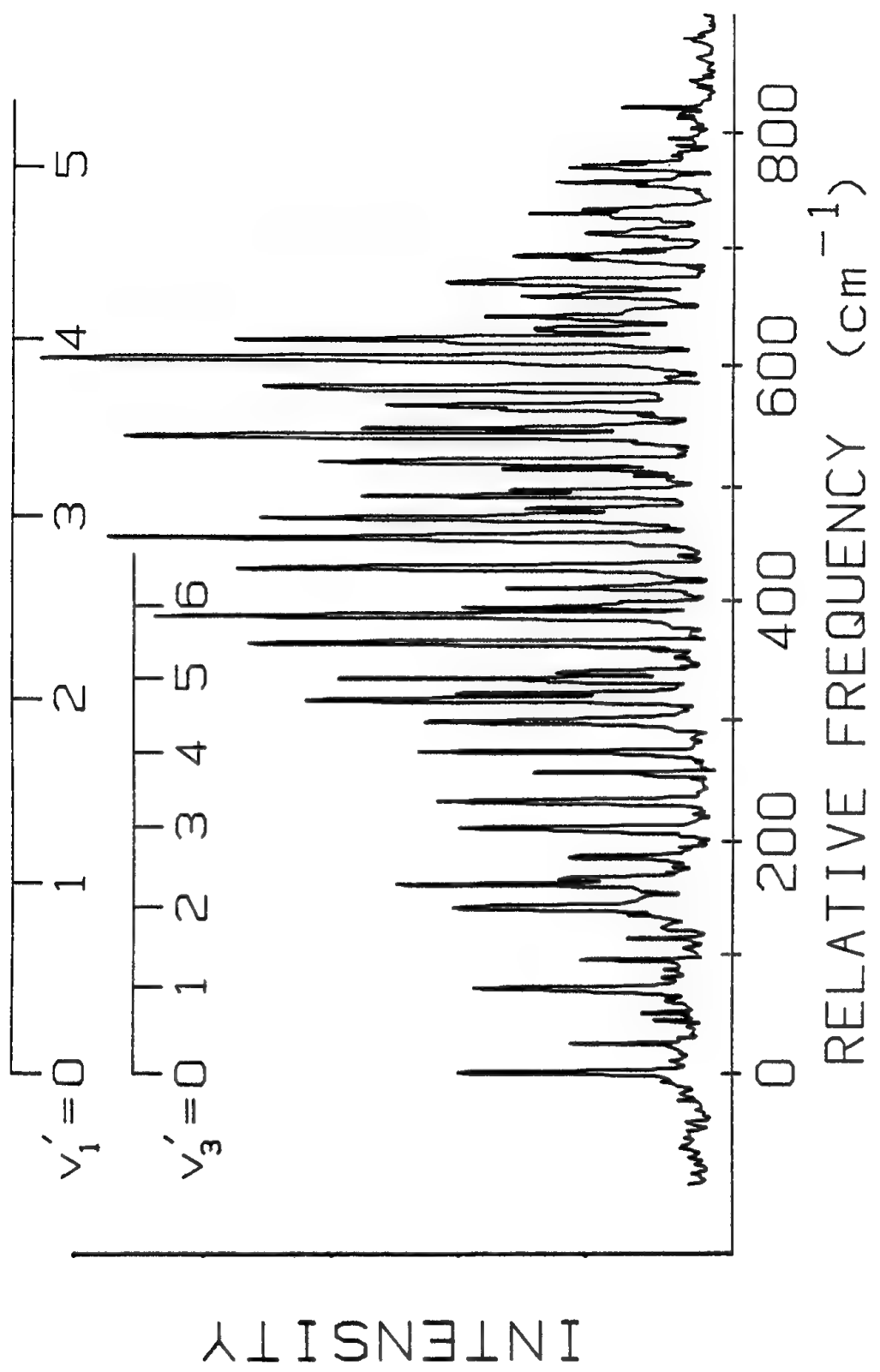


Figure 2. R2PI electronic spectrum of $\text{Ag}_2\text{-Kr}$ with an origin at $34,998 \text{ cm}^{-1}$.

Metastable Metals in Matrix Materials

N. Presser and D. Randall
Chemistry and Physics Laboratory
The Aerospace Corporation

Introduction

We have previously proposed¹ a fuel for improving the Isp of launch vehicles. This fuel consists of free metal atoms (FMAs) and dimers suspended in a weakly binding cryogenic matrix. The stabilization of free metal atoms in a weakly binding matrix eliminates the need to overcome the enthalpies of liquefaction and vaporization and potential energy is thereby stored in the matrix. The optimal matrix material in this kind of fuel is H₂ and the metal must be appropriately chosen.

This concept has been tested by calculating the the potential Isp of various metal matrix fuels using a standard Isp code, EDCONVU. In these simulations O₂ was the oxidant and a statistical model was used to predict the distribution of metal as atoms, dimers and higher clusters. These simulations indicated that there were, indeed, a number of systems which might improve on the Isp of the current standard H₂ + O₂. What was equally evident was that there was only a narrow range of metal atom concentrations over which significant improvement could occur and that what was critical to the success of this type of fuel was attaining sufficient free metal atom concentration.

Quantifying the free metal atom concentration in the matrix accurately is then a major concern. What affects the accuracy of concentration determinations in the matrix, the experiments which need to be performed and the techniques which we have applied to address these various issues have been described in an earlier report in this series². When these techniques were applied to the Na/Xe model system the results indicated that in this system at least, adequate free metal atom concentrations could be attained and, equally important, that monomer and dimer concentrations could be predicted statistically.

The results were however subject to some uncertainty. Our determination of metal atom concentrations relied in part on optical absorption measurements and there is some question as to what value to assign to the oscillator strength of the FMA in the matrix. The associated uncertainty could produce an overestimate of at worst 30 per cent in the concentration determination. In principle this value can be established by combined measurements of the in situ radiative lifetime for the transition and the quantum efficiency of the radiative process.

There was an additional concern. Our results indicated that the metal monomer and dimer distribution could be described statistically in both the Li/Xe and Na/Xe systems.

Such a description would be valuable in describing other systems if it could be shown to have general validity. In some sense then, if the two systems studied are to lend support to this proposition, the expectation is that their optical behavior should be similar. This is certainly true in the case of absorption. By contrast their behavior in emission has been reported³ to be distinctly different. During this past year an LIF facility has been established in order to address some of these concerns.

Results

Temperature dependent measurements of the optical absorption observed in Na/Xe matrices can provide information about the ground and excited state interactions in the metal/matrix system. These measurements have been performed on samples prepared by codepositing known amounts of Na and Xe on a sapphire substrate attached to the cold finger of a liquid helium cryostat. The details of the instrumentation associated with the absorption measurements have been previously reported³. Figure 1 is typical of the absorption spectra observed in these systems at the outset of a temperature sequence. There are two set of triplets whose centroids lie to the blue and red of the free metal atom gas phase transition at 588.9 nm. These are distinguished by their thermal behavior, with one set being much more thermally labile. In our analysis the focus is on the peak at 548nm. It is the most isolated and contains the smallest contribution from neighboring members of the transition.

The analysis that has been performed is done within the context of the configuration coordinate model. This model was originally devised to explain the optical behavior of F⁻ centers in ionic lattices. It has subsequently been applied to a number of other insulator systems containing impurity species. The model approximates the thermal motion of the crystal around an impurity by the eigenmodes of a smaller system typically composed of the impurity and its nearest neighbor shell of matrix atoms. The eigenmodes obtained in this analysis yield effective eigenfrequencies for the host matrix and the possibility that the ground and excited state potential minima are offset is allowed for. The intensity of a transition in this scenario is given by the product of the transition probability and the Franck-Condon overlap factor. The transition probability is assumed independent of the vibrational quantum number. A further simplification which is often invoked assumes that the impurity couples primarily with one particular vibrational mode. This reduces the dimensionality of the problem. In order to make the transition to the experiment, the data are analyzed by the method of moments. This is effectively a truncated Fourier Transform technique and the details of this kind of analysis have appeared previously in the

⁴ literature. Several bits of information can be derived from this analysis. These are the frequency of the matrix eigenmode which couples most effectively to the impurity and the stability and vibrational frequency on the excited state surface at the point of transition. Based on the data (Fig. 2) the following can be said about the Na/Xe system. In the ⁻¹ ground state the chromophore couples to a matrix vibration with a frequency of 24cm^{-1} and the excited state vibrational frequency is negative. The latter may be viewed as indicative of a vertical transition from the ground state which results in an unstable excited state configuration. The system will distort spontaneously and the result may be a exciplex formation.

These measurements and analysis identify this system along with Li/Xe, as one to which the configuration coordinate model may reasonably be applied. However, the ⁵ reported emission from this system does not conform to this expectation. In order to identify the reason for these differences laser induced fluorescence measurements have been performed on Na/Xe matrices.

The experimental configuration for these experiments is shown schematically in Figure 3. Light from an excimer pumped dye laser operating with either Coumarin 540 or Rhodamine B is used to excite a metal matrix sample deposited on a sapphire substrate and maintained at a temperature between 3.04 and 38.2°K . In order to avoid local thermal damage to the matrix, a recurring problem in these kinds of experiments, the source is ² heavily attenuated. Input energies range from 100-500 nanojoules per pulse in a 2.8mm spot. Fluorescence from the excited sample is dispersed with a .125 meter monochrometer having a resolution of 2.5nm. The signal from the photomultiplier tube (R928,Hammamatsu) mounted behind the monochrometer is fed into a PAR 162/165 boxcar integrator. The measurements are typically taken with the boxcar operating with 5 microsecond windows and a 100 microsecond integrator time constant. The stripchart data obtained is subsequently digitized and analyzed using a MacIntosh based spread sheet program.

Initial experiments were performed by irradiating the metal atom containing sample in the region associated with either the red or blue absorption triplet. Pumping of the matrix with 578nm radiation corresponding to the red absorption triplet produced banded emission peaked at $\sim 790\text{nm}$ (Fig. 4). An excitation spectrum of the feature using emission at 790nm as a monitor produced an excitation which corresponded roughly to the red triplet absorption. It was dominated by an excitation peak centered at 580 nm. with a long blue tail extending out to 530nm. By contrast the initial experiments produced no observable resonance or Stokes shifted emission at any level which could be distinguished from the

bright fluorescence emanating from the substrate. The latter was characterized by a very intense feature at 697nm attached to a broad band emission extending with varying intensity over the entire spectral range accessible to the photomultiplier tube (600-885nm.). Interestingly, the peaks reported in the previous measurements correlate well with the emission observed from the substrate. That emission is presumably associated with Cr and Ti ion emissions from the sapphire. The peak at 697 nm correlates to the Cr lasing transition in ruby and the broad underlying background is most probably a combination of phonon sidebands of the (0-0) Cr transition and Ti ion transitions. These are two of the primary impurities observed in sapphire and may have affected some of the earlier results.

Discussion

Based on our experiments the following picture emerges for the Na/Xe system. First, the correlation observed in the statistical description of FEM distributions in the Na/Xe and Li/Xe systems extends beyond their absorption properties. Both systems are amenable to analysis with in the context of a configuration coordinate picture and both produce gaussian like emission bands whose peak values depend on the solvent matrix. Like the absorption spectra , the emission spectra should be amenable to a configuration coordinate analysis. This will yield excited state vibrational frequencies for the coupling modes involved and is currently being undertaken. Finally there are still some outstanding questions. Among these, one of the more notable deals with the emission from the blue triplet region. If it exists, why is it so inefficient and how does the absorbed energy degrade. There is evidence which suggests that absorption in the blue band produces an almost quantitative transfer of population from matrix configurations characterized by the blue triplet to those associated with red triplet absorption. If this is the case then it may be necessary to rethink the traditional picture which has evolved for these systems, that of two distinct matrix sites. A more appropriate description may be a single compound site containing two potential minima separated by a small barrier. This barrier could be overcome by the absorption of optical energy allowing diffusion between these minima.

References

1. N. Presser and A. T. Pritt, Jr., "High Energy Density Materials in Cryogenic Matrices," Proceedings of the High Energy Matter (HEDM) Conference, W. J. Lauderdale and W. A. Sowell (eds.), Rosslyn, VA, 12-13 May, 1987.
2. A. T. Pritt, Jr., N. Presser, and R. R. Herm, "Limitations on Atom Densities Cryogenic Matrices," Proceedings of the High Energy Matter (HEDM) Conference, T. G. Wiley and R. van Opijnen (eds.), New Orleans, LA, 12-15 March, 1989.

3. N. Presser, R. Poole, and A. T. Pritt, Jr., Proceedings of the High Energy Density Materials Contractors Conference, L. P. Davis and F. J. Wodarczak (eds.), Long Beach CA. 25-28 February, 1990.
4. M. Lax, J. Chem. Phys. **20**, 1752, (1952)
5. L. C. Balling, M. D. Havey and J. F. Dawson , J. Chem. Phys. **69**, 1670, (1978)

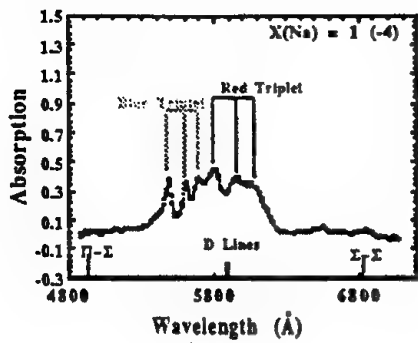


Figure 1

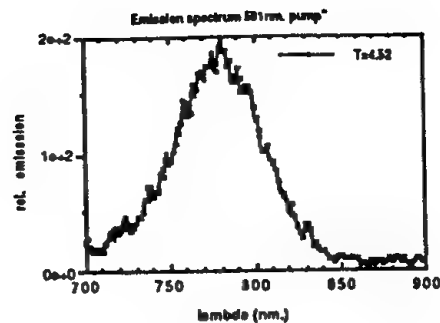


Figure 3

LIF EXPERIMENT

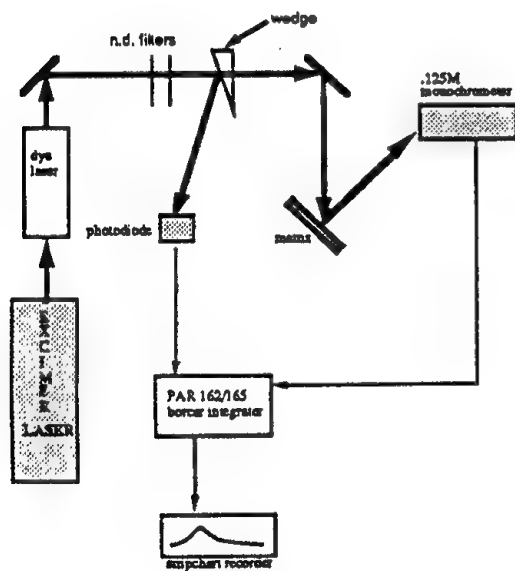


Figure 2

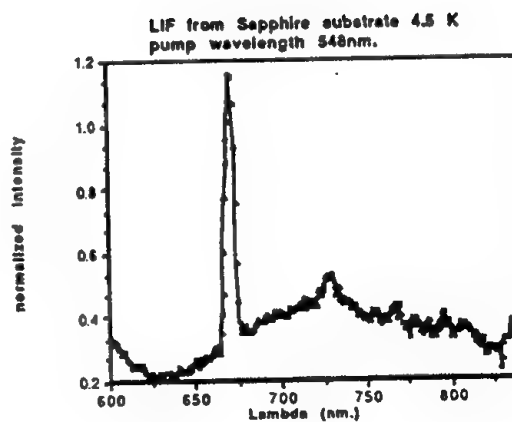


Figure 4

HIGH SYMMETRY METASTABLE MOLECULES

H. Helm, C. Bordas, M. J. Dyer, D. L. Huestis,
D. C. Lorents, Y. K. Bae and H. Bissantz

SRI International
Molecular Physics Laboratory

ABSTRACT

We present new data on three classes of molecules that we investigated recently in connection with the HEDM project work. A study of the stability of triatomic hydrogen in weak electric fields, a study of the stability of C₆₀ in multiphoton excitation, and a study of molecule formation in a high-pressure fully ionized oxygen plasma.

STABILITY OF TRIATOMIC HYDROGEN IN ELECTRIC FIELDS

Among the sequence of Rydberg states of H₃, we have discovered islands of instability of the molecule against predissociation.¹⁻³ The only exit channel for predissociation is the repulsive ground state surface of H₃. This surface does not intersect the Rydberg state surface. The unstable states are localized in well defined energy regions pointing to an underlying energy pattern of indirect coupling to the dissociation continuum (see Figure 1).

A most striking feature is that the stability is influenced by extremely weak electric fields. An example are the d-electron states in the region around of n = 61. These states of H₃ lie approximately 4 meV below the ionization threshold. Typically an electric field of 30 V/cm is required to field-ionize these states and this is how these states are detected. We see from Figure 2 that the n = 61 state population decays when very weak electric fields are applied, while neighboring states are largely unaffected.

A study of the p electron series in this energy range revealed that predissociation of (n = 61)p states occurs in the absence of an electric field. This finding indicates that the following sequence of events occurs:



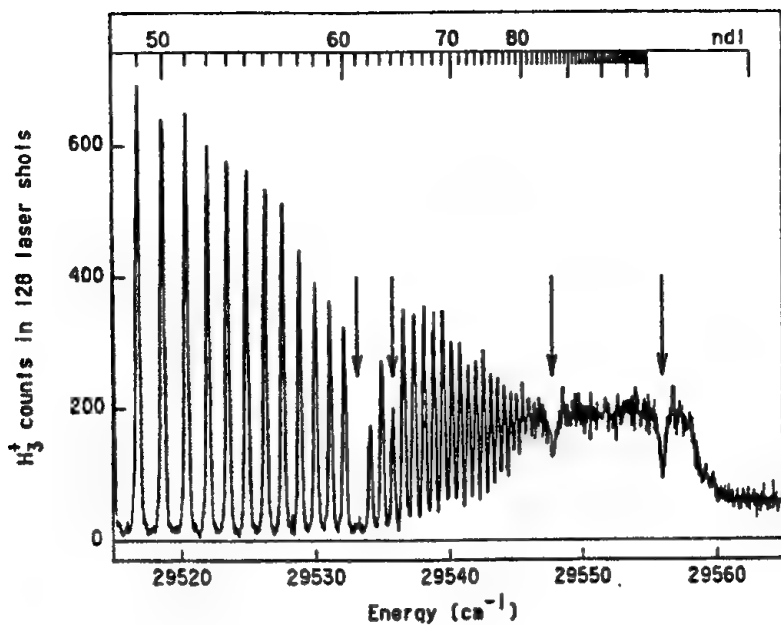


Figure 1. Photoexcitation of d-electron series at 0.5 V/cm.

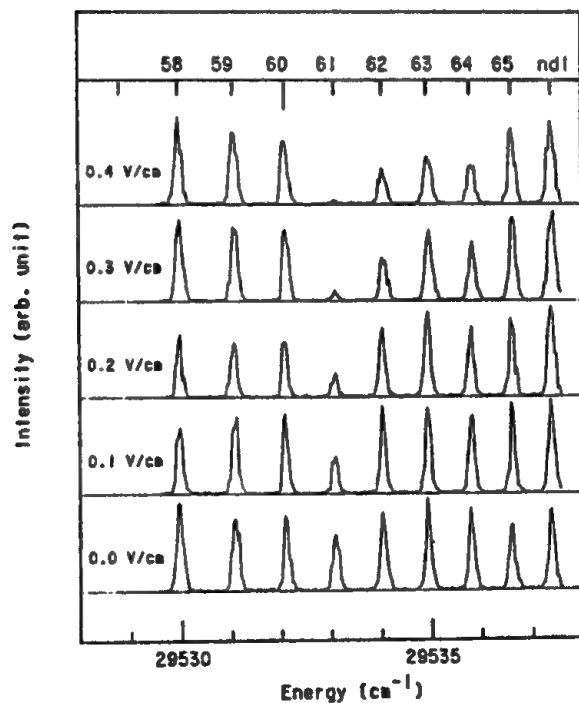
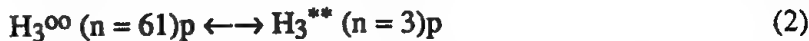


Figure 2. Onset of predissociation with electric field strength.

The ($n = 61$)p state is nearly degenerate with a highly vibrationally excited low- n Rydberg state.



The vibrationally excited Rydberg (vibrational excitation of ~ 2.5 eV) in turn is predissociated rapidly.

This experiment shows clearly that Rydberg states near the ionization threshold, and well removed from the ground state surface are predissociated. These paths have so far not been considered in the dissociative recombination process but they may explain the finite rate observed for $H_3^+ + e$ for thermal electrons.

STABILITY OF C_{60} IN MULTIPHOTON EXCITATION

We have carried out an exploratory study on the spectroscopy of C_{60} . The experiment uses a thermal beam of C_{60} molecules emerging from a Knudsen cell heated to 200-1000°C. Three sample results are shown in Figures 3-5.

Multiphoton ionization of C_{60} leads to significant fragmentation of the molecule as evident from Figure 3. A striking pattern emerges in the sense that fragment ions that have shed pairs of carbon atoms are prevalent. C_{32}^+ (half a soccer ball plus one C_2 molecule) is the lowest strong fragment ion. If the time-of-flight mass spectrometer is operated in such a way that fragments born with excess kinetic energy are rejected a much simplified fragmentation pattern emerges as shown in Figure 4.

A first measurement of the heat of sublimation of C_{60} from the magnitude of the MPI signal as a function of temperature of the Knudsen cell is given in Figure 5.

MOLECULAR OXYGEN

In our effort to search for the formation of polyatomic oxygen molecules larger than O_3 we have begun the proposed experiments for studying oxygen products from a high-pressure oxygen plasma environment. A very high-pressure, translationally and electronically hot (1-5 eV) oxygen plasma is deemed necessary to efficiently drive the reaction



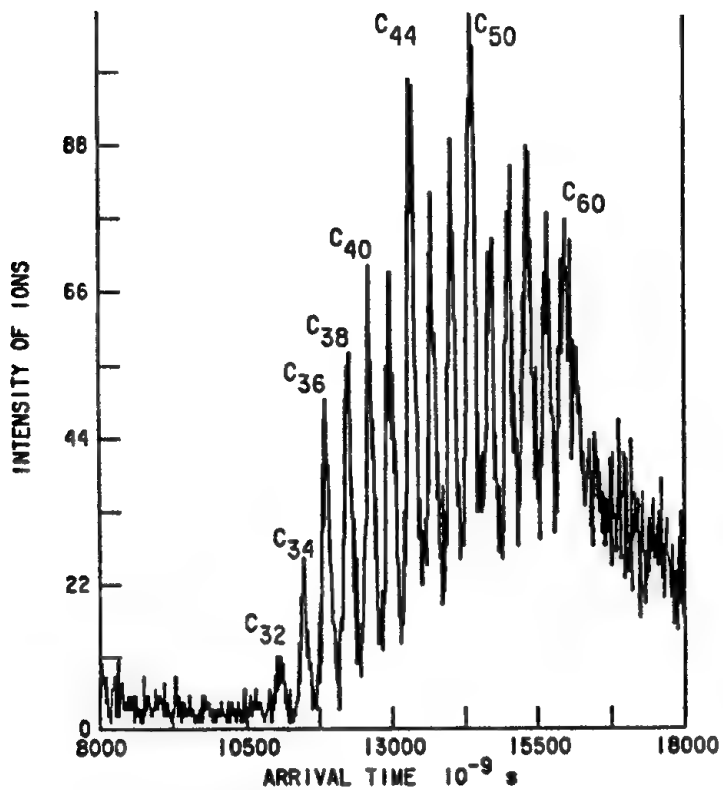


Figure 3. Photodissociation of C_{60} at 350 nm 10^9 W/cm^2

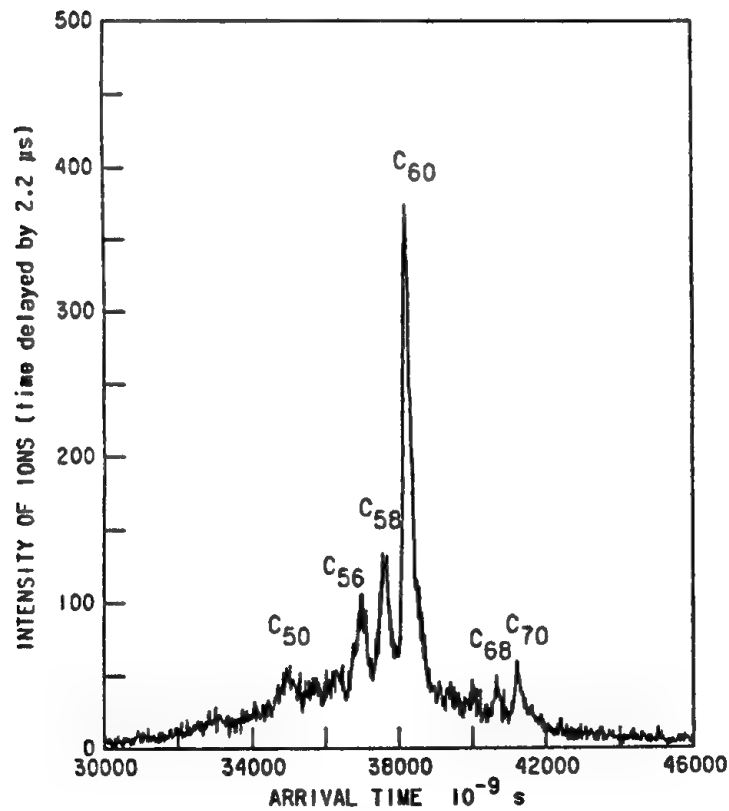


Figure 4. C_{60}/C_{70} mixture (823 K) at 340 nm $5 \cdot 10^8 \text{ W/cm}^2$

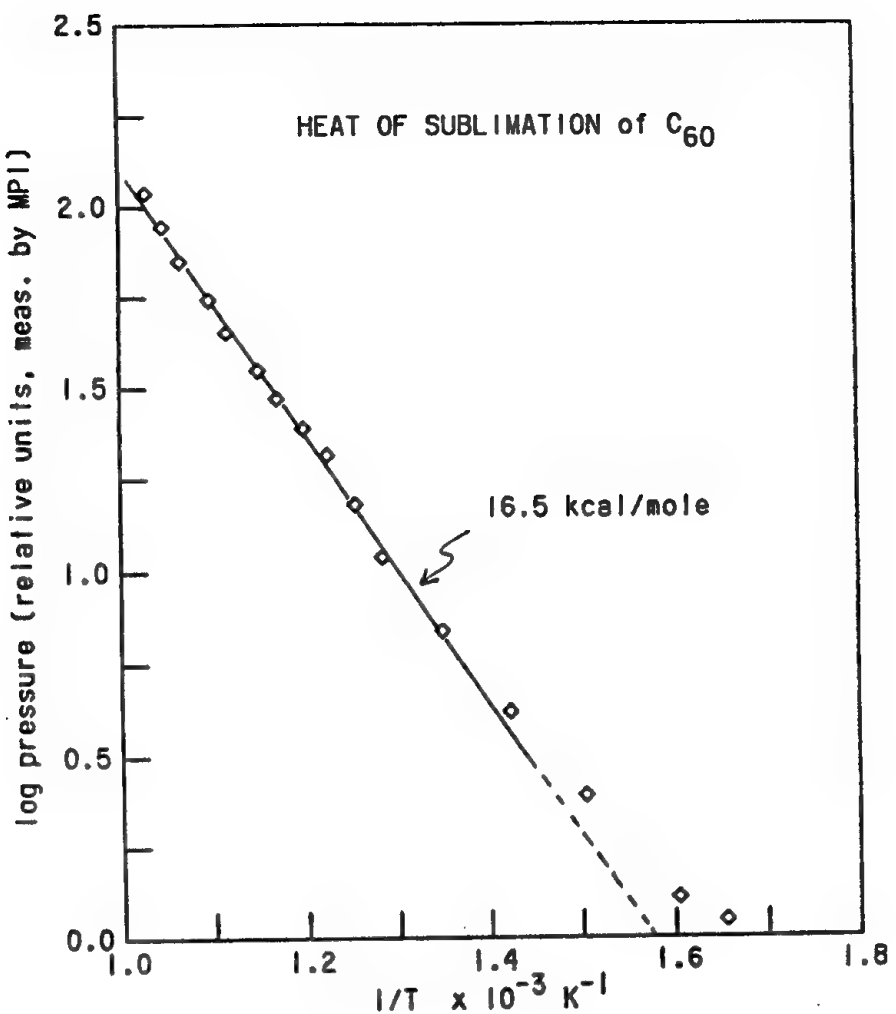


Figure 5. Vapor pressure from Knudsen cell filled with C₆₀

which according to the theoretical work of Seidl and Schaefer⁴ is endothermic by approximately 50 kcal/mole. In reaction (3) the O₄ species is not the van-der Waals dimer but the crown shaped ring-structure



This metastable O₄ species is predicted to be trapped in a localized well of the ground state surface, approximately 2 eV above the O₂ + O₂ limit, separated from the continuum by a barrier of about 150 meV. Similar "hot" reactants are required for forming the larger ring-species predicted by Schaefer, O₈ and O₁₂.

In the proposal stage to this contract we had anticipated employing a high-pressure hollow-cathode arc discharge for generating translationally and electronically hot atomic and molecular oxygen. Since the inception of this contract we have gained access to an extremely high-power tunable laser system. We will show below that this laser can generate extreme plasma environments not previously investigated. We anticipate that these conditions are very favorable for the our planned oxygen work and we describe the experimental concept and first results obtained.

We coin the experimental concept "oxygen focus" because it both describes the method used and the size of the reaction volume under study. The set-up is shown schematically in Figure 6. The idea is to use a tightly focused high power laser pulse to prepare a miniature volume ($\sim 10^{-8} \text{ cm}^3$) of fully ionized oxygen at near atmospheric pressure. Under these conditions dissociative recombination of O₂⁺ converts the molecular ions into translationally hot neutral oxygen atoms within 10^{-12} second. The next key to the experiment is to freeze three-body chemistry after approximately 50 - 200 ns by expanding this miniature volume into a high-vacuum region. The product states should then be examined by multiphoton photoionization.

The laser to accomplish this experiment is a home-built tunable dye laser with pulse duration 300-500 fs and with pulse energies exceeding 1 mJ. When this laser is focused to a beam waist of 15 μm diameter, the peak intensities in the focal volume exceed 10^{15} W/cm^2 . Since the focal volume ($\sim 10^{-8} \text{ cm}^3$) fills a nozzle which separates a high pressure region (100-1000 Torr) from a high vacuum region (10^{-6} Torr) the gas present in the focal volume is in the process of expanding into the vacuum region as shown schematically in Figure 1. This expansion freezes the three-body chemistry within a few nozzle diameters from the exit, thus preserving radicals and metastable species that could be deactivated otherwise.

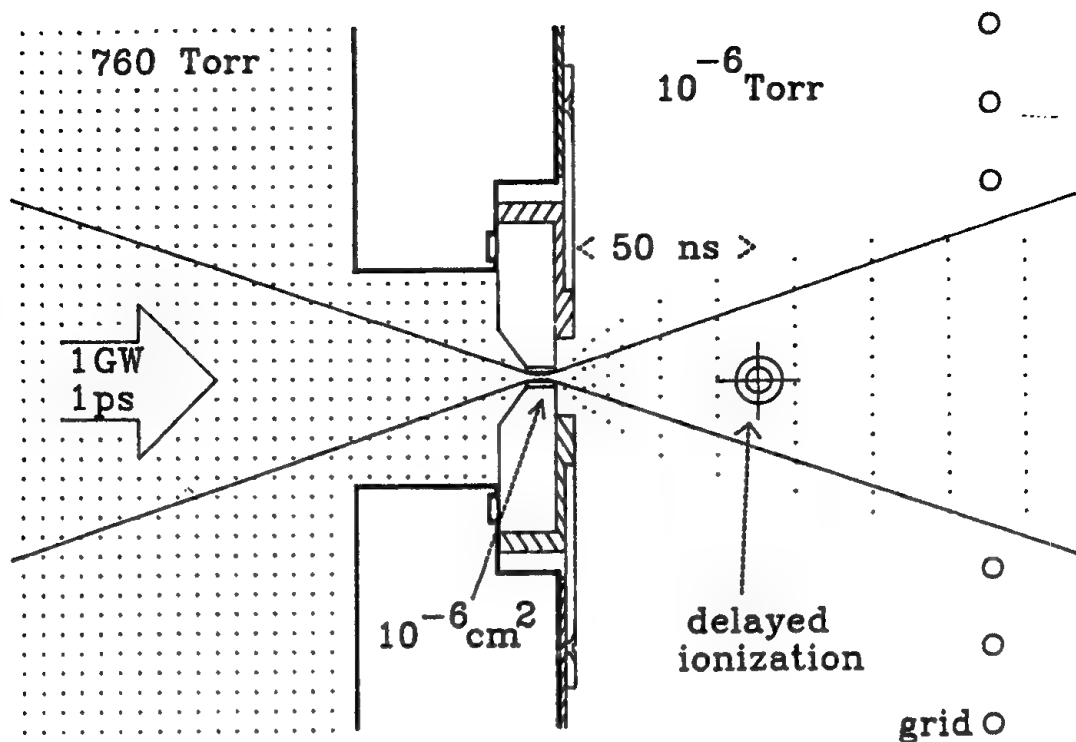


Figure 6. Oxygen Focus

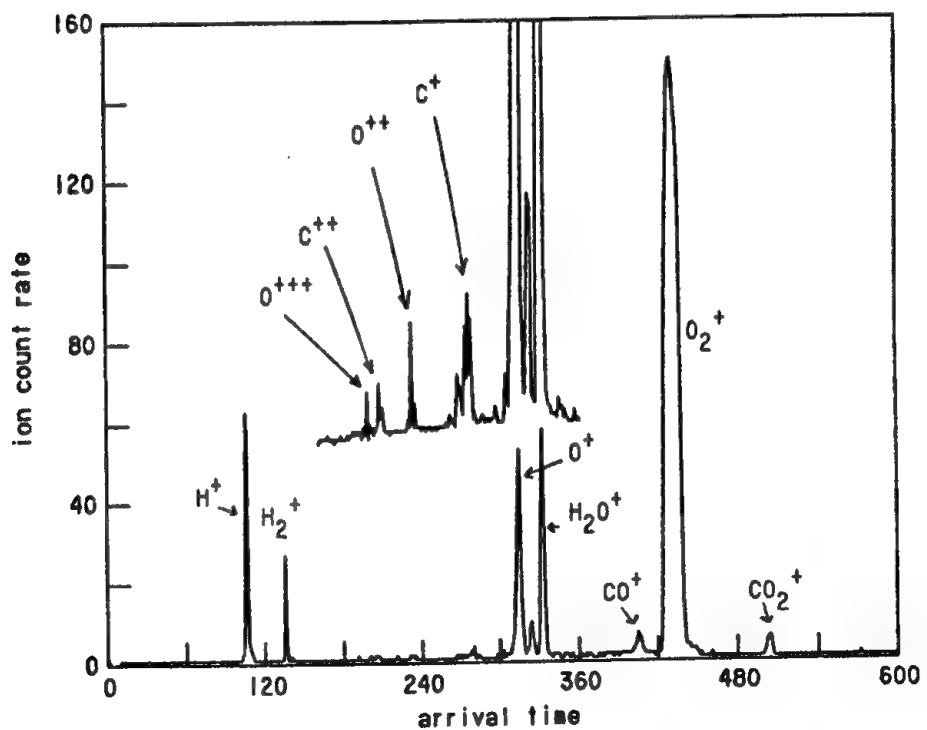


Figure 7. Photoionization of O_2 (635 nm, $\sim 5 \times 10^{13} W/cm^2$)

The energy density with which the focal region is illuminated amounts to ~ 100 kJ/cm³. At atmospheric pressure we then have approximately 30,000 photons per molecule in the focal region. This is in principle sufficient to multiple ionize every single molecule, and sufficient to generate O₂⁺, O⁺, O⁺⁺ and possibly a small amount of O⁺⁺⁺. This is indeed observed as shown in the low pressure photoionization spectrum of molecular oxygen using the high power laser given in Figure 7.

However, at high gas pressure, the high density of multi-photon dressed molecules may lead to harmonic generation by four wave mixing. The non-linear generation of higher harmonics will then compete with ionization, and is likely to diminish the rate of ionization.⁵ While the exact sequence of events is not known we may safely assume that a finite ionization rate will prevail at high intensities. Experimentally this is born out by the observation of breakdown in the focal volume.

To investigate the sequence of events after the laser has passed through the focal volume we looked at elementary processes that are expected to dominate the initial phase of the plasma afterglow. The by far fastest process should be dissociative recombination of O₂⁺, followed by ambipolar loss of charged particles, followed by slow reactions towards rebuilding oxygen species from the translationally and electronically hot oxygen atoms produced by dissociative recombination.

In initial experiments with the setup in Figure 6 we have used as nozzle a diamond pinhole with diameter of 0.0005 inch. We used rare gases in our first runs to save the pinhole surface until the tricks of the experiment were well enough understood. Our main observations so far are that the pinhole opens in reasonably short time to about (twice) this diameter although the laser beam is near diffraction limited and should pass at 1/e² intensities through the aperture. The conclusion is that intensities outside the focal waist are sufficient to significantly ablate diamond. This is also evidenced by the fact that C⁺, C₂⁺ and C₃⁺ have always been the dominant ions emerging from the focal region.

We have then begun to drill holes with the laser itself into 0.2 mm thick tungsten but find also in this case rapid (a few hundred laser shots) opening of the aperture. Our current attempts focus on ceramic material in which we have been able to sustain holes as small as 10 μm for extended periods of time.

REFERENCES

1. H. Helm, Phys. Rev. Lett. **56**, 42 (1986); and Phys. Rev. A**38**, 3425 (1988).
2. C. Bordas, and H. Helm, Phys. Rev. A **43**, April 1st (1991).
3. L. J. Lembo and H. Helm, Chem. Phys. Lett. **163**, 425 (1989).
4. E. T. Seidl and H. F. Schaefer III , J. Chem. Phys. **88**, 7043 (1988).

Extended Abstract

Theoretical Studies of Metastable Ions: NH₄⁻ and PH₄⁻

Nikita Matsunaga and Mark S. Gordon

North Dakota State University

Introduction

The hypervalent NH₄⁻ anion has been observed via Fourier-transform mass spectrometry[1]. The authors have concluded that the ion observed in their deuterium labeling study is best described as a hydride ion solvated by an ammonium. The other experimental evidence, photoelectron spectroscopy[2,3], has suggested that the tetrahedral structure of NH₄⁻ exists on the potential energy surface(PES). Several theoretical calculations have been done to date[4-9]. The complex between NH₃ and H-, in which the hydride ion is almost colinear with one of the N-H bonds, has been speculated to be the global minimum on the PES. Also, the tetrahedral structure was found[7,9] to be a metastable minimum.

The phosphorus analog, PH₄⁻, has received little attention theoretically or experimentally. Trinquier *et al.*[10], have used a pseudopotential method to investigate two structures, C_{2v}(distorted trigonal bipyramidal where the two axial hydrogens are bent) and C_{4v}(square-pyramidal). They have proposed that there might be a pseudorotational motion taking place for the conversion of the two structures.

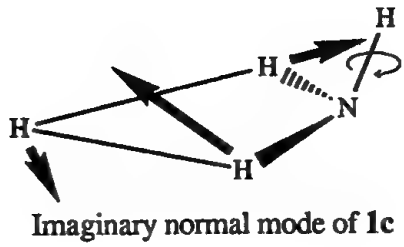
Hypervalent molecules are often metastable. The above mentioned hypervalent species could, therefore, be considered as potential HEDM molecules. We report here the results of *ab initio* calculations of NH₄⁻ and PH₄⁻ ions. Calculations are in progress to examine the reaction coordinates of the ions by means of intrinsic reaction coordinate(IRC)[11] calculations. These IRC's will be used to construct reaction path hamiltonians to facilitate dynamics calculations, such as variational transition state theory.

Method

The structures are optimized at the MP2/6-31++G(d,p) and MP2/6-311++G(d,p) levels of theory and are verified as minima or transition states by diagonalizing the matrix of energy second derivatives(hessian). The energies are further refined with MP4 using the above mentioned basis sets and two other basis sets, 6-311++G(2d,2p) and 6-311++G(2df,2pd), at MP2/6-311++G(d,p) structures. QCI calculations are performed with 6-311++G(2d,2p). The QCI/6-311++G(2df,2pd) energy is deduced by assuming the basis set corrections due to higher polarization functions (f functions on heavy atoms and d functions on hydrogens) and the higher order correlation corrections are additive. This is similar to the procedure used in G1 theory[12].

NH₄⁺

The total energies and the zero point energies(ZPE) of the reference atom and molecules, i.e. H⁺, H₂, NH₃, NH₂⁺, PH₃, and PH₂⁺, are shown in Table 1. The structures of the NH₄⁺ stationary points are shown in Figure 1. The lowest energy structure of NH₄⁺ (**1a**) has C_{3v} symmetry, in which the hydride ion is solvated by an ammonia. It lies 8.8 kcal/mol below the dissociation limit, NH₃ + H⁺, at the QCI/6-311++G(2df,2pd) level of theory(see Table 2). The MP2/6-31++G(d,p) IRC calculations obtained by following the imaginary normal mode of **1e** shows that it is connected to the global minimum (**1a**) gaining 9.8 kcal/mol and to another transition state (**1b**) on the PES(see Figure 2). The imaginary normal mode of **1b** suggests that it also leads to **1a**. The bifurcated structure of NH₄⁺ (**1c**) is a transition state, and the imaginary normal mode shows that the two bifurcated hydrogens are moving out of the symmetry plane with a pivoting N-H bond.

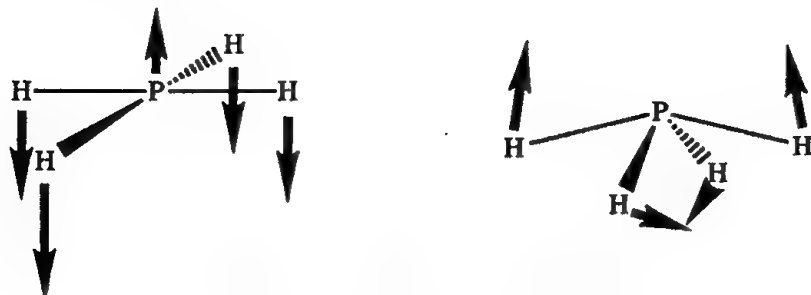


The T_d structure (**1d**) is confirmed to be a minimum at both MP2/6-31++G(d,p) and MP2/6-311++G(d,p) levels of theory. It is 20.9 kcal/mol above the global minimum at the highest level of theory. The bond distances are somewhat larger in comparison to NH_3 as expected. The highest occupied MO of the tetrahedral species is diffuse and totally symmetric(A_1), and, therefore, the electrons are loosely held.

PH_4^-

The lowest energy minimum of PH_4^- (**2a**) also has C_s symmetry, however, the structure is quite different from NH_4^+ . The structure can be described as a molecular hydrogen complexed very weakly with PH_2^- owing to the fact that the $\text{PH}_2^- + \text{H}_2$ is substantially lower in energy than the dissociation to $\text{PH}_3 + \text{H}^-$ (see Table 3). **2a** lies only 1.21 kcal/mol below $\text{PH}_2^- + \text{H}_2$ and 34.6 kcal/mol below $\text{PH}_3 + \text{H}^-$ at the QCI/6-311++G(2df,2pd) level of theory. The C_{2v} structure (**2b**) is a transition state leading to **2a**. There is no transition state connecting the global minimum (**2a**) with **2b** in PH_4^- as found in NH_4^+ since the direct conversion of **2b** to **2a** is readily accessible. The MP2/6-31++G(d,p) bifurcated structure (**2c**) is a transition state with an associated frequency $161.0i\text{ cm}^{-1}$. The imaginary frequency disappears at the MP2/6-311++G(d,p) level of theory to become a minimum on the PES. The tetrahedral structure (**2d**) is a minimum which lies 69.2 kcal/mol above the dissociation to $\text{PH}_2^- + \text{H}_2$. The transition state connecting **2d** to any other structures has not yet been identified. There are two PH_4^- structures which are not found in NH_4^+ , D_{4h} (**2e**) and C_{4v} (**2f**). **2e** is 5.9 kcal/mol higher in energy than **2f**. These are transition states of

possible pseudorotation motion. The imaginary normal mode of $2e$ corresponds to the bending of all four hydrogens to become $2f$.



Imaginary normal modes of $2e$ and $2f$

The motion of the hydrogens in $2f$ is similar to the pseudorotation found in SiH_5 [13] except the fact that an equatorial substituent is replaced by a phosphorus lone pair.

References

1. J. C. Kleingeld, S. Ingemann, J. E. Jalonen, and N. M. M. Nibbering, *J. Am. Chem. Soc.*, 105, 2474 (1983)
2. J. V. Coe, J. T. Snodgrass, C. B. Freidhoff, K. M. McHugh, and K. H. Bowen, *J. Chem. Phys.* 83, 3169 (1985)
3. J. T. Snodgrass, J. V. Coe, C. B. Freidhoff, K. M. McHugh, and K. H. Bowen, *Faraday Discuss. Chem. Soc.*, 86, 241 (1988)
4. C. D. Ritchie and H. King, *J. Am. Chem. Soc.*, 90, 838 (1968)
5. J. Kalcher, P. Rosmus, and M. Quack, *Can. J. Phys.*, 62, 1323 (1984)
6. D. Cremer and E. Kraka, *J. Am. Chem. Soc.*, 90, 33 (1986)
7. H. Cardy, C. Larrieu, and A. Dargelos, *Chem. Phys. Lett.*, 131, 507 (1986)
8. J. V. Ortiz, *J. Chem. Phys.*, 87, 3557 (1987)
9. J. V. Ortiz, *J. Phys. Chem.*, 94, 4762 (1990)
10. G. Trinquier, *J. Am. Chem. Soc.*, 106, 4794 (1984)
11. K. K. Baldridge, M. S. Gordon, R. Steckler, and D. G. Truhler, *J. Phys. Chem.*, 93, 5107 (1989)
12. J. A. Pople, M. Head-Gordon, D. J. Fox, K. Raghavachari, and L. Curtiss, *J. Chem. Phys.*, 90, 5622 (1989)
13. T. L. Windus, M. S. Gordon, L. P. Davis, and L. W. Burgraf, *J. Am. Chem. Soc.*, 112, 7167 (1990)

Table 1. Total energies and zero point energies of the reference atom and molecules. (Energies in hartree)

Theory	6-31++G(d,p) ^a	6-311++G(d,p) ^b	6-311++G(2d,2p) ^b	6-311++G(2df,2pd) ^b
NH ₃				
RHF	-56.20085	-56.21436	-56.21768	-56.21874
MP2	-56.39633	-56.43468	-56.45440	-56.47582
MP3	-56.40794	-56.44608	-56.46523	-56.48720
MP4	-56.41420	-56.45425	-56.47442	-56.49678
ZPE ^c	0.03534	0.03489		
NH ₂ ⁺				
RHF	-55.52742	-55.54122	-55.54448	-55.83614
MP2	-55.73552	-55.77458	-55.79780	-55.81819
MP3	-55.73837	-55.77673	-55.79933	-55.82030
MP4	-55.75051	-55.79132	-55.81495	-55.83614
ZPE ^c	0.01899	0.01886		
PH ₃				
RHF	-342.45503	-342.47896	-342.48251	-342.48475
MP2	-342.59289	-342.66045	-342.68686	-342.71155
MP3	-342.61381	-342.68318	-342.71087	-342.73632
MP4	-342.62008	-342.69042	-342.71910	-342.74530
ZPE ^c	0.02523	0.02498		
PH ₂ ⁺				
RHF	-341.85779	-341.88105	-341.88328	-341.88510
MP2	-341.99299	-342.05891	-342.09164	-342.11489
MP3	-342.01088	-342.07799	-342.11238	-342.13662
MP4	-342.01718	-342.08528	-342.12036	-342.14583
ZPE ^c	0.01358	0.01345		
H ₂				
RHF	-1.13140	-1.13250	-1.13301	-1.13301
MP2	-1.15777	-1.16030	-1.16280	-1.16466
MP3	-1.16328	-1.16627	-1.16875	-1.17028
MP4	-1.16469	-1.16776	-1.17026	-1.17174
ZPE ^c	0.01047	0.01033		
H				
RHF	-0.48707	-0.48693	-0.48696	-0.48696
MP2	-0.50363	-0.50561	-0.50958	-0.51049
MP3	-0.50828	-0.51070	-0.51584	-0.51629
MP4	-0.51039	-0.51285	-0.51820	-0.51859

a) Geometries optimized at MP2/6-31++G(d,p)

b) Geometries optimized at MP2/6-311++G(d,p)

c) ZPE, zero-point energies are calculated at MP2 level of theory for corresponding basis set

**Table 2. The Enthalpy Difference of NH_3^+ with respect to $\text{NH}_3 + \text{H}^+$ (kcal/mol)
and Zero-Point Energies(hartree)**

Theory	6-31++G(d,p) ^a	6-311++G(d,p) ^b	6-311++G(2d,2p) ^b	6-311++G(2df,2pd) ^b
1a(C ₁)	RHF	-4.4	-4.1	-3.9
	MP2	-7.8	-8.5	-9.0
	MP3	-7.3	-8.1	-8.6
	MP4	-7.5	-8.4	-9.0
	QCI ^c			-8.8
	ZPE ^d	0.03736	0.03681	
1e(C ₁ [ts])	RHF	17.0	16.5	16.8
	MP2	4.6	-1.2	-2.0
	MP3	0.6	0.4	3.6
	MP4	2.4	0.3	0.1
	QCI ^c			1.5
	ZPE ^d	0.03736	0.03203	
1d(T _d)	RHF	16.7	17.0	17.5
	MP2	11.5	8.3	11.9
	MP3	6.9	8.2	12.8
	MP4	6.0	7.5	12.1
	QCI ^c			12.7
	ZPE ^d	0.04489	0.04428	
1b(C _{2v} [ts])	RHF	13.2	12.3	12.6
	MP2	2.5	-2.6	-3.7
	MP3	3.2	2.6	2.2
	MP4	0.1	-1.0	-1.3
	QCI ^c			0.1
	ZPE ^d	0.03335	0.03287	
1c(C ₁)	RHF	-4.3	-4.1	-3.9
	MP2	-2.0	-6.7	-6.7
	MP3	-6.0	-6.5	-6.7
	MP4	-6.1	-6.6	-6.9
	QCI ^c			-7.0
	ZPE ^d	0.03650	0.03606	
NH ₃ +H ₂	RHF	14.6	13.8	13.5
	MP2	0.5	-0.2	-1.5
	MP3	5.4	5.1	4.6
	MP4	2.2	1.4	1.1
	QCI ^c			2.5

a) Geometries are optimized at MP2/6-31++G(d,p).

b) Geometries are optimized at MP2/6-311++G(d,p).

c) QCI/6-311++G(2d,2p) results are of actual calculations and QCI/6-311++G(2df,2pd) values are deduced by modified G1 method.

d) ZPE, zero-point energies are calculated at MP2 level of theory for corresponding basis set.

**Table 3. The Enthalpy Difference of PH₃ with respect to PH₃ + H (kcal/mol)
and Zero-Point Energies(hartree)**

Theory	6-31++G(d,p) ^a	6-311++G(d,p) ^b	6-311++G(2d,2p) ^b	6-311++G(2df,2pd) ^b
2a(C ₁)	RHF	-29.2	-29.4	-28.9
	MP2	-34.6	-34.0	-37.0
	MP3	-33.2	-32.3	-34.7
	MP4	-32.8	-32.0	-34.1
	QCI ^c			-33.0
	ZPE ^d	0.02689	0.02679	-33.5
2b(C _{2v} ,[ts])	RHF	-29.6	-30.0	-29.5
	MP2	-34.8	-34.2	-37.2
	MP3	-33.4	-32.5	-35.0
	MP4	-33.0	-32.2	-34.4
	QCI ^c			-33.2
	ZPE ^d	0.2644	0.2612	-33.8
2d(T _d)	RHF	43.6	42.2	42.0
	MP2	32.8	31.7	35.9
	MP3	33.3	32.4	38.0
	MP4	32.6	31.4	36.8
	QCI ^c			37.4
	ZPE ^d	0.02555	0.02384	37.0
2e(D _{4h})	RHF	22.8	22.1	21.3
	MP2	10.5	8.3	5.0
	MP3	11.8	9.7	7.2
	MP4	12.0	9.7	7.5
	QCI ^c			8.8
	ZPE ^d	0.03073	0.03049	5.3
2f(C _{4v})	RHF	14.0	13.2	12.5
	MP2	4.0	1.4	-1.0
	MP3	5.2	2.4	0.5
	MP4	5.4	2.4	0.6
	QCI ^c			1.8
	ZPE ^d	0.02930	0.02898	-0.6
2c(C ₁)	RHF	-2.0	-1.4	-1.8
	MP2	-2.8	-3.1	-4.1
	MP3	-2.6	-3.0	-4.0
	MP4	-2.6	-3.0	-4.1
	QCI ^c			-4.3
	ZPE ^d	0.02574	0.02605	-4.1
PH ₃ +H ₂	RHF	-31.0	-30.6	-30.1
	MP2	-36.4	-34.1	-37.2
	MP3	-35.0	-32.4	-34.9
	MP4	-34.6	-32.0	-34.2
	QCI ^c			-32.4
	ZPE ^d			-32.3

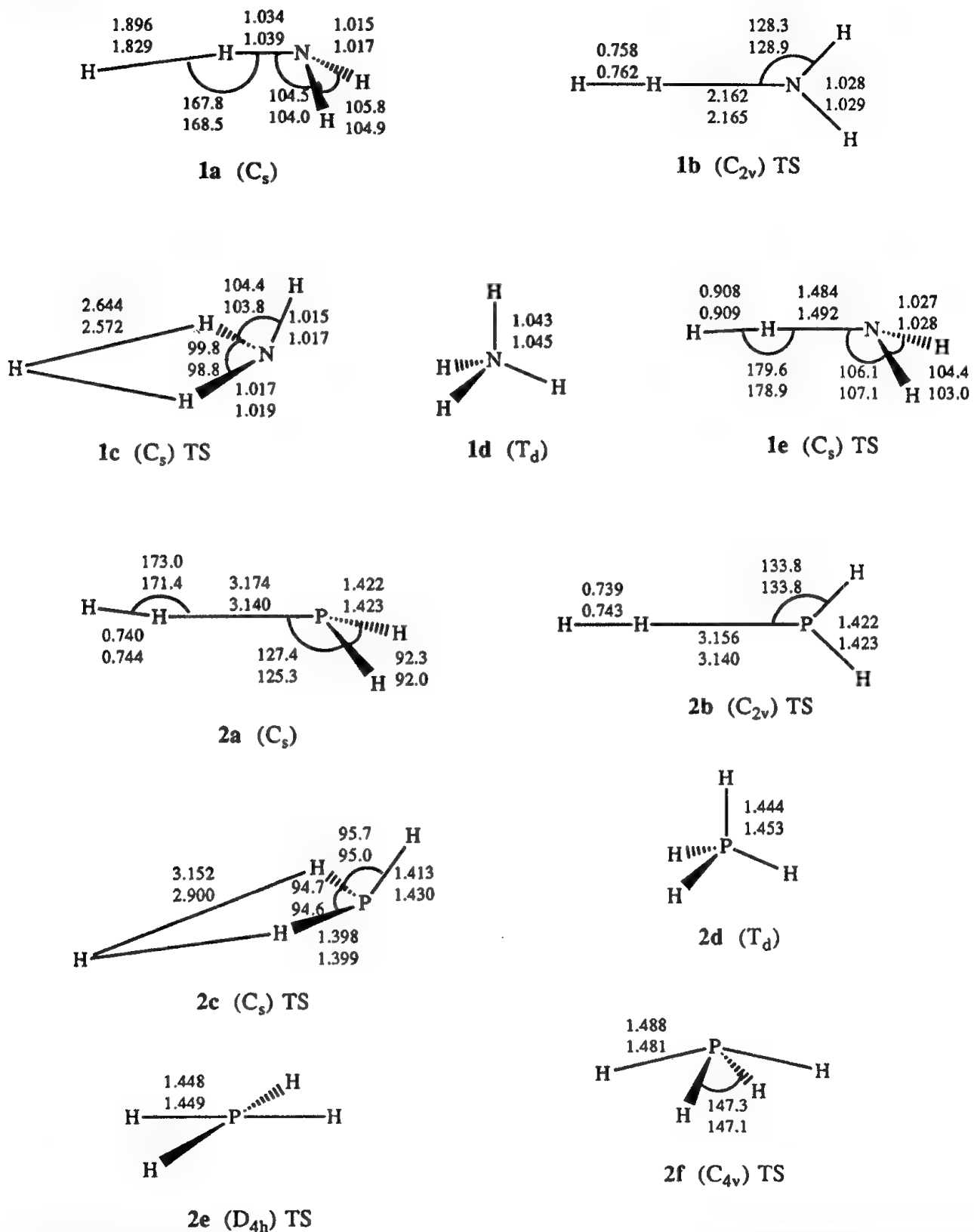
a) Geometries are optimized at MP2/6-31++G(d,p).

b) Geometries are optimized at MP2/6-311++G(d,p).

c) QCI/6-311++G(2d,2p) results are of actual calculations and QCI/6-311++G(2df,2pd) values are deduced by modified G1 method.

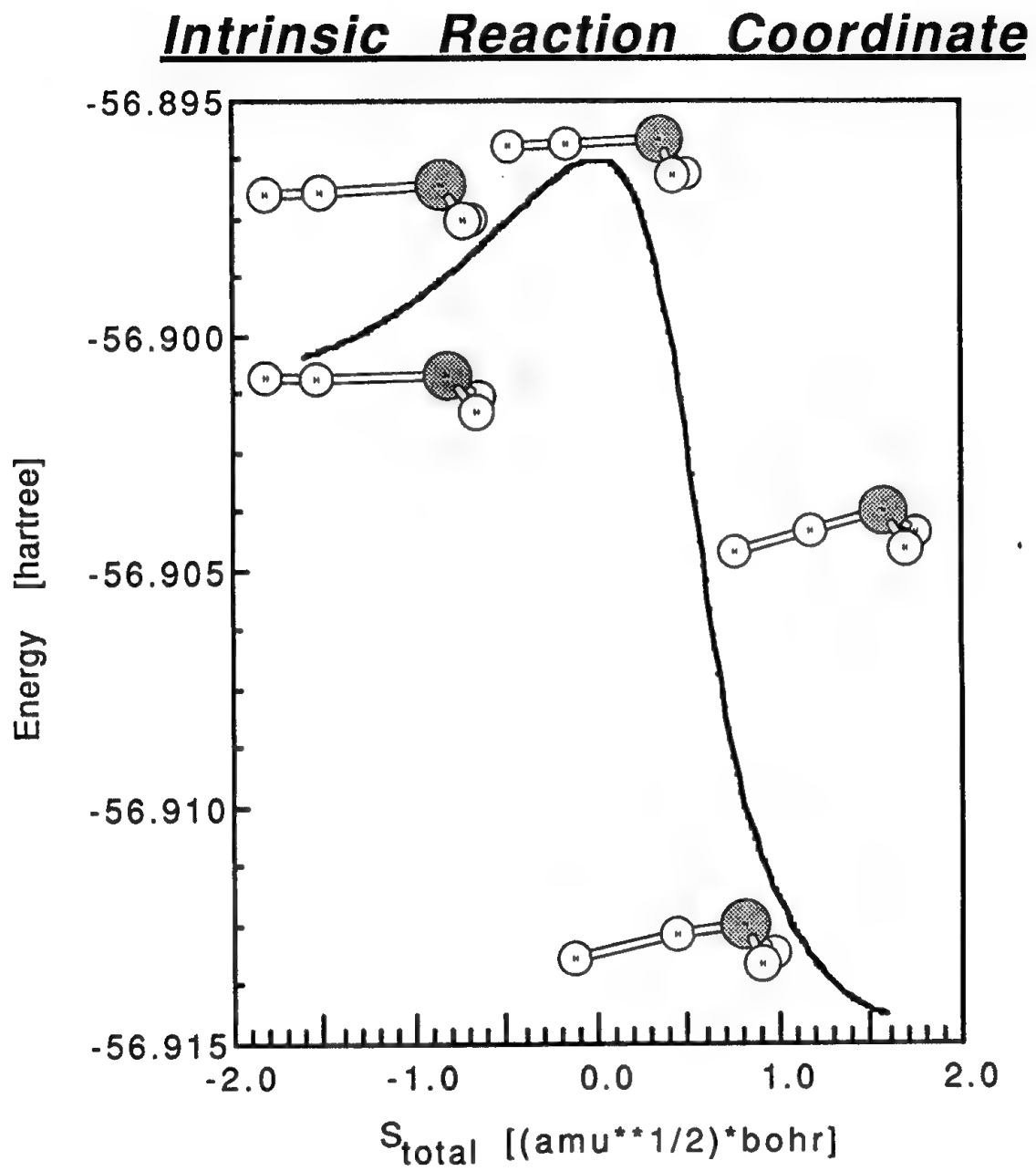
d) ZPE, zero-point energies are calculated at MP2 level of theory for corresponding basis set.

Figure 1. MP2 optimized structures^{a)} of NH_4^+ and PH_4^+



a) The geometries are optimized with MP2/6-31++G(d,p)(the values on the top) and MP2/6-311++G(d,p)(the values on the bottom) levels of theory.

Figure 2. Intrinsic Reaction Coordinate^{a)} Starting from 1e



a) Calculations are done at 6-31++G(d,p) level of theory.

THE SEARCH FOR LITHIUM-ALUMINUM

P. G. Carrick
Phillips Laboratory
Propulsion Directorate
Edwards Air Force Base, CA

and

C. R. Brazier
University of Dayton Research Institute
Phillips Laboratory
Propulsion Directorate
Edwards Air Force Base, CA

MOTIVATION: Trapping of metal atoms or small metal clusters in cryogenic propellants can lead to significant increases in the specific impulse of currently available rocket propulsion systems. One goal of the High Energy Density Materials (HEDM) program at the Propulsion Directorate of the Phillips Laboratory is to stabilize these metallic atoms or molecules in solid hydrogen. The specific metals of interest include lithium, boron, magnesium, and aluminum. The intermetallic diatomic molecules composed of these metals are also of interest, as illustrated in Figure 1. Of these intermetallic molecules, very few have singlet (and presumably more stable) ground states. One such intermetallic diatomic molecule that is predicted to have a singlet ground state is the lithium-aluminum (LiAl) molecule.

APPROACH: High level calculations are necessary to determine if LiAl has a singlet ground state and additionally to provide information about the excited vibrational and electronic states for spectroscopic observation. Multi-reference CI calculations determined that LiAl has a singlet sigma ground state and several bound excited states (see the abstract for M. Rosenkrantz's presentation). This provided enough information to begin an experimental search for the LiAl molecule.

SEARCH: Several different techniques have been used in the search for LiAl. The products from laser ablation of a commercial lithium-aluminum alloy (4:1 Al:Li) with a pulsed Nd:YAG laser were examined by mass spectrometry using a triple quadrupole mass spectrometer. No LiAl signal was observed upon electron impact ionization of the neutral metal ablation products, but direct detection of ions produced in the plasma showed a weak LiAl⁺ signal, as shown in Figure 2. Other molecular species detected in the laser ablation source include ⁷Li₂⁺ and ⁶Li⁷Li⁺, indicating good sensitivity to molecular formation. However, essentially no Al₂⁺ was observed. Attempts to observe Laser Induced Fluorescence (LIF) in this source were plagued by variations in the ablation intensity due to pulse-to-pulse variations in the Nd:YAG ablation laser and irregularities in the rotating target. The laser ablation experiments will be modified to use shorter wavelength ablation (193 nm) and photoionization with mass spectroscopic detection to overcome these problems.

Recently, the reaction of sputtered aluminum atoms with lithium vapor has been studied. An aluminum sputtering source was constructed to direct a flow of aluminum atoms into a lithium heat pipe. Windows in the interaction region allow laser excitation of the products and detection of fluorescence or emission. A band was observed near 655.0 nm from reaction of the sputtered atoms with the lithium. This could not be conclusively assigned to any known species and further work remains to confirm that this system is due to LiAl. Several different sputtering sources were used in this work. They were all plagued to some extent by interaction of the lithium vapor with the discharge process. A modification of the final, fairly successful, design is underway in the hope of obtaining stable and reproducible conditions.

Further experiments are underway to determine if the spectra obtained are from LiAl. Two other sources are under construction. The first consists of a dual thermal oven source in which aluminum and lithium are separately vaporized and allowed to mix in the presence of an argon buffer gas, which will be probed by laser excitation of either the atomic aluminum line at 396.15 nm or the atomic lithium line at 670.78 nm (or both) with chemiluminescence emission and by LIF. The second source is a jet expansion ablation source which will be examined by mass spectroscopy using laser photoionization and resonant two photon ionization.

Isp Payoffs with Metal Diatomics

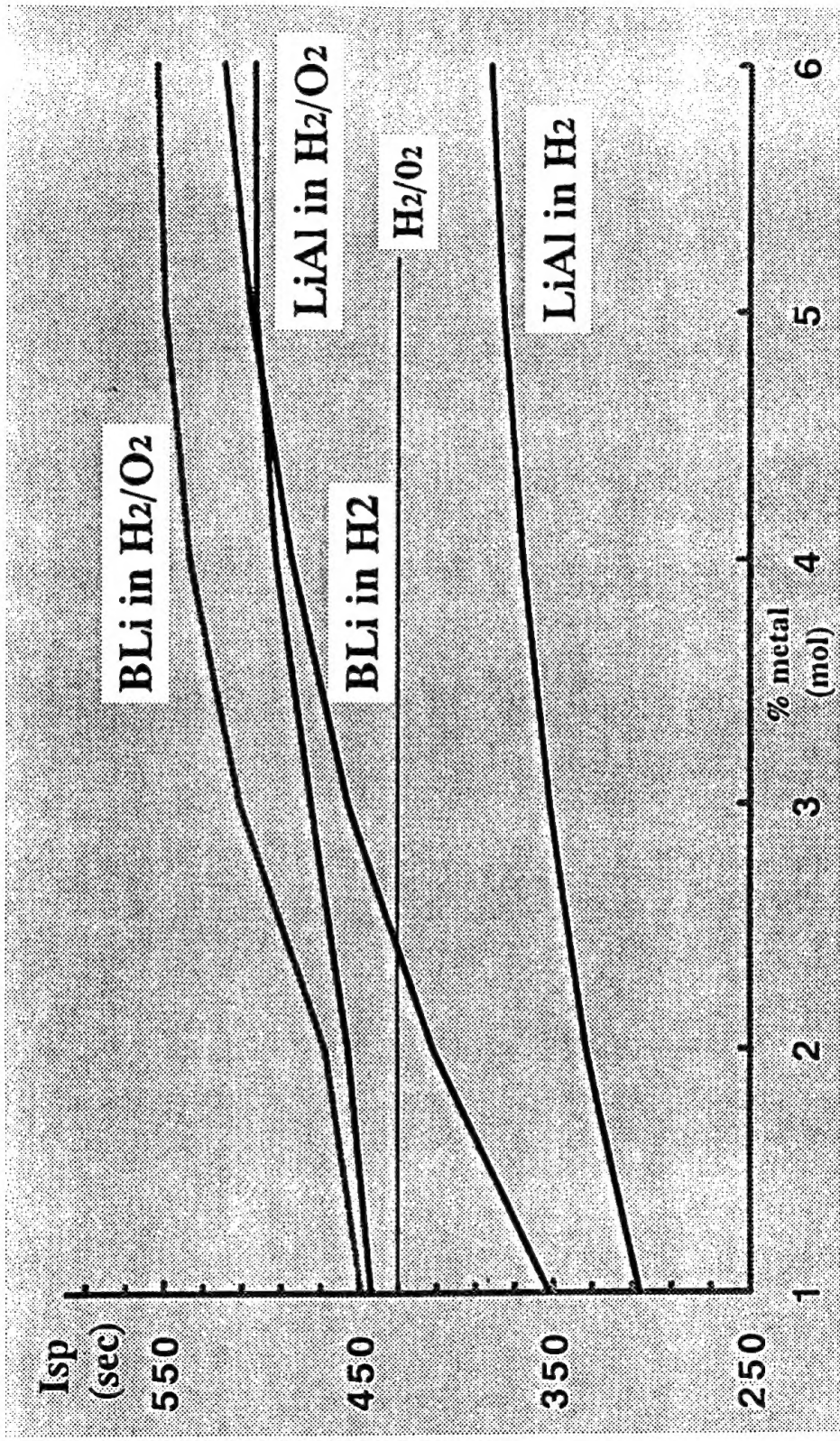


Figure 1

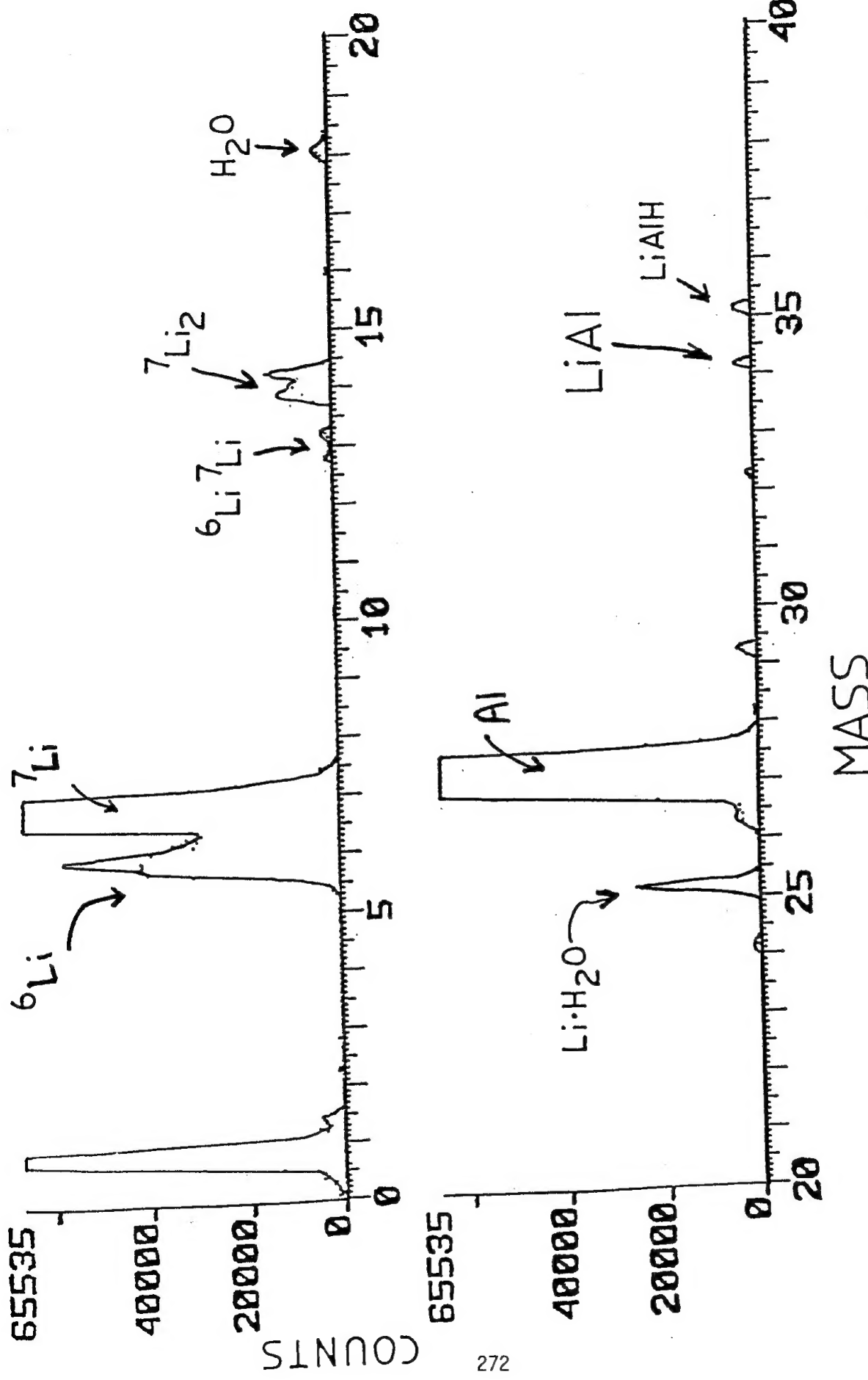
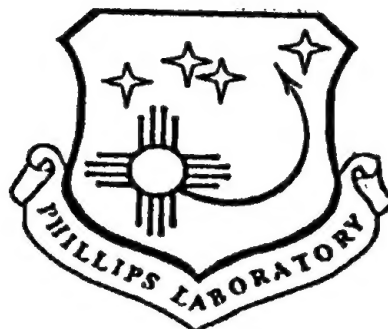


Figure 2

The Phillips Laboratory

at

Edwards Air Force Base, CA



is looking for NRC resident research associates in experimental and computational chemistry.
All interested candidates are encouraged to apply.

For more information, please call:

Dr Stephen Rodgers	(805) 275-5623
Dr Jerry Boatz	(805) 275-5364
Dr Pat Carrick	(805) 275-5883
Dr Robert Cohn	(805) 275-5753
Dr Mario Fajardo	(805) 275-5946
Dr Jeff Gilman	(805) 275-5749
Dr Dan Konowalow	(805) 275-5761
Dr Marcy Rozenkrantz	(805) 275-5762

Or write to any of the above at:
OLAC PL/RFE
Edwards Air Force Base
California 93523-5000